

Diss. ETH No 11338

# Measuring the partonic structure of the photon at the $ep$ collider HERA

A dissertation submitted to the  
**Swiss Federal Institute of Technology Zurich**  
for the degree of  
**Doctor of Natural Sciences**

presented by

**Marco Arpagaus**

dipl. phys. ETH

born 1st November 1965

citizen of Uors-Peiden (GR) and

Illnau-Effretikon (ZH)

accepted

on the recommendation of

Prof. Dr. R.A. Eichler, examiner, and

Prof. Dr. F. Pauss, co-examiner

1995



# Abstract

This thesis presents the measurements of the inclusive parton cross-sections  $d\sigma/dp_t$  and  $d\sigma/d\eta$  in the photoproduction régime of electron proton scattering as well as the determination of the gluon density function of the (quasi-real) photon,  $f_{g/\gamma}(x_\gamma)$ . All three quantities are sensitive to the partonic structure of the photon, especially to its gluon content.

The results are derived by studying 2-jet events measured with the H1 detector at the  $ep$  collider HERA. The data on which this analysis is based were collected during 1993 and amount to an integrated luminosity of  $L = 255 \text{ nb}^{-1}$ .

The major difficulty in obtaining the above results is to control the influence of a still poorly understood transverse energy flow seen in the data but absent in the theoretical predictions for the studied processes. Three different methods to account for the influence of this energy flow are presented and the results of the three approaches compared.

The results, most notably the inclusive parton cross-section  $d\sigma/d\eta$  for the kinematical range  $\sqrt{s_{ep}} = 296 \text{ GeV}$ ,  $Q^2 < 0.01 \text{ GeV}^2$ ,  $0.25 < y < 0.7$  and  $p_t > 6 \text{ GeV}/c$  and the measured gluon density function,  $f_{g/\gamma}(x_\gamma)$ , exclude a high gluon density at large  $x_\gamma$  as well as a steeply rising gluon density function for small  $x_\gamma$ .

# Zusammenfassung

Diese Arbeit beschreibt die Messung der inklusiven Parton-Wirkungsquerschnitte  $d\sigma/dp_t$  und  $d\sigma/d\eta$  für den Spezialfall der Photoproduktion bei Elektron Proton Streuprozessen sowie die Bestimmung der Gluon-Dichte-Funktion  $f_{g/\gamma}(x_\gamma)$  des (quasi-reellen) Photons. Alle drei Grössen sind sensitiv auf die partonische Struktur des Photons, vor allem auf dessen gluonischen Inhalt.

Die Resultate beruhen auf der Untersuchung von 2-Jet-Ereignissen, die vom H1 Detektor am  $ep$  Beschleuniger HERA aufgezeichnet worden sind. Die Daten für diese Analyse wurden im Jahre 1993 aufgenommen und entsprechen einer totalen integrierten Luminosität von  $L = 255 \text{ nb}^{-1}$ .

Das Hauptproblem bei der Gewinnung obiger Resultate besteht darin, den Einfluss eines bis heute ungenügend verstandenen transversalen Energieflusses, der in den Daten sichtbar ist, von allen theoretischen Vorhersagen aber nicht erklärt werden kann, zu kontrollieren. Es werden drei verschiedene Methoden vorgestellt, die einen möglichen verfälschenden Einfluss dieses unverständenen Energieflusses auf die Messresultate korrigieren. Die aus den drei Methoden gewonnenen Resultate werden aufgeführt und miteinander verglichen.

Die Resultate, allen voran die Messung des inklusiven Parton-Wirkungsquerschnittes  $d\sigma/d\eta$  für den kinematischen Bereich  $\sqrt{s_{ep}} = 296 \text{ GeV}$ ,  $Q^2 < 0.01 \text{ GeV}^2$ ,  $0.25 < y < 0.7$  und  $p_t > 6 \text{ GeV}/c$  sowie die gemessene Gluon-Dichte-Funktion  $f_{g/\gamma}(x_\gamma)$ , schliessen eine grosse Gluondichte für grosses  $x_\gamma$  ebenso aus wie ein starkes Ansteigen der Gluon-Dichte-Funktion für kleines  $x_\gamma$ .

# Contents

<b>Abstract</b>	<b>1</b>
<b>Zusammenfassung</b>	<b>2</b>
<b>Introduction</b>	<b>6</b>
<b>1 Structure functions and parton density functions</b>	<b>7</b>
1.1 Proton . . . . .	7
1.1.1 Kinematics of electron proton scattering . . . . .	8
1.1.2 Proton structure functions in deep inelastic electron proton scattering and their relation to parton density functions of the proton . . . . .	9
1.2 Photon . . . . .	11
1.2.1 The Vector Dominance Model . . . . .	11
1.2.2 Photon structure functions in deep inelastic electron photon scattering and their relation to parton density functions of the photon . . . . .	13
1.2.3 Parton density functions of the photon in photoproduction at HERA . . . . .	16
1.2.3.1 Kinematics . . . . .	17
1.2.3.2 Properties of hard photoproduction reactions . . . . .	18
1.2.3.3 Measuring the parton density functions of the photon at HERA . . . . .	20
1.2.3.4 Existing measurements and parametrizations of the parton density functions of the photon . . . . .	24
<b>2 HERA and H1</b>	<b>26</b>
2.1 HERA . . . . .	26
2.2 H1 . . . . .	27

<b>3</b>	<b>Monte Carlo simulations</b>	<b>31</b>
3.1	Pythia . . . . .	32
<b>4</b>	<b>Jets and jet algorithms</b>	<b>35</b>
4.1	Cone algorithms . . . . .	35
4.2	Cluster algorithms . . . . .	36
4.3	Longitudinally-boost-invariant $k_{\perp}$ -clustering algorithm . . . . .	36
4.4	Reconstruction of parton kinematics using the $k_{\perp}$ -algorithm . . . . .	39
4.4.1	Jet parton correlations . . . . .	41
4.4.2	$x_{\gamma}$ -resolution . . . . .	45
<b>5</b>	<b>Data selection</b>	<b>49</b>
5.1	First level trigger . . . . .	49
5.1.1	Efficiency of first level trigger . . . . .	53
5.2	Level 4 trigger . . . . .	53
5.2.1	Efficiency of level 4 trigger . . . . .	55
5.3	Level 5 trigger . . . . .	55
5.4	Three more cuts . . . . .	57
5.5	Jet-finding . . . . .	60
5.6	Luminosity . . . . .	61
<b>6</b>	<b>Comparison of data with Monte Carlo simulations</b>	<b>64</b>
6.1	Jet properties and jet jet correlations . . . . .	65
6.2	Energy flow . . . . .	69
6.3	Forward energy problem . . . . .	72
6.3.1	Energy scale of the LAr calorimeter . . . . .	72
6.3.2	Trigger bias . . . . .	73
6.3.3	Pile-up . . . . .	73
6.3.3.1	Rates . . . . .	74
6.3.3.2	Proton current and bunch selection . . . . .	74
6.3.3.3	Trigger veto . . . . .	75
6.4	Correction of energy flow description . . . . .	76
6.4.1	Multiple interactions . . . . .	76
6.4.2	Pedestal energy . . . . .	78

6.4.3	Pedestal subtraction . . . . .	80
6.4.4	Alternatives to pedestal subtraction . . . . .	87
6.4.5	Choice of energy flow correction method . . . . .	95
<b>7</b>	<b>Measurement of <math>d\sigma/dp_t</math>, <math>d\sigma/d\eta</math> and <math>f_{g/\gamma}(x_\gamma)</math></b>	<b>100</b>
7.1	Unfolding procedure . . . . .	103
7.2	Measurement of $d\sigma/dp_t$ and $d\sigma/d\eta$ . . . . .	106
7.2.1	Determination of $d\sigma/dp_t$ . . . . .	108
7.2.2	Determination of $d\sigma/d\eta$ . . . . .	109
7.2.3	Systematic errors . . . . .	112
7.3	Measurement of $f_{g/\gamma}(x_\gamma)$ . . . . .	123
7.3.1	Unfolding the $x_\gamma^{\text{jets}}$ -distribution . . . . .	124
7.3.2	Determination of $f_{g/\gamma}(x_\gamma)$ . . . . .	125
7.3.3	Systematic errors . . . . .	128
	<b>Summary</b>	<b>136</b>
	<b>Bibliography</b>	<b>137</b>
	<b>List of figures</b>	<b>143</b>
	<b>List of tables</b>	<b>146</b>
	<b>Acknowledgements</b>	<b>147</b>
	<b>Curriculum vitae</b>	<b>148</b>

# Introduction

The aim of this analysis is to measure the partonic structure of the photon. The ideal setup for such a measurement is to collide real photons with other particles at a large center-of-mass energy to allow for a high spatial resolution when probing the internal structure of the photon. The  $ep$  collider HERA offers an almost ideal setup by providing collisions of electrons (which dominantly emit quasi-real photons, *i.e.*,  $Q^2 \approx 0$ ) with protons at a center-of-mass energy of  $\sqrt{s_{ep}} = 296$  GeV. The use of protons instead of photons (or electrons) as the colliding partners for the quasi-real photons has the advantage that already the leading order scattering processes are sensitive to both the quark and gluon content of the photon.

Chapter 1 gives a short introduction to the methods commonly used to investigate the structure of an extended object and to their theoretical background. It will be motivated why we believe that the photon does have a structure at all and some care is taken to explain the approach of measuring the partonic structure of the photon at HERA.

Chapter 2 gives a concise overview of the  $ep$  collider HERA and describes the H1 detector. Emphasis is put on those aspects most important for this analysis.

Chapter 3 introduces an important tool for this analysis, the modeling of physical processes by Monte Carlo simulations.

Chapter 4 concentrates on the description of jets and introduces a novel cluster algorithm to physics analysis at HERA.

Chapter 5 describes the data selection.

Chapter 6 is dedicated to the comparison of the data with the above-mentioned Monte Carlo simulations. Unfortunately, the description of the data by the Monte Carlo simulations is not good enough to be used for a determination of the partonic content of the photon as such but asks for a correction of this deficiency. Three different methods to improve the description of the data by the Monte Carlo simulations are discussed in detail.

Finally, chapter 7 presents the measurement of quantities most sensitive to the partonic structure of the (quasi-real) photon, *i.e.*, the inclusive parton cross-sections  $d\sigma/dp_t$  and  $d\sigma/d\eta$  as well as the gluon density function of the photon,  $f_{g/\gamma}(x_\gamma)$ .

A short summary concludes the thesis.

# Chapter 1

## Structure functions and parton density functions

In this chapter we give an introduction to one of the main physics topics at HERA, the measurement of structure functions and parton density functions. As the name suggests, structure functions describe the structure of an extended object and the parton density functions give the density of a particular parton within the extended object under consideration.

In the following, we will introduce the concept of structure functions in deep inelastic electron proton scattering and will then concentrate on the properties of the photon, that is, its structure functions and parton density functions. We will thereby give a more detailed description of the interplay between structure functions and parton density functions.

### 1.1 Proton

The traditional way of defining and measuring the proton structure functions is by means of deep inelastic scattering (DIS) of a lepton off the proton. With this method, some very important discoveries have been made. Among others the fact that the proton is built up of point-like “partons”, which was first demonstrated at SLAC in the late sixties and which was honoured with the 1990 Nobel Prize for Physics for Friedman, Kendall and Taylor [1].

To show in more detail what is meant by deep inelastic scattering, let us first introduce the kinematics relevant for electron proton scattering. We henceforth restrict the general case of lepton proton scattering to electron proton scattering.

### 1.1.1 Kinematics of electron proton scattering

The kinematics of electron proton scattering can be fully described by three independent variables. If the center-of-mass energy  $\sqrt{s_{ep}}$  is fixed as is the case at HERA, where  $\sqrt{s_{ep}}$  amounts to 296 GeV, we are left with two independent variables. The most commonly used (Lorentz-invariant) variables are Björken- $x_{\text{Bj}}$ , which in the naïve quark parton model (see below) can be interpreted as the momentum fraction of the parton in the proton<sup>1</sup>, and  $Q^2$ , the negative four-momentum transfer squared of the gauge boson exchanged between the electron and the proton. Another variable often used is  $y$ , the relative energy loss of the electron in the proton rest-frame.

In detail (see figure 1.1, too):

$$s_{ep} := (p + k)^2 \quad (1.1)$$

$$Q^2 := -q^2 \quad (1.2)$$

$$x_{\text{Bj}} := \frac{Q^2}{2(p \cdot q)} \quad (1.3)$$

$$y := \frac{p \cdot q}{p \cdot k} \quad (1.4)$$

$$W^2 := (p + q)^2 \quad (1.5)$$

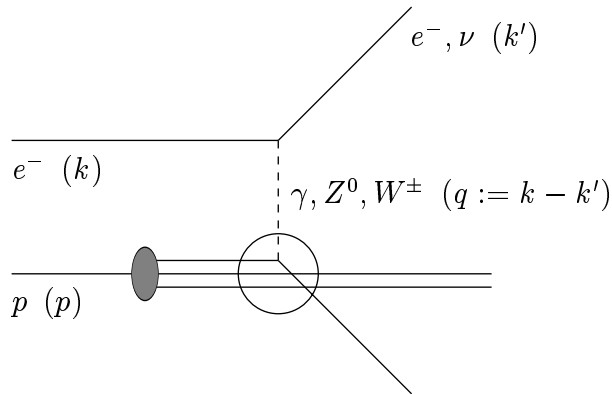


Figure 1.1: Kinematics of electron proton scattering. Henceforth, a shaded oval stands for a structured object and a transparent circle indicates an interaction with a parton from the extended object. Any lines emerging from either one are purely suggestive.

<sup>1</sup>If we denote the momentum of the incoming quark as  $\xi p$  and the invariant mass squared of the outgoing quark as  $m_q^2$ , then  $m_q^2 = (\xi p + q)^2$  and (neglecting on-shell masses)  $\xi = x_{\text{Bj}}(1 + (m_q^2/Q^2))$ . Hence,  $x_{\text{Bj}}$  is the fractional momentum of the quark from the proton as long as  $Q^2 \gg m_q^2$ .

$Q^2$ ,  $x_{\text{Bj}}$  and  $y$  can be expressed in directly measurable quantities such as  $E_e$ ,  $E'_e$  and the angle  $\theta_e$  between the scattered electron and the initial proton direction (*cf.* figure 2.2), conventionally called the forward direction (we neglect particle masses throughout):

$$Q^2 = 4E_e E'_e \cos^2 \frac{\theta_e}{2} \quad (1.6)$$

$$y = 1 - \frac{E'_e}{E_e} \sin^2 \frac{\theta_e}{2} \quad (1.7)$$

$$x_{\text{Bj}} = \frac{Q^2}{y s_{ep}} \quad (1.8)$$

There are other ways of extracting  $Q^2$ ,  $x_{\text{Bj}}$  and  $y$  from measured quantities which are more related to the hadronic final state [2]. Some of them will be introduced below.

In the special case of  $ep$  scattering, where  $Q^2$  is small ( $Q^2 \approx 0$ ), the main process is the interaction of quasi-real photons with protons since contributions from  $Z^0$  or  $W^\pm$  exchange are negligible. This is called the *photoproduction* régime of electron proton scattering.

### 1.1.2 Proton structure functions in deep inelastic electron proton scattering and their relation to parton density functions of the proton

Deep inelastic electron proton scattering is an inelastic scattering (*i.e.*,  $W^2 \gg m_p^2$ ) where the exchanged gauge boson is highly virtual, that is,  $Q^2 \gg \Lambda_{\text{QCD}}^2$ . The high virtuality of the gauge boson translates to high spatial resolution when probing the internal structure of the proton. In the following, we restrict the discussion of deep inelastic electron proton scattering to the process where the exchanged gauge boson is a photon.

Now, if the proton was an elementary particle like *e.g.* a lepton, the elastic scattering  $ep \rightarrow e'p'$  would be *fully* described by the standard model, *i.e.*, without the need of any phenomenological factors. But since we know that the proton is an extended object, we have to introduce factors which describe the unknown structure of the proton — the proton structure functions (for elastic rather than inelastic scattering off an extended object, these factors are called “form factors”). The double differential cross-section for the reaction  $ep \rightarrow e'X$  can then be described by [3, 4]

$$\frac{d^2 \sigma_{ep \rightarrow e'X}}{dx dQ^2} = \frac{4\pi \alpha^2}{x Q^4} \left\{ (1-y) F_2^p(x, Q^2) + xy^2 F_1^p(x, Q^2) \right\} \quad ; \quad x = x_{\text{Bj}} \quad (1.9)$$

$x$  is the fractional momentum of the partons from the proton, in DIS approximately given by  $x_{\text{Bj}}$ .

Equation (1.9) defines the proton structure functions  $F_1^p$  and  $F_2^p$ . In the naïve quark parton model (QPM) introduced by Björken, Paschos and Feynman [5], these structure functions can be related to parton density functions if one thinks of the inelastic electron proton scattering as being an incoherent sum of elastic point-like electron parton scatterings, that is, elastic scattering off massless non-interacting quarks in the proton.

In the limit of large  $Q^2$  with  $x$  fixed, one finds [3, 4]

$$F_2^p(x) = 2xF_1^p(x) = \sum_{i=1}^{2n_f} e_i^2 x f_{q_i/p}(x) \quad ; \quad x = x_{\text{Bj}} \quad , \quad (1.10)$$

where the sum runs over all quarks<sup>2</sup> ( $n_f$  is the number of flavours) and  $e_i$  is the fractional electric charge of the quarks.  $f_{q_i/p}(x)$  is the quark density function of the proton, describing the probability to find a quark in the proton with momentum fraction  $x$ .

The first part of equation (1.10) is known as the Callan-Gross relation [6] whereas the second part illustrates what is meant by *scaling* of the structure function<sup>3</sup>:  $F_2^p(x)$  and  $F_1^p(x)$  do not depend on the scale  $Q^2$  [7].

Although  $F_2^p(x)$  (and  $F_1^p(x)$ ) — as opposed to the parton density functions — is a quantity which can be directly measured in experiments (for HERA-results, see [8]), parton density functions are more widely used for theoretical calculations. This is due to the fact that the definition of a structure function is always related to a certain process (*e.g.* DIS) whereas parton density functions are independent of the process under consideration. This basic property of parton density functions relies on the theorem of factorization [9], which states that any cross-section can be written as a convolution of matrix elements for partonic hard scattering cross-sections with probability functions for finding the incoming partons in a given particle. Therefore, we will in the following concentrate on parton density functions rather than structure functions, nevertheless referring to structure functions where appropriate.

Quantum Chromodynamics (QCD) introduces corrections to the naïve quark parton model, mainly due to gluon emission of the quarks and  $g \rightarrow q\bar{q}$  splitting. In first order  $\alpha_s$ , the coupling constant of QCD, the parton density functions (and the structure functions) no longer scale, *i.e.*, they not only depend on  $x$  but also on the sensitivity of the probe, given by  $Q^2$  in the case of deep inelastic  $ep$  scattering. This evolution of the parton density functions is given by the Altarelli-Parisi equations [10], which in  $\mathcal{O}(\alpha_s)$  are

<sup>2</sup>By the term quarks, we always mean quarks and anti-quarks.

<sup>3</sup>The term structure function always refers to all the structure functions needed to describe the structure of a particle.

$$\frac{\partial f_{q_i/p}(x, Q^2)}{\partial \ln Q^2} = \tag{1.11}$$

$$\frac{\alpha_s(Q^2)}{2\pi} \int_x^1 \frac{dx'}{x'} \left\{ P_{q/q} \left( \frac{x}{x'} \right) f_{q_i/p}(x', Q^2) + P_{q/g} \left( \frac{x}{x'} \right) f_{g/p}(x', Q^2) \right\}$$

$$\frac{\partial f_{g/p}(x, Q^2)}{\partial \ln Q^2} = \tag{1.12}$$

$$\frac{\alpha_s(Q^2)}{2\pi} \int_x^1 \frac{dx'}{x'} \left\{ \sum_{i=1}^{2n_f} P_{g/q} \left( \frac{x}{x'} \right) f_{q_i/p}(x', Q^2) + P_{g/g} \left( \frac{x}{x'} \right) f_{g/p}(x', Q^2) \right\} .$$

$P_{q/q}(z)$ ,  $P_{q/g}(z)$ ,  $P_{g/q}(z)$  and  $P_{g/g}(z)$  are the Altarelli-Parisi splitting functions describing the probability to find *e.g.* a quark in a quark with fraction  $z$  of the parent quark momentum.  $x$  is, in the naïve quark parton model, again given by  $x_{Bj}$ .

## 1.2 Photon

The proton is an extended object. Therefore, it makes sense to talk about a structure of the proton and hence to define a structure function of the proton. Now, the photon seems to be quite a different particle — it is the gauge boson of the electromagnetic interaction and has never shown any sign of compositeness. It is considered to be a truly elementary particle! But then, why should we want to talk about a structure of the photon?

Historically, the first hint for a “hadronic structure” of the photon was the observation that when the photon interacts with a hadron, it behaves like a hadron (for a compilation of results, mainly from fixed target experiments, see [11]). This observation introduced a new view of the photon as a superposition of a “bare” photon and a “hadronic” photon. In the so called “Vector Dominance Model” (VDM) [12], the hadronic photon is regarded as a superposition of different vector mesons. As a consequence of this new picture of the photon, one started to study the photon structure via deep inelastic scattering analogous to the proton case.

In the following subsections we will be more explicit about the VDM picture and give some more details on the photon structure functions measured in  $e^+e^-$  reactions. Finally, we will turn towards the photoproduction régime of  $ep$  scattering, where the structure of the photon plays a prominent rôle.

### 1.2.1 The Vector Dominance Model

The phenomenological Vector Dominance Model assumes the photon to be a superposition of a bare photon and a hadronic photon, where the hadronic photon

itself is a superposition of the three lightest vector mesons  $\rho$ ,  $\omega$  and  $\phi$ , which have the same quantum numbers as the photon ( $J^{PC} = 1^{--}$ ). More generalized models which include even heavier vector mesons do exist [13] but we will restrict ourselves to the simplest case.

The intuitive picture behind this model is the following [14]: the photon, owing to its fundamental property to couple directly to charged partons, fluctuates between bare and hadronic states. This picture relies on the assumption that the typical fluctuation time  $t_f$  is larger than the typical interaction time  $t_i$ , allowing a  $q\bar{q}$ -pair originating from a  $\gamma \rightarrow q\bar{q}$  splitting to form a bound state. In the target rest-frame, the fluctuation time  $t_f$  is of the order of ( $\hbar = 1$ )

$$t_f \approx \frac{2E_\gamma}{m_V^2 - q^2} \quad , \quad (1.13)$$

where  $E_\gamma$  is the photon energy,  $m_V$  is the mass of the vector meson and  $q^2$  is the four momentum squared of the photon. This has to be compared with the typical interaction time  $t_i$ , which is given by the time the photon needs to traverse the target, *e.g.* the diameter of the proton ( $c = 1$ ):

$$t_i \approx 2r_p \quad . \quad (1.14)$$

Therefore, the VDM picture is only valid as long as

$$E_\gamma \gg (m_V^2 - q^2) r_p \quad . \quad (1.15)$$

For on-shell photons ( $q^2 = 0$ ) and using  $m_V = m_\rho = 770 \text{ MeV}/c^2$  and  $r_p \approx 1 \text{ fm}$ , this is equivalent to

$$E_\gamma \gg 3 \text{ GeV} \quad (1.16)$$

in the target rest-frame.

The probability that the photon fluctuates into a vector meson state is given by  $4\pi\alpha/f_V^2$ , where  $f_V$  reflects the strength of the  $\gamma V$  coupling and can be determined by experiment, *e.g.* via the decay  $V \rightarrow (\gamma \rightarrow) e^+e^-$ . Within the Vector Dominance Model, the  $\gamma$ -hadron ( $\gamma h$ ) cross-section is then given as a sum of  $V$ -hadron ( $Vh$ ) cross-sections:

$$\sigma_{\gamma h}^{\text{VDM}} = \sum_{V=\rho,\omega,\phi,\dots} \frac{4\pi\alpha}{f_V^2} \sigma_{Vh} \quad . \quad (1.17)$$

This and other predictions of the Vector Dominance Model agree well with “low” energy data ( $E_\gamma \lesssim 20 \text{ GeV}$  in the target rest-frame) [11] and make the Vector Dominance Model a very successful tool for photon hadron physics in the low energy

range (to account for the observed increase in the  $\gamma p$  cross-section [15], which could not be explained by the Vector Dominance Model, Gotsman *et al.* [16] proposed in 1979, that the missing contribution is due to photoproduction of jets). Moreover, it suggests that the photon has a nontrivial structure, possibly even at “high” energies.

### 1.2.2 Photon structure functions in deep inelastic electron photon scattering and their relation to parton density functions of the photon

With the existence of  $e^+e^-$  colliders, one started to examine the photon structure by interpreting the electron photon reactions as deep inelastic scattering on a photon target analogous to the proton case (for a review, see [17, 18]). This analogy makes sense in view of the hadronic nature of the photon discovered in low energy photon hadron reactions. To stress the similarity between electron proton and electron photon scattering, we sketch in figure 1.2 the diagrams for deep inelastic  $ep$  and  $e\gamma$  scattering, where in the latter case the almost real photon is emitted from the positron (henceforth, we again restrict ourselves to the case where the exchanged gauge boson is a photon):

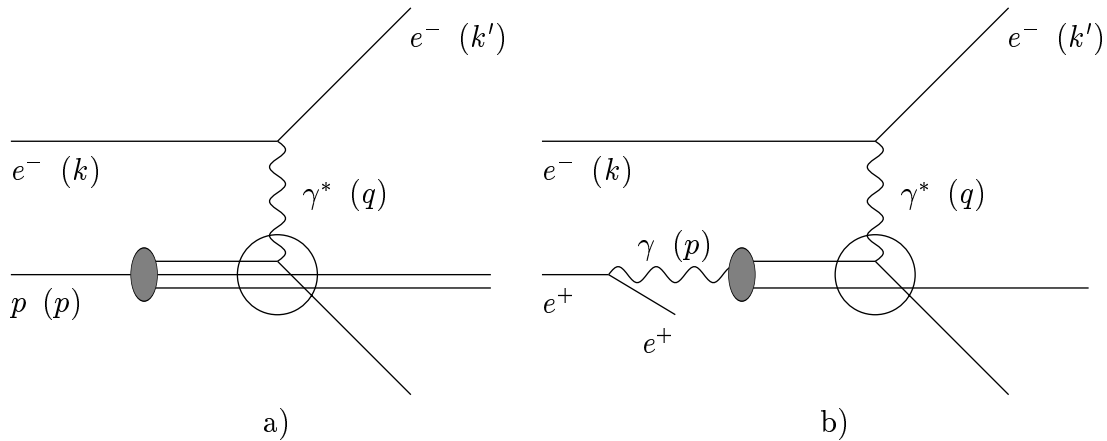


Figure 1.2: Diagrams describing deep inelastic scattering off a) a proton b) a quasi-real photon emitted from a positron.

The term deep inelastic electron photon scattering refers to the case where  $Q^2 \gg \Lambda_{\text{QCD}}^2$  (as in deep inelastic electron proton scattering) and  $p^2 \approx 0$ . Note that  $p$  denotes the four momentum of the target which is the proton in case of  $ep$  scattering (and therefore  $p^2 = m_p^2 \approx 0$ ) and the quasi-real photon in the  $e\gamma$  case. This redefines  $x_{\text{Bj}}$ .

In the same way as for the proton, one can derive the double differential cross-section for  $e\gamma \rightarrow e'X$ , thereby defining the photon structure functions  $F_1^\gamma$  and  $F_2^\gamma$  [3, 17]:

$$\frac{d^2 \sigma_{e\gamma \rightarrow e'X}}{dx dQ^2} = \frac{4\pi\alpha^2}{xQ^4} \left\{ (1-y) F_2^\gamma(x, Q^2) + xy^2 F_1^\gamma(x, Q^2) \right\} \quad ; \quad x = x_{Bj} \quad . \quad (1.18)$$

Additionally, one needs to link the cross-section for  $e\gamma \rightarrow e'X$  to the cross-section for  $ee \rightarrow e'X$  via

$$\frac{d^2 \sigma_{ee \rightarrow e'X}}{dx dQ^2} = \int_0^1 dz f_{\gamma/e}(z) \left\{ \frac{d^2 \sigma_{e\gamma \rightarrow e'X}}{dx dQ^2} \right\}_{E_\gamma = zE_e} \quad , \quad (1.19)$$

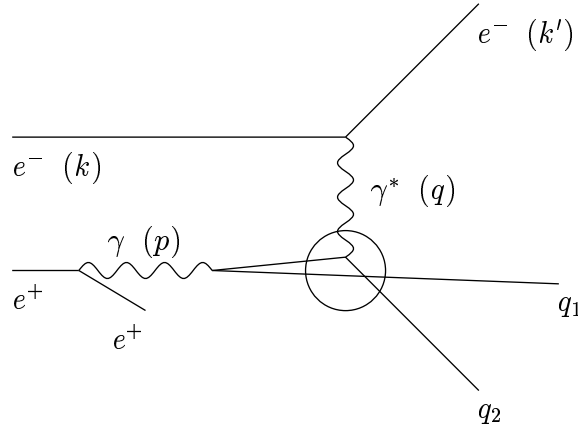
where  $f_{\gamma/e}(z)$  is the probability that an electron (positron) emits a quasi-real photon with momentum fraction  $z$  (Weizsäcker-Williams approximation, see section 1.2.3.1).

By analogy to the proton case, the QPM links  $F_2^\gamma$  with the sum of momentum weighted parton densities inside the photon:

$$F_2^\gamma(x, Q^2) = 2xF_1^\gamma(x, Q^2) = \sum_{i=1}^{2n_f} e_i^2 x f_{q_i/\gamma}(x, Q^2) \quad ; \quad x = x_{Bj} \quad . \quad (1.20)$$

However, there is one major difference between the structure functions of the proton and the photon. In the proton case, we thought of the deep inelastic  $ep$  scattering as being the incoherent sum of elastic scatterings off massless, non-interacting quarks in the proton. The same picture may be used for interactions with the hadronic photon as described by VDM. Note that the Vector Dominance Model referred to earlier was relevant mainly for low photon energies. At higher energies, as reached in colliders, we may think of the photon as being a hadron just as in the Vector Dominance Model, but the theory relevant for the reaction, *i.e.*, the parton parton scattering, being perturbative QED/QCD rather than VDM. This is sometimes referred to as the “hard VDM component” [19]. This refined VDM picture of the photon, however, is definitely not complete: The photon can in addition couple directly to a  $q\bar{q}$ -pair! To illustrate this point, let’s consider the contribution to the structure function from the diagram of figure 1.3 (note that the diagram depicted in figure 1.3 is contained in the diagram of figure 1.2 b)).

Contrary to the case of a proton target, the lower part of the diagram is known and calculable [20, 21], the main result being that this contribution to the structure function has a  $\ln Q^2$  dependence, which means that the photon structure function does not scale, even in the naïve QPM (*i.e.*, at zeroth order in  $\alpha_s$ ). The  $\ln Q^2$  dependence stems from the integration over the kinematical variables of the unobserved quark  $q_1$ , *i.e.*,  $\int_{\Lambda^2}^{p_t^{\max}} dp_t^2 p_t^{-2}$  with  $p_{t,\max}^2 = \hat{s}(\gamma^*\gamma)/4$  and  $\hat{s}(\gamma^*\gamma) = Q^2((1-x)/x)$  [17]. Therefore, the physical reason for the increase in the photon structure function as a function of  $Q^2$  is the fact that a large  $Q^2$  of the probing photon opens up the phase-space for the  $\gamma \rightarrow q\bar{q}$  splitting, which makes the appearance of this contribution more likely as  $Q^2$  grows.

Figure 1.3:  $\gamma^* \gamma \rightarrow q_1 q_2$ .

The modified Altarelli-Parisi evolution equations for the photon read (in first order  $\alpha$  and  $\alpha_s$ ,  $x = x_{Bj}$ ) [21]:

$$\frac{\partial f_{q_i/\gamma}(x, Q^2)}{\partial \ln Q^2} = e_i^2 \frac{\alpha(Q^2)}{2\pi} P_{q/\gamma}(x) + \quad (1.21)$$

$$\frac{\alpha_s(Q^2)}{2\pi} \int_x^1 \frac{dx'}{x'} \left\{ P_{q/q} \left( \frac{x}{x'} \right) f_{q_i/\gamma}(x', Q^2) + P_{q/g} \left( \frac{x}{x'} \right) f_{g/\gamma}(x', Q^2) \right\}$$

$$\frac{\partial f_{g/\gamma}(x, Q^2)}{\partial \ln Q^2} = \quad (1.22)$$

$$\frac{\alpha_s(Q^2)}{2\pi} \int_x^1 \frac{dx'}{x'} \left\{ \sum_{i=1}^{2n_f} P_{g/q} \left( \frac{x}{x'} \right) f_{q_i/\gamma}(x', Q^2) + P_{g/g} \left( \frac{x}{x'} \right) f_{g/\gamma}(x', Q^2) \right\} .$$

The term  $P_{q/\gamma}$  accounts for the  $\gamma \rightarrow q\bar{q}$  splitting and has a similar structure as the other splitting functions (for the exact form of the splitting functions see *e.g.* [21]).  $e_i$  is the fractional electric charge of the quarks. Note that the evolution equations are inhomogeneous (since the two evolution equations are coupled, we refer to a set of equations rather than to the quark evolution equation as being inhomogeneous). A solution for this set of equations is given by a superposition of the general solution of the corresponding set of homogeneous equations and a particular solution of the inhomogeneous one. One may argue that the solution of the inhomogeneous set of equations is due to the contribution of the  $\gamma \rightarrow q\bar{q}$  splitting to the parton density functions. In this approach, the solution of the homogeneous set of equations, which fulfills the hadron-like Altarelli-Parisi evolution equations (the homogeneous evolution equations are, of course, identical to the hadronic evolution equations), may then be assigned to the “hadronic” photon. However, this decomposition (which is used for some parametrizations of the parton density functions of the photon, see

section 1.2.3.4) depends on  $Q_0^2$ , the reference  $Q^2$  at which the  $Q^2$ -evolution, given by the Altarelli-Parisi equations, is started [19].

### 1.2.3 Parton density functions of the photon in photoproduction at HERA

In the photoproduction régime of  $ep$  scattering, that is,  $Q^2 \approx 0$ , parton density functions of the photon play a vital rôle.

Due to the large center-of-mass energy  $\sqrt{s_{\gamma p}}$  of the photon proton system reached at HERA, we expect to see “hard” processes. The picture of a “hard” photon proton scattering process is that of a “hard” scattering of partons in the photon and the proton, which is calculable in perturbative Quantum Chromodynamics if the transverse momentum of the outgoing partons relative to the incident direction is much larger than  $\Lambda_{\text{QCD}}$ . Such processes depend strongly on the distribution of the partonic content of the photon and therefore offer the possibility to measure the parton density functions of the photon.

The fact that we can measure the parton density functions of the photon in hard photoproduction processes relies on the factorization theorem. To *intuitively* see why the measurement of the parton density functions of the photon in deep inelastic electron photon scattering is closely related to hard photoproduction reactions in electron proton scattering, figures 1.2 and 1.4 have to be compared:

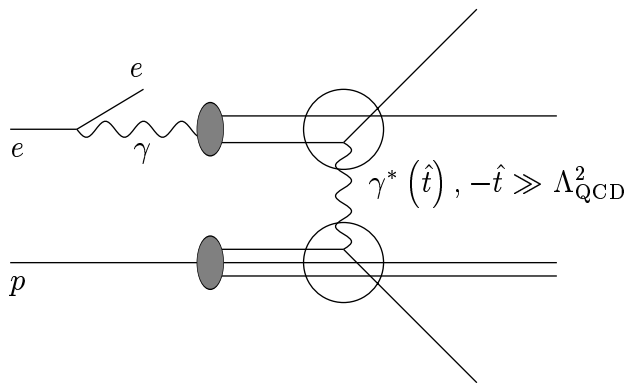


Figure 1.4: Hard scattering in photoproduction.

The lower part of figure 1.4 is identical to the lower part of figure 1.2 a), and the upper part of figure 1.4 is identical to the lower part of figure 1.2 b) — the partons in the photon and the partons in the proton may be thought of as undergoing deep inelastic scattering off the other particle [22]. Of course, the process depicted in figure 1.4 is not the dominant one but the most obvious one for the argument!

After introducing the kinematics relevant for photoproduction at HERA, we will focus on *hard* photon proton interactions. We will discuss typical properties of such processes and will then describe in more detail how one can measure the parton density functions of the photon at HERA. It will be shown that HERA offers the possibility to measure the parton density functions of the photon for lower  $x_{\text{parton}/\gamma}$  than was possible at  $e^+e^-$  colliders and that we have a better sensitivity to the gluon content of the photon. A short summary of existing parametrizations of the parton density functions for the photon will conclude the chapter.

### 1.2.3.1 Kinematics

As mentioned earlier, photoproduction processes are characterized by  $Q^2 \approx 0$ . If one only considers  $ep$  processes, where the electron is scattered through a large angle  $\theta_e \approx 180^\circ$  (or, more intuitively, through small angle  $\vartheta_e \equiv 180^\circ - \theta_e$ ), the following relations hold (*cf.* equations (1.1–1.8)):

$$Q^2 = 4E_e E'_e \cos^2 \frac{\theta_e}{2} \approx 0 \quad (1.23)$$

$$y = 1 - \frac{E'_e}{E_e} \sin^2 \frac{\theta_e}{2} \approx 1 - \frac{E'_e}{E_e} \quad (1.24)$$

$$\sqrt{s_{\gamma p}} \equiv W \approx \sqrt{y s_{ep}} \quad (1.25)$$

Therefore, the requirement of a scattered electron at large angle  $\theta_e$  ensures photoproduction processes. Note that the above requirement allows to interpret  $y$  as the energy loss of the scattered electron, irrespective of the Lorentz-frame used. The typical photon proton center-of-mass energy reached at HERA is  $150 \text{ GeV} \lesssim \sqrt{s_{\gamma p}} \lesssim 250 \text{ GeV}$  compared to  $\sqrt{s_{\gamma p}} \lesssim 20 \text{ GeV}$  for fixed target experiments. This translates into a photon energy in the rest-frame of  $E_\gamma \approx 20 \text{ TeV}$  compared to  $E_\gamma \lesssim 200 \text{ GeV}$  reached in earlier experiments.

To relate electron proton cross-sections  $\sigma_{ep}$  with photon proton cross-sections  $\sigma_{\gamma p}$ , we use the Weizsäcker-Williams approximation [23], valid for  $Q^2 \approx 0$ :

$$\begin{aligned} \frac{d\sigma_{ep}}{dy} &= f_{\gamma/e}(y) \sigma_{\gamma p} \quad (1.26) \\ &= \frac{\alpha}{2\pi} \left\{ \frac{1 + (1-y)^2}{y} \ln \left( \frac{Q_{\text{max}}^2(y)}{Q_{\text{min}}^2(y)} \right) - \frac{2(1-y)}{y} \left( 1 - \frac{Q_{\text{min}}^2(y)}{Q_{\text{max}}^2(y)} \right) \right\} \sigma_{\gamma p} \quad . \end{aligned}$$

Here,  $f_{\gamma/e}(y)$  is the photon flux-factor or, equivalently, the probability in order  $\alpha$ , that an electron emits a quasi-real photon with momentum fraction  $y$ .  $Q_{\text{min}}^2(y)$  and  $Q_{\text{max}}^2(y)$  depend on the experimental conditions, *e.g.* if the scattered electron is tagged at small angle  $\vartheta_e$ , *i.e.*, its scattering angle is restricted to  $0^\circ < \vartheta_e < \vartheta_{e,\text{max}}$ , then  $Q_{\text{min}}^2(y) = (y^2 m_e^2)/(1-y)$  and  $Q_{\text{max}}^2 = Q_{\text{max}}^2(\vartheta_{e,\text{max}})$ .

### 1.2.3.2 Properties of hard photoproduction reactions

There are various possibilities of classifying different subprocesses in hard photoproduction interactions, which sometimes leads to confusion rather than clarity [24]. We will here adopt the terminology proposed by the working group on photoproduction at the Durham workshop [19].

The photon, as opposed to hadrons, has the fundamental property that it can interact directly with the partons from the proton. Therefore, we distinguish between *direct* processes where the photon itself participates in the hard subprocess and the *resolved* processes where the photon is resolved into quarks and gluons which then participate in the hard subprocess. The topology of these two types of processes are significantly different, but only in leading order (LO) QCD (see figures 1.5 and 1.6):

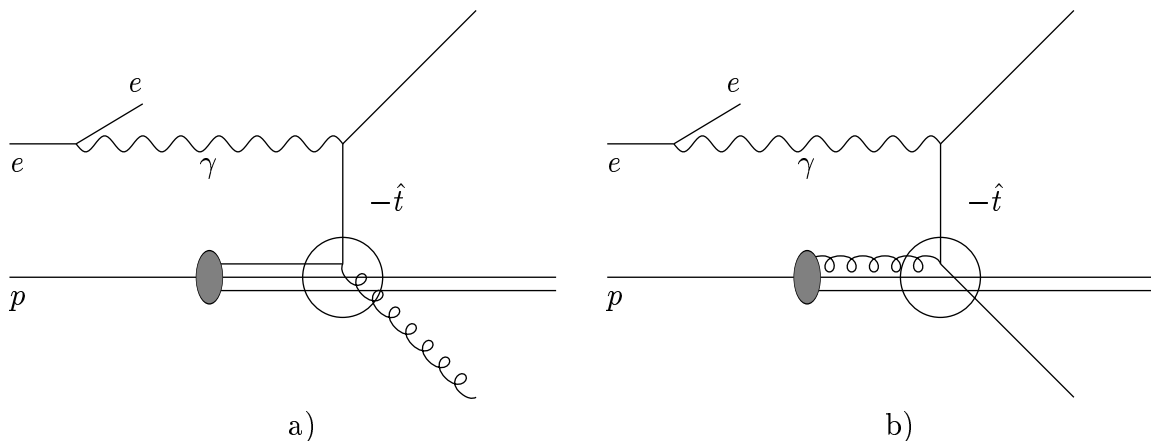


Figure 1.5: Direct processes (LO QCD) in photon proton scattering:  
a) QCD Compton scattering  $\gamma q \rightarrow gq$ , b) photon gluon fusion  $\gamma g \rightarrow q\bar{q}$ .

The resolved processes have a remnant of the proton *and* the photon moving roughly along the incident direction of the proton and the electron, respectively, whereas direct processes only have a proton remnant. Since hard processes can experimentally be identified by so-called jets<sup>4</sup> which are the result of the hadronization<sup>5</sup> of the scattered partons, resolved processes are sometimes referred to as having a four-jet structure (two transverse jets from the hard parton parton scattering and two remnant jets) and direct processes as having a three-jet structure (two transverse jets from the hard parton parton scattering and the proton remnant jet). A further subdivision of the processes, particularly of the resolved processes into an “anomalous” and a “VDM” or “hadronic” component [25], is not considered.

<sup>4</sup>A jet may be thought of as a collimated bunch of particles.

<sup>5</sup>Hadronization (or fragmentation) is the transition from coloured partons, as described within perturbative QCD, to colourless hadrons, as observed by experiments, which can only be described phenomenologically.

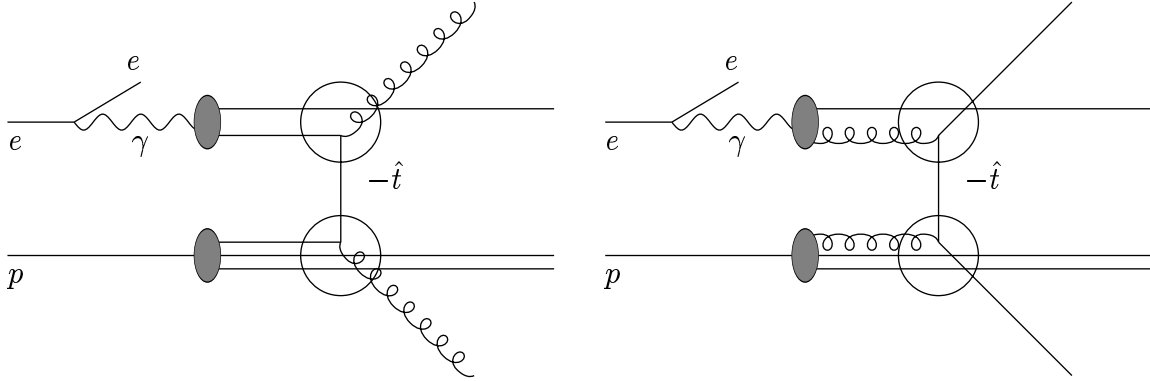


Figure 1.6: Two of the many possible resolved processes (LO QCD) in photon proton scattering.

Is this distinction between direct and resolved processes relevant for photoproduction processes at HERA or is one of the two types of processes highly dominant? There are at least two points to be considered:

- Both types of processes are of the same order in  $\alpha, \alpha_s$ ! For the direct processes we have  $\mathcal{O}(\alpha\alpha_s)$  from the hard subprocess. For the resolved processes it is a bit more complicated. Firstly, we get  $\mathcal{O}(\alpha_s^2)$  from the hard subprocess (or  $\mathcal{O}(\alpha^2)$  for photon exchange, but this is definitely negligible compared to gluon or quark exchange). Secondly, we get another factor  $\alpha$  from the quark or gluon density functions in the photon. This may be seen from the VDM picture of the photon, where the probability that the photon fluctuates into a vector meson is given by  $4\pi\alpha/f_V^2$ , or, equivalently, from the special behaviour of the photon structure function due to the direct coupling of the photon to a  $q\bar{q}$  pair. This adds up to  $\mathcal{O}(\alpha\alpha_s^2)$  for the resolved processes. But as we have seen in section 1.2.2, the photon structure function in addition depends on  $\ln Q^2$ , or, more generally,  $\ln \mu^2$ , where  $\mu^2$  is the factorization scale. The factorization scale is normally set equal to the renormalization scale which itself is mostly set equal to the scale relevant for the process under consideration (see below). This compensates for one order in  $\alpha_s$  since the running of the strong coupling constant can in the leading logarithm approximation be described by [3, 4]

$$\alpha_s(\mu^2) = \frac{12\pi}{(33 - 2n_f) \ln(\mu^2/\Lambda_{\text{QCD}}^2)} \sim \frac{1}{\ln \mu^2} . \quad (1.27)$$

Thus, we end up with  $\mathcal{O}(\alpha\alpha_s)$  for the resolved processes as is the case for the direct ones.

- The direct processes dominate the higher end of the perturbative  $p_t$ -range, because all energy of the photon is available for the hard subprocess whereas

for the resolved processes only a fraction of the photon energy enters into the hard subprocess. This makes the direct processes more efficient at producing jets with  $p_t$  close to the kinematical boundary of  $\sqrt{s_{\gamma p}}/2$ .

As we shall see later, the resolved processes do actually dominate the lower end of the perturbative  $p_t$ -range at HERA energies and we have therefore good chances to be sensitive to the parton density functions of the photon.

Experimental evidence for *hard* scattering in photoproduction reactions has been found in various fixed target experiments (*e.g.* [26, 27]). Additionally, hard photon scattering reactions have been found in  $\gamma\gamma$  physics at  $e^+e^-$  colliders (*e.g.* [28, 29, 30]) and in deep inelastic lepton proton scattering at fixed target experiments (*e.g.* [31]).

The OMEGA Photon Collaboration [27] measured the contribution of *direct* photoproduction processes by comparing the high- $p_t$  particle production of photon induced reactions with hadron (*i.e.*, pion and kaon) induced reactions measured in the same detector. Due to the low center-of-mass energy reached at this fixed target experiment ( $\sqrt{s_{\gamma p}} \approx 10 - 20$  GeV), the direct processes dominate the resolved ones in the entire perturbative  $p_t$ -range and hence the measurements are mainly sensitive to the direct processes.

Evidence for hard scattering due to *resolved* photoproduction processes was obtained by the HERA experiments already after a few weeks of running [32], based mainly on transverse energy flow distributions as a function of polar angle which can only be described by including resolved processes. Evidence for resolved processes in  $\gamma\gamma$  reactions has first been reported by the TRISTAN experiments [29], but indications of their existence (as well as for direct processes) have already been seen by the JADE and TASSO Collaborations [28].

### 1.2.3.3 Measuring the parton density functions of the photon at HERA

“Measuring” the parton density functions of the photon may be done either “directly” or “indirectly”. For either case, we have to rely on the property of the theory (*i.e.*, QCD) that a scattering can be factorized into a soft part, given by the parton density functions which describe the probability to find a parton in the incoming particle, and a hard subprocess, calculable in perturbative QCD:

$$\sigma_{\gamma p \rightarrow X} = \sum_{ijkl} \int_0^1 \int_0^1 dx_{i/\gamma} dx_{j/p} f_{i/\gamma}(x_{i/\gamma}, \mu_1^2) f_{j/p}(x_{j/p}, \mu_1^2) \hat{\sigma}_{ij \rightarrow kl}(\mu_2^2). \quad (1.28)$$

Here,  $f_{i/\gamma}$  ( $f_{j/p}$ ) are the parton density functions of the photon (proton) which depend on the momentum fractions  $x_{i/\gamma}$  ( $x_{j/p}$ ), henceforth shortly written  $x_\gamma$  ( $x_p$ ), and the factorization scale  $\mu_1^2$ .  $\hat{\sigma}_{ij \rightarrow kl}(\mu_2^2)$ <sup>6</sup> is the cross-section for the hard parton

<sup>6</sup> ^ will always refer to variables connected with the hard subprocess.

parton subprocess  $ij \rightarrow kl$ , which depends on the renormalization scale  $\mu_2^2$ . Finally,  $\sigma_{\gamma p \rightarrow X}$  stands for some hard photoproduction cross-section, *e.g.*  $\sigma_{\gamma p \rightarrow 2\text{jets}+X}$ .

Given this relation for any hard photoproduction cross-section, one may *e.g.* measure an inclusive parton (jet) cross-section, which is sensitive to  $f_{i/\gamma}(x_\gamma, \mu_1^2)$ , or one may try to measure the  $x_\gamma$ -distribution “directly” (the  $x_\gamma$ -distribution is “directly” proportional to  $f_{i/\gamma}(x_\gamma, \mu_1^2)$ ), *e.g.* for 2-jet events, by determining  $x_\gamma$  via kinematical quantities of the two jets found. The description and use of these two methods to “measure” the parton density functions of the photon is the main goal of this work and will be discussed in detail in further chapters.

Before we set off actually doing it, we have to be a bit more precise on what the scales in equation (1.28) are and how one can determine  $x_\gamma$  in 2-jet events.

Physical results should always be independent of factorization and renormalization scales. The dependence of theoretical calculations on the factorization and renormalization scales is due to the fact that perturbative series have to be limited to a few terms. Therefore, scales should be chosen such that corrections due to the omission of higher order terms in the power series are small. However, the choice of the factorization and renormalization scale is not obvious for photoproduction processes, but it is definitely not given by  $Q^2$  (which — by definition — is essentially zero for photoproduction) as in deep inelastic scattering. Normally, the scales are chosen as

$$\mu_1^2 = \mu_2^2 \approx \hat{p}_t^2 \quad , \quad (1.29)$$

where  $\hat{p}_t$  is the transverse momentum of the outgoing partons relative to the incident parton direction. This is reasonable for a factorization scale, which should separate soft from hard processes. For a renormalization scale, one should choose some energy typical for the hard subprocess under consideration. This is — in other circumstances — often taken as  $\hat{s}$ , which is related to  $\hat{p}_t$  via (massless partons)

$$\hat{t} = -\frac{\hat{s}}{2} \left( 1 \pm \sqrt{1 - \frac{4\hat{p}_t^2}{\hat{s}}} \right) \quad (1.30)$$

and

$$\hat{p}_{t,\text{max}} = \frac{\sqrt{\hat{s}}}{2} \quad . \quad (1.31)$$

Thus, for large  $\hat{p}_t \approx \hat{p}_{t,\text{max}}$ , we get

$$\hat{t} \approx -\frac{\hat{s}}{2} \approx -2\hat{p}_t^2 \quad . \quad (1.32)$$

Taking  $\hat{p}_t^2$  as the renormalization scale is therefore similar to taking  $\hat{s}$  (we ensure a large  $\hat{p}_t$  by asking for *e.g.* two high- $p_t$  jets) and additionally provides a large

virtuality of the exchanged particle, which reminds us of a probe similar to DIS. However, there are  $s$ -channel parton parton processes additional to the  $t$ -channel ones, which do not offer such an easy identification of a probe! Nevertheless,  $\hat{p}_t^2$  looks like a reasonable scale for this processes, too.

The determination of  $x_\gamma$  and  $x_p$  can be done in many ways [33]. It must be emphasized that  $x_{Bj}$  can no longer be interpreted as the momentum fraction of the parton from the proton as was possible in the case of DIS. For photoproduction processes, we have to find new expressions both for  $x_\gamma$  and  $x_p$ . Neglecting transverse momenta, we may start with (leading order only; see figure 1.7)

$$x_\gamma q + x_p p = p_1 + p_2 \quad (1.33)$$

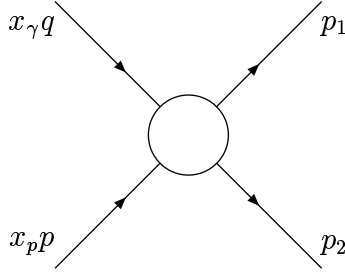


Figure 1.7: Hard parton parton scattering.

Multiplying equation (1.33) with  $p$  (or  $q$ ), assuming  $\vec{q} \parallel \vec{p} \parallel z$ -direction and neglecting masses, one can derive the following expressions for  $x_\gamma$  and  $x_p$ :

$$x_\gamma = \frac{1}{2yE_e} \sum_{i=1}^2 (E_i - p_{z,i}) \quad (1.34)$$

$$= \frac{1}{2yE_e} \sum_{i=1}^2 (E_i (1 - \cos \theta_i)) \quad ; \quad yE_e = E_\gamma$$

$$x_p = \frac{1}{2E_p} \sum_{i=1}^2 (E_i + p_{z,i}) \quad (1.35)$$

$$= \frac{1}{2E_p} \sum_{i=1}^2 (E_i (1 + \cos \theta_i)) \quad .$$

These expressions may be rewritten using the so-called rapidity  $r$

$$r = \frac{1}{2} \ln \left( \frac{E + p_z}{E - p_z} \right) \quad (1.36)$$

or its approximation for massless particles

$$\eta = -\ln\left(\tan\frac{\theta}{2}\right) \quad (1.37)$$

which is called pseudo-rapidity. The rapidity has the advantage over the polar angle  $\theta$  that differences in rapidity are invariant under boosts in  $z$ -direction. This property will be of great importance when defining a jet-finding algorithm.

The expressions for  $x_\gamma$  and  $x_p$  are then

$$x_\gamma = \frac{1}{2yE_e} \sum_{i=1}^2 p_{t,i} \cdot e^{-\eta_i} \quad ; \quad yE_e = E_\gamma \quad (1.38)$$

$$x_p = \frac{1}{2E_p} \sum_{i=1}^2 p_{t,i} \cdot e^{+\eta_i} \quad . \quad (1.39)$$

The question on how we can measure the transverse energy ( $E_t \equiv p_t$  for massless partons) and pseudo-rapidity of the hard partons will be discussed later.

Two important points can be made clear already now. One is that the energies available at HERA make the accessible range in  $x_\gamma$  larger than was possible at previous  $e^+e^-$  colliders:

$$4\hat{p}_t^2 \leq \hat{s} = x_\gamma x_p s_{\gamma p} = x_\gamma x_p y s_{ep} \quad (1.40)$$

and therefore ( $x_\gamma, x_p \in [0, 1]$ )

$$x_\gamma, x_p \geq \frac{4\hat{p}_t^2}{y s_{ep}} \quad . \quad (1.41)$$

For typical values  $\sqrt{s_{\gamma p}} = \sqrt{y s_{ep}} \approx 200$  GeV and  $\hat{p}_t \gtrsim 3-5$  GeV/ $c$  one in principle (detector acceptances *etc.* may reduce this) reaches values for  $x_\gamma, x_p$  as low as  $(1-2.5) \cdot 10^{-3}$  compared to  $x_\gamma \gtrsim 0.01$  for earlier measurements<sup>7</sup>. To be sensitive to the parton density functions of the photon one has to know the parton density functions of the proton for the entire range of  $x_p$ . This is guaranteed, mainly by measurements at HERA itself [8, 34].

The other important point is that photoproduction processes are more sensitive to the *gluon* density function of the photon than  $\gamma\gamma$  reactions, since gluons from the photon may interact with partons from the proton whereas in two-photon physics, the main scattering process is the interaction of a virtual photon with the quarks in the quasi-real photon. One may extract the gluon density function of the photon via

<sup>7</sup>Most existing measurements are in the  $x_\gamma$ -range well above 0.1, the only exceptions being measurements of the TOPAZ, OPAL and DELPHI Collaborations (see below).

the Altarelli-Parisi equations from the  $\mu^2$ -dependence of the quark density function of the photon, but this has the disadvantage that the main  $\mu^2$ -dependence of the quark density function comes from the unique property of the photon to couple directly to quarks, and not from the evolution of the gluon density function. Another possibility explored in deep inelastic electron proton scattering is to restrict the gluon density function by applying momentum sum rules to the parton density functions. However, the fact that the photon may show a hadronic structure or remain an elementary, structureless object makes it more difficult to use such sum rules in the case of the photon. Therefore, the gluon density function of the photon is still poorly known!

To conclude this chapter, we give a very short overview of the existing measurements and parametrizations of the parton density functions of the photon.

#### 1.2.3.4 Existing measurements and parametrizations of the parton density functions of the photon

Many *measurements* of the parton density functions of the photon exist, mainly from  $e^+e^-$  collider experiments (for a review, see *e.g.* [17, 18]). New results include measurements from the TOPAZ, OPAL and DELPHI Collaborations [35], which have measured the photon structure function  $F_2^\gamma$  in deep inelastic electron photon scattering for values of  $x_\gamma$  as low as 0.001–0.01 ( $x_\gamma = 0.001$ –0.01 is the lowest value reached — the average  $\langle x_\gamma \rangle$  of the lowest bin is as high as  $\langle x_\gamma \rangle \approx 0.02$ –0.07). Constraints on the parton density functions of the photon from measurements of the inclusive jet cross-section and multi-hadron production in  $\gamma\gamma$ -physics exist from various recent experiments (*e.g.* [29, 30, 36]).

In addition, there are quite a few *parametrizations* of the parton density functions of the photon [37, 38, 39, 40], all of them describing the available data at the time, but differing a lot where there is no data available, *e.g.* for low  $x_\gamma$ .

Since most parametrizations use the complete Altarelli-Parisi equations to describe the evolution as a function of the scale  $\mu^2$ , starting from some input distribution at a fixed scale  $\mu_0^2$ , the main differences in the parametrizations are the input distribution functions and the choice of  $\mu_0^2$ . Some parametrizations (*e.g.* [40]), however, are derived by subdividing the parton density functions into a hadronic part fulfilling the homogeneous Altarelli-Parisi equations and a so-called “anomalous” part, which fulfills the inhomogeneous Altarelli-Parisi equations and is calculable in perturbative QCD. In this case, an input distribution is only needed for the hadronic part of the parton density functions.

We finish with a short description of the most important parton density function parametrizations of the photon:

- Glück, Reya and Vogt (GRV) [37] use a hadronic ( $\pi$ ) input distribution for the parton density functions and start the evolution at  $\mu_0^2 = 0.25 \text{ GeV}^2$ .

- Abramowicz, Charchuła and Levy (LAC) [38] use an analytical ansatz for the quark and gluon density functions and start their evolution at  $\mu_0^2 = 4 \text{ GeV}^2$  (LAC I+II) and  $\mu_0^2 = 1 \text{ GeV}^2$  (LAC III). The difference between LAC I and LAC II is the parametrization of the gluon density function for  $x_\gamma \rightarrow 0$ .
- Drees and Grassie (DG) [39] use the same approach as [38] (they however use a different analytical ansatz), thereby starting the evolution at  $\mu_0^2 = 1 \text{ GeV}^2$ .
- Gordon and Storrow (GS) [40] try to set up the parton density functions as a sum of two contributions, one being described by the perturbatively calculable contribution from the  $\gamma \rightarrow q\bar{q}$  or  $\gamma \rightarrow q\bar{q}g$  splitting and the other one being described by a hadronic ( $\rho^0$ ) input distribution which is then evolved starting from  $\mu_0^2 = 5.3 \text{ GeV}^2$ .

To give an example of three fairly different parton density function parametrizations, figure 1.8 shows the leading order momentum weighted gluon density function parametrizations GRV-LO, LAC I and LAC III.

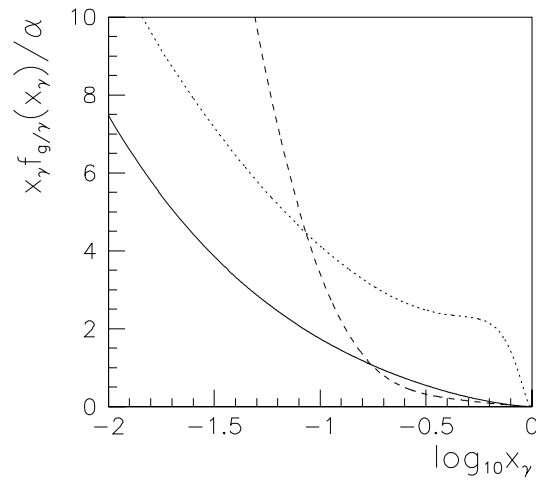


Figure 1.8: Different parametrizations of the momentum weighted gluon density function  $x_\gamma f_{g/\gamma}(x_\gamma, \mu^2)/\alpha$ . Comparison of the GRV-LO (full line), LAC I (dashed line) and LAC III (dotted line) parametrizations at  $\mu^2 = 75 \text{ GeV}^2$ .

For a more detailed discussion on theoretical aspects of parton density functions of the photon and its parametrizations, see *e.g.* [18, 41].

# Chapter 2

## HERA and H1

The following chapter briefly describes the  $ep$  collider HERA and one of the two detectors situated at HERA, H1.

### 2.1 HERA

HERA is the first ever constructed electron proton storage-ring, situated at the DESY laboratory in Hamburg, Germany.

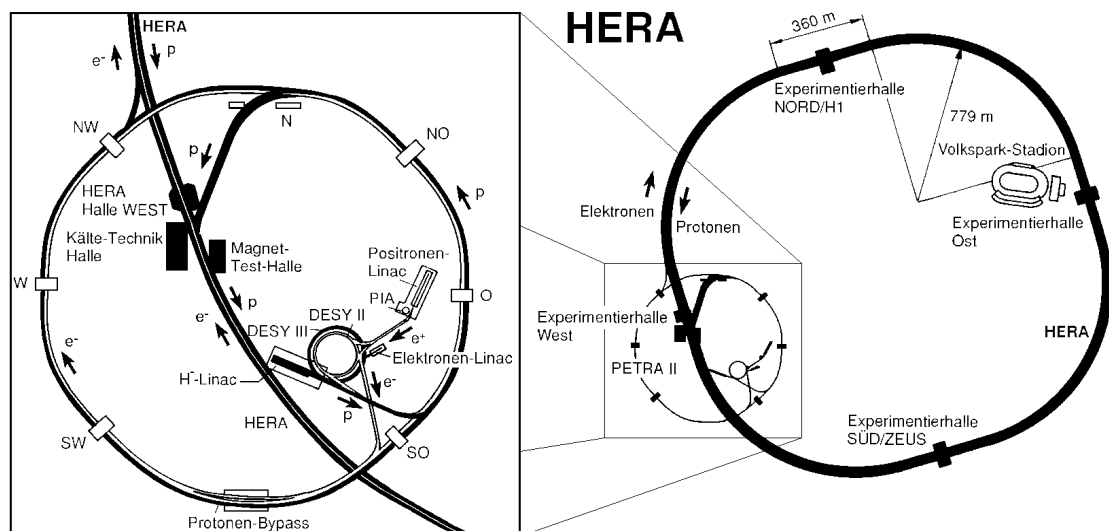


Figure 2.1: HERA and its pre-accelerators.

With various smaller systems (see figure 2.1), electrons and protons are pre-accelerated to an energy of 12 GeV and 40 GeV, respectively. They are then injected

into the main ring of 6.3 km circumference, where they are accelerated to their final energy of 26.7 GeV and 820 GeV. Finally, electrons and protons are brought to head-on collision in two halls, where two experiments — ZEUS and H1 — record the events.

Detailed information on the accelerator can be found in [42]. However, a few specialities of this new collider need to be mentioned:

- The particles are packed into a maximum of 210 bunches, resulting in a bunch crossing frequency of 10.4 MHz or, equivalently, in a bunch crossing distance of 28.8 m (96 ns). In the 1993 running period, 94 electron and 90 proton bunches were filled out of which 84 were colliding. The bunches with no colliding partner, called pilot bunches, are an important tool to check beam induced background.
- Due to the frequencies of the cavities for the proton ring of 52 MHz and 208 MHz, which is a factor of 5 and 20 higher than the bunch crossing frequency, respectively, some of the protons are not in the correct bunch but in a bunch adjacent to the nominal proton bunch. These satellite bunches have a shorter lifetime but nevertheless collide with electron bunches, leading to interactions that do not lie in the nominal interaction zone.

## 2.2 H1

This section shortly describes the H1 detector, one of the two general purpose detectors at HERA. A more detailed description can be found in [43].

An overview of the H1 detector is given in figure 2.2. In the same figure, the coordinate system as used by the H1 Collaboration is sketched: the  $z$ -direction is given by the flight direction of the initial proton and the polar angle  $\theta$  is defined relative to the positive  $z$ -direction. The main components of the H1 detector are:

- Central tracking chambers [2]:  
Closest to the interaction point, a set of six cylindrical chambers — two  $r\varphi$ -drift chambers, two  $z$ -drift chambers and two multi-wire proportional chambers (MWPCs) — cover a theta range of roughly  $25^\circ \lesssim \theta \lesssim 155^\circ$  (equivalent to  $1.5 \gtrsim \eta \gtrsim -1.5$ ). They are mainly used for momentum measurements of charged particles and for triggering purposes.
- Forward tracking chambers and transition radiators [3]:  
In the forward region (incident proton flight direction), a set of drift chambers, multi-wire proportional chambers and transition radiators extend the coverage of the tracking system to the theta range  $5^\circ \lesssim \theta \lesssim 25^\circ$  ( $3.1 \gtrsim \eta \gtrsim 1.5$ ).

## H1 detector

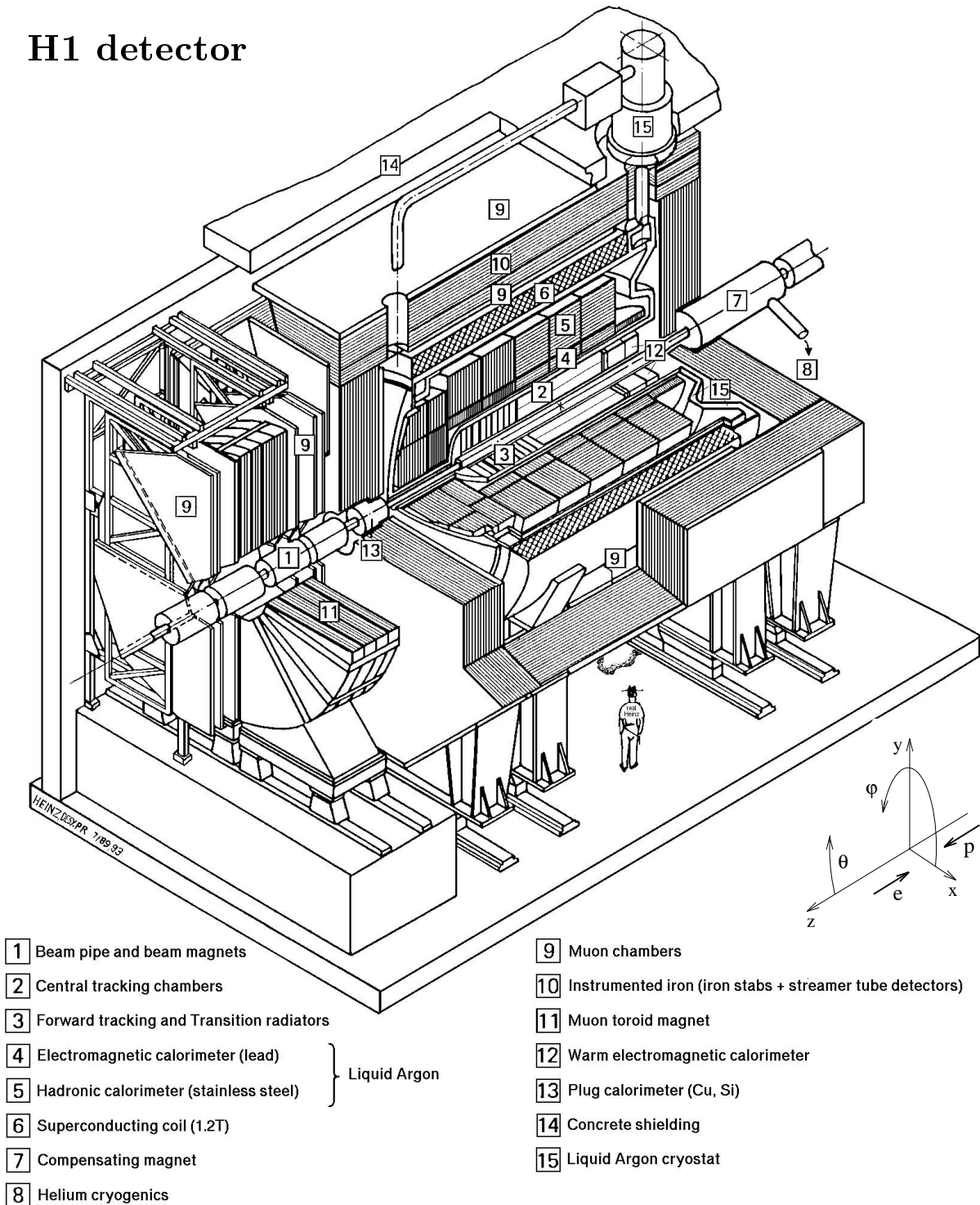


Figure 2.2: The H1 detector with its main components. On the right, the coordinate system as used by the H1 Collaboration is defined.

- Electromagnetic and hadronic calorimeter [4] [5]:  
The calorimeter [44] surrounds the tracking system in the central (barrel) and forward region. It is a non-compensating liquid argon (LAr) calorimeter, consisting of an electromagnetic part ([4]) with lead absorbers and a hadronic part ([5]) with stainless steel absorbers. The measurement of the hadronic energy is performed by applying a weighting technique [43, 45] to account for the non-compensating nature of the calorimeter. The angular coverage of this highly segmented ( $\approx 45000$  cells) calorimetric system is  $4^\circ < \theta < 155^\circ$  ( $3.4 > \eta > -1.5$ ). Note that the most backward part of the LAr calorimeter ( $145^\circ < \theta < 155^\circ$ ) only consists of an electromagnetic section. The depth of the calorimeter varies between 20 to 30 radiation lengths ( $X_0$ , electromagnetic section) and 4.7 to 7.0 absorption lengths ( $\lambda_{\text{abs}}$ , hadronic section).

Test-beam measurements have shown an energy resolution of the calorimeter modules of  $\sigma(E)/E \approx 12\%/\sqrt{E [\text{GeV}]} \oplus 1\%$  for electrons [46] and  $\sigma(E)/E \approx 50\%/\sqrt{E [\text{GeV}]} \oplus 2\%$  for charged pions [45].

Both the energy scales and the resolutions have been verified in the H1 experiment. By comparing the measured track momentum of electrons with their corresponding energy deposition in the LAr calorimeter, the absolute electromagnetic energy scale is presently known to 3%. The absolute hadronic energy scale as determined from studies of the transverse momentum balance in deep inelastic scattering events is known to a precision of 5%.

- Backward electromagnetic calorimeter [12]:  
The backward electromagnetic calorimeter (BEMC) completes the energy measurements in the backward direction. The theta range covered amounts to  $151^\circ < \theta < 177^\circ$  ( $-1.4 > \eta > -3.6$ ). This lead-scintillator sandwich calorimeter provides a good electromagnetic energy measurement ( $22.5 X_0$ ;  $\sigma(E)/E \approx 10\%/\sqrt{E [\text{GeV}]} \oplus 2\%$  [47]) but a poor measurement of the hadronic energy ( $1 \lambda_{\text{abs}}$ ).

- Magnet [6]:  
A superconducting magnet surrounds the LAr calorimeter, providing a homogeneous solenoidal field of 1.2 T parallel to the beam axis.

- Time-of-flight system (ToF):  
2 m upstream of the interaction zone, just behind the BEMC, two scintillator walls are installed. The time resolution of  $\approx 2$  ns per counter allows the discrimination between particles coming from the nominal interaction point and particles coming from background processes in the backward region, *e.g.* interactions of protons with the residual gas outside of the H1 detector.

- Luminosity system:  
The luminosity system consists of two crystal calorimeters for the measurement of electrons and photons scattered at very small angles  $\vartheta$  ( $\vartheta \equiv 180^\circ - \theta$ ).

The electron detector (“*e*-tagger”) is situated at  $z = -33$  m and the photon detector at  $z = -103$  m. The system provides an accurate determination of the luminosity by measuring the Bethe-Heitler process  $ep \rightarrow ep\gamma$ . Additionally, the electron detector can be used to measure (“tag”) scattered electrons with an energy fraction between 0.2 and 0.8 with respect to the electron beam energy and scattering angles  $0^\circ \leq \vartheta < 0.3^\circ$ . The two crystal calorimeters have a resolution of  $\sigma(E)/E \approx 10\%/\sqrt{E [\text{GeV}]} \oplus 1\%$ .

To protect the photon detector against synchrotron radiation, a  $2 X_0$  lead absorber together with a  $1 X_0$  water Čerenkov counter is installed right in front of the photon detector. The Čerenkov counter can be used as a veto against photon-conversion (*e.g.* of Bremsstrahlung photons) in the lead absorber.

Many detector components provide information for subdetector-triggers. The results of these subdetector-triggers are then combined into so-called subtriggers. In the following, we mention the subdetector-triggers which are important for this analysis:

- Drift chamber  $r\varphi$  trigger (DC- $r\varphi$  trigger) [48]:  
The information from the two central  $r\varphi$ -drift chambers is used to find charged particles which, in the  $r\varphi$  ( $xy$ ) projection, originate from the beam axis.
- $z$ -vertex trigger [80]:  
Both central and one forward multi-wire proportional chamber are used to determine the event-vertex position along the beam axis.
- ToF trigger:  
Both planes of the ToF system provide trigger information. In conjunction with the HERA-clock, which is in phase with the bunch crossings of the electron and proton beam, “interaction” and “background” gates can be formed.
- *e*-tag trigger:  
The *e*-tagger of the luminosity system is used to trigger on electrons scattered at very small angles  $\vartheta$ .

# Chapter 3

## Monte Carlo simulations

The following chapter is devoted to the modeling of physical processes. Software programs that aim to model physical processes are often called “event generators”. One such event generator will be described in detail.

The reason for the use of event generators in experimental particle physics is twofold. Firstly, one wants to be able to compare the measured data with theoretical expectations. However, since most detectors such as H1 are fairly complicated systems, it is hard to compare data directly with the output of such event generators. Therefore, one in addition to the event generators normally uses a program that simulates the response of the detector. Hence, the use of an event generator together with the detector simulation program is a tool to produce the “same” information as obtained from the detector itself — if both the modeling of the physical processes and the detector simulation are correct! Due to the technique used for these event generators and detector simulation programs, they are often called Monte Carlo (MC) simulations. The information as obtained from the Monte Carlo simulations is then treated in the same way as data from the detector, *i.e.*, it is reconstructed (the reconstruction program converts signals from tracking chambers and calorimeters into tracks of charged particles and energy depositions, respectively) and analyzed with the identical programs. The final two sets of events are then referred to as MC and data. A comparison of data with the theoretical expectations as given by the MC is now straightforward, but one has to bear in mind that the MC simulation includes more than just the modeling of the physics processes as given by the event generators.

The second reason for the use of Monte Carlo simulations is the need to simulate properties of the detector such as geometrical acceptance, detecting efficiency for certain physical processes, finite resolution of measured quantities, *etc.* This then allows to calculate absolute cross-sections or to determine correlations between measured and “true” physical quantities.

For this analysis, the event generator PYTHIA 5.6 [50] for photon proton interactions is used together with a generator for quasi-real photons as emitted from the electron.

For the hadronization process, the JETSET 7.3 [51] package, which incorporates the Lund fragmentation model [52], is used. More details on the H1 detector simulation program can be found in [43].

In the following section, we will discuss the ingredients of PYTHIA in more detail.

### 3.1 Pythia

PYTHIA is an event generator based on leading order  $\alpha_s$  QCD matrix elements for hard  $2 \rightarrow 2$  parton parton processes. Additionally, a parton shower model for initial- and final-state radiation is included, which can partly account for higher order corrections to the leading order  $2 \rightarrow 2$  processes. The strong coupling constant is determined from the leading logarithm equation (1.27), where  $\Lambda_{\text{QCD}} = 200 \text{ MeV}$  and  $n_f = 4$  is used.

Due to the fact that the leading order cross-sections for  $2 \rightarrow 2$  processes with massless partons diverge for vanishing transverse momentum, one has to introduce a lower cutoff for the transverse momentum  $\hat{p}_t$  of the outgoing partons relative to the direction of the incident partons. This cutoff for the hard subprocess is set to  $\hat{p}_{t,\text{min}} = 2 \text{ GeV}/c$ . The value for this cutoff is somewhat arbitrary. However, the resulting cross-section  $\sigma_{\text{hard}}(\hat{p}_{t,\text{min}})$  should not be larger than the total cross-section  $\sigma_{\text{tot}}$ , which puts a lower bound on  $\hat{p}_{t,\text{min}}$ . Measurements indicate that a value of  $\hat{p}_{t,\text{min}} = 2 \text{ GeV}/c$  is reasonable [53]. Note that for the final Monte Carlo sample selected for the comparison with data, the cut on the transverse momentum of the hard process must not cut into the  $\hat{p}_t$ -distribution of the MC events, since this would introduce an unwanted bias.

The above cut on  $\hat{p}_t$  additionally ensures that the process is calculable in perturbative QCD, *i.e.*, that the process is hard enough.

PYTHIA not only models hard parton parton scatterings, it also allows to introduce parton density functions for the incoming beam particles. The parton density functions used for this analysis are the leading order parametrizations of Glück, Reya and Vogt (GRV-LO) for the proton [54] and the photon [37]. The GRV-LO parametrization for the proton describes well the  $F_2^p$ -measurements as obtained from DIS [8] and the GRV-LO parametrization for the photon gives a consistent description of the hard photoproduction data as will be shown below. The factorization and renormalization scales as used for the parton density functions and the strong coupling constant  $\alpha_s$  are chosen as  $\mu_1^2 = \mu_2^2 = \hat{p}_t^2$ .

The  $p_t$ -distributions of the partons within the beam particles (named “intrinsic  $p_t$ ” or “primordial  $k_t$ ”) are modeled as  $\sim \exp(-k_t^2/\sigma^2) dk_t^2$  ( $\sigma = 0.44 \text{ GeV}/c$ , upper cutoff at  $2 \text{ GeV}/c$ ) for the proton and  $\sim 1/(k_{t,0}^2 + k_t^2) dk_t^2$  ( $k_{t,0} = 0.60 \text{ GeV}/c$ , upper cutoff given by  $\hat{p}_t$  of the hard subprocess or  $5 \text{ GeV}/c$ , whichever is smaller) for the photon. The power-like behaviour for the primordial  $k_t$  of the partons within the photon is suggested by the  $p_t$ -dependence of the  $\gamma \rightarrow q\bar{q}$  splitting.

This intrinsic transverse momentum together with the transverse momentum produced by the initial-state radiation introduces a net transverse momentum for the hard subprocess. Therefore, the two partons from the hard process are no longer scattered back to back in the plane transverse to the beam direction as expected from a leading order calculation.

PYTHIA optionally allows for additional interactions within the same event, that is, within one single  $\gamma p$  scattering. Since this so-called *multiple interaction (mi)* option will play an important rôle in the forthcoming analysis, we will discuss some details of this model [55]. Multiple interactions within the same event are modeled with leading order  $2 \rightarrow 2$  parton parton scattering processes just as the hard subprocess, *i.e.*, one assumes more than one scattering of partons from the photon and the proton. One thereby still requires that the hardest scattering needs to have a transverse momentum  $\hat{p}_t$  above  $\hat{p}_{t,\min}$  but now allows for additional scatterings with  $\hat{p}_t > \hat{p}_{t,\min}^{\text{mi}}$  and  $\hat{p}_{t,\min}^{\text{mi}} < \hat{p}_{t,\min}$ <sup>1</sup>. Since the  $2 \rightarrow 2$  parton cross-section is divergent as  $\hat{p}_t$  goes to zero, one can achieve infinitely large cross-sections  $\sigma_{\text{hard}}(\hat{p}_t)$ , which is unreasonable. However, one may interpret the fraction  $\sigma_{\text{hard}}(\hat{p}_{t,\min}^{\text{mi}})/\sigma_{\text{tot}}$ , where  $\sigma_{\text{tot}}$  is the observed total photon proton cross-section (in the actual implementation of this model, the inelastic non-diffractive cross-section  $\sigma_{\text{nd}}$  is used rather than the total cross-section  $\sigma_{\text{tot}}$ ), as the average number of parton parton scatterings *per event*. So, by varying  $\hat{p}_{t,\min}^{\text{mi}}$ , one effectively varies the average number of scatterings per event. The fluctuation of the number of scatterings per event is governed by Poisson statistics. The transverse momentum cutoff for the multiple interaction option is set to  $\hat{p}_{t,\min}^{\text{mi}} = 1.45 \text{ GeV}/c$ .

The observation of multiple interactions in hadron hadron (or photon proton) physics is not well established. The AFS [56], UA2 [57] and CDF [58] Collaborations have published results on the topic, but only two of them ([56, 58]) claim evidence for double parton interactions (for a discussion of the results, see [58]).

There are many more knobs and switches to turn in PYTHIA, but apart from the ones mentioned above, all are set to their default values (the value of  $1.45 \text{ GeV}/c$  for the transverse momentum cutoff for the multiple interaction option,  $\hat{p}_{t,\min}^{\text{mi}}$ , and the values for the intrinsic  $k_t$  of the partons from the proton are the default values, too). Most parameters of PYTHIA were tuned at various earlier experiments and should be a good starting point.

To conclude this chapter, let us make a few remarks on the statistics for the Monte Carlo sample. The production of simulated events is very computer-intensive, the average computing time per event lying somewhere around a minute (the most time-intensive part is the simulation of the detector response). Some improvement can be achieved by weighting events, *e.g.* events with a small transverse momentum  $\hat{p}_t$  of the hard subprocess are weighted with factors up to  $\lesssim 10$  such that only

---

<sup>1</sup>The hardest scattering within an event is assumed to be well described by perturbative QCD, *i.e.*,  $\hat{p}_{t,\min}$  should be large enough.  $\hat{p}_{t,\min}^{\text{mi}}$  however may well extend into the low- $p_t$  region and the QCD description of these scatterings is assumed to be a good guess for “soft” physics processes.

a fraction of these events — which have the largest cross-section — are actually produced. Events that are more seldom are weighted with a smaller factor or not at all. Another possibility to reduce the computing-time for the production of MC events is to only (fully) simulate events that fulfill a certain selection requirement, *e.g.* that the scattered electron is “measured” by the electron tagger of the luminosity system. This reduction method was adopted for the first of the two MC samples mentioned below. The vast amount of computing time needed puts a limit on the number of different MC samples that can be produced.

The MC samples that were produced for this analysis are listed in table 3.1.

$\hat{p}_{t,\min}$	$\hat{p}_{t,\min}^{\text{mi}}$	number of events generated <sup>a</sup>	number of events reconstructed <sup>b</sup>	luminosity <sup>c</sup>
2 GeV/c	1.45 GeV/c	$\approx 950'000$	$\approx 100'000$	$\approx 590 \text{ nb}^{-1}$
4 GeV/c	none <sup>d</sup>	$\approx 130'000$	$\approx 15'000$	$\approx 320 \text{ nb}^{-1}$

<sup>a</sup>Number of events produced with the event generator.

<sup>b</sup>Number of events that were fed through the entire MC-chain: generation, detector simulation and reconstruction. The difference in number with respect to the generated events is due to the reduction techniques described above.

<sup>c</sup>The luminosity of a MC sample is the luminosity that would be needed to get the number of (generated) events contained in the MC sample, assuming that the cross-section is correctly described by the MC.

<sup>d</sup>*i.e.*, no multiple interactions.

Table 3.1: MC samples used for this analysis.

# Chapter 4

## Jets and jet algorithms

The goal of this work is to measure hard parton parton scatterings in photoproduction processes. However, the experimental observation of coloured partons seems to be impossible (confinement property of Quantum Chromodynamics). What can be observed experimentally is the formation of “jets” in hard scattering processes. But what exactly do we mean by the term “jet” and what is the intuitive picture behind it? As mentioned earlier, a jet may be thought of as a bunch of collimated, colourless particles which themselves are the result of the hadronization of the scattered hard partons. This picture suggests that a jet is the experimentally measurable observable most closely related to a parton. However, this is only a naïve picture [59]. Physical processes and constraints such as initial- and final-state parton showers, multiple interactions, fragmentation effects and particle decays as well as conservation of four-momentum and colour *etc.*, make the unambiguous description of a jet as the result of the parton scattering impossible. Therefore, many quantitatively different definitions of a jet exist. Common to all of them is the aim that the properties of a jet, *i.e.*, its energy and momentum, are as close as possible to the same quantities of the hard parton that initiated the jet.

In the following, we will discuss two classes of jet-finding algorithms, cone algorithms and cluster algorithms. We will then discuss the so-called “longitudinally-boost-invariant  $k_{\perp}$ -clustering algorithm” in more detail. Using the latter, we will explore the correlation of jet and parton properties such as  $p_t$ ,  $\eta$  and  $\varphi$  and will study the resolution of  $x_{\gamma}$  determined from  $p_t$  and  $\eta$  of the two  $p_t$ -leading jets.

### 4.1 Cone algorithms

A cone-type algorithm essentially sums up the energy within a fixed cone in  $(\eta, \varphi)$  space ( $\varphi$  measured in radians). If the transverse energy relative to the beam direction within the cone exceeds some threshold  $E_{t,\min}$ , a jet is found. The use of the  $(\eta, \varphi)$  coordinates has the advantage that the definition of the cone-size is independent with respect to boosts in the beam direction.

Various forms of cone-type algorithms exist, which sometimes makes a comparison of results from different experiments a difficult task. However, in 1990, a common standard for cone algorithms, the “Snowmass Accord”, was set up [60]. Cone-type algorithms are mainly used in hadron hadron physics. At HERA, cone algorithms are used for photoproduction physics by both experiments, ZEUS and H1, and for some analysis in deep inelastic scattering. In DIS, one normally chooses some other preferred direction instead of the beam direction. In this case, one needs to redefine  $\eta$  accordingly.

## 4.2 Cluster algorithms

Cluster algorithms have three main ingredients: a distance measure, a recombination prescription and a cut variable. The distance between all pairs of particles (*e.g.* given as tracks in a tracking chamber or as energy clusters in a calorimeter) is calculated and the pair with minimal distance is recombined to form a new “particle”. The procedure is then repeated until the distance measure exceeds the value given by the cut variable. The remaining “particles” or objects are then called jets.

As for the cone algorithms, there exist various different forms of cluster algorithms, differing mainly in the distance measure and the recombination prescription used. Cluster algorithms are mostly used in  $e^+e^-$  physics. At HERA, cluster algorithms have been used *e.g.* for the determination of  $\alpha_s$  in deep inelastic scattering [61]. No cluster algorithm has so far been applied to hard photoproduction processes at HERA<sup>1</sup>. It is the aim of this analysis to introduce a cluster algorithm to photoproduction physics at HERA. The cluster algorithm chosen is the *longitudinally-boost-invariant  $k_{\perp}$ -clustering algorithm*. A detailed description of this novel cluster algorithm is the subject of the next section.

## 4.3 Longitudinally-boost-invariant $k_{\perp}$ -clustering algorithm

The longitudinally-boost-invariant  $k_{\perp}$ -clustering algorithm for hadron hadron collisions [63, 64] (henceforth shortly called  $k_{\perp}$ -algorithm) is a newly proposed cluster algorithm, which is a non-trivial generalization of the so-called “Durham”-algorithm [65] used in  $e^+e^-$  physics. Note that the Durham-algorithm is also known as “ $k_{\perp}$ -algorithm for  $e^+e^-$  physics”. Here however, we will always refer to the longitudinally-boost-invariant  $k_{\perp}$ -clustering algorithm when talking about “the  $k_{\perp}$ -algorithm”.

---

<sup>1</sup>The ZEUS Collaboration has used a cluster algorithm to study the photon remnant in resolved photoproduction processes [62].

The main extension of the  $k_{\perp}$ -algorithm compared to the Durham-algorithm is that it has to deal with the hadron (or photon) remnants present in hadron hadron (photon proton) interactions and isolate them from the high- $p_t$  jets produced by the hard scattering of partons. This is achieved by a pre-clustering which separates “beam jets” from “hard final state jets”. An analogous generalization of the Durham-algorithm for deep inelastic scattering does also exist [63]. Another very similar algorithm to the  $k_{\perp}$ -algorithm for hadron hadron physics is the “successive combination jet algorithm” [66].

The exact prescription for the  $k_{\perp}$ -algorithm is the following:

*pre-clustering:*

- For every final state “particle” (object)  $k$  and for every pair  $(kl)$ , compute the corresponding values of the resolution variables ( $k, l = 1, \dots, n$ )

$$d_{kB} = p_{t,k}^2 \quad (4.1)$$

$$d_{kl} = \min(p_{t,k}^2, p_{t,l}^2) \left\{ (\eta_k - \eta_l)^2 + (\varphi_k - \varphi_l)^2 \right\} \quad (4.2)$$

$d_{kB}$  is the distance to the beam whereas  $d_{kl}$  is the distance between two objects. Note that  $d_{kl}$  (in the small angle limit) is the minimal relative transverse momentum  $k_{\perp(kl)}^2$  of one “particle” relative to the other [65, 64]. Additionally note that both variables,  $d_{kB}$  and  $d_{kl}$ , are invariant under boosts in the beam direction. Hence the name for the algorithm.

- Determine the smallest value among  $\{d_{kB}, d_{kl}\}$ ,  $d_n := \min(d_{kB}, d_{kl})$ . If  $d_n$  is given by  $d_{ij}$ , the two “particles”  $i$  and  $j$  have to be merged into a single object using the recombination scheme

$$p_{t,(ij)} = p_{t,i} + p_{t,j} \quad (4.3)$$

$$\eta_{(ij)} = \frac{p_{t,i} \cdot \eta_i + p_{t,j} \cdot \eta_j}{p_{t,(ij)}} \quad (4.4)$$

$$\varphi_{(ij)} = \frac{p_{t,i} \cdot \varphi_i + p_{t,j} \cdot \varphi_j}{p_{t,(ij)}} \quad (4.5)$$

If  $d_n$  is given by  $d_{iB}$ , the “particle”  $i$  is included in the “beam jets” and removed from the list of objects.

- This pre-clustering procedure is repeated as long as  $d_n$  is smaller than some stopping parameter  $d_{\text{cut}}$ . If  $d_n$  is larger than  $d_{\text{cut}}$ , we are left with the beam jets and objects which are called “hard final state jets”.

*resolving jet-structure:*

- Define a new resolution variable  $\delta_{\text{cut}} = Q_0^2/d_{\text{cut}} \leq 1$ .
- For every pair of “particles” ( $kl$ ) in a hard final state jet, compute the rescaled resolution variable ( $k, l = 1, \dots, m; m \leq n$ )

$$\delta_{kl} = \frac{d_{kl}}{d_{\text{cut}}} \quad . \quad (4.6)$$

Note that one starts again with the initial set of “particles”. However, “particles” already assigned to the beam jets in the pre-clustering step do not participate.

- If  $\delta_{ij} := \min(\delta_{kl})$  is smaller than  $\delta_{\text{cut}}$ , the two “particles”  $i$  and  $j$  are merged according to the recombination scheme (4.3–4.5) given above.
- This process of resolving the jet structure is repeated as long as  $\delta_{ij}$  is smaller than  $\delta_{\text{cut}}$ . If all pairs of objects have  $\delta_{kl}$  larger than  $\delta_{\text{cut}}$ , we are left with the so-called “sub-jets”.

The pre-clustering procedure separates the hard scattering subprocess from the low- $p_t$  scattering fragments. In other words, it factorizes the hadron hadron (or photon proton) interaction into a soft part and a hard subprocess. This factorization property of the  $k_{\perp}$ -algorithm is very important and will be discussed further below. The stopping parameter  $d_{\text{cut}} \hat{=} p_{t,\text{cut}}^2$  defines the hard scale (factorization scale) of the process.

Once the hard subprocess has been defined, one can then proceed to resolve the jet-structure in the same way as is done for  $e^+e^-$  processes, *i.e.*, the clustering prescription is identical to the  $k_{\perp}$ -algorithm used in  $e^+e^-$  physics.

The  $k_{\perp}$ -algorithm for hadron hadron physics offers many possibilities for the distance measure and the recombination scheme [64]. The one described above is the simplest one and the one most closely related to cone-type algorithms due to its definition of the distance measure.

The main difference between the longitudinally-boost-invariant  $k_{\perp}$ -clustering algorithm and a cone-type algorithm — apart from their totally different definition — is, that the  $k_{\perp}$ -algorithm is able to factorize a scattering process into a hard subprocess and a low- $p_t$  part [64]. As already mentioned earlier, the factorization theorem states that hard scattering cross-sections can be calculated perturbatively in terms of hard partonic subprocesses and universal parton density functions of the colliding beam particles (*cf.* equation (1.28)):

$$\sigma_{\gamma p \rightarrow X} = \sum_{ijkl} \int_0^1 \int_0^1 dx_{\gamma} dx_p f_{i/\gamma}(x_{\gamma}, \hat{p}_t^2) f_{j/p}(x_p, \hat{p}_t^2) \hat{\sigma}_{ij \rightarrow kl}(\hat{p}_t^2) \quad . \quad (4.7)$$

The factorization scale which separates the hard subprocess from the low- $p_t$  fragments is given by  $\hat{p}_t^2$ . To allow for the comparison of experimental results with theoretical predictions, a jet algorithm needs to be able to factorize a process into a soft part and a hard subprocess in the same way as is done for the theoretical calculations. The  $k_{\perp}$ -algorithm does have this property (the factorization scale is given by  $d_{\text{cut}} \hat{=} p_{t,\text{cut}}^2$ , see above) whereas cone-type algorithms don't!

Other necessary properties of jet algorithms for hadron hadron processes are fulfilled by both the  $k_{\perp}$ -algorithm and cone-type algorithms [60, 63, 64].

Apart from this fundamental superiority of the  $k_{\perp}$ -algorithm over cone-type algorithms, effects due to soft emission of gluons or non-perturbative processes (*e.g.* fragmentation, multiple interactions) are expected to be smaller for the  $k_{\perp}$ -algorithm than for cone algorithms [64]. Last but not least, cluster algorithms do not have the ambiguities that cone-type algorithms have when it comes to overlapping jets, *i.e.*, how jets with overlapping cones are treated.

In the following section we want to study the correlation for variables such as  $p_t$ ,  $\eta$ ,  $\varphi$  and  $x_{\gamma}$  when applying the  $k_{\perp}$ -algorithm to photoproduction processes at HERA.

## 4.4 Reconstruction of parton kinematics using the $k_{\perp}$ -algorithm

Before we set out to describe the jet parton correlations obtained when applying the  $k_{\perp}$ -algorithm to photoproduction processes, we have to be more specific on the parameters for the  $k_{\perp}$ -algorithm and the Monte Carlo sample used.

For the longitudinally-boost-invariant  $k_{\perp}$ -clustering algorithm described above, we have to fix the stopping parameters  $d_{\text{cut}}$  and  $\delta_{\text{cut}}$  :

$$d_{\text{cut}} = 6^2 \text{ GeV}^2/c^2 \quad (4.8)$$

$$\delta_{\text{cut}} = 1 \quad . \quad (4.9)$$

Hence, we do not attempt to resolve jet-structures but only ask for jets with transverse momentum  $p_t$  larger than  $6 \text{ GeV}/c$ . This mode of the  $k_{\perp}$ -algorithm most strongly resembles cone-type algorithms [64]. As input objects for the algorithm, we use clusters of energy in the LAr calorimeter and the BEMC.

The input data used for this investigation (and throughout this chapter) is a Monte Carlo sample based on the event generator PYTHIA and includes multiple interactions. We then ask for at least two jets found by the  $k_{\perp}$ -algorithm, where the transverse energy<sup>2</sup> of the jets has to exceed  $6 \text{ GeV}$  (see above). The value for the

---

<sup>2</sup>Since the  $k_{\perp}$ -algorithm does not produce massive objects,  $E_t^{\text{jet}}$  is identical to  $p_t^{\text{jet}}$ .

minimal transverse momentum of the jets was chosen such that the  $\hat{p}_t$ -distribution of the selected events is not affected by the cut at  $\hat{p}_{t,\min}$  introduced when generating the events. The two jets with the highest transverse energy then have to pass the following cut:

$$0 < \eta^{\text{jet}} < 2.5 \quad . \quad (4.10)$$

The reason for this cut is manifold:

- The backward electromagnetic calorimeter (BEMC) only provides a poor measurement of the hadronic energy flow. We therefore ensure that the jets are well contained within the liquid argon calorimeter, which covers the pseudo-rapidity range  $-1.5 < \eta < 3.4$ .
- We are mainly interested in resolved photon processes, that is, in low  $x_\gamma$ . According to equation (1.38), this asks for small transverse momenta and large pseudo-rapidities of the two jets. Our aim therefore is to measure jets with pseudo-rapidities as large as possible. The backward region (*i.e.*, small pseudo-rapidities) is less important.
- Due to the energy-asymmetry of the two HERA-beams, the electron proton center-of-mass system moves with pseudo-rapidity  $\eta_{ep} = 1.7$  relative to the laboratory system. The pseudo-rapidity of the photon proton center-of-mass system is even larger ( $1.9 < \eta_{\gamma p} < 2.4$  for  $0.25 < y < 0.7$ ). An ideal pseudo-rapidity range for the measurement of hard photon proton processes would be symmetric to  $\eta_{\gamma p}$ , resulting in the hard process typically being in the center of the accessible  $\eta$ -range (assuming  $\langle x_\gamma \rangle \approx \langle x_p \rangle$ ) and both remnants as far away as possible. This, however, can not be achieved. We therefore expect to be influenced by the remnants, especially the photon remnant.

Figure 4.1 shows the pseudo-rapidity distribution of the two  $p_t$ -leading jets. The full line shows the  $\eta^{\text{jet}}$ -distribution for jets which were successfully matched (the matching criterion is described in section 4.4.1) with a parton from the hard subprocess, whereas the dashed and dotted lines show the  $\eta^{\text{jet}}$ -distribution for jets which were matched with the photon or proton remnant, respectively. The remnants are mimicked by the four-momentum sum of the spectator partons and the partons from the initial-state radiation given within the event generator. The term “spectator” refers to the partons within the photon and the proton which do not take part in the hard subprocess. A “remnant” of the photon or the proton more globally includes all soft (*i.e.*, low- $p_t$ ) partons of the “final state” (before fragmentation) which move along the incident direction of the photon or the proton, respectively. Partons emerging from soft multiple interactions of the spectators are normally not assigned to the remnants. To ensure that these remnants can possibly initiate a jet, a transverse momentum of at least 6 GeV/ $c$  is required for a possible matching with a jet.

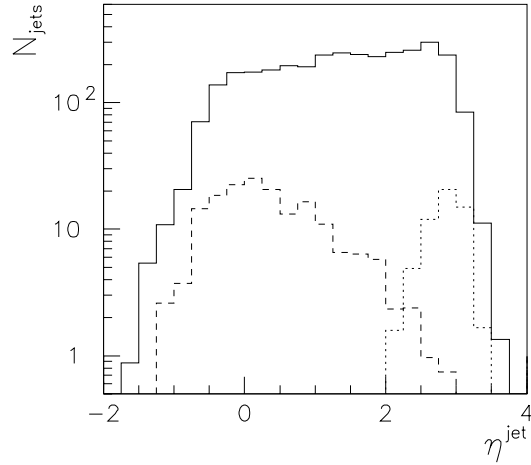


Figure 4.1:  $\eta^{\text{jet}}$ -distribution for jets ( $E_t^{\text{jet}} > 6$  GeV) which were successfully matched with a parton from the hard subprocess (full line) and for jets matched with the photon (dashed line) or proton (dotted line) remnant.

We will now examine the reconstruction of the parton kinematics for this 2-jet sample. For another analysis of the reconstruction quality of the  $k_{\perp}$ -algorithm, see [67]. There, the “successive combination jet algorithm” [66], which is very similar to the  $k_{\perp}$ -algorithm, was studied.

#### 4.4.1 Jet parton correlations

In the following, we investigate the correlation between parton properties as given by the event generator and properties of the jets found by the  $k_{\perp}$ -algorithm. To be able to correlate a jet to its underlying parton, we have to apply a matching criterion. This is done by calculating the distance between the two  $p_t$ -leading jets and the two partons from the hard subprocess in the  $(\eta, \varphi)$  plane:

$$R_{kl} = \sqrt{(\eta_k^{\text{jet}} - \eta_l^{\text{parton}})^2 + (\varphi_k^{\text{jet}} - \varphi_l^{\text{parton}})^2} \quad . \quad (4.11)$$

The pair  $ij$  with the minimal distance  $R_{ij} := \min(R_{kl})$  ( $k, l = 1, 2$ ) is matched first and the jet and parton remaining make up the second pair.

For the determination of the parton kinematics, we use the properties of the two partons emerging from the hard subprocess after initial-state radiation but before final-state radiation and fragmentation. Hence, the partons do not need to be balanced in transverse momentum.

Figure 4.2 shows the jet parton correlation for  $p_t$ ,  $\eta$  and  $\varphi$ . Henceforth,  $p_t$  ( $E_t$ ) will always be given in GeV/ $c$  (GeV) and  $\varphi$  in radians (if not mentioned otherwise).

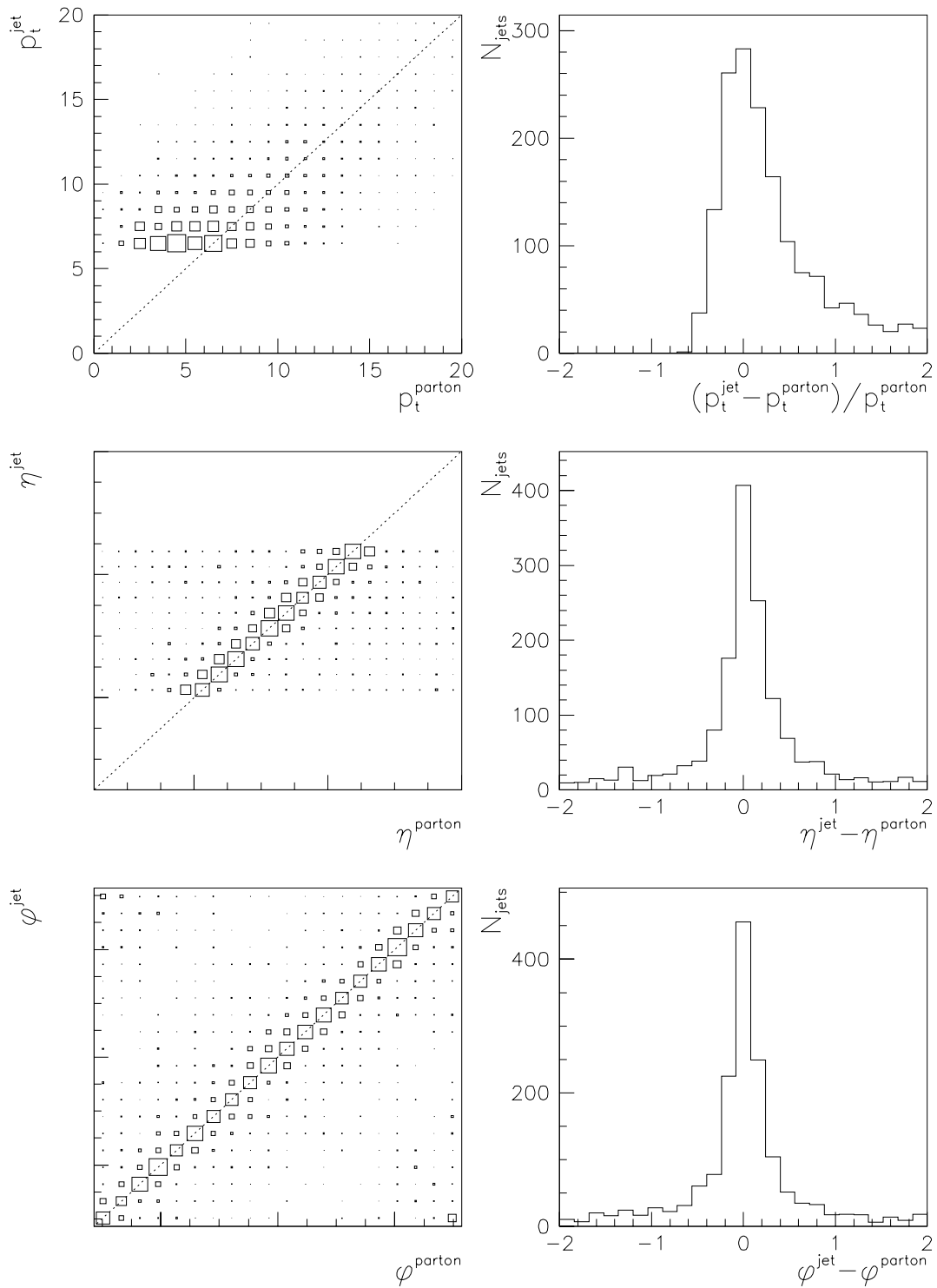


Figure 4.2: Jet parton correlation for  $p_t$ ,  $\eta$  and  $\phi$ .

The correlation in  $p_t$  is somewhat poor, whereas the correlation in  $\eta$  and  $\varphi$  is very good. There are various reasons for the poor correlation in  $p_t$ :

- Energy clusters assigned to the jets which are not due to the hard subprocess itself, but due to some other source, *e.g.* multiple interactions within the same event or photon and proton remnants. The main reason for the average shift of  $p_t^{\text{jet}}$  towards too high values compared to  $p_t^{\text{parton}}$  is due to energy contributions from multiple interactions.
- Final-state radiation and fragmentation effects.
- Resolution of the LAr calorimeter for hadronic energy measurements.

As already mentioned, the correlation in  $\eta$  and  $\varphi$  is good. However, there are long tails in both the  $\eta^{\text{jet}} - \eta^{\text{parton}}$  and the  $\varphi^{\text{jet}} - \varphi^{\text{parton}}$  distribution. These are due to misidentified jets, that is, jets that were initiated by other sources than the partons from the hard subprocess, *i.e.*, parton showers, photon and proton remnants, *etc.* The only possibility to reduce events with misidentified jets is by applying appropriate kinematical cuts.

Some of the misidentified jets come from events where particles from the photon remnant are identified as a jet. We call these jets “photon remnant jets”. These “photon remnant jets” mostly have a small pseudo-rapidity, whereas the second jet in such events often has a large pseudo-rapidity. This can be explained by the fact that the probability for a misidentified jet due to the photon remnant rises with falling  $x_{\gamma}$ , since for small  $x_{\gamma}$  most of the initial photon energy is left for the remnant. A small  $x_{\gamma}$  however is equivalent to large pseudo-rapidities for both partons from the hard subprocess (*cf.* equation (1.38)). Therefore, events where particles from the photon remnant are misidentified as a jet have two jets with large pseudo-rapidity difference  $|\eta_1^{\text{jet}} - \eta_2^{\text{jet}}|$ . The fact that the pseudo-rapidity of the two partons at low  $x_{\gamma}$  is large in turn leads to the tail at negative values of  $\eta^{\text{jet}} - \eta^{\text{parton}}$ . Figure 4.3 shows the pseudo-rapidity difference  $|\eta_1^{\text{jet}} - \eta_2^{\text{jet}}|$  of the two jets for events where both jets were successfully matched with the hard partons (full line) and for events where one of the jets was matched with the photon (dashed line). Figure 4.3 a) includes all events, whereas figure 4.3 c) only includes events at low  $x_{\gamma}$  ( $x_{\gamma} < 0.1$ ). As expected, the effect explained above is much more prominent at low  $x_{\gamma}$ .

To reduce the number of “photon remnant jets” we apply an additional cut to our event sample:

$$|\Delta\eta^{\text{jets}}| = |\eta_1^{\text{jet}} - \eta_2^{\text{jet}}| < 1.2 \quad . \quad (4.12)$$

The reduction of the negative tail for the  $\eta^{\text{jet}} - \eta^{\text{parton}}$  distribution at low  $x_{\gamma}$  is shown in figure 4.4.

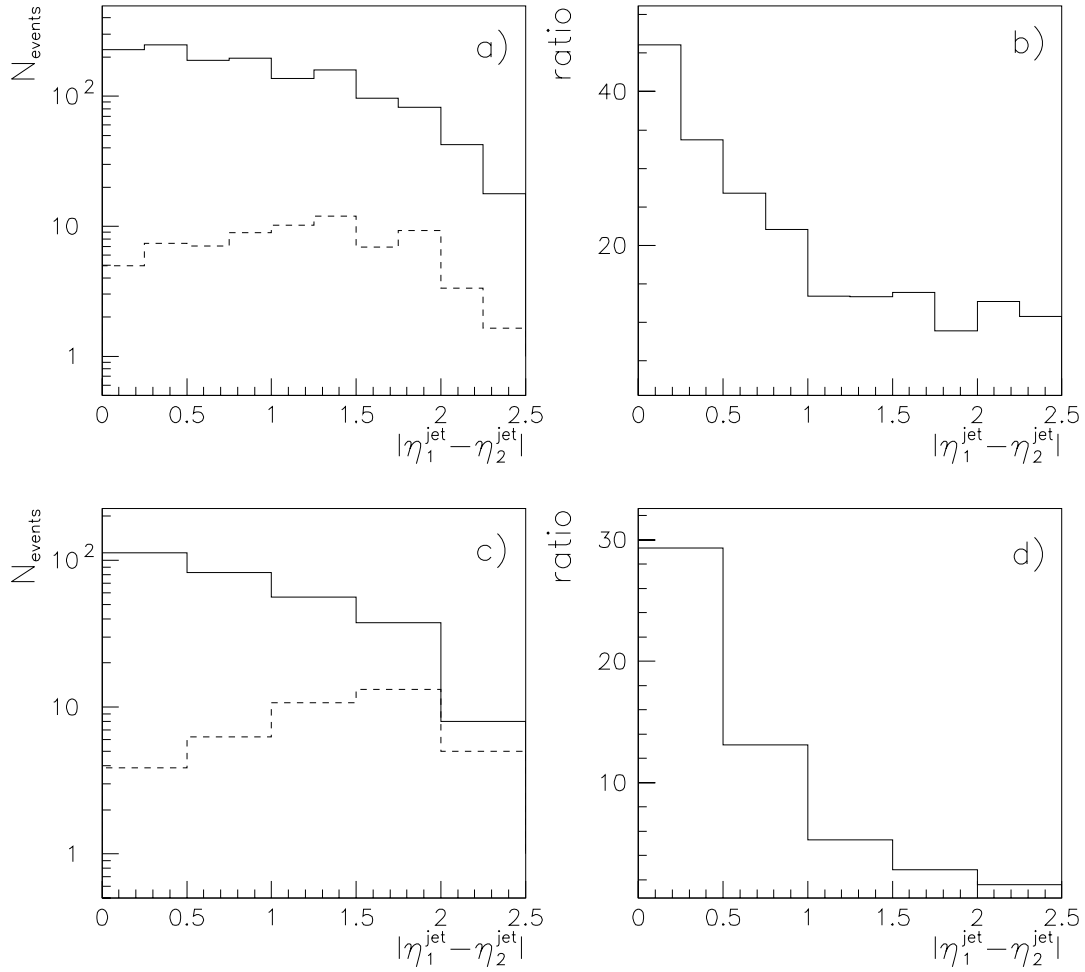


Figure 4.3: Pseudo-rapidity difference  $|\eta_1^{\text{jet}} - \eta_2^{\text{jet}}|$ . Events with no misidentified jets (full line) and events where one of the jets was matched with the photon remnant (dashed line) are shown for the entire  $x_\gamma$ -range (a,b)) and for  $x_\gamma < 0.1$  (c,d)). Figures b) and d) show the ratio of the two contributions.

For events with no misidentified jets, a cut on  $\Delta\eta^{\text{jets}}$  translates to a cut on the scattering angle<sup>3</sup>  $\theta^*$  of the two partons in the center-of-mass system of the hard subprocess (we assume  $\eta^{\text{jet}} \approx \eta^{\text{parton}}$ ):

$$\Delta\eta^{\text{jets}} \approx -2 \ln \left( \tan \frac{\theta^*}{2} \right) . \quad (4.13)$$

The distribution of this scattering angle  $\theta^*$  is an important prediction of Quantum Chromodynamics and will be discussed further in chapter 6.

<sup>3</sup> \* will always refer to variables in the center-of-mass system of the hard subprocess.

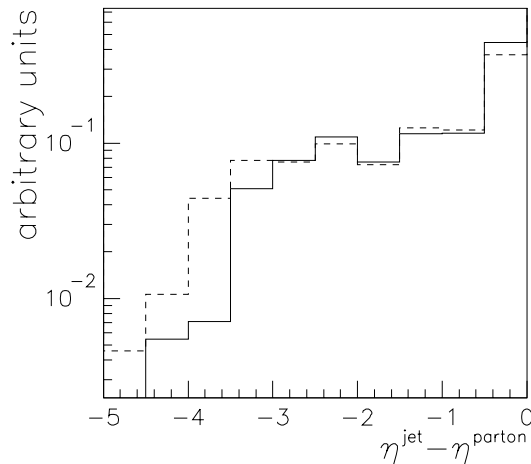


Figure 4.4: Jet parton correlation for  $\eta$  at low  $x_{\gamma}$  ( $x_{\gamma} < 0.1$ ) before (dashed line) and after (full line) applying the cut on  $|\Delta\eta^{\text{jets}}|$ . Both distributions are normalized to unit area.

#### 4.4.2 $x_{\gamma}$ -resolution

The determination of  $x_{\gamma}$  relies on equations (1.34) and (1.38) which we repeat for completeness:

$$x_{\gamma}^{\text{partons}} = \frac{1}{2yE_e} \sum_{i=1}^2 (E_i^{\text{parton}} - p_{z,i}^{\text{parton}}) = \frac{1}{2yE_e} \sum_{i=1}^2 p_{t,i}^{\text{parton}} \cdot e^{-\eta_i^{\text{parton}}} \quad . \quad (4.14)$$

Hence, to determine  $x_{\gamma}$ , one needs the transverse momenta and the pseudo-rapidities of the two partons from the hard process as well as the photon energy  $E_{\gamma} = yE_e$ . To prove that equation (4.14) correctly reproduces  $x_{\gamma}$  (*i.e.*, that the assumptions for the derivation of equation (4.14) are adequate), the correlation of  $x_{\gamma}^{\text{partons}}$  derived from equation (4.14) with  $x_{\gamma}$  as used within the event generator (“true”  $x_{\gamma}$ ) was checked and found to be very good (not shown). We can therefore proceed to study the correlation between true  $x_{\gamma}$  and the value for  $x_{\gamma}$  as determined by

$$x_{\gamma}^{\text{jets}} = \frac{1}{2yE_e} \sum_{i=1}^2 (E_i^{\text{jet}} - p_{z,i}^{\text{jet}}) = \frac{1}{2yE_e} \sum_{i=1}^2 p_{t,i}^{\text{jet}} \cdot e^{-\eta_i^{\text{jet}}} \quad . \quad (4.15)$$

We hereby assume that the transverse momenta and the pseudo-rapidities of the hard partons are reproduced by  $p_t$  and  $\eta$  of the two  $p_t$ -leading jets. However, there is an additional complication — we also have to determine the energy of the photon,  $yE_e$ .

One way of measuring  $y$  is by measuring the energy of the scattered electron in the electron tagger of the luminosity system (*cf.* equation (1.24)):

$$y_{\text{tag}} = 1 - \frac{E'_e}{E_e} \quad . \quad (4.16)$$

Another possibility of measuring  $y$ , which is due to Jacquet and Blondel [68], relies on the measurement of all particles but the scattered electron in the final state:

$$y_{\text{JB}} = \frac{1}{2E_e} \sum_i (E_i - p_{z,i}) \quad ; \quad i = \text{all particles except scattered electron.} \quad (4.17)$$

As long as one measures the scattered electron in the  $e$ -tagger,  $y_{\text{tag}}$  provides a much better determination of true  $y$  than does  $y_{\text{JB}}$ , mainly because some final state particles will always escape detection and therefore  $y_{\text{JB}}$  will typically be too low. The loss of particles is especially harmful for backward-going particles, since they may have a large contribution to  $E - p_z$ . Additionally, the BEMC, which covers the backward region of the detector, measures the hadronic energy flow only poorly, which also leads to an underestimation of  $E - p_z$ . Figure 4.5 shows the correlation of  $y_{\text{tag}}$  and  $y_{\text{JB}}$  with  $y$  as taken from the event generator. The data sample used is the same as the one described above. It only contains events where the scattered electron is measured in the electron tagger. Note that the events were generated with the cut  $0.25 < y < 0.7$ .

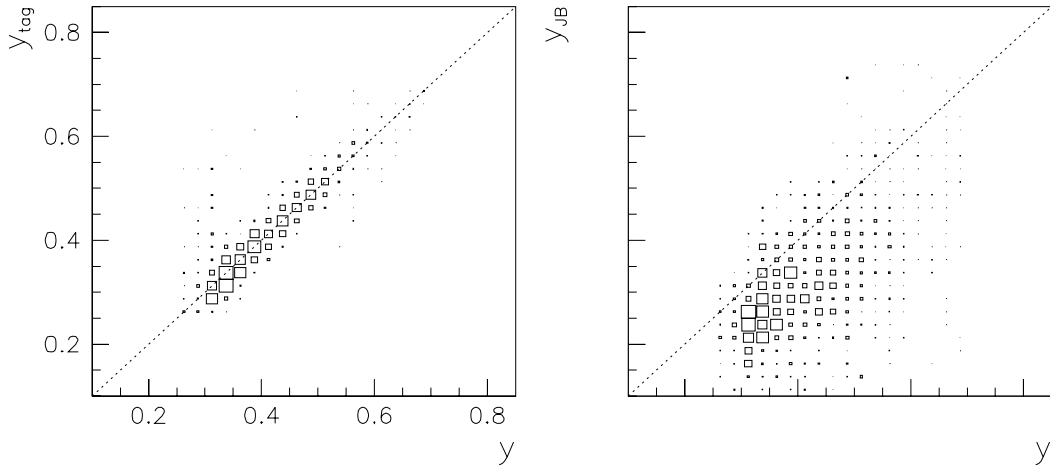


Figure 4.5: Correlation of true  $y$  with  $y_{\text{tag}}$  and  $y_{\text{JB}}$ , respectively.

As expected, the correlation between  $y_{\text{tag}}$  and true  $y$  is much better than the correlation between  $y_{\text{JB}}$  and  $y$ .

We now turn towards the question of the resolution of  $x_\gamma$  when applying the  $k_\perp$ -algorithm to photoproduction data at HERA. Figure 4.6 shows the correlation between  $x_\gamma^{\text{jets}}$  as determined by equation (4.15) and true  $x_\gamma$  as given by the event

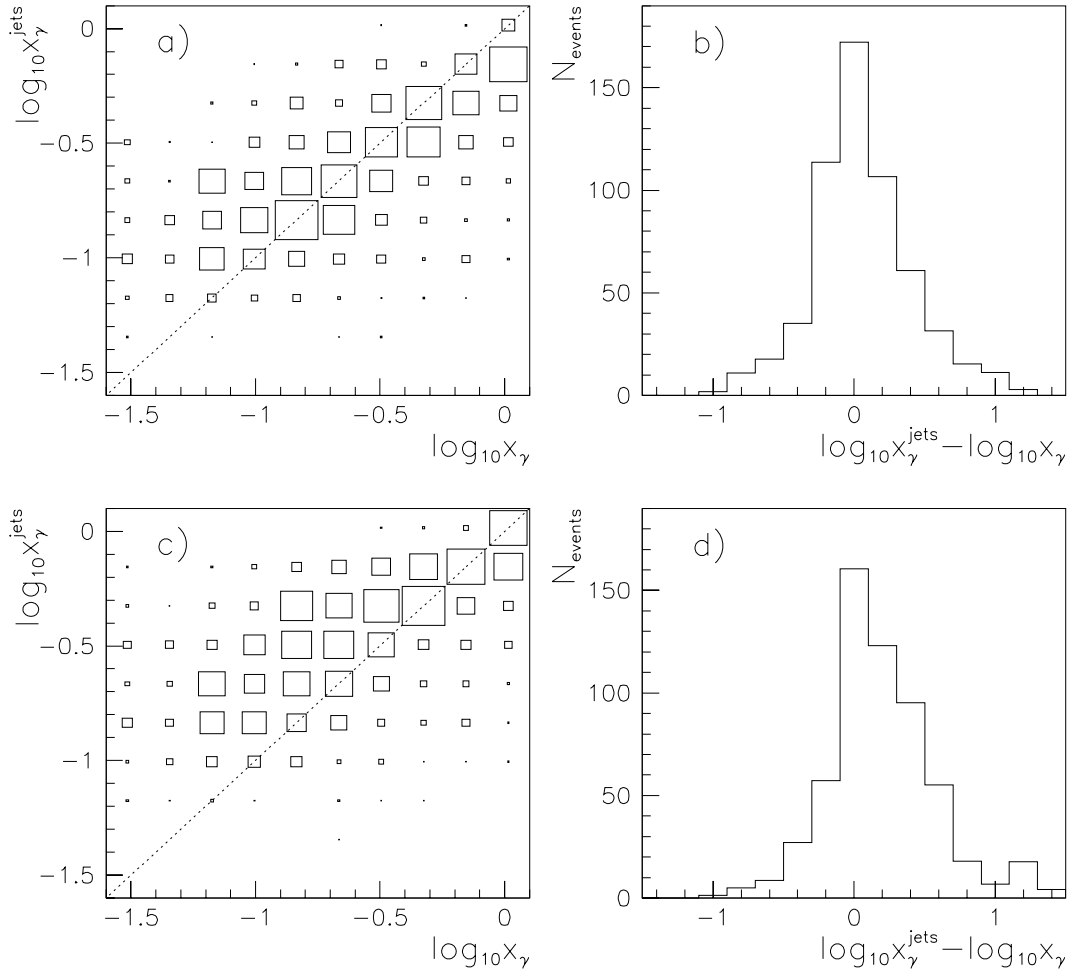


Figure 4.6: Correlation between  $x_{\gamma}^{\text{jets}}$  and true  $x_{\gamma}$ . For figures a) and b),  $y_{\text{tag}}$  is used for the determination of  $x_{\gamma}^{\text{jets}}$  whereas for figures c) and d)  $y_{\text{JB}}$  is used.

generator. For figures a) and b)  $x_{\gamma}^{\text{jets}}$  is calculated using  $y_{\text{tag}}$  whereas for figures c) and d)  $y_{\text{JB}}$  is used.

The correlation is generally better if  $y$  is determined from the electron tagger information. However, at very large  $x_{\gamma}$ , the correlation may be slightly better when using  $y_{\text{JB}}$ . This can be explained by the fact that the deficiencies of  $y_{\text{JB}}$  mentioned above are less severe for large  $x_{\gamma}$ . This is because there is no or only a very soft photon remnant at very large  $x_{\gamma}$ . Additionally, for  $x_{\gamma} \approx 1$ , the sums of  $E - p_z$  run over the same energy clusters (*cf.* equations (4.15) and (4.17):  $x_{\gamma} = (E - p_z)^{\text{jets}} / (E - p_z)^{\text{all except } e'}$ ) such that errors due to fluctuations in the energy measurement cancel.

Because the correlation for  $x_{\gamma}$  when using  $y_{\text{tag}}$  for the determination of  $x_{\gamma}$  is good in the entire  $x_{\gamma}$ -range and especially for low  $x_{\gamma}$ , we will henceforth use  $y$  as calculated from the electron tagger information.

The accessible  $x_{\gamma}$ -range is given by our cuts on the transverse momenta and the

pseudo-rapidities:

$$x_{\gamma,\min} \approx \frac{2 \cdot 6 \cdot e^{-2.5}}{2yE_e} . \quad (4.18)$$

For  $y < 0.7$  this leads to  $x_{\gamma,\min} \gtrsim 0.025$  ( $\log_{10} x_{\gamma} \gtrsim -1.6$ ) as can be seen in figure 4.6.

# Chapter 5

## Data selection

In this chapter we want to describe the selection of hard photoproduction processes. To select *hard* processes, we will apply the  $k_{\perp}$ -algorithm and ask for at least two jets to be found. *Photoproduction* processes will be selected by requiring the scattered electron to be measured in the electron detector of the luminosity system.

The data selection can be divided into two steps, an online and an offline data selection. The online selection is performed by a sophisticated trigger system, which itself is subdivided into four (five) trigger levels (for details on the H1 trigger system, see [43]). The offline selection is part of the offline analysis.

The data used for this analysis was recorded by the H1 detector in the fall of 1993. With currents of typically  $I_e \approx 8$  mA and  $I_p \approx 11$  mA for the electron and proton beam, respectively, and an average specific luminosity of  $L_{\text{spec}} \approx 3 \cdot 10^{29} \text{ cm}^{-2} \text{ s}^{-1} \text{ mA}^{-2}$ , the (uncorrected) integrated luminosity for this period adds up to  $L \approx 300 \text{ nb}^{-1}$ .

For the description of the different selection criteria and cuts applied to the data, we follow a chronological order. However, when quoting the efficiency of a certain selection or cut, we always refer to the final data set as described in section 5.5. Note that due to the limited statistics of the final data and MC samples (579 and 1075 events, respectively), all efficiency determinations have a statistical error of the order of  $\lesssim 1\%$ . The MC sample referred to in this chapter is based on the event generator PYTHIA and includes multiple interactions.

### 5.1 First level trigger

The first level trigger (L1 trigger) of H1 is the trigger system that is confronted with the full event rate provided by the HERA collider. This means that the L1 subtriggers have to decide on whether to accept or reject an event every 96 ns. Due to the pipelined architecture of the hardware subdetector-triggers, this trigger system operates dead-time free with an effective decision-time of  $2.3 \mu\text{s}$ .

The L1 subtriggers need to be able to trigger on genuine  $ep$  collisions with a high efficiency and at the same time reject background processes effectively. The main background processes are

- proton induced background:

Due to the large hadron hadron scattering cross-section, proton induced background is the major trigger source. The beam protons may either collide with molecules from the residual gas ( $\text{H}_2$ ,  $\text{CO}$ ,  $\text{H}_2\text{O}$ ,  $\text{CO}_2$ , *etc.*) within the beampipe (proton-gas background) or they may hit the walls or other structures of the beampipe (proton-wall background). Both processes can either occur within the H1 detector or upstream, *i.e.*, behind the time-of-flight system (background processes can take place downstream, too, but leave no signal in the H1 detector). The center-of-mass energy for these background processes amounts to  $\sqrt{s} = \sqrt{2E_p A m_n} \approx \sqrt{A} \cdot 40 \text{ GeV}$  ( $A$  = number of nucleons per nucleus,  $m_n$  = mass of a nucleon  $\approx 1 \text{ GeV}/c^2$ ).

- electron induced background:

The main electron induced background stems from synchrotron radiation of the electron beam as well as from Bremsstrahlung on the residual gas. Both background processes occur within and outside of the H1 detector and may produce a signal in the main H1 detector *or* the luminosity system.

Another possible electron induced background is due to the interaction of electrons with the residual gas (photoproduction). The center-of-mass energy for this latter background process, which may take place within or outside of the main H1 detector, is  $\sqrt{s} \leq \sqrt{2E_e A m_n} \approx \sqrt{A} \cdot 7 \text{ GeV}$ .

The L1 subtrigger for the selection of (hard) photoproduction processes used in this analysis is a logical “AND” of the following information (trigger-elements) provided by four subdetector-triggers:

- *eTAG*: energy deposition in the electron tagger of the luminosity system. The trigger-element eTAG is one of the trigger-elements provided by the luminosity system. For the eTAG trigger to be set, the following conditions have to be fulfilled in coincidence:
  - Energy measured in the electron detector.
  - No energy measured in the photon detector.
  - No signal from the water Čerenkov counter.

The latter two requirements reduce triggers due to Bremsstrahlung events (the average geometrical acceptance of the photon detector for Bremsstrahlung photons is  $\approx 98\%$  [43]).

- *DCRPh-Ta*: at least one track with  $p_t \gtrsim 400 \text{ MeV}/c$ .

The DC- $r\varphi$  trigger uses the information from the two central  $r\varphi$ -drift chambers to find tracks of charged particles originating from the beam axis. This is done by mapping the drift-time information from a number of signal-wires of both drift chambers into drift-bins, each one of them corresponding to actual drift lengths of  $\approx 5 \text{ mm}$  (a fraction of the drift-bins correspond to drift lengths of  $\approx 2.5 \text{ mm}$ ). Chamber pulses, which are discriminated, then result in a logical bit for the corresponding drift-bin. A track in the  $(r, \varphi)$  plane thus translates to a special bit-pattern ( $r$  is given by the position of the sense-wire,  $\varphi$  is reflected by the drift-bin). The trigger searches for such bit-patterns by comparing the actual bit-pattern with programmed masks.

For the generation of these masks, tracks are assumed to originate from the nominal beam axis. This results in a cut on the distance of closest approach ( $dca$ ) of a track.  $dca$  is the distance between the point of the particle track (a helix for a charged particle in a constant solenoidal magnetic field) closest to the  $z$ -axis (the DCA) and the  $z$ -axis itself. The sign of  $dca$  is equal to that of the vector product  $\vec{dca} \times \vec{p}_t$  with  $\vec{dca}$  being the vector from the origin of the coordinate system to DCA (note that  $\vec{dca}$  and  $\vec{p}_t$  lie in the  $(r, \varphi)$  plane). The measured  $dca$ -distribution for the tracks triggered by the DC- $r\varphi$  trigger has a full-width-at-half-maximum (FWHM) of 8 cm [69] (1993 running period), which is much smaller than the diameter of the beampipe of 19 cm. Hence, the DC- $r\varphi$  trigger does not trigger on tracks originating from the beampipe (*e.g.* due to proton-wall interactions). Note that the lower cutoff on the transverse momentum of a track for the generation of the trigger masks was set to 400 MeV/ $c$  for the 1993 data-taking [69].

The trigger-element DCRPh-Ta is set if at least one track is found.

- *zVtx-T0*: at least one track found by the  $z$ -vertex trigger.

The  $z$ -vertex trigger uses the information from the multi-wire proportional chambers (MWPCs) to determine the event-vertex position along the beam axis. The event-vertex is found by (geometrical) interconnection of every pair of signals from the cathode pads of the multi-wire proportional chambers (every MWPC consists of two independent pad layers) with straight lines in the  $(r, z)$  plane. The intersection of this straight line with the  $z$ -axis leads to an entry in a 16 bin wide histogram ( $-44 \text{ cm} < z < 44 \text{ cm}$ ). The event-vertex is found by searching for a peak in the above histogram. Wrong entries in the histogram, which are not due to particle tracks but due to misconnection of pads, are unavoidable but only lead to a flat background.

The trigger-element  $zVtx-T0$  asks for at least one entry in the histogram. Due to the fast response of the multi-wire proportional chambers, the  $zVtx-T0$  signal allows an unambiguous identification of the bunch crossing that resulted in the observed scattering process.

- *!ToF-BG*: no background signal from the ToF system.

Proton-gas and proton-wall events originating from upstream produce particle showers which mostly run through both scintillator walls of the time-of-flight system. Hits in the ToF due to  $ep$  scattering products are common, too. However, a “background” and an “interaction” timing window derived from the HERA-clock allows to discriminate between hits in the scintillator planes due to  $ep$  reactions or due to proton induced background events from upstream. The ToF-BG bit is set if signals from both scintillator walls in coincidence fall into the “background” window. This ToF-BG bit is then used as a veto, *i.e.*, the trigger-element *!ToF-BG* is set if ToF-BG is not.

The combination of these trigger-elements is known as “subtrigger 83” within the H1 Collaboration (1993 running period).

The reasons for this choice of subtrigger are the following:

- By measuring the scattered electron in the  $e$ -tagger of the luminosity system, we ensure a small scattering angle  $\vartheta_e$  ( $0^\circ \leq \vartheta_e < 0.3^\circ$ ;  $\vartheta_e \equiv 180^\circ - \theta_e$ ). This then leads to a maximal  $Q^2$  of  $Q_{\max}^2 \approx 0.01 \text{ GeV}^2$  (*cf.* equations (1.23–1.24);  $y = 0.2$  for  $Q^2 = Q_{\max}^2$ ). Hence, the selected events are due to photoproduction processes.

The measurement of the energy of the scattered electron in the electron tagger in addition provides a good determination of  $y$ .

- The requirement of a measured scattered electron in the  $e$ -tagger combined with the necessity for some activity in the main detector (tracks) reduces proton and electron induced backgrounds drastically. The only relevant source of background left<sup>1</sup> is due to random coincidences of proton and electron induced background reactions within the same bunch crossing.
- The above subtrigger proved to reject background processes effectively. In addition, the trigger rate due to genuine photoproduction processes was small enough such that every event could be processed further. In comparison, “subtrigger 80”, which consists of the same trigger-elements except for the DCRPh-Ta element, had an output trigger rate that was too high as an input rate for the next level in the trigger chain. Therefore, subtrigger 80 had to be prescaled, *i.e.*, only a fraction of the triggered events could be accepted.

---

<sup>1</sup>The only background source that could lead to signals in the main H1 detector *and* the  $e$ -tagger in coincidence is the electron induced photoproduction on the residual gas. However, due to the limited center-of-mass energy of this process ( $\sqrt{s} \lesssim \sqrt{A} \cdot 7 \text{ GeV}$ ), it is very unlikely that 2 jets of  $6 \text{ GeV}/c$  transverse momentum (see section 5.5) can be found in these background events.

### 5.1.1 Efficiency of first level trigger

The efficiency of the above trigger-elements to trigger 2-jet events is very high. For subtrigger 80, that is, the coincidence of the trigger-elements eTAG, zVtx-T0 and !ToF-BG, the efficiency to trigger the 2-jet events as described in section 5.5 is determined from Monte Carlo simulations and is equal to 100%, *i.e.*, no single event is rejected by the requirement of a subtrigger 80 bit. This efficiency includes the geometrical acceptance for the  $z$ -vertex trigger, but does not include the acceptance for the electron tagger, *i.e.*, we demand the scattered electrons to be measured in the  $e$ -tagger. The simulation of the  $e$ -tag and  $z$ -vertex trigger efficiencies was compared with efficiencies derived from data for other physical processes than 2-jet production and showed very good agreement [70].

The efficiency for the DCRPh-Ta trigger-element is derived from data. By selecting 2-jet events that were triggered by subtrigger 80, we have an unbiased data sample. Since the only difference between subtriggers 83 (st83) and 80 (st80) is the trigger-element DCRPh-Ta, the trigger efficiency for the DCRPh-Ta trigger-element is now given by the ratio (efficiency calculation is based on the binomial distribution  $P_\varepsilon(n) = \binom{N}{n} \varepsilon^n (1-\varepsilon)^{N-n}$  for the probability  $P_\varepsilon(n)$  to observe  $n$  out of  $N$  events given the efficiency  $\varepsilon$ ; the variance  $\sigma^2 = N\varepsilon(1-\varepsilon)$  of the binomial distribution  $P_\varepsilon(n)$  is used to determine the error:  $\sigma_\varepsilon = \sqrt{\varepsilon(1-\varepsilon)/N}$ )

$$\varepsilon_{\text{DCRPh-Ta}} = \frac{\text{number of events triggered by st83}}{\text{number of events triggered by st80}} \quad (5.1)$$

This efficiency includes the geometrical acceptance. In figure 5.1,  $\varepsilon_{\text{DCRPh-Ta}}$  is given as a function of  $p_t^{\text{jet}}$ ,  $\eta^{\text{jet}}$ ,  $\eta_1^{\text{jet}} + \eta_2^{\text{jet}}$  and  $x_\gamma^{\text{jets}}$ .

The average efficiency is  $97 \pm 1_{(\text{stat})}\%$ . The variation of the efficiency as a function of the different jet parameters and of  $x_\gamma^{\text{jets}}$  is weak. Note that for some points the statistics are rather poor. The MC simulation leads to the same qualitative behaviour but has a global efficiency of only 94%. This is due to the fact that the DC- $r\varphi$  trigger simulation underestimates the average number of hits in the drift chambers and thus underestimates the efficiency per track [71]. For forthcoming comparisons with MC simulations, the MC events are therefore rescaled with a global factor 97/94.

After the first level trigger, a second (L2) and third (L3) level trigger may accept or reject the L1-accepted events. In 1993 however, neither the L2 nor the L3 trigger was operational.

## 5.2 Level 4 trigger

The level 4 (L4) trigger, a processor farm, uses the information from all detector parts and performs a crude event reconstruction. Its main function is to verify the

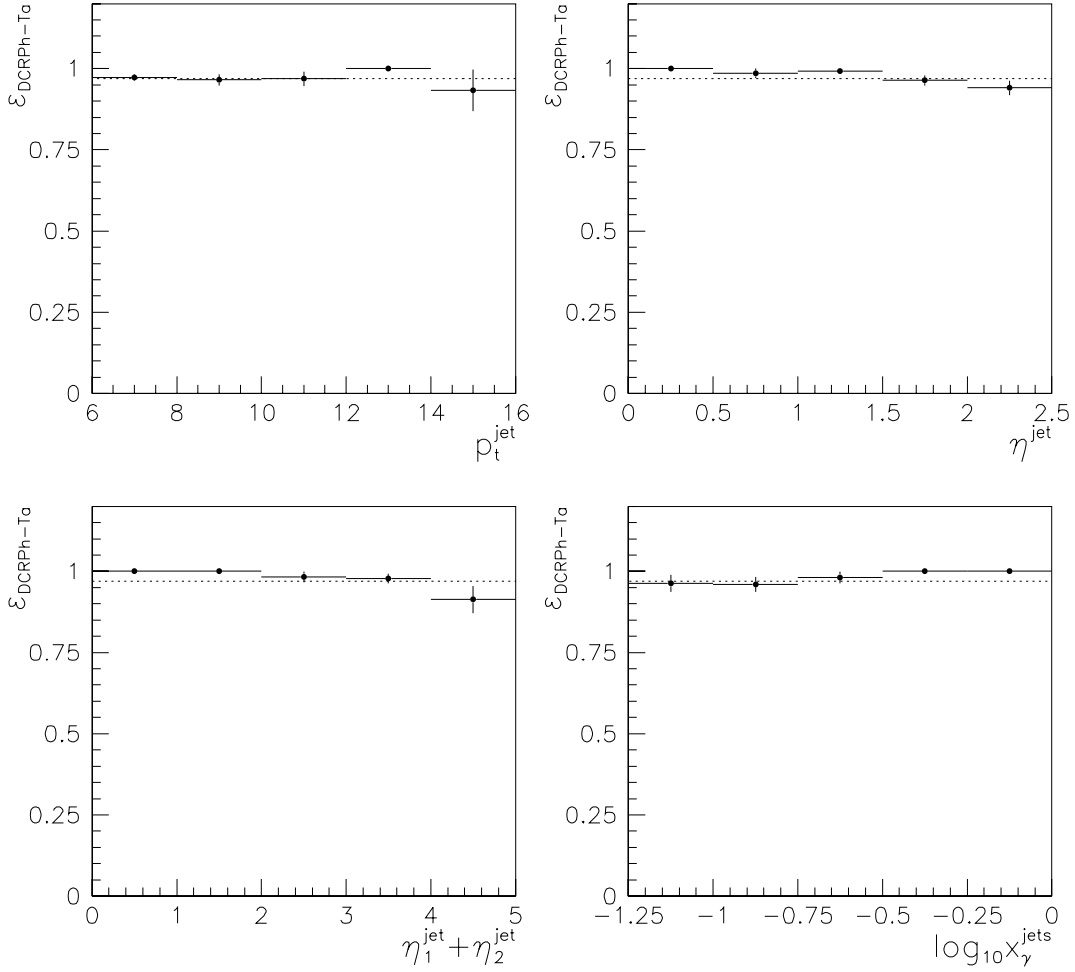


Figure 5.1: Efficiency of the DCRPh-Ta trigger-element as a function of  $p_t^{\text{jet}}$ ,  $\eta^{\text{jet}}$ ,  $\eta_1^{\text{jet}} + \eta_2^{\text{jet}}$  and  $\log_{10} x_\gamma^{\text{jets}}$ . The dotted line indicates the average efficiency of 97%.

L1 subtrigger decisions and to reject proton induced background events. Accepted events are stored on tape.

For events triggered by the L1 subtrigger 83, the L4 trigger verifies the L1 trigger decision by requiring at least one (reconstructed) track measured in the central drift chambers which originates from the nominal interaction region (*i.e.*,  $|dca| < 2$  cm,  $|z(\text{defined at DCA})| < 60$  cm).

Additionally, events triggered by subtrigger 83 are rejected if

- more than two upstream tracks ( $z(\text{defined at DCA}) < -100$  cm) exist, or
- a “beam-gas” finding routine, based on the event-variables  $\sum_{\text{all}} p_z / \sum_{\text{all}} |\vec{p}|$  and  $y_{\text{JB}}$  positively identifies the event as being a proton induced background event.

The above cuts aim at reducing the proton induced background events. The first cut reduces proton-gas and proton-wall events from outside the nominal interaction region, whereas the second cut reduces background events from the nominal interaction point by making use of the different energy flow patterns in  $\gamma p$  events and in proton induced background events. The rejection cut based on  $y_{\text{JB}}$  and  $\sum_{\text{all}} p_z / \sum_{\text{all}} |\vec{p}|$  makes use of the observation that  $y_{\text{JB}}^{\text{background}} \lesssim y_{\text{JB}}^{\gamma p}$  and  $(\sum_{\text{all}} p_z / \sum_{\text{all}} |\vec{p}|)^{\text{background}} \gtrsim (\sum_{\text{all}} p_z / \sum_{\text{all}} |\vec{p}|)^{\gamma p}$ .

### 5.2.1 Efficiency of level 4 trigger

The efficiency of the L4 trigger for 2-jet photoproduction events can be determined from Monte Carlo simulations or from “L4 rejected events”. 1% of the events that are rejected by the L4 trigger are nevertheless stored, but labeled as “L4 rejected events”. This allows to monitor the behaviour of the level 4 trigger and can additionally be used for efficiency cross-checks. The L4 trigger efficiency as determined from MC simulations (*i.e.*, application of the L4 trigger code to MC events) is 100%. Consistently, no event from the L4-rejected event sample passes all selection cuts. This cross-check, however, has a very limited significance since only one 2-jet event found in the L4-rejected event sample translates to 100 effectively rejected events! To get a better cross-check, we relax our selection cuts by lowering the  $p_t$ -cut (*cf.* equation (5.4)) and skipping the cuts on  $\eta^{\text{jet}}$  (*cf.* equations (5.6) and (5.7)). For  $p_t^{\text{jet}} > 4 \text{ GeV}/c$ , we find no single event in the L4-rejected event sample compared to 7961 2-jet events in the data. Hence, the inefficiency of the L4 trigger is lower than 2.9% at 90% confidence level.

## 5.3 Level 5 trigger

The level 5 (L5) trigger is the first trigger level that operates offline. It uses the full detector information and performs a detailed and final<sup>2</sup> event reconstruction. Based on reconstructed kinematical quantities, it labels the different events as being of a particular event class (*e.g.* hard photoproduction, DIS,  $D^{*\pm}$  candidate, *etc.*; every event can be assigned to several different event classes). Hence, the L5 trigger does not actually reject events such that they are lost, but only attributes them to a particular event class. Therefore, the term “L5 trigger” may be misleading — it’s rather the “first level analysis”.

Before we describe the event classification criteria, some remarks on the event reconstruction have to be made. Since our jet-finding algorithm is based on calorimetric quantities, we concentrate on the energy reconstruction in the LAr calorimeter and the BEMC. More details can be found in [43, 45].

---

<sup>2</sup>Apart from re-reconstructions due to better calibration constants, improved reconstruction code, *etc.*

- Noise suppression for the LAr calorimeter:  
The electronic noise for the different calorimeter cells is measured to be  $\sigma_{\text{noise}} \approx 10\text{--}30\text{ MeV}$ . An online noise suppression is performed by only considering signals that are equivalent to an energy  $|E_{\text{cell}}| > 2\text{--}3\sigma_{\text{noise}}$  (geometry dependent; stronger cuts in the forward region of the LAr). An additional noise suppression is performed offline by only keeping cells with an energy  $E_{\text{cell}} > 4\sigma_{\text{noise}}$  and its directly neighbouring cells as well as all cells with energy  $E_{\text{cell}} < -4\sigma_{\text{noise}}$ . Keeping negative energy cells automatically compensates for part of the positive energy noise cells. After this noise suppression, the total noise contribution to an event as derived from randomly triggered (“empty”) events is  $\langle E_{\text{tot,noise}} \rangle = 0.1\text{ GeV}$  with a variance of  $\sigma_{\text{tot,noise}} = 0.5\text{ GeV}$  [43].
- Clustering and reweighting for the LAr calorimeter:  
All cells passing the noise suppressing step are subject to clustering which aims at grouping neighbouring cells (for details, see [43, 45]). As a result of this clustering procedure, cells which are not assigned to a cluster (*e.g.* isolated cells) are suppressed. This leads to a further improvement of the noise contribution in “empty” events which now results in a  $\langle E_{\text{tot,noise}} \rangle$ -distribution with a peak at zero and  $\sigma_{\text{tot,noise}} = 0.25\text{ GeV}$  (see figure 5.6 in [43]).  
Based on these clusters, corrections for energy losses in dead material and the reweighting of the hadronic energies, which is necessary due to the non-compensating nature of the LAr calorimeter, are performed [43, 45].
- Noise suppression and clustering for the BEMC:  
The average noise per BEMC element (“stack”) amounts to  $E_{\text{noise}} \approx 150\text{ MeV}$  [43]. Therefore, a simple cut on  $E_{\text{stack}} > 250\text{ MeV}$  is applied for every BEMC stack. The BEMC clustering procedure, which combines the measured energies of up to 9 stacks (out of a total of 88 stacks), and the corrections for the energy losses in dead material are described in [72]. Finally, a global hadronic weighting factor of 1.6 is applied to the reconstructed energies to account for the fact that the BEMC energy reconstruction is performed under the assumption that the traced particle (*e.g.* an electron) underwent electromagnetic interactions within the backward electromagnetic calorimeter. However, the observation that hadrons typically only deposit  $\approx 30\%$  of their energy in the BEMC and that about 30% of all hadrons do not interact at all [43] make the BEMC a poor device for the measurement of hadronic energies.

Note that special “noise-files” are produced from “empty” events where no online noise suppression has been performed. These “noise-events” are added to the MC simulation events to model the influence of the electronic noise. The MC events are then subjected to the same noise suppression steps (*i.e.*, online noise suppression and offline noise suppression as described above) as the data.

For this analysis, only events labeled as being of “hard photoproduction”<sup>3</sup> type were

---

<sup>3</sup>H1 internal naming: class 20 plus WAMP selection (1993 running period).

used. The event classification criteria for this event class are the following:

- Verification of L1 and L4 trigger decisions, *e.g.*
  - Energy measured in the electron tagger of the luminosity system is above 4 GeV and the possible energy measured in the photon detector is below 2 GeV.
  - At least one reconstructed track in the central tracker coming from the nominal interaction region.
- Selection of a hard process by asking for a minimal transverse energy of  $E_{t,\text{event}} > 14$  GeV, based on energies measured in the LAr calorimeter and the BEMC.
- Rejection of background events, *e.g.*
  - Cosmic muons: Reject events where two tracks of opposite charge can be fitted to a single track and the total number of tracks is less than 7.
  - Halo muons: Halo muons cross the detector horizontally. If the event-vertex is assumed to be in the nominal interaction region, these halo muons lead to a large measured transverse energy flow. Halo muons are rejected by looking for “horizontal” energy-bands (*i.e.*, fixed  $r$  and  $\varphi$ ) in the calorimeters.
  - Proton induced background events: Proton-gas and proton-wall background events are rejected based on  $y_{\text{JB}}$  and  $\sum_{\text{all}} p_z / \sum_{\text{all}} |\vec{p}|$  as well as by looking for tracks coming from upstream. These rejection criteria are similar to the ones used for the L4 trigger. To “verify” the L4 trigger decision, which relies on a simplified event reconstruction, the final — stronger — rejection criteria are applied by the L5 trigger.
  - Coherent noise: Some events with large transverse energy are due to coherent (electronic) noise in the LAr calorimeter. These events are rejected by searching for a typical (channel related) pattern of distributed energy.

The *efficiency* of the L5 trigger as determined from Monte Carlo simulations is equal to 100%.

After all these cuts (L1, L4, L5), we end up with roughly 50'000 data events. The total selection efficiency of these 3 trigger levels amounts to  $97 \pm 1_{(\text{stat})} \%$ .

## 5.4 Three more cuts

In addition to the above-mentioned event classification criteria, we apply three more cuts to our data (and MC) sample.

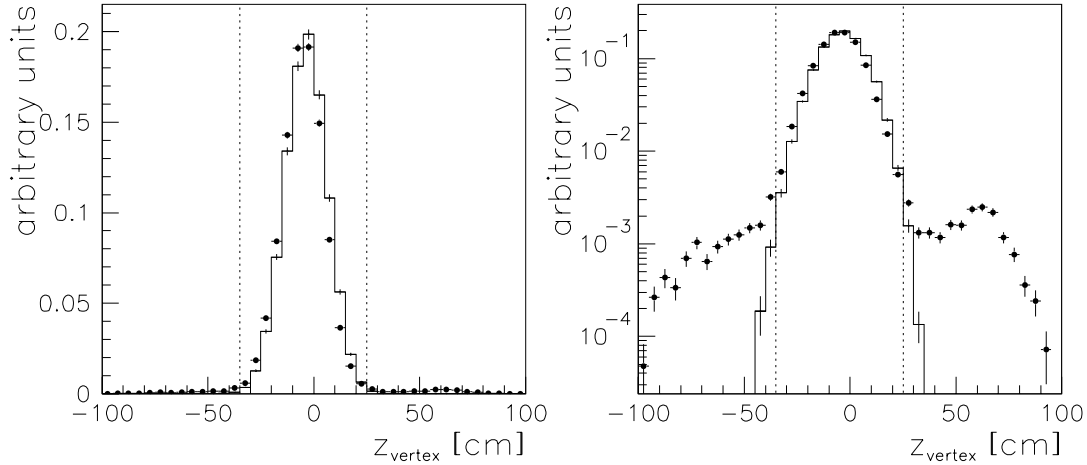


Figure 5.2:  $z$ -distribution (in linear and logarithmic scale) of the event-vertex for data (points) and MC (histogram). Data and MC are normalized to unit area. The dotted lines indicate the cut values.

The first one is a cut on the  $z$ -position of the event-vertex. Figure 5.2 shows the  $z$ -distribution of the event-vertex for data and MC.

The main peak has its center at  $z_{\text{vertex}} = -5$  cm and the distribution has a variance of  $\sigma = 10$  cm. At  $z_{\text{vertex}} \approx 60$  cm, one nicely sees a second peak (data only) which stems from the early proton satellite bunch. We apply a cut

$$-35 \text{ cm} < z_{\text{vertex}} < 25 \text{ cm} \quad (5.2)$$

to make sure that the event-vertex is well centered within the H1 detector and to remove the events due to the proton satellite bunch. Additionally, this cut removes possible proton-gas background events occurring outside of the beam crossing area.

The other two cuts are related to the energy measurement in the electron tagger. Firstly, for a good containment of the electromagnetic shower within the  $e$ -tagger, we restrict the shower-center to  $|x_{\text{tag}}| < 6.5$  cm (possible maximum at  $x_{\text{tag,max}} = \pm 7.7$  cm, Molière radius  $R_M = 2.1$  cm). Secondly, we restrict the energy of the scattered electron. Figure 5.3 shows the energy distribution measured in the electron tagger of the luminosity system for data and MC. Additionally shown is the energy distribution in the  $e$ -tagger for events triggered by the eTAG trigger-element alone. These latter events mainly stem from Bremsstrahlung processes. Since the major source of background events is necessarily due to random coincidences of proton and electron induced background events within the same bunch crossing<sup>4</sup>, this distribution represents the background.

<sup>4</sup>The Bremsstrahlung “background” processes which are in coincidence with a proton induced background process are not only due to  $eA \rightarrow eA\gamma$  processes, but mainly to  $ep \rightarrow ep\gamma$  reactions.

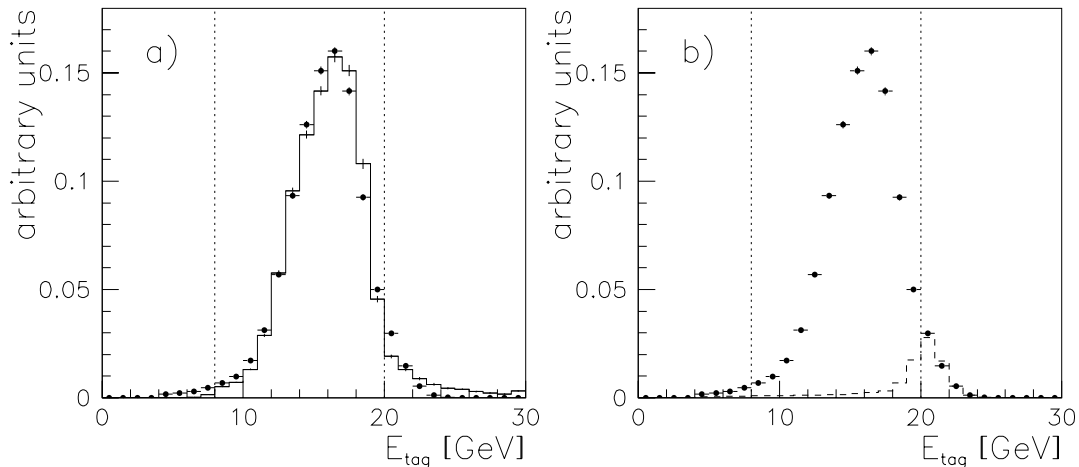


Figure 5.3:  $E_{\text{tag}}$ -distribution for data, MC and background events. In figure a), the  $E_{\text{tag}}$ -distribution (normalized to unit area) for data (points) and MC (histogram) is shown. Figure b) again shows the data distribution (points) together with the  $E_{\text{tag}}$ -distribution for the background events (dashed histogram). The background distribution is normalized such that the number of events above 20 GeV is equal for both distributions. The dotted lines indicate the cut values.

The data (and MC) distribution peaks at around  $E_{\text{tag}} \approx 16$  GeV, whereas the background distribution peaks at  $E_{\text{tag}} \approx 20$  GeV. We apply a cut at

$$8 \text{ GeV} < E_{\text{tag}} < 20 \text{ GeV} \quad , \quad (5.3)$$

which is equal to the cut  $0.25 < y_{\text{tag}} < 0.7$ . This cut selects the  $E_{\text{tag}}$  ( $y_{\text{tag}}$ ) region where the  $e$ -tagger acceptance is reasonably large and in addition reduces the possible background due to random coincidences of proton and electron induced background events. If we assume that all events with  $E_{\text{tag}} > 20$  GeV are background events, the background contamination of our data sample after applying the cut on  $E_{\text{tag}}$  is 4%. However, the comparison of the  $E_{\text{tag}}$ -distribution for data and MC (see figure 5.3 a)) suggests that the background contribution to our data sample can only be a (small) fraction of this conservative estimation of 4%. By normalizing the data and MC distributions between  $8 \text{ GeV} < E_{\text{tag}} < 16 \text{ GeV}$  and adding the appropriate fraction of background events in the region  $20 \text{ GeV} < E_{\text{tag}} < 24 \text{ GeV}$  such that the total number of data events in this region equals the sum of MC and background events, we can estimate the background contamination in the signal region  $8 \text{ GeV} < E_{\text{tag}} < 20 \text{ GeV}$  to be 0.2%. We therefore neglect this possible contamination.

## 5.5 Jet-finding

The last but most stringent selection criterion is the existence of jets. We apply the longitudinally-boost-invariant  $k_{\perp}$ -clustering algorithm (see sections 4.3 and 4.4) with the parameters (*cf.* equations (4.8) and (4.9))

$$d_{\text{cut}} = 6^2 \text{ GeV}^2/c^2 \quad (5.4)$$

$$\delta_{\text{cut}} = 1 \quad (5.5)$$

to our data and ask for at least two jets to be found. As input objects for the  $k_{\perp}$ -algorithm, we use clusters of energy in the LAr calorimeter and the BEMC.

Additionally, the two jets with the highest transverse energy (“ $p_t$ -leading jets”) have to pass the following cuts (*cf.* equations (4.10) and (4.12)):

$$0 < \eta^{\text{jet}} < 2.5 \quad (5.6)$$

$$|\Delta\eta^{\text{jets}}| = |\eta_1^{\text{jet}} - \eta_2^{\text{jet}}| < 1.2 \quad (5.7)$$

The reasons for the requirements above are described in more detail in section 4.4.

The demand for at least two jets with transverse energy above 6 GeV reduces our data sample drastically. After the additional cuts on the jet properties (*i.e.*, cuts (5.6) and (5.7)), we are left with 579 events. The MC sample includes 1075 events (equivalent to 580 events if all weights (see section 3.1) are taken into account and if the MC sample is normalized to the integrated luminosity of the data sample). We will refer to these two samples as the “final 2-jet event” samples. The two jets referred to are the two  $p_t$ -leading jets.

Note that the cut on  $E_{t,\text{event}} > 14 \text{ GeV}$  applied by the L5 trigger does not cut into our final data sample although the transverse energies of the two jets may be as low as  $E_t \geq 12 \text{ GeV}$ . This is reflected by the efficiency of the L5 trigger of 100% and in addition has been checked by investigating the  $E_{t,\text{event}}$ -distribution of the final data (and MC) sample.

Figures 5.4 and 5.5 show two out of these 579 selected events. They both have two jets with transverse momentum above  $10 \text{ GeV}/c$  each.

The event depicted in figure 5.4 has some energy flow in the backward direction whereas no activity in the BEMC is seen for the event shown in figure 5.5. Thus, the former event is a candidate for a resolved photoproduction process, whereas the latter may be due to direct photoproduction. The value of  $x_{\gamma}^{\text{jets}}$  determined from the two jets is 0.23 and 0.79, respectively.

The correlation of jet quantities such as  $p_t$ ,  $\eta$  and  $\varphi$  with the same quantities of the underlying parton is described in section 4.4.1. Except for the missing cut on  $\Delta\eta^{\text{jets}}$ ,

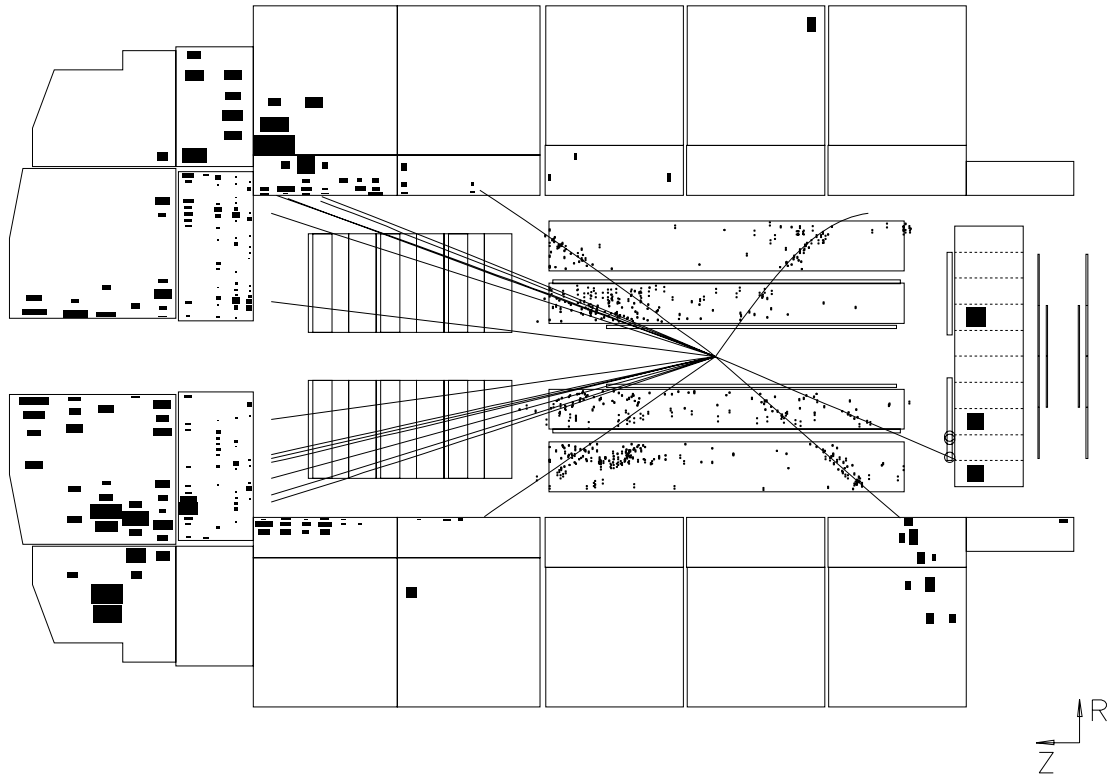


Figure 5.4: 2-jet event. Candidate for a resolved photoproduction event. Depicted is a cross-section of the H1 detector along the  $z$ -axis, showing the liquid argon calorimeter, the BEMC and the tracking chambers. The measured energy in the LAr calorimeter and the BEMC is represented by black squares. The size of the squares is thereby proportional to the deposited energy. Additionally shown are the hits in the central tracking chambers together with the reconstructed particle tracks.

the MC events used for the correlation plots passed all the selection criteria and cuts discussed in this chapter. For the  $x_\gamma$ -resolution studies as described in section 4.4.2, the final MC sample of 1075 events was used.

What remains to be done is to determine the integrated luminosity for our final data sample.

## 5.6 Luminosity

The luminosity is determined by measuring the rate of the Bethe-Heitler process  $ep \rightarrow ep\gamma$  [73]. Since the cross-section is large and well known, this Bremsstrahlung process can be used for an exact measurement of the luminosity.

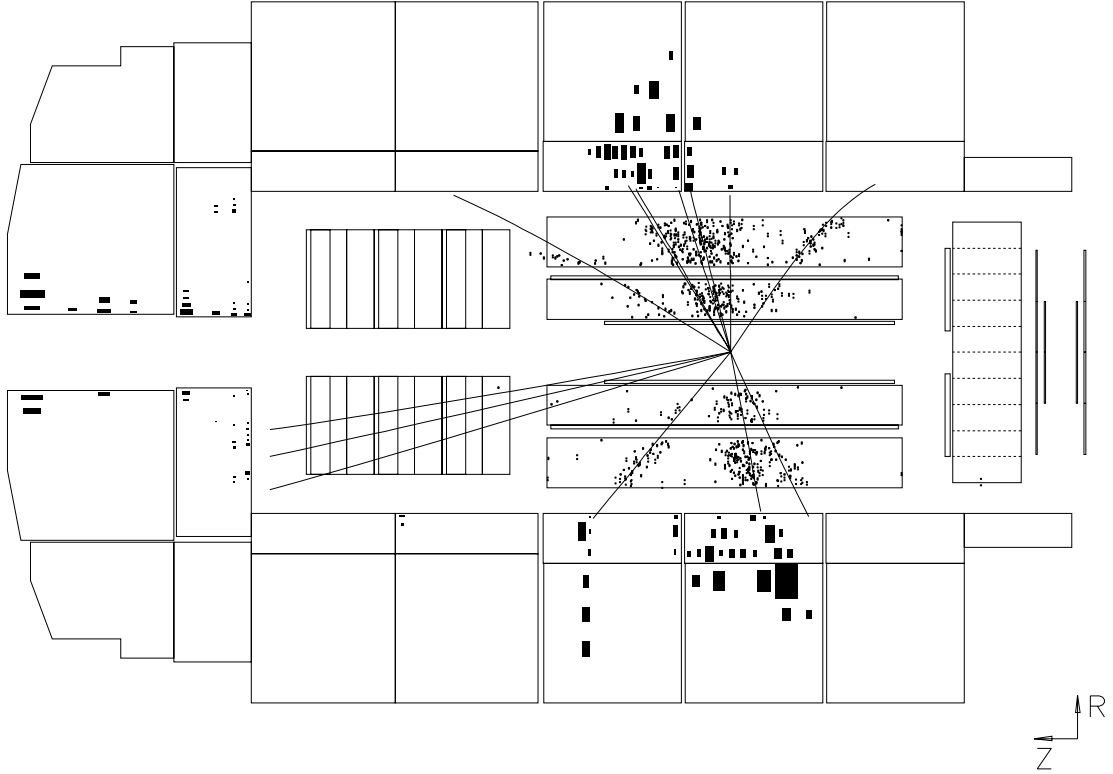


Figure 5.5: 2-jet event. Candidate for a direct photoproduction event. Depicted is a cross-section of the H1 detector along the  $z$ -axis, showing the liquid argon calorimeter, the BEMC and the tracking chambers. The measured energy in the LAr calorimeter and the BEMC is represented by black squares. The size of the squares is thereby proportional to the deposited energy. Additionally shown are the hits in the central tracking chambers together with the reconstructed particle tracks.

The integrated luminosity of the data sample used for this analysis is equal to

$$L = 255 \text{ nb}^{-1} \quad . \quad (5.8)$$

It includes the following corrections:

- Only data periods, where all detector parts relevant for this analysis (*i.e.*, LAr calorimeter, central  $r\phi$ -drift chambers, central multi-wire proportional chambers, ToF and the luminosity system) were properly working, are taken into account. Additionally, a short period has to be excluded due to malfunctioning of the DC- $r\phi$  trigger [71].
- The appearance of coherent electronic noise in the LAr calorimeter reduces the effective data-taking time, since all events with that particular pattern of distributed energy are rejected. This correction varies for different periods and in average amounts to 4.5% [74].

- The cut on  $z_{\text{vertex}}$  removes events in the tails of the  $z_{\text{vertex}}$ -distribution and especially events due to the collision of proton satellite bunches with electron bunches. Since the luminosity measurement is (largely) independent of  $z_{\text{vertex}}$ , *i.e.*, the proton satellite bunches contribute to the total luminosity, the cut on  $z_{\text{vertex}}$  has to be corrected for in the luminosity measurement. For the 1993 running period, this correction is determined to be  $3.3^{+3.0}_{-0.8(\text{syst})}\%$  [73].

The total systematic error of the luminosity measurement is 4.5% [73] and includes the uncertainty ( $\approx 3\%$ ) of the geometrical acceptance of the electron tagger. Other contributions to the systematic error are due to the background subtraction ( $\approx 1.5\%$ ) and the trigger efficiency ( $\approx 1\%$ ). More details can be found in [73].

# Chapter 6

## Comparison of data with Monte Carlo simulations

This chapter is devoted to the comparison of our final data sample (as described in the last chapter) with Monte Carlo simulations.

The aim of this analysis is to determine the inclusive parton cross-sections  $d\sigma/dp_t$  and  $d\sigma/d\eta$  in hard photoproduction processes and to measure the parton density function of the photon. This can only be achieved with the help of a Monte Carlo simulation which allows to relate measured quantities (*e.g.*  $p_t^{\text{jet}}$ ,  $x_\gamma^{\text{jets}}$ ) with parton quantities (*e.g.*  $p_t^{\text{parton}}$ ) and  $x_\gamma$ . The MC simulation thereby models the predictions of the theory, in our case Quantum Chromodynamics, as well as the response of the detector. The possibility to relate measured quantities with parton quantities by means of a Monte Carlo simulation however requires that the MC simulation describes the measured data well. It is therefore important to check that the properties of our 2-jet sample are well reproduced by the MC simulation, especially those properties which are not influenced by the choice of parton density function parametrization for the photon or the proton. The MC samples used in this chapter are based on the event generator PYTHIA. As parton density functions, the parametrizations of Glück, Reya and Vogt (GRV-LO) are used for the photon as well as for the proton.

In the following, we will investigate various properties of our data sample such as jet properties ( $p_t^{\text{jet}}$ ,  $\eta^{\text{jet}}$ ) and jet jet correlations ( $|p_{t,1}^{\text{jet}} - p_{t,2}^{\text{jet}}|$ ,  $|\eta_1^{\text{jet}} - \eta_2^{\text{jet}}|$ ,  $|\varphi_1^{\text{jet}} - \varphi_2^{\text{jet}}|$ ,  $x_\gamma$  and  $x_p$ ). We will then check the MC prediction for the energy flow observed in data and see that the MC simulations fail to describe the transverse energy flow around the jet direction properly. Hence, the rest of the chapter will then be devoted to detailed studies of this mismatch and to a “jet-pedestal subtraction” procedure that corrects for this observed deficiency of the MC simulations. Alternatives to the pedestal subtraction method will be discussed as well.

## 6.1 Jet properties and jet jet correlations

As a first check of the Monte Carlo description of our data we want to compare the transverse momenta and the pseudo-rapidities of the two jets in our data sample with the predictions of the MC simulation. In figure 6.1, the  $p_t^{\text{jet}}$ - and  $\eta^{\text{jet}}$ -distribution is shown. The number of jets found in the data sample is compared with the absolute prediction of the Monte Carlo simulation (the MC is normalized to the integrated luminosity of the data sample). The MC sample used includes multiple interactions.

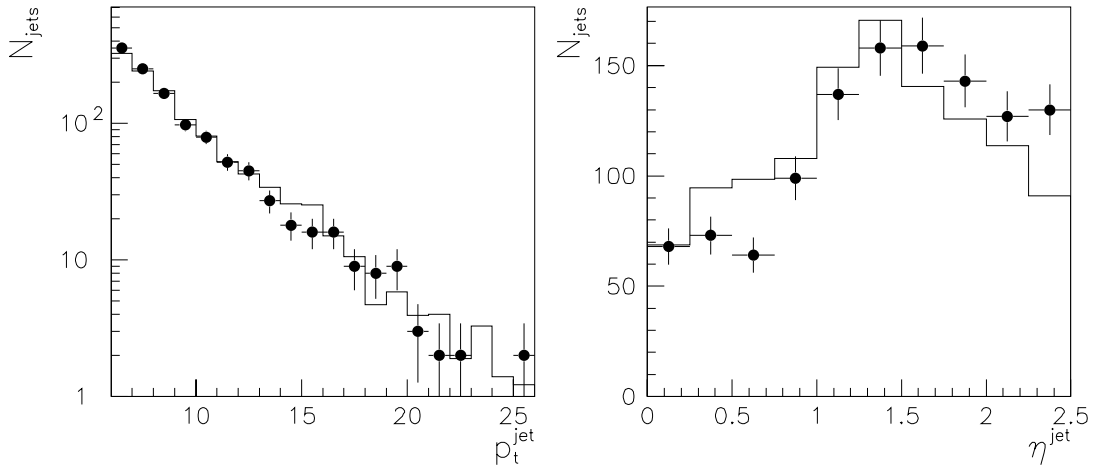


Figure 6.1:  $p_t^{\text{jet}}$ - and  $\eta^{\text{jet}}$ -distribution for 2-jet events. The number of jets found in the data sample (points) is compared with the absolute prediction of the Monte Carlo simulation (histogram; the MC is normalized to the integrated luminosity of the data sample). The MC sample used includes multiple interactions. We omit to plot the statistical errors for the MC simulations in this chapter in order not to overload the figures.

The shape of the  $p_t^{\text{jet}}$ -distribution is well described by the MC simulation, whereas for the  $\eta^{\text{jet}}$ -distribution the MC simulation predicts somewhat less jets in the very forward region but somewhat more jets at small  $\eta^{\text{jet}}$ . However, the discrepancy in the  $\eta^{\text{jet}}$ -distribution is only weak, and, moreover, we do expect some impact on the shape of the  $\eta^{\text{jet}}$ -distribution from the parton density function parametrization used for the photon (see below)!

For the absolute normalization, the rate of 2-jet events in the data is — somewhat surprisingly — very well predicted by the Monte Carlo simulation. The slight surprise about the fact that the MC simulation perfectly describes the 2-jet event rate in the data is due to the following reasons:

- The errors given in figure 6.1 are only statistical. Systematic errors due to the uncertainty in the energy scale of the LAr calorimeter or the luminosity measurement are not included. These and other systematic errors are described in detail in the next chapter.
- The Monte Carlo simulation used for this comparison is based on an event generator (PYTHIA) that only includes leading order (LO) matrix elements for the hard  $2 \rightarrow 2$  parton parton scattering. Theoretical calculations indicate a difference between LO and next-to-leading order (NLO) predictions of up to 30% [75, 76, 77, 78], depending on factorization and renormalization scales,  $p_t$ - and  $\eta$ -ranges and jet-algorithm parameters used.
- The MC sample used for the comparison in figure 6.1 includes multiple interactions. It has to be shown in the following that the use of a MC simulation which includes multiple interactions is sensible.

Note that a MC simulation without additional interactions poorly fails to describe the  $p_t^{\text{jet}}$ - and  $\eta^{\text{jet}}$ -distribution for 2-jet events, *i.e.*, the predicted rate is low by  $\approx 40\%$  and the shape of both the  $p_t^{\text{jet}}$ - and the  $\eta^{\text{jet}}$ -distribution is inconsistent with the data (not shown).

- The  $p_t^{\text{jet}}$ - and  $\eta^{\text{jet}}$ -distribution for the MC sample depend on the parton density function parametrizations used when generating the events. This sensitivity to the parton density function of the photon — after all — is the reason why we want to measure the inclusive parton (jet) cross-sections! In figure 6.1, the GRV-LO parton density function parametrizations are used for the photon and the proton. As shown in *e.g.* [78, 77], different parametrizations for the photon mainly influence the absolute rate of 2-jet events and the shape of the  $\eta^{\text{jet}}$ -distribution. The shape of the  $p_t^{\text{jet}}$ -distribution is only weakly affected by the choice of parton density function parametrization for the photon. Note that different parametrizations for the proton have no effect on the  $p_t^{\text{jet}}$ - and  $\eta^{\text{jet}}$ -distribution since the parton density functions of the proton are already well measured in the relevant  $x_p$ -range.

The fact that the  $p_t^{\text{jet}}$ - and  $\eta^{\text{jet}}$ -distribution is influenced by the choice of the parton density function parametrization for the photon proves the earlier remark that the resolved contribution to the hard photoproduction cross-section is relevant at HERA energies. For a plot of the theoretical expectations for the resolved and direct contributions to the  $p_t$ -distribution see *e.g.* [75].

Another reason for a possible discrepancy in the 2-jet event rate as observed in data and MC is the influence of the  $\hat{p}_t$ -cut introduced when generating the MC events (see section 3.1). In figure 6.2, the  $\hat{p}_t$ -distribution for the final MC sample (including multiple interactions) is shown.

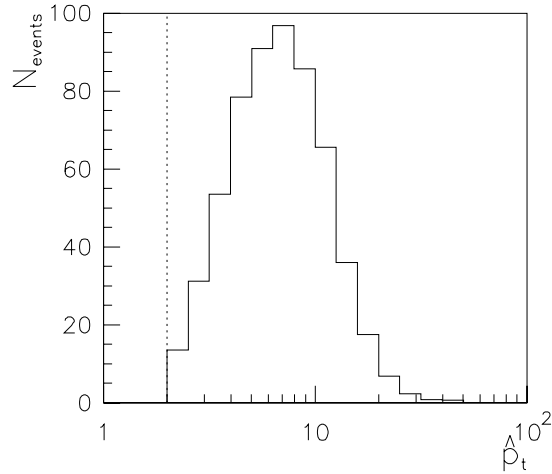


Figure 6.2:  $\hat{p}_t$ -distribution for the final MC sample (including multiple interactions). The cut on  $\hat{p}_t$  when generating the MC events was set to  $\hat{p}_{t,\text{min}} = 2 \text{ GeV}/c$  (dotted line).

The  $\hat{p}_t$ -distribution is at most very weakly influenced by the cut at  $\hat{p}_{t,\text{min}} = 2 \text{ GeV}/c$ . Hence, we do not expect a large impact on the 2-jet event rate as predicted by the Monte Carlo simulation due to the cut on  $\hat{p}_t$ . The main reason for the presence of events with  $\hat{p}_t$  as low as  $\hat{p}_t \gtrsim 2 \text{ GeV}/c$  in this MC sample is the additional energy from multiple interactions which may lead to jets with transverse momenta as high as  $p_t^{\text{jet}} > 6 \text{ GeV}/c$  (see also section 4.4.1)!

Figure 6.3 shows the jet jet correlations  $|p_{t,1}^{\text{jet}} - p_{t,2}^{\text{jet}}|$ ,  $\eta_1^{\text{jet}} - \eta_2^{\text{jet}}$  and  $|\varphi_1^{\text{jet}} - \varphi_2^{\text{jet}}|$ . The numbering scheme for the jets adopted in the following is such that  $p_{t,1}^{\text{jet}} \geq p_{t,2}^{\text{jet}}$ .

All three distributions are pretty well described by the Monte Carlo simulation.

The  $|p_{t,1}^{\text{jet}} - p_{t,2}^{\text{jet}}|$  and  $|\varphi_1^{\text{jet}} - \varphi_2^{\text{jet}}|$  distributions are sensitive to the transverse momentum of the hard parton parton scattering system. According to the Monte Carlo simulation, the main contribution to the transverse momentum of the hard scattering system comes from initial-state radiation. Another source of transverse momentum is the intrinsic transverse momentum of the partons within the photon and the proton. Note that the qualitative behaviour of the  $|p_{t,1}^{\text{jet}} - p_{t,2}^{\text{jet}}|$  and  $|\varphi_1^{\text{jet}} - \varphi_2^{\text{jet}}|$  distributions is due to these two effects and not an artifact of the  $p_t$ - and  $\varphi$ -resolution of the jet-algorithm. We can therefore conclude that the Monte Carlo description of the initial-state parton showers and the  $k_t$ -distributions reproduce the behaviour of the data well.

The  $\eta_1^{\text{jet}} - \eta_2^{\text{jet}}$  distribution is directly related to the distribution of the scattering angle  $\theta^*$  of the two partons in the center-of-mass system of the hard subprocess (*cf.* equation (4.13):  $\Delta\eta^{\text{jets}} \approx -2 \ln(\tan(\theta^*/2))$ ). The distribution of this scattering angle  $\theta^*$  is an important prediction of Quantum Chromodynamics. The description of the final  $\eta_1^{\text{jet}} - \eta_2^{\text{jet}}$  distribution by the Monte Carlo simulation is pretty good and

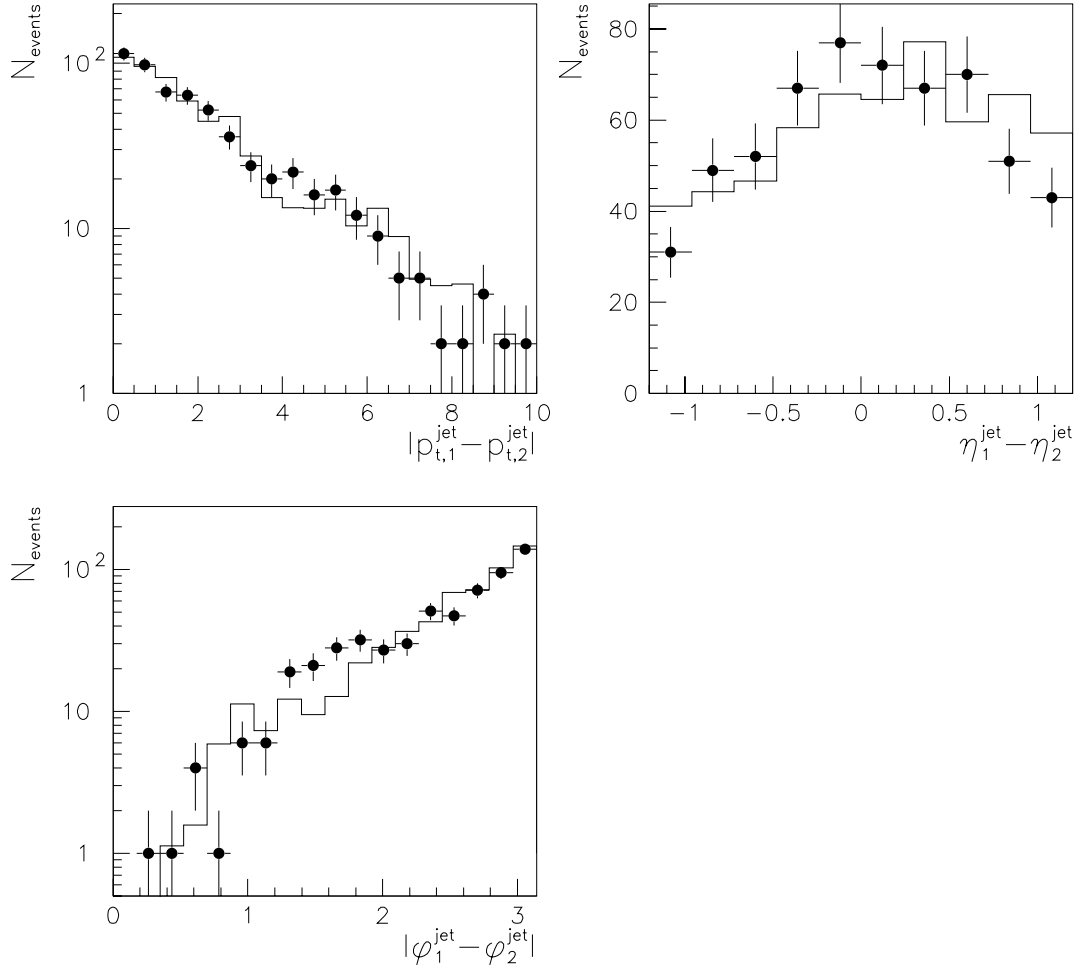


Figure 6.3:  $|p_{t,1}^{\text{jet}} - p_{t,2}^{\text{jet}}|$ ,  $\eta_1^{\text{jet}} - \eta_2^{\text{jet}}$  and  $|\varphi_1^{\text{jet}} - \varphi_2^{\text{jet}}|$  distribution for 2-jet events. Comparison of data (points) and MC (histogram; the MC is normalized to the integrated luminosity of the data sample). The MC sample used includes multiple interactions.

hence this basic prediction of Quantum Chromodynamics well confirmed.

To conclude this section, we show the distribution of  $x_\gamma^{\text{jets}}$  and  $x_p^{\text{jets}}$  in figure 6.4.

Both distributions are reasonably well reproduced by the Monte Carlo simulation. The MC is based on the GRV-LO parton density function parametrizations for the photon and the proton.

To sum up, all jet properties and jet jet correlations of the final 2-jet event sample are pretty well described by the Monte Carlo simulation. Hence, for these quantities, the parton density function parametrization for the photon by Glück, Reya and Vogt (GRV-LO) leads to a good description of the hard photoproduction data. However, there are some problems when considering the energy flow in 2-jet events.

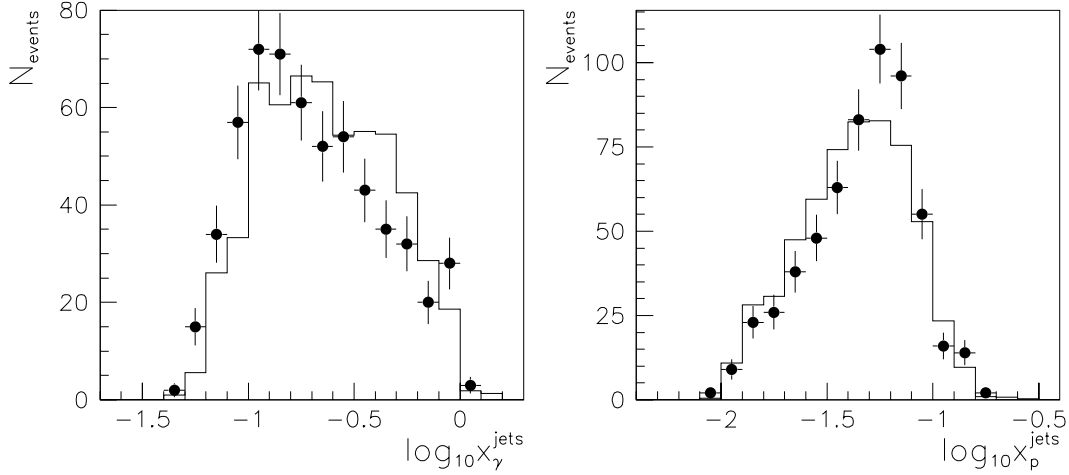


Figure 6.4:  $\log_{10}x_{\gamma}^{\text{jets}}$ - and  $\log_{10}x_p^{\text{jets}}$ -distribution for 2-jet events. Comparison of data (points) and MC (histogram; the MC is normalized to the integrated luminosity of the data sample). The MC sample (which includes multiple interactions) is based on the GRV-LO parton density function parametrizations for the photon and the proton.

## 6.2 Energy flow

In figure 6.5, the transverse energy flow (per jet) around the jet direction in a slice of  $|\eta^{\text{cell}} - \eta^{\text{jet}}| < 1$  is shown versus the distance in  $\varphi$  from the jet axis (“jet-profile in  $\varphi$ ”)<sup>1</sup>. Jets are selected with  $6 \text{ GeV}/c < p_t^{\text{jet}} < 8 \text{ GeV}/c$  to reduce effects due to the jet energy. These jet-profiles are given in different bins of  $\eta^{\text{jet}}$ .

The cuts applied when generating the MC events cannot influence the quality of the MC description of these jet-profiles, since  $p_t^{\text{jet}}$  and  $\eta^{\text{jet}}$  are fixed. For the Monte Carlo simulation with multiple interactions, the  $\hat{p}_t$ -cut applied does not even affect the  $\hat{p}_t$ -distribution (see above) and for the MC without additional interactions, the above-made statement is suggested by the following check. We compare the jet-profiles for the MC that includes multiple interactions with and without a cut applied at  $\hat{p}_{t,\text{min}} = 4 \text{ GeV}/c$  (*i.e.*, the value used for the MC without additional interactions, see section 3.1). No significant difference can be seen.

The transverse energy flow around the jet axis is reasonably well described in the central region, *i.e.*, for small  $\eta^{\text{jet}}$ , by both the MC with multiple interactions and the MC without multiple interactions. At large  $\eta^{\text{jet}}$  ( $\eta^{\text{jet}} \gtrsim 1$ ) however, both MC simulations fail to describe the data! The region of poor description is in between the two jets (note that the second jet is always visible at  $|\varphi^{\text{cell}} - \varphi^{\text{jet}}| \approx \pi$  due to the requirement  $|\eta_1^{\text{jet}} - \eta_2^{\text{jet}}| < 1.2$ , *cf.* equation (5.7)). This region, where the transverse energy flow is reduced but not vanishing, is called the (*jet-*) *pedestal* region.

<sup>1</sup>We use cells instead of clusters to enlarge the statistics.

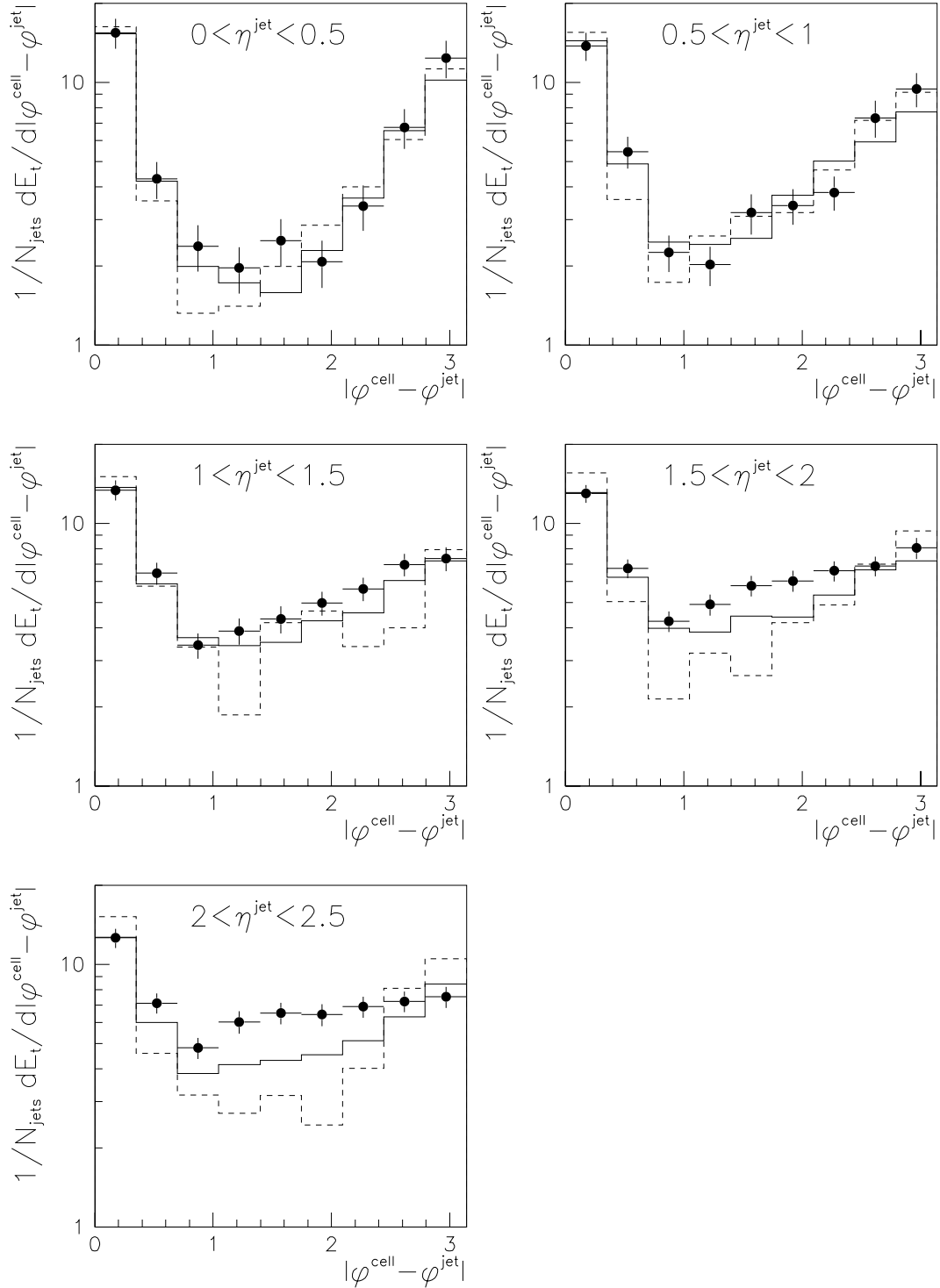


Figure 6.5: Jet-profiles in  $\varphi$  (see text) as a function of  $\eta^{\text{jet}}$ . Jets are selected with  $6 \text{ GeV}/c < p_t^{\text{jet}} < 8 \text{ GeV}/c$ . Data (points) is compared with a Monte Carlo simulation that includes multiple interactions (full histogram) and a MC simulation without multiple interactions (dashed histogram).

The energy contributions to the pedestal region have different sources:

- Final-state radiation:

The final-state parton showering leads to energy depositions around the initial direction of the scattered hard parton. This energy deposition, however, is correlated with the energy and the direction of the scattered hard parton. The event generator PYTHIA includes effects due to final-state radiation by means of a parton shower model.

- Fragmentation effects:

According to the Lund fragmentation model, the hadronization of the coloured partons into colourless hadrons leads to energy depositions in between the different partons, *i.e.*, between the scattered hard partons and the coloured beam remnants.

- Multiple interactions:

Multiple interactions within the same event lead to an energy deposition which in the  $(\eta, \varphi)$  space is uncorrelated with the energy flow from the hard subprocess. The only correlation between the energy flow from multiple soft interactions and the hard scattering process is via  $x_\gamma$ : the larger  $x_\gamma$  (or the lower  $\eta^{\text{jet}}$ , *cf.* equations (4.14) and (4.15)), the less photon energy is left<sup>2</sup> for subsequent multiple interactions and eventually totally vanishes for direct photoproduction processes (*i.e.*,  $x_\gamma \equiv 1$ ).

The main impact of multiple interactions is expected at large pseudo-rapidities  $\eta \approx \eta_{\gamma p}$  ( $1.9 < \eta_{\gamma p} < 2.4$  for  $0.25 < y < 0.7$ ).

Both final-state radiation and fragmentation effects are rather well known from other experiments at comparable energies (*e.g.* experiments at CERN (LEP, SPS) and at the Fermi Laboratory (TEVATRON)) and the event generators were tuned to describe those data. Moreover, a poor description of these two effects by the MC simulation would presumably lead to a poor description of the data for all  $\eta^{\text{jet}}$ .

As can be seen in figure 6.5, the Monte Carlo simulation that includes multiple interactions is able to describe the data better than the MC simulation without additional interactions. However, the difference between data and MC is still too large to be neglected (see also section 6.4.2). The same mismatch between data and MC can be seen in the “jet-profiles in  $\eta$ ”, *i.e.*, the transverse energy flow (per jet) around the jet direction in a slice of  $|\varphi^{\text{cell}} - \varphi^{\text{jet}}| < 1$  versus the distance in  $\eta$  from the jet axis (not shown).

Note that the above-mentioned difference between data and MC cannot be due to a poor choice for the parton density function parametrization of the photon in the MC. A totally different  $x_\gamma$ -distribution (which is disfavoured, *cf.* figure 6.4) would

---

<sup>2</sup>There is no ordering in time between the different interactions. We do however refer to the hard parton parton scattering as the “first” scattering within the event.

only lead to a different mixture in  $p_t^{\text{jet}}$  and  $\eta^{\text{jet}}$  for the second jet, but the influence of this second jet is marginal in the jet-pedestal region studied above. However, an explicit check for the dependence of the energy flow in the pedestal region on  $x_\gamma$  for the plots in figure 6.5 has been performed and proved the statement made above<sup>3</sup>.

Although the multiple interaction picture offers a natural explanation of the observed effects (see also section 6.4.1), we first want to make sure that the mismatch between the data and the Monte Carlo simulations discussed above, known as “the forward energy problem” within the H1 Collaboration, is not due to any other source.

### 6.3 Forward energy problem

Some investigations described in this section will be based on the comparison between the jet-profiles and the energies of the jet-pedestals (see section 6.4.2) as seen in the data and the MC simulation which includes multiple interactions. Since the statistical significance of the transverse energy flow as shown in figure 6.5 is somewhat limited, we enlarge our data and MC sample by lowering the  $p_t^{\text{jet}}$ -cut (*cf.* equation (5.4)) and skipping the cuts on  $\eta^{\text{jet}}$  (*cf.* equations (5.6) and (5.7)). The enlarged data sample comprises 3914 events. The fact that the resulting MC sample is affected by the  $\hat{p}_t$ -cut applied when generating the events does not introduce any bias, since we only compare the transverse energy flow for fixed  $p_t^{\text{jet}}$  and  $\eta^{\text{jet}}$ . Hence, the jet-profiles are not sensitive to the 2-jet event rate or to the  $p_t^{\text{jet}}$ - and  $\eta^{\text{jet}}$ -distribution.

#### 6.3.1 Energy scale of the LAr calorimeter

A variation of the absolute energy scale for the LAr calorimeter as a function of the polar angle  $\theta$  could possibly lead to the observed forward energy problem. If the energy flow in the forward region was overestimated, this could lead to the comparison of data jets with MC jets of higher energy. Since low energy jets are broader than high energy jets, an effect as described in section 6.2 would be possible.

As mentioned earlier, the uncertainty in the absolute energy scale for the LAr calorimeter as determined from the  $p_t$ -balance in deep inelastic scattering events is 5%. The variation of the absolute energy scale as a function of the polar angle  $\theta$  however is as small as 2% [79].

---

<sup>3</sup>For a MC simulation that includes multiple interactions, there is an additional dependence of the transverse energy flow (at fixed  $x_\gamma$ ) on the parton density function parametrization of the photon due to the variation in the probability for an additional soft interaction at a fixed  $x_\gamma^{\text{mi}}$ . However, a substantial influence on the jet-profiles due to this effect is improbable, since the  $x_\gamma^{\text{jets}}$ -distribution is rather well described by the parton density function parametrization used (*cf.* figure 6.4).

A comparison of the jet-profiles in data and MC when changing the absolute energy scale for the LAr calorimeter by 2% or even 5% (data only!) does not improve the MC description.

### 6.3.2 Trigger bias

The geometrical acceptance of the DC- $r\varphi$  and  $z$ -vertex trigger is limited to  $|\eta| \lesssim 1.6$  [69] and  $|\eta| \lesssim 2.6$  [80], respectively. While the restriction in the acceptance introduced by the  $z$ -vertex trigger is no worry (we cut on  $\eta^{\text{jet}} < 2.5$ , *cf.* equation (5.7)), the limited acceptance of the DC- $r\varphi$  trigger could introduce a bias. For jets in the very forward region, say  $\eta^{\text{jet}} \approx 2.5$ , only a track as far away as  $\eta^{\text{track}} - \eta^{\text{jet}} \approx 0.9$  from the jet axis fires the DC- $r\varphi$  trigger, hence broader jets have better chances to be triggered on than narrower ones. This could — if the MC simulation did not account for this effect, *e.g.* because the number of charged tracks per event was underestimated — lead to the observed forward energy problem.

A data sample triggered by subtrigger 80, *i.e.*, the requirement of the same trigger-elements as for subtrigger 83 (the subtrigger used for this analysis, see chapter 5) except for the DCRPh-Ta element, shows the same forward energy problem. This is, despite the rather limited acceptance of the DC- $r\varphi$  trigger, not very surprising considering the fact that the trigger efficiency of the DCRPh-Ta element for the final data sample is measured to be  $97 \pm 1\%$  (see section 5.1.1). Moreover, the forward energy problem already starts at  $\eta^{\text{jet}} \gtrsim 1$  which is well below the boundary of the acceptance region of the DC- $r\varphi$  trigger.

Data samples triggered by subtriggers based on the eTAG trigger-element in coincidence with a trigger-element from the forward ray trigger (“subtrigger 84”; the forward ray trigger uses the information from the three forward multi-wire proportional chambers and the central inner proportional chamber) or from the liquid argon calorimeter trigger (“subtrigger 81”)<sup>4</sup> lead to the same conclusion, *i.e.*, that the forward energy problem is not due to a trigger bias.

### 6.3.3 Pile-up

The background contamination of the final data sample has been checked to be negligible (see section 5.4). As an alternative confirmation of this observation, the  $z_{\text{vertex}}$ -distribution (see section 5.4) for the data sample with all selection cuts but the cut on  $-35 \text{ cm} < z_{\text{vertex}} < 25 \text{ cm}$  applied (see chapter 5) has been re-examined (not shown). From the number of events with an event-vertex outside the nominal interaction region  $-35 \text{ cm} < z_{\text{vertex}} < 25 \text{ cm}$ , one can estimate the contamination of the final data sample due to proton-gas or proton-wall processes (in random coincidence with an electron induced background event) to be below 1%.

<sup>4</sup>For more information on these triggers see [43].

There is, however, the possibility that a genuine photoproduction event occurs in random coincidence with another event, most probably a proton-gas or proton-wall background event. The “second” event may thereby appear in the very same bunch crossing or — because the analog signals from the LAr calorimeter have a rise- and decay-time of a few  $\mu\text{s}$  [43, 44] — in a bunch crossing adjacent to the bunch crossing in which the photoproduction event occurs. The extra energy flow from such overlaid proton-gas or proton-wall events ( $\eta_{pH} \approx 3.7$ ,  $\eta_{pO} \approx 2.3$ ) may possibly lead to the observed forward energy problem. Various different strategies to control this possible “pile-up” effect have been pursued and will be described below.

### 6.3.3.1 Rates

As a first rough estimate of the possible pile-up contribution to our data sample, we consider the trigger rate  $R_{1\text{track} \times !\text{ToF-BG}}$  (*i.e.*, the trigger rate for the trigger-element “1 track” (*e.g.* DCRPh-Ta or zVTx-T0)  $\times$  !ToF-BG; for a description of the trigger-elements see section 5.1), which is dominated by proton induced background processes. For the 1993 running period, this trigger rate has been measured to be  $R_{1\text{track} \times !\text{ToF-BG}} = 500 \text{ Hz}$  [81].

This background rate  $R_{1\text{track} \times !\text{ToF-BG}}$ <sup>5</sup> has now to be compared to the bunch crossing frequency of 10.4 MHz. It then translates into a pile-up probability  $P_{\text{pile-up}}$  of  $P_{\text{pile-up}} = R_{1\text{track} \times !\text{ToF-BG}} [\text{Hz}] \cdot 10^{-7} [\text{Hz}^{-1}] = 5 \cdot 10^{-5}$ .

Considering the fact that a proton induced background event may take place in a bunch crossing adjacent to the bunch crossing in which the genuine photoproduction event occurs, the total number of pile-up events may be at most a factor of 40 higher<sup>6</sup> (*i.e.*, we allow the background event to “lie as far away” as 20 bunch crossings or  $\approx 2 \mu\text{s}$ ; the half-width-at-half-maximum of the LAr analog signal however is only  $\lesssim 1 \mu\text{s}$  [44]). Therefore, at most 0.2% of the events are contaminated by pile-up.

### 6.3.3.2 Proton current and bunch selection

In the following, we explore two different ways of influencing a possible pile-up effect (*i.e.*, the addition of extra transverse energy) in the jet-profiles.

One possible explanation for the poor description of the data by the MC simulation is that effects due to noise and especially pile-up are not correctly modeled by the addition of the “noise-files” as described in section 5.3. We have therefore *additionally* added randomly triggered events (*i.e.*, events where no trigger but a random trigger was set; “empty” events) to the Monte Carlo events. Roughly 1%

<sup>5</sup>We require at least one track for the background events, since these events need to leave some energy in the LAr calorimeter in order to account for the forward energy problem.

<sup>6</sup>Only true if no ToF-BG trigger-element is set in the adjacent bunch crossings. For the final data sample, the number of events with a ToF-BG trigger-element set in an adjacent bunch crossing is marginal (see section 6.3.3.3).

of these randomly triggered events have a transverse energy  $E_{t,\text{event}} > 2 \text{ GeV}$  and  $\approx 0.2\%$  of the added events have  $E_{t,\text{event}} > 10 \text{ GeV}$ . The electronic noise in the LAr calorimeter is constant in time but the pile-up is expected to be proportional to the proton current and to the vacuum in the interaction region. Since the “noise-file” only consists of events from a short running period, a variation of the noise and pile-up contribution due to different proton currents or a varying vacuum is not taken into account. The variation in the quantity “proton current  $\times$  vacuum” was at most a factor of 5 over the whole 1993 running period. However, to explain the jet-profiles, we would have to add randomly triggered events to the MC events corresponding to two orders of magnitude higher currents in the machine.

To directly check the impact of the proton current on the potential pile-up contribution, the jet-profiles for data taken at high and low proton currents are compared. Again, we assume the jet-profiles to be more affected by pile-up events when the total proton current in HERA is high. However, no such observation can be made.

The second possibility explored to influence a possible pile-up effect is to select special proton bunches. As mentioned earlier, only 90 out of 210 possible proton bunches were filled in the 1993 running period and only 84 out of those had a colliding partner. The 90 proton bunches were filled in 9 packs of 10 bunches interleaved with 8·14 empty bunches. The ninth pack included 4 colliding and 6 proton pilot bunches and was followed by another 8 empty bunches. Due to this structure, we expect that  $ep$  scattering events from proton bunches at the edge of such packs are less affected by background events in bunch crossings adjacent to the bunch crossing in which the  $ep$  scattering took place than photoproduction events from proton bunches in the middle of these packs. The comparison of jet-profiles of events from proton bunches at the beginning, in the middle or at the end of these proton bunch packs does not show any such difference.

### 6.3.3.3 Trigger veto

Pile-up events which are due to a background event in a bunch crossing adjacent to the bunch crossing in which the photoproduction event occurs may set some trigger-elements in the respective bunch crossing. We therefore check for different trigger-elements in the bunch crossings around the actual bunch crossing of the event (the corresponding information is only recorded for  $\pm 5$  bunch crossings). Note however that not every trigger-element is suited for this investigation, because some trigger-elements are allowed (by design) to be set during more than one bunch crossing (for one single event) or they may “accidentally” be set due to their trigger history, *e.g.* triggers based on multi-wire proportional chambers often trigger in the bunch crossings after the actual bunch crossing of the event because of the after-pulsing of the signals from the cathode pads.

One trigger-element checked to veto background events in adjacent bunch crossings is the ToF-BG trigger-element (see section 5.1). The removal of all events that have the trigger-element ToF-BG set in neighbouring bunch crossings (29 events for the

enlarged data sample) does not lead to an improved description of the jet-profiles by the MC simulation.

Two more trigger-elements were used to veto pile-up events, the zVtx-T0 trigger-element (11 events in the enlarged data sample) and the FwdRay-T0 trigger-element from the forward ray trigger (112 events). These two trigger-elements were only used to veto early background events, *i.e.*, events that occurred in an earlier bunch crossing than the photoproduction event. However, no difference in the respective jet-profiles is seen.

Note that for the final data sample (579 events, see section 5.5) only 19 events are vetoed by the sum of the above “veto-triggers” (6, 2 and 11 due to the ToF-BG, the zVtx-T0 and the FwdRay-T0 trigger-element, respectively). We do however not remove these events since they are included in the Monte Carlo simulation due to the addition of the “noise-files” obtained from randomly triggered events (see above)<sup>7</sup>.

To sum up the results of this section, we do not have any indication that the forward energy problem observed in the jet-profiles is due to pile-up events or due to other systematic errors (*e.g.* absolute energy scale in the LAr calorimeter, *etc.*).

Nevertheless, we must find a solution to correct for the poor description of the jet-profiles by the Monte Carlo simulations (see also section 6.4.2).

## 6.4 Correction of energy flow description

The aim of this section is to describe different energy flow correction methods, *i.e.*, methods that correct for the poor description of the transverse energy flow by the MC simulations. These energy flow correction methods are all inspired by the assumption that the poor description of the data is due to soft processes (*e.g.* multiple interactions) which are not correctly described by the Monte Carlo simulations. To emphasize that this assumption is indeed very tempting, the first subsection shows that the data does have properties expected for multiple interactions.

### 6.4.1 Multiple interactions

As discussed in section 6.2, multiple interactions within the same event offer a natural explanation for the poor description of the jet-profiles by the Monte Carlo simulations.

To demonstrate that the data has additional properties expected for multiple interactions, we plot the jet-profiles in  $\eta$  for data and MC for low and high  $x_\gamma$  at fixed  $\eta^{\text{jet}}$  ( $0 < \eta^{\text{jet}} < 1$ , see figures 6.6 and 6.7; as in section 6.3, we enlarge our data and MC samples by lowering the  $p_t$ -cut and skipping the cuts on  $\eta^{\text{jet}}$ ). Note that

---

<sup>7</sup>For the FwdRay-T0 trigger-element, the trigger bit has most probably been set due to a malfunctioning of the trigger in the respective running period.

the jet-profiles in  $\eta$  are asymmetric, showing a higher transverse energy flow in the direction of the proton remnant ( $\eta^{\text{cell}} - \eta^{\text{jet}} > 0$ ) compared to the photon remnant direction ( $\eta^{\text{cell}} - \eta^{\text{jet}} < 0$ ).

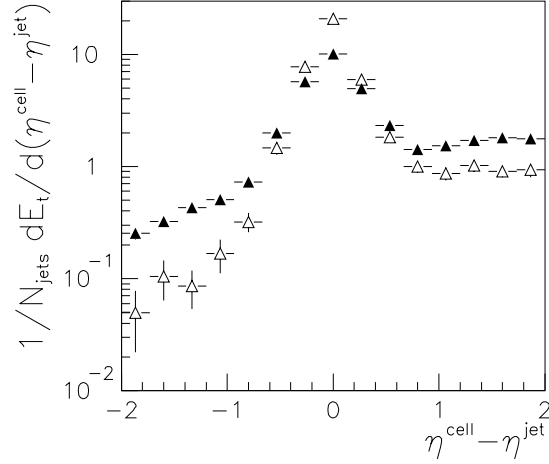


Figure 6.6: Jet-profile in  $\eta$  for the final data sample. Transverse energy flow (per jet) around the jet direction in a slice of  $|\varphi^{\text{cell}} - \varphi^{\text{jet}}| < 1$  versus the distance in  $\eta$  from the jet axis. Jets are selected with  $0 < \eta^{\text{jet}} < 1$  and the profiles are given for  $x_{\gamma}^{\text{jets}} < 0.5$  (▲) and  $x_{\gamma}^{\text{jets}} > 0.7$  (△).

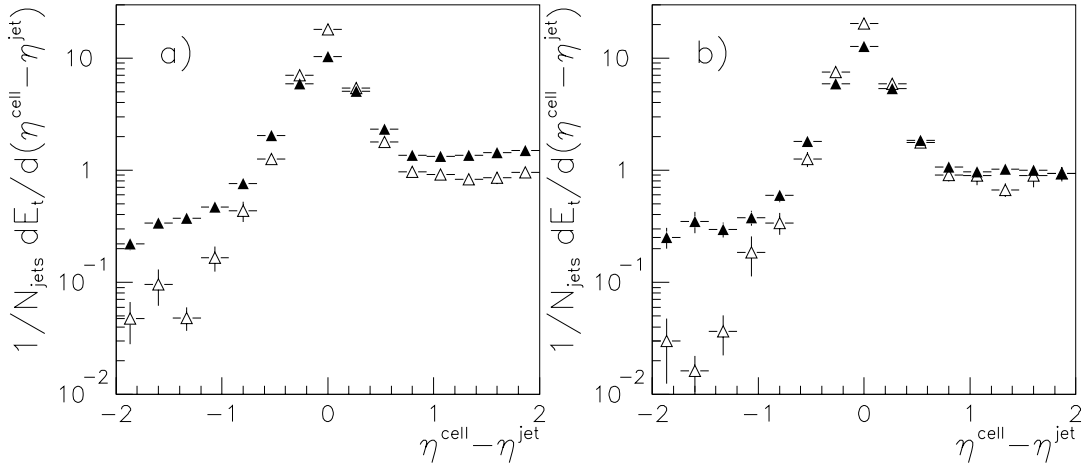


Figure 6.7: Jet-profile in  $\eta$  for the MC simulations. Transverse energy flow (per jet) around the jet direction in a slice of  $|\varphi^{\text{cell}} - \varphi^{\text{jet}}| < 1$  versus the distance in  $\eta$  from the jet axis. Jets are selected with  $0 < \eta^{\text{jet}} < 1$  and the profiles are given for  $x_{\gamma}^{\text{jets}} < 0.5$  (▲) and  $x_{\gamma}^{\text{jets}} > 0.7$  (△). Figure a) shows the jet-profile for a MC simulation that includes multiple interactions whereas b) shows the profile for a MC simulation without additional soft interactions.

Within the multiple interaction scenario, the energy (squared) left for multi-

ple *soft* interactions of partons from the photon and the proton is given by  $s_{\text{spectators}} = (1 - x_\gamma)(1 - x_p)ys_{ep}$  (neglecting masses and transverse momenta), where  $x_\gamma$  and  $x_p$  refer to the fractional momenta of the partons from the photon and the proton, respectively, determined from the *hard* (“*first*”) parton-parton scattering. Since  $x_p$  is typically small ( $x_p^{\text{jets}} \lesssim 0.1$ , cf. figure 6.4) and the  $y$ -range is limited to  $0.25 < y < 0.7$  (see section 5.4), the main variation in  $s_{\text{spectators}}$  is due to  $x_\gamma$ , which may vary between  $x_\gamma^{\text{jets}} \approx 0.05$  and  $x_\gamma^{\text{jets}} \approx 1$  (cf. figure 6.4). Effects due to multiple interactions should therefore depend on  $x_\gamma$  and are expected to show up mainly at large pseudo-rapidities ( $1.9 < \eta_{\gamma p} < 2.4$  for  $0.25 < y < 0.7$ ).

In figure 6.6, one sees an enhanced energy flow for small  $x_\gamma^{\text{jets}}$  for both  $\eta^{\text{cell}} - \eta^{\text{jet}}$  small (negative) and large (positive). The increase in the energy flow for negative  $\eta^{\text{cell}} - \eta^{\text{jet}}$  with decreasing  $x_\gamma^{\text{jets}}$  may be attributed to the presence of the photon remnant (for  $x_\gamma \equiv 1$ , *i.e.*, direct processes, there is no photon remnant at all!). The additional energy flow for *positive*  $\eta^{\text{cell}} - \eta^{\text{jet}}$  at small  $x_\gamma^{\text{jets}}$  however can be interpreted as the additional energy flow due to multiple interactions! Note that a MC simulation that includes multiple interactions shows the same behaviour (see figure 6.7 a)), whereas for a MC simulation without additional interactions there is no significant increase in the energy flow at positive  $\eta^{\text{cell}} - \eta^{\text{jet}}$  for low  $x_\gamma^{\text{jets}}$  (see figure 6.7 b)).

The above observation is a strong hint that we see effects due to multiple interactions in our data. However, we do not consider this to be a proof of the existence of multiple interactions in hard photoproduction processes.

Since a Monte Carlo simulation which includes multiple interactions describes our data much better than a MC simulation without additional interactions, it is very tempting to improve the MC description even more by increasing the activity due to multiple interactions, *e.g.* by lowering the  $\hat{p}_{t,\text{min}}^{\text{mi}}$ -cutoff (see section 3.1). Such investigations have been pursued, but did not lead to convincing results, mainly because the additional energy flow due to multiple interactions spoiled the jet-profiles at low  $\eta^{\text{jet}}$ . Nevertheless, these studies have to be repeated for future analysis when more statistics allow for more elaborate checks. Additionally, improved (PYTHIA 5.7 [82] and HERWIG 5.8 [83]) and new (PHOJET [84]) event generators seem to describe the data better [85]. However, fully simulated and reconstructed Monte Carlo samples that are based on these improved or new generators do not exist yet. Hence, we have to stick to the MC samples mentioned in chapter 3.

## 6.4.2 Pedestal energy

The poor description of the jet-profiles in  $\varphi$  in the pedestal region prevents us from relating the transverse energies of the jets with the transverse momenta of the partons reliably. If we assume that the additional energy seen in the jet-pedestal region of the jet-profiles in the data sample compared to the jet-profiles in the MC samples is also present within the jet-core (*i.e.*,  $R_{(\eta,\varphi)} := \sqrt{(\eta^{\text{cell}} - \eta^{\text{jet}})^2 + (\varphi^{\text{cell}} - \varphi^{\text{jet}})^2} < 1$ ), the relation between  $p_t^{\text{jet}}$  and  $p_t^{\text{parton}}$  is not described correctly by the MC simula-

tions. This assumption is supported by the fact that the poor description of the jet-profiles in  $\varphi$  is not only restricted to the pedestal region, but also affects the bins for  $|\varphi^{\text{cell}} - \varphi^{\text{jet}}| < 1$  (*cf.* figure 6.5; most prominent for  $2 < \eta^{\text{jet}} < 2.5$ ). Hence, a measurement of the differential parton cross-section  $d\sigma/dp_t$  is not possible since even a small error in the energy measurement leads to large errors in  $d\sigma/dp_t$  due to the steeply falling distribution ( $d\sigma/dp_t^{\text{jet}} \sim (p_t^{\text{jet}})^{-5.5}$  [86]).

In the following, we will try to determine this possible contribution to the transverse energy flow within the jet-core by assuming that the additional energy flow seen in the jet-pedestal region of the jet-profiles (data versus MC) is present in the entire  $(\eta, \varphi)$  space and that it is constant as a function of  $\varphi$  (as would — in average — be expected if this additional energy flow was due to multiple interactions). As a first energy flow correction method, we will then subtract this additional energy.

We determine the *pedestal energy* of a jet, that is, the contribution to the transverse energy flow (per jet) within the jet-core extrapolated from the energy flow in the pedestal region, by measuring the (rescaled) average transverse energy flow around the jet direction:

$$E_t^{\text{pedestal}} = \frac{A_{\text{jet-core}}}{A_{\text{pedestal region}}} \sum_{\substack{-1 < \eta^{\text{cell}} - \eta^{\text{jet}} < 1 \\ \text{excluding jet-cores}}} E_t^{\text{cell}} \quad . \quad (6.1)$$

The transverse energy flow is summed up in the slice  $-1 < \eta^{\text{cell}} - \eta^{\text{jet}} < 1$  (all  $\varphi$ ), thereby excluding the jet-core ( $R_{(\eta,\varphi)} < 1$ ) and the possible contribution to the energy flow from the second jet (*i.e.*,  $R_{(\eta,\varphi)}^{\text{second jet}} < 1$ ). This defines the area  $A_{\text{pedestal region}}$ . The transverse energy flow is then scaled to  $A_{\text{jet-core}}/A_{\text{pedestal region}}$ , with  $A_{\text{jet-core}} = \pi R_{(\eta,\varphi)}^2$ ,  $R_{(\eta,\varphi)} = 1$ .

Before we calculate the pedestal energy for the jets in the data and MC samples, we first have to show that the jet-core is well defined by the requirement  $R_{(\eta,\varphi)} < 1$ . In figure 6.8, the transverse energy flow (per jet) as a function of  $R_{(\eta,\varphi)}$  is shown. Only energy clusters which were assigned to the jet by the  $k_{\perp}$ -algorithm contribute to the plot.

The  $k_{\perp}$ -algorithm used for this analysis most closely resembles a cone-type algorithm with fixed cone-size  $R_{(\eta,\varphi)} = 1$  (see chapter 4). The jet-radius (*i.e.*,  $R_{(\eta,\varphi),\text{max}}$ ) for the  $k_{\perp}$ -algorithm may however vary from jet to jet and can be both smaller or larger than  $R_{(\eta,\varphi)} = 1$ . As can be seen in figure 6.8, most of the energy flow is contained in a radius of  $R_{(\eta,\varphi)} = 1$ . Note that the difference in the energy flow between data and MC is restricted to the region  $R_{(\eta,\varphi)} \lesssim 0.7$  (MC with multiple interactions) and  $R_{(\eta,\varphi)} \lesssim 1.2$  (MC without multiple interactions; difference small for  $R_{(\eta,\varphi)} \gtrsim 1.0$ ). To measure the *additional* pedestal energy present in the data in comparison with the MC simulations, an average jet-core area of  $\pi R_{(\eta,\varphi)}^2 = \pi$  looks reasonable.

In figure 6.9 the measured  $E_t^{\text{pedestal}}$ -distribution is given for different bins in  $\eta^{\text{jet}}$ .

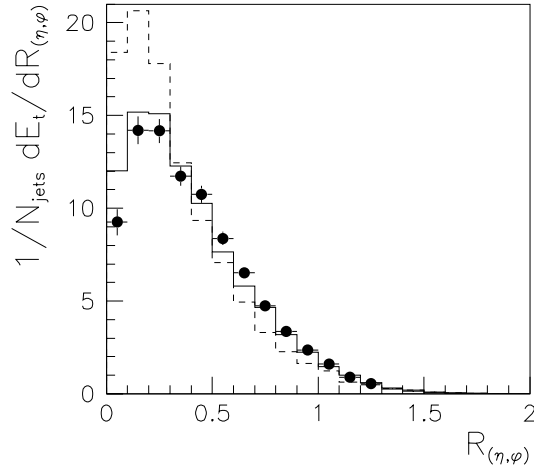


Figure 6.8: Transverse energy flow (per jet) as a function of  $R_{(\eta,\varphi)}$  ( $R_{(\eta,\varphi)} := \sqrt{(\eta^{\text{cluster}} - \eta^{\text{jet}})^2 + (\varphi^{\text{cluster}} - \varphi^{\text{jet}})^2}$ ) for jets in the final data (points) and MC samples (full histogram: including multiple interactions, dashed histogram: no additional interactions). Only energy clusters which were assigned to the jet by the  $k_{\perp}$ -algorithm contribute to the plot.

Similar to the jet-profiles in  $\varphi$  (see above), the MC simulation that includes multiple interactions can better describe the data than the MC simulation without any additional interactions. However, the average jet-pedestal energies as observed in the data are larger ( $\eta^{\text{jet}} \gtrsim 1$ ) than predicted by both MC simulations (see also figure 6.10). Note that the *fluctuations* in the pedestal energies are large, especially at large  $\eta^{\text{jet}}$ . This is not only true for the data but also for both MC simulations. Do further note that the pedestal energy fluctuations in the data, too, are reasonably well described for  $\eta^{\text{jet}} \lesssim 1$  by both Monte Carlo simulations.

For jet pseudo-rapidities between 2 and 2.5, the difference in the pedestal energy determined for the data and the MC simulation which includes multiple interactions is as large as  $\approx 1.1$  GeV. As mentioned before, this is far too much to be neglected! We will therefore have to correct for this discrepancy.

### 6.4.3 Pedestal subtraction

A possible correction of the observed mismatch between the jet-profiles in data and MC is to subtract the *full* pedestal energy from the jet energy  $E_t^{\text{jet}}$ . This would however lead to wrong results, since the pedestal energy is determined based on the assumption that the transverse energy flow in the pedestal region continues constantly (as a function of  $\varphi$ ) into the jet-core as suggested by the multiple interaction scenario. But we see from figure 6.5 (dashed histogram) that the transverse energy flow in the pedestal region is non-vanishing even in the absence of multiple interactions. This is due to final-state radiation and fragmentation effects (*i.e.*, effects

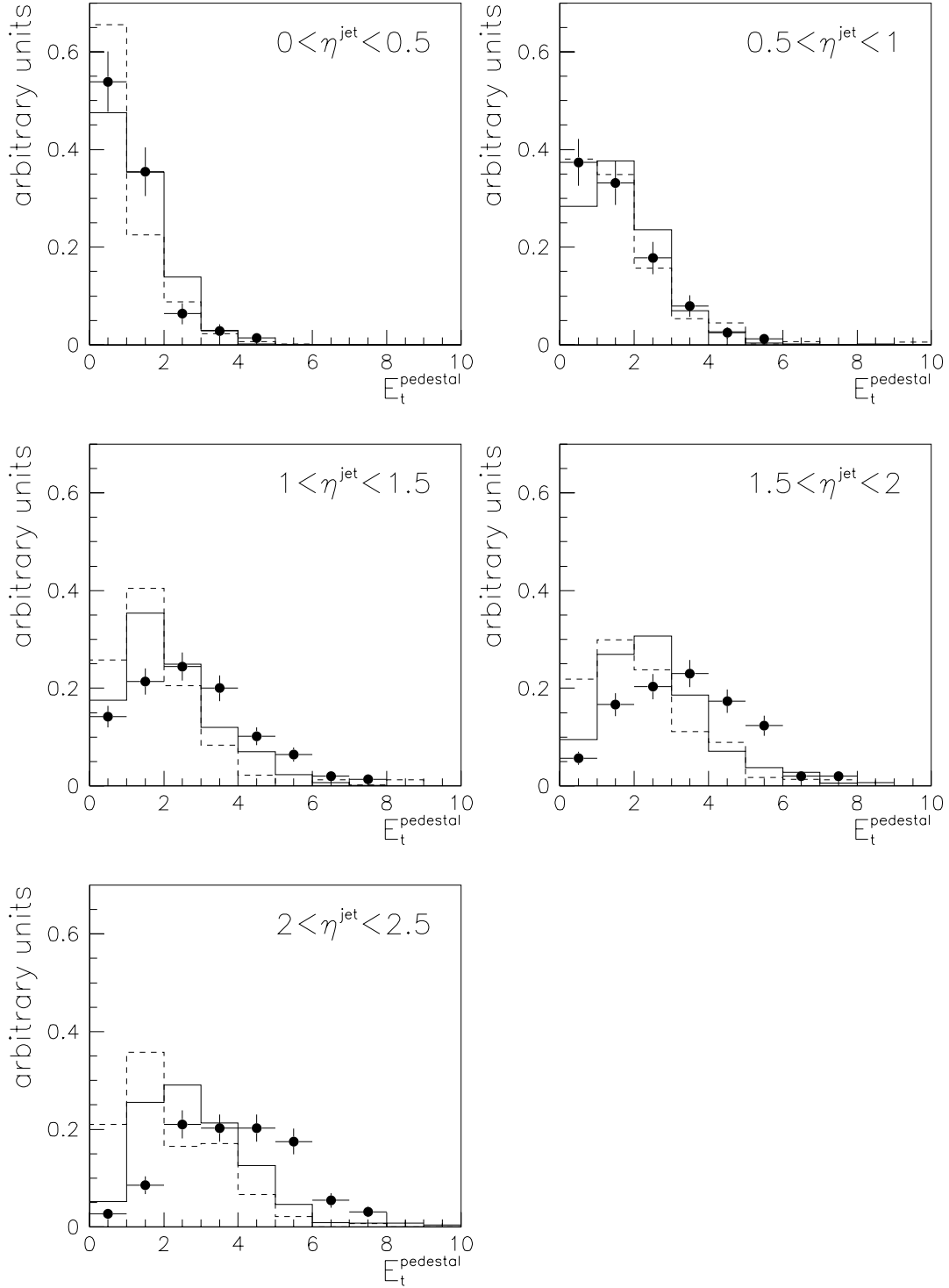


Figure 6.9:  $E_t^{\text{pedestal}}$ -distribution as a function of  $\eta^{\text{jet}}$ . Data (points) is compared with a Monte Carlo simulation that includes multiple interactions (full histogram) and a MC simulation without additional interactions (dashed histogram). The distributions are normalized to unit area.

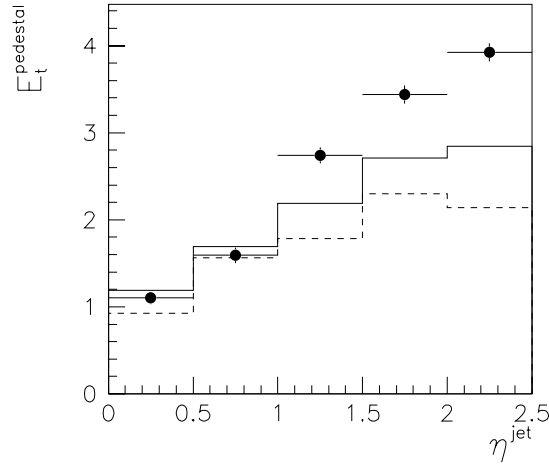


Figure 6.10: Average  $E_t^{\text{pedestal}}$  as a function of  $\eta^{\text{jet}}$ . Comparison of data (points) and Monte Carlo simulations (full histogram: including multiple interactions, dashed histogram: no additional interactions).

related to the hard scattering process) which lead to an energy flow in the pedestal region, too. We do not expect that this contribution to the energy flow is constant as a function of  $\varphi$ .

Consistently, the correlation between  $E_t^{\text{jet}} - E_t^{\text{pedestal}}$  and  $p_t^{\text{parton}}$  (or better, the correlation between  $E_t^{\text{jet}} - (E_t^{\text{pedestal}} \cdot R_{(\eta,\varphi),\text{max}}^2)$  and  $p_t^{\text{parton}}$ , see below) is worse than the correlation between  $E_t^{\text{jet}}$  and  $p_t^{\text{parton}}$  as has been checked for the MC sample that includes multiple interactions (for an extensive study of the jet-profiles and pedestal energies in photoproduction at HERA, see [87], too).

We therefore need to correct for the *additional* pedestal energy seen in data (and in the MC simulation that includes multiple interactions — we have no proof for the existence of multiple interactions) compared to the predictions of the Monte Carlo simulation without additional soft interactions.

Since the fluctuation in the pedestal energy is large for the MC simulation without multiple interactions (and hence also for data and for the MC simulation that does include multiple interactions), a subtraction of the *additional* pedestal energy on an event by event basis is not possible.

The pedestal subtraction applied to both the data and the MC sample which includes multiple interactions is therefore based on the *average* pedestal energies:

$$E_{t,\text{corrected}}^{\text{jet}} = E_t^{\text{jet}} - \left( \Delta E_t^{\text{pedestal}} \cdot R_{(\eta,\varphi),\text{max}}^2 \right) \quad (6.2)$$

with

$$\Delta E_t^{\text{pedestal}} = \langle E_t^{\text{pedestal}} \rangle - \langle E_{t,\text{non-mi MC}}^{\text{pedestal}} \rangle \quad . \quad (6.3)$$

$\langle E_t^{\text{pedestal}} \rangle$  is thereby given by the average pedestal energy (*cf.* equation (6.1)) of the jets in the data and the MC sample, respectively. The dependence of  $\Delta E_t^{\text{pedestal}}$  on  $\eta^{\text{jet}}$  (see figure 6.10) is parameterized by a second order polynomial in  $\eta^{\text{jet}}$ . The dependence of  $\Delta E_t^{\text{pedestal}}$  (at fixed  $\eta^{\text{jet}}$ ) on  $p_t^{\text{jet}}$  and on the pseudo-rapidity of the second jet is marginal (note that the available statistics are rather limited for such an investigation) and will be neglected. The variation in  $\Delta E_t^{\text{pedestal}}$  is determined to be  $0.1 \text{ GeV} \lesssim \Delta E_t^{\text{pedestal}} \lesssim 2.2 \text{ GeV}$  and  $0.2 \text{ GeV} \lesssim \Delta E_t^{\text{pedestal}} \lesssim 0.9 \text{ GeV}$  for the final data and MC samples, respectively. Note that the average pedestal energy difference  $\Delta E_t^{\text{pedestal}}$  which is subtracted from  $E_t^{\text{jet}}$  to get the corrected jet energy  $E_{t,\text{corrected}}^{\text{jet}}$  is scaled with the jet-radius squared  $R_{(\eta,\varphi),\text{max}}^2$  to take into account the varying jet-radius for the  $k_{\perp}$ -algorithm (the influence of  $R_{(\eta,\varphi),\text{max}}$  on the determination of  $E_t^{\text{pedestal}}$  is small, which can be seen from the fact that the summed transverse energy flow for  $R_{(\eta,\varphi)} > 1$  (*cf.* figure 6.8) is much smaller than the average pedestal energy (*cf.* figures 6.9 and 6.10); for  $\Delta E_t^{\text{pedestal}}$ , the fact that  $R_{(\eta,\varphi),\text{max}}$  may be larger than unity has an even smaller influence as has already been discussed above). The  $R_{(\eta,\varphi),\text{max}}$ -distribution is shown in figure 6.11.

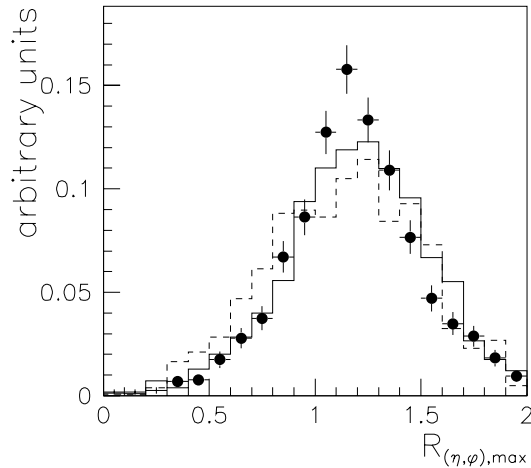


Figure 6.11:  $R_{(\eta,\varphi),\text{max}}$ -distribution for the final data (points) and MC samples (full histogram: including multiple interactions; dashed histogram: no additional interactions).  $R_{(\eta,\varphi),\text{max}}$  is given by the cluster assigned to the jet by the  $k_{\perp}$ -algorithm which has the largest distance  $R_{(\eta,\varphi)} = \sqrt{(\eta^{\text{cluster}} - \eta^{\text{jet}})^2 + (\varphi^{\text{cluster}} - \varphi^{\text{jet}})^2}$  from the jet axis. To account for the fact that the reconstruction code may produce clusters of vanishing energy (*e.g.* due to noise suppression procedures), a minimal energy of  $E_{\text{cluster},\text{min}} = 50 \text{ MeV}$  is asked for every cluster.

After the pedestal subtraction, we again ask for a minimal transverse energy of the two jets of 6 GeV (see section 5.5) to ensure that we are left with hard photoproduction processes only. The corrected jet energy will then again be called  $E_t^{\text{jet}}$  (instead of  $E_{t,\text{corrected}}^{\text{jet}}$ ).

To prove that such an average pedestal subtraction can correct for the additional

energy flow within the jet-core (we henceforth refer to the jet-core as the area  $\pi R_{(\eta,\varphi),\max}^2$ ) due to *e.g.* multiple interactions, *i.e.*, that it removes the influence of these multiple interactions on the  $p_t^{\text{jet}}$ -,  $\eta^{\text{jet}}$ - and  $x_\gamma^{\text{jets}}$ -distribution, we compare the pedestal subtracted MC sample which includes multiple interactions with the MC sample without any additional interactions. For this comparison, we apply the same  $\hat{p}_t$ -cut to the MC sample that includes multiple interactions as was used for the generation of the MC sample without multiple interactions, *i.e.*,  $\hat{p}_{t,\min} = 4 \text{ GeV}/c$  (see section 3.1). Figure 6.12 shows the  $p_t^{\text{jet}}$ - and  $\eta^{\text{jet}}$ -distribution of the two  $p_t$ -leading jets for both samples together with the distribution for the MC sample that includes multiple interactions *before* the pedestal subtraction.

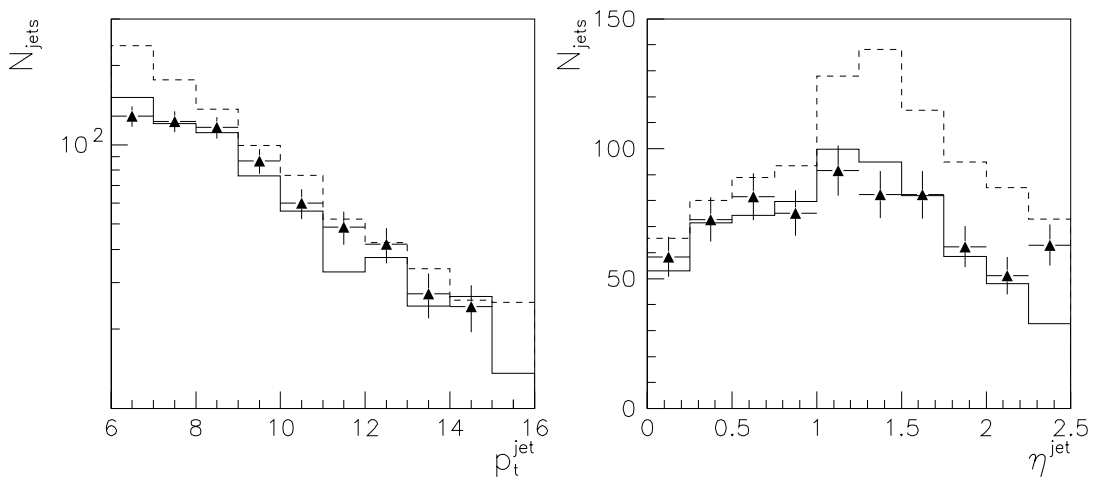


Figure 6.12:  $p_t^{\text{jet}}$ - and  $\eta^{\text{jet}}$ -distribution for different MC samples. Shown are the distributions for the MC without additional interactions (triangles) together with the distributions for the MC that includes multiple interactions before (dashed histogram) and after (full histogram) the pedestal subtraction. All distributions are normalized to the same integrated luminosity and have a cut applied at  $\hat{p}_t = 4 \text{ GeV}/c$ .

The distributions for the pedestal subtracted MC that includes multiple interactions and the MC simulation without additional interactions should coincide. As can be seen in figure 6.12, this is fulfilled fairly well. Note that the absolute prediction for the 2-jet rate of the pedestal subtracted Monte Carlo that includes multiple interactions and the MC simulation without additional interactions agree within the statistical errors.

Figure 6.13 shows the  $x_\gamma^{\text{jets}}$ - and  $x_\gamma$ -distribution for the same MC samples.

The coincidence between the distribution for the pedestal subtracted MC sample which includes multiple interactions and the MC simulation without additional interactions is good. Note the slight disagreement at large  $x_\gamma$  ( $x_\gamma^{\text{jets}}$ ) which is due to the fact that we subtract some jet energy for *all* events. This is probably inadequate at very large  $x_\gamma$ , *e.g.* for direct processes (*i.e.*, for events with  $x_\gamma \equiv 1$ ).

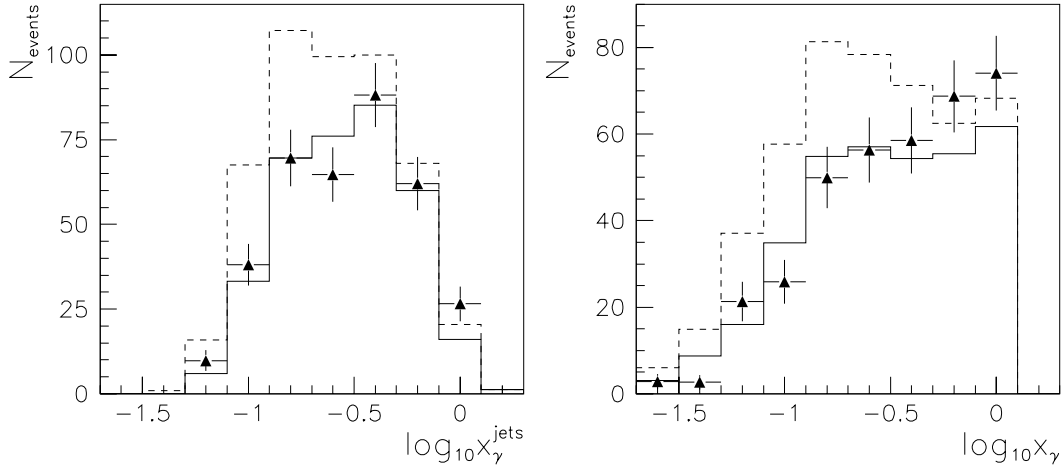


Figure 6.13:  $x_\gamma^{\text{jets}}$ - and  $x_\gamma$ -distribution for different MC samples. Shown are the distributions for the MC without additional interactions (triangles) together with the distributions for the MC that includes multiple interactions before (dashed histogram) and after (full histogram) the pedestal subtraction. All distributions are normalized to the same integrated luminosity and have a cut applied at  $\hat{p}_t = 4 \text{ GeV}/c$ .

We will apply the above-mentioned pedestal subtraction to both our data and MC sample. Due to the large values of  $\Delta E_t^{\text{pedestal}}$  (see above), this last selection cut (we again ask for  $p_t^{\text{jet}} > 6 \text{ GeV}/c$ ) reduces our “final” data and MC samples substantially and leaves us with 258 and 780 (396) events, respectively. We will henceforth call these samples the “final, pedestal subtracted” samples.

Figure 6.14 shows the corrected  $E_t^{\text{pedestal}}$ -distribution, *i.e.*, the distribution of

$$E_t^{\text{pedestal}} - \Delta E_t^{\text{pedestal}} = E_t^{\text{pedestal}} - \left( \langle E_t^{\text{pedestal}} \rangle - \langle E_{t,\text{non-mi}}^{\text{pedestal}} \rangle \right) \quad (6.4)$$

for data and MC.

At large  $\eta^{\text{jet}}$ , the pedestal energies are still somewhat poorly described by the Monte Carlo simulation. This can be explained by the fact that the pedestal subtraction method only uses the average pedestal energies and can therefore not correct for large fluctuations of the additional energy flow within the jet-core.

Finally, we again show the  $\hat{p}_t$ -distribution for the final, pedestal subtracted MC sample (*cf.* figure 6.15).

The cut at  $\hat{p}_{t,\text{min}} = 2 \text{ GeV}/c$  does not influence the distribution. Note that even after the pedestal subtraction, a few MC events which have a  $\hat{p}_t$  as low as  $\hat{p}_t \gtrsim 2-3 \text{ GeV}/c$  remain in the sample. This is again due to the above-mentioned fact that the fluctuations in the pedestal energy are large and that the pedestal subtraction only uses the average pedestal energies for the subtraction.

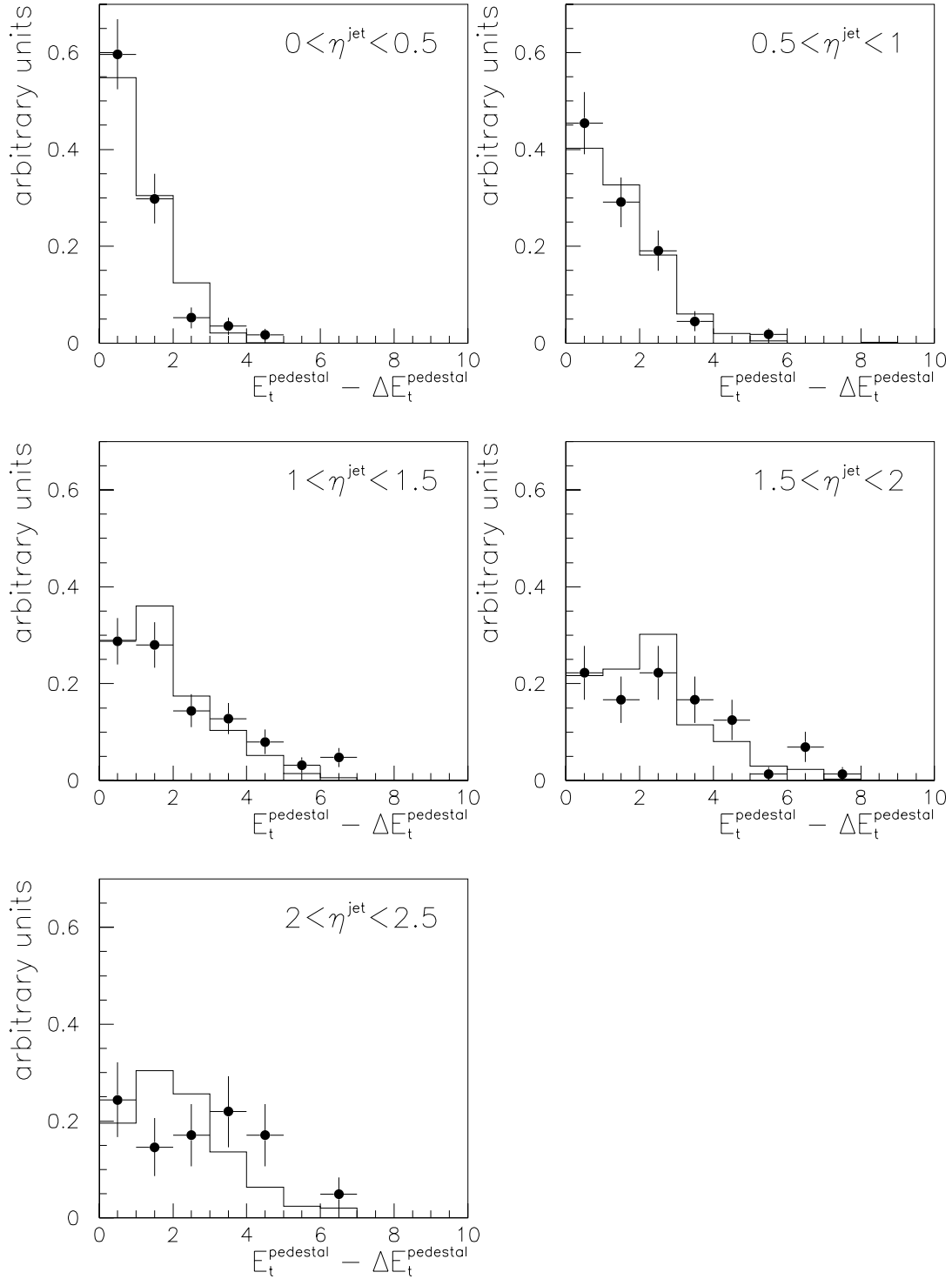


Figure 6.14:  $E_t^{\text{pedestal}} - \Delta E_t^{\text{pedestal}}$  distribution as a function of  $\eta^{\text{jet}}$ . Comparison of data (points) and Monte Carlo simulation (full histogram). The distributions are normalized to unit area.

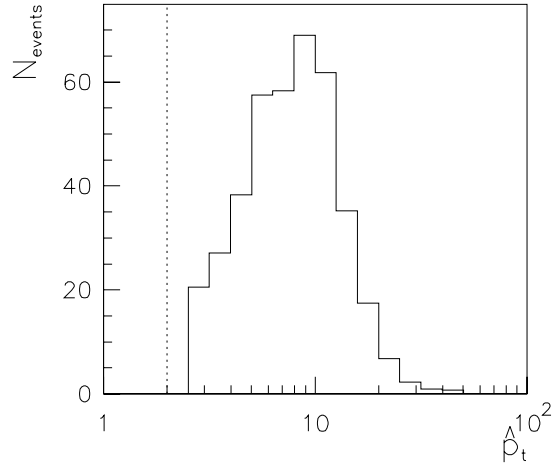


Figure 6.15:  $\hat{p}_t$ -distribution for the final, pedestal subtracted MC sample. The cut on  $\hat{p}_t$  when generating the MC events was set to  $\hat{p}_{t,\min} = 2 \text{ GeV}/c$  (dotted line).

#### 6.4.4 Alternatives to pedestal subtraction

In the previous subsection, we tried to correct for the observed difference between the jet-profiles in data and MC by subtracting the energy flow within the jet-core that is not due to a hard parton parton interaction but to some other process, *e.g.* multiple soft interactions. This energy flow was estimated from the energy flow measured around the jet direction.

This pedestal subtraction method however does have some drawbacks. Firstly, the proof that this method works is only valid under the assumption that the additional energy flow seen in the data behaves qualitatively similar to the additional energy flow due to multiple interactions as modeled by the event generator PYTHIA (*i.e.*, distribution of energy flow in  $(\eta, \varphi)$  space, *etc.*). This may not be the case. Secondly, if the additional energy flow (as compared to a MC simulation that does not include multiple interactions) is due to soft multiple interactions, we expect that the contributions to the energy flow within the jet-core fluctuate. The pedestal subtraction method described above, however, only uses the average pedestal energies. Finally the determination of the additional pedestal energy  $\Delta E_t^{\text{pedestal}}$  (*cf.* equation (6.3)) does not take into account that the pedestal energies  $E_t^{\text{pedestal}}$  are distributed asymmetrically around the mean  $\langle E_t^{\text{pedestal}} \rangle$ . This may in average lead to a subtraction of too much energy. Remarkably, the two latter points do not prevent the successful proof of the method (*i.e.*, that the pedestal subtraction corrects for the influence of multiple interactions on the  $p_t^{\text{jet}}$ -,  $\eta^{\text{jet}}$ - and  $x_\gamma^{\text{jets}}$ -distribution) for the MC simulation which includes multiple interactions (see last subsection). But again, we do not know whether the same is true when the pedestal subtraction method is applied to the data.

In the following, we want to describe two alternative “correction” methods, which

aim to improve the Monte Carlo description of the data by applying additional cuts to the data and MC samples (for the rest of this section, we again refer to the final data and MC samples as described in section 5.5, *i.e.*, the data and MC samples *before* the previously described pedestal subtraction). Since the MC simulation which includes multiple interactions describes the data better than the MC simulation without additional interactions, we concentrate on the former.

The first possibility found to improve the MC description of the data is to cut on the transverse energy flow not associated to the hard process. As an example for such a quantity, the distribution of  $(E_{t,1}^{\text{jet}} + E_{t,2}^{\text{jet}})/E_{t,\text{event}}$  for data and MC is shown in figure 6.16.

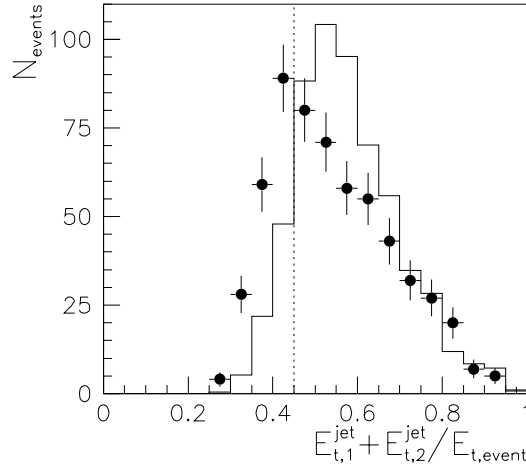


Figure 6.16:  $(E_{t,1}^{\text{jet}} + E_{t,2}^{\text{jet}})/E_{t,\text{event}}$ -distribution. Comparison of data (points) and MC (histogram; the MC is normalized to the integrated luminosity of the data sample). The MC sample used includes multiple interactions. The dotted line indicates the cut applied.

We apply the cut

$$\frac{E_{t,1}^{\text{jet}} + E_{t,2}^{\text{jet}}}{E_{t,\text{event}}} > 0.45 \quad (6.5)$$

to our final data and MC sample. This cut removes events where more than 55% of the total transverse energy flow is not due to the hard process. If multiple interactions are a source of transverse energy flow (which they definitely are for the MC sample), we remove events which have a large contribution to the total transverse energy flow due to these soft interactions.

Figure 6.17 shows the impact of the cut on  $(E_{t,1}^{\text{jet}} + E_{t,2}^{\text{jet}})/E_{t,\text{event}}$  for different bins in  $\eta^{\text{jet}}$ .

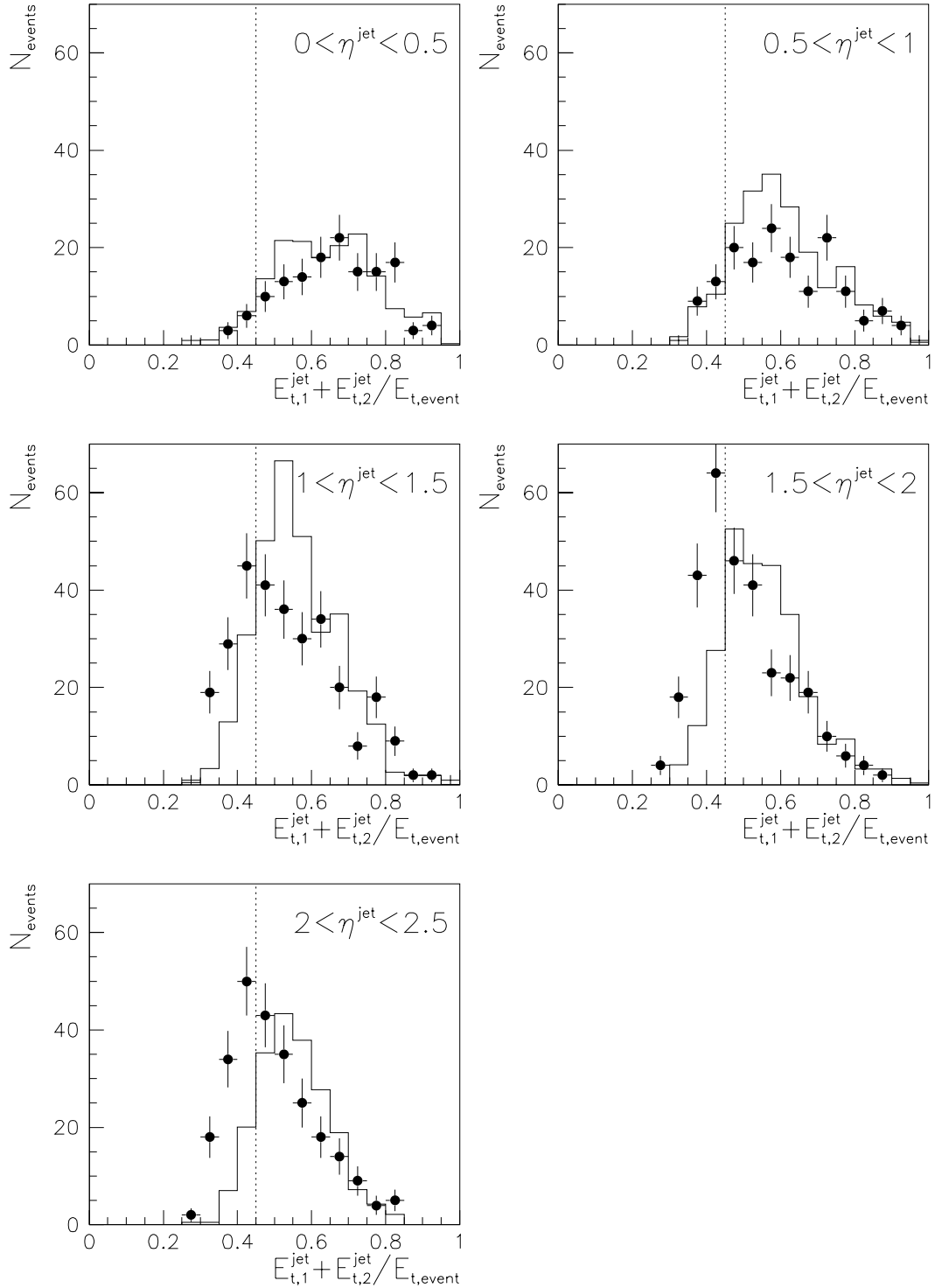


Figure 6.17:  $(E_{t,1}^{\text{jet}} + E_{t,2}^{\text{jet}})/E_{t,\text{event}}$ -distribution as a function of  $\eta^{\text{jet}}$ . Comparison of data (points) and MC (histogram; the MC is normalized to the integrated luminosity of the data sample). The MC sample used includes multiple interactions. The dotted line indicates the cut applied.

The cut dominantly removes events at large  $\eta^{\text{jet}}$  (or, equivalently, small  $x_\gamma^{\text{jets}}$ ) for both MC *and* data (small  $x_\gamma^{\text{jets}}$  implies large  $s_{\text{spectators}}$  and hence a possibly large energy flow due to multiple interactions, see section 6.4.1). Without the cut on  $(E_{t,1}^{\text{jet}} + E_{t,2}^{\text{jet}})/E_{t,\text{event}}$ , the MC simulation can fairly well describe the  $(E_{t,1}^{\text{jet}} + E_{t,2}^{\text{jet}})/E_{t,\text{event}}$ -distribution at small  $\eta^{\text{jet}}$  but fails for large  $\eta^{\text{jet}}$  (*i.e.*,  $\eta^{\text{jet}} \gtrsim 1$ ). After the cut  $(E_{t,1}^{\text{jet}} + E_{t,2}^{\text{jet}})/E_{t,\text{event}} > 0.45$  however, the description is reasonably good for large  $\eta^{\text{jet}}$ , too, at least when considering the shape of the  $(E_{t,1}^{\text{jet}} + E_{t,2}^{\text{jet}})/E_{t,\text{event}}$ -distribution. Note that a different parametrization of the parton density function for the photon may affect the  $\eta^{\text{jet}}$ -distribution and therefore also the absolute rates for the  $(E_{t,1}^{\text{jet}} + E_{t,2}^{\text{jet}})/E_{t,\text{event}}$ -distribution, *i.e.*, we do not necessarily expect a good description of the rates by the MC simulation, especially at large  $\eta^{\text{jet}}$  (low  $x_\gamma^{\text{jets}}$ ).

The jet-profiles in  $\varphi$  for data and MC after this cut on  $(E_{t,1}^{\text{jet}} + E_{t,2}^{\text{jet}})/E_{t,\text{event}}$  are given in figure 6.18.

The description of the data by the MC simulation has improved considerably (*cf.* figure 6.5)! Note, however, that a harder cut on  $(E_{t,1}^{\text{jet}} + E_{t,2}^{\text{jet}})/E_{t,\text{event}}$  improves the description in the pedestal region even further but worsens it for  $|\varphi^{\text{cell}} - \varphi^{\text{jet}}| \lesssim 1$ , *i.e.*, within the jet-core (not shown).

Additionally, the  $E_t^{\text{pedestal}}$ -distribution after the cut on  $(E_{t,1}^{\text{jet}} + E_{t,2}^{\text{jet}})/E_{t,\text{event}}$  is shown in figure 6.19.

The Monte Carlo simulation describes the  $E_t^{\text{pedestal}}$ -distribution reasonably well, at least much better than before the cut on  $(E_{t,1}^{\text{jet}} + E_{t,2}^{\text{jet}})/E_{t,\text{event}}$  (*cf.* figure 6.9).

We may try to explain why the Monte Carlo description improves when cutting on  $(E_{t,1}^{\text{jet}} + E_{t,2}^{\text{jet}})/E_{t,\text{event}}$ . We give two possible alternatives:

- The cut removes “wrong” events, *i.e.*, events which are not due to hard photoproduction processes. The remaining events are well described by the MC simulation which includes multiple interactions.

Since the cut mainly removes events from the data sample, such an explanation is possible. However, the fact that some distributions reflect a clear 2-jet structure (*e.g.*  $|\varphi_1^{\text{jet}} - \varphi_2^{\text{jet}}| \approx \pi$ ,  $|p_{t,1}^{\text{jet}} - p_{t,2}^{\text{jet}}|$  small) does not make this explanation very convincing.

- The cut removes events where the additional energy flow in the event due to *e.g.* soft interactions is large and hence the shift in  $E_t^{\text{jet}}$  towards too large values as compared to  $p_t^{\text{parton}}$  severe. Without this large additional energy flow, the jet energy  $E_t^{\text{jet}}$  would not have been above the threshold of 6 GeV. For the remaining data and MC events, the additional energy flow within the jet-core is equal for both samples. Note that we hereby ignore the possibility that a “proper” hard photoproduction event (*i.e.*, parton energies above  $\approx 6$  GeV) is overlaid with an additional large energy flow due to multiple soft interactions and hence removed from the sample. This latter contribution to

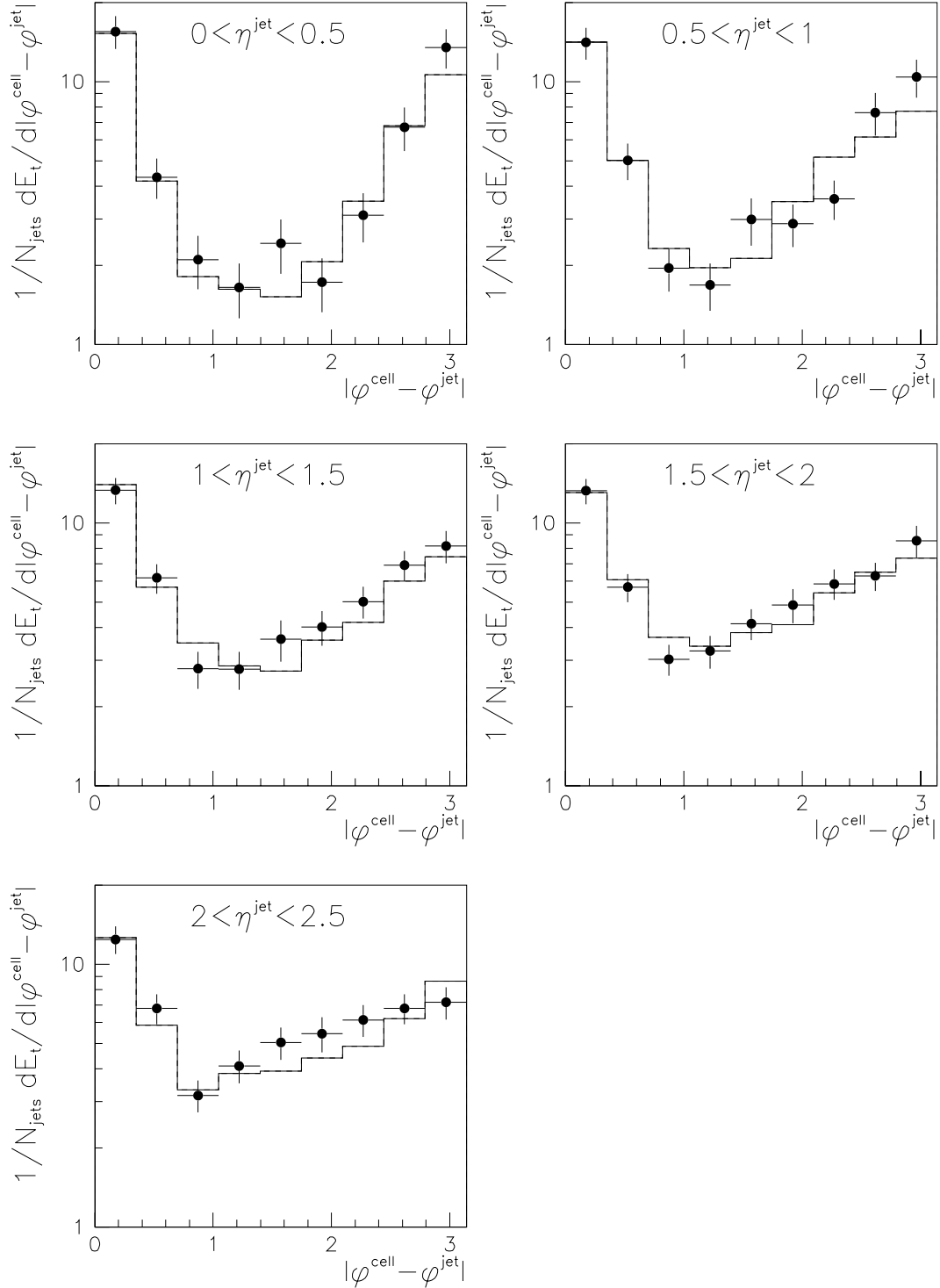


Figure 6.18: Jet-profiles in  $\varphi$  as a function of  $\eta^{\text{jet}}$  after the cut on  $(E_{t,1}^{\text{jet}} + E_{t,2}^{\text{jet}})/E_{t,\text{event}}$ . Jets are selected with  $6 \text{ GeV}/c < p_t^{\text{jet}} < 8 \text{ GeV}/c$ . Data (points) is compared with a Monte Carlo simulation that includes multiple interactions (full histogram).

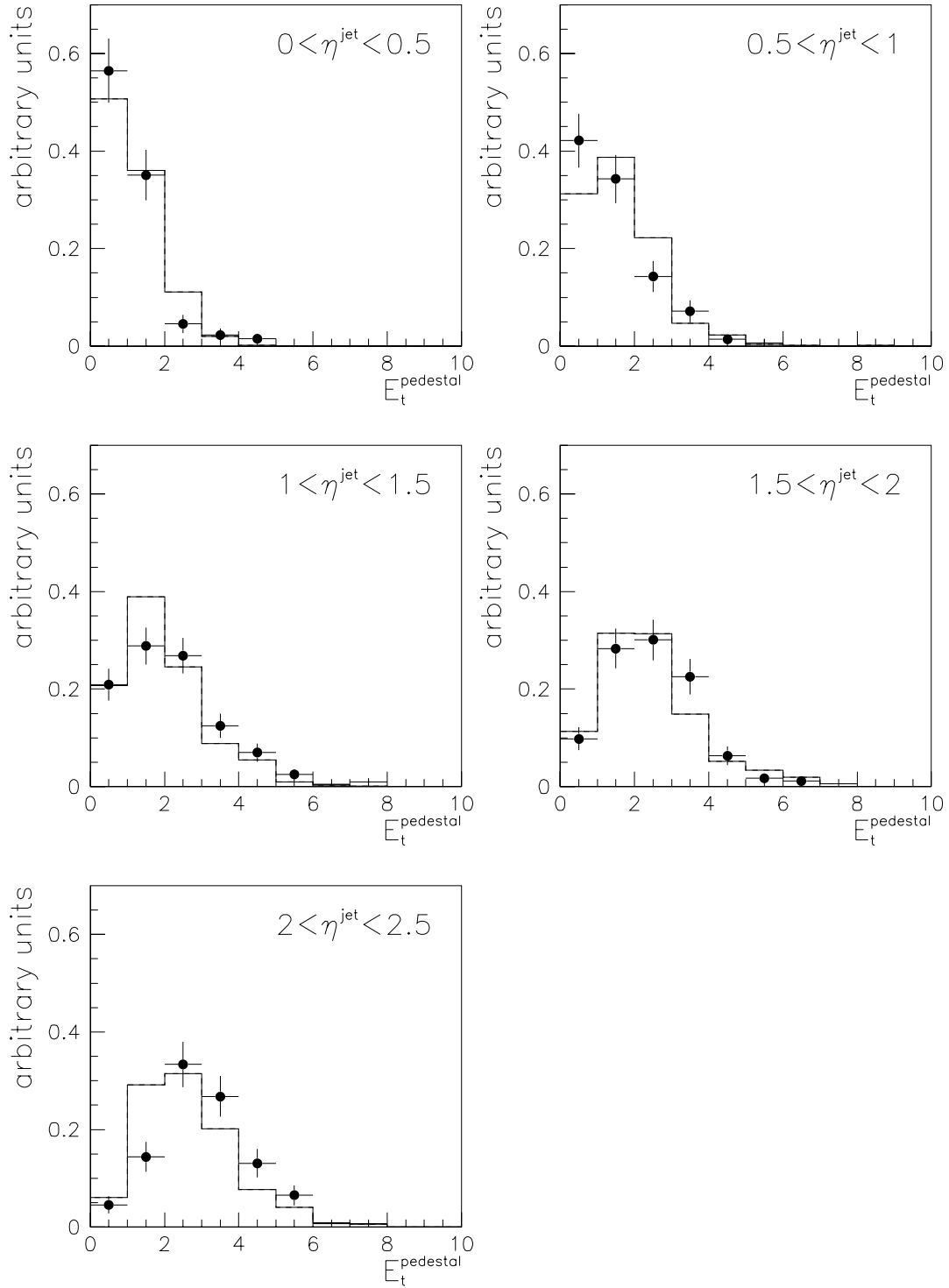


Figure 6.19:  $E_t^{\text{pedestal}}$ -distribution as a function of  $\eta^{\text{jet}}$  after the cut on  $(E_{t,1}^{\text{jet}} + E_{t,2}^{\text{jet}})/E_{t,\text{event}}$ . Comparison of data (points) and MC (histogram). The MC sample used includes multiple interactions. The distributions are normalized to unit area.

the rejected events would call for a correction factor to account for the different cut-efficiency for data and MC. Because of the steeply falling distribution  $d\sigma/dp_t^{\text{jet}}$ , we however expect that the events removed from the sample “by mistake” only account for a small fraction of the rejected events<sup>8</sup>. In other words, we assume that the efficiency of the cut  $(E_{t,1}^{\text{jet}} + E_{t,2}^{\text{jet}})/E_{t,\text{event}} > 0.45$  for hard photoproduction events (*i.e.*, parton energies above  $\approx 6$  GeV) is large and equal for data and MC.

The explanation above suggests that the cut on  $(E_{t,1}^{\text{jet}} + E_{t,2}^{\text{jet}})/E_{t,\text{event}}$  removes similar events from the data and MC samples as does the pedestal subtraction method described in the last subsection. Some differences between the two methods however exist. The cut on  $(E_{t,1}^{\text{jet}} + E_{t,2}^{\text{jet}})/E_{t,\text{event}}$  only rejects events with a *large* additional energy flow, whereas the pedestal subtraction method corrects for all additional energy flow due to *e.g.* multiple soft interactions by subtraction of an average additional pedestal energy  $\Delta E_t^{\text{pedestal}}$  as a function of  $\eta^{\text{jet}}$ . Hence, events with very large additional energy flow are removed by the  $(E_{t,1}^{\text{jet}} + E_{t,2}^{\text{jet}})/E_{t,\text{event}}$ -cut, but may survive the pedestal subtraction procedure as can be seen in figure 6.20.

Note that figure 6.20 points to a problem for the final, pedestal subtracted samples, namely that the  $(E_{t,1}^{\text{jet}} + E_{t,2}^{\text{jet}})/E_{t,\text{event}}$ -distribution is not well described by the Monte Carlo simulation (comparison of open triangles ( $\Delta$ ) in figures 6.20, a) and b)). This difference could be due to a wrong parametrization of the parton density function for the photon, hence we need to check the description of the shape for different bins in  $\eta^{\text{jet}}$  ( $x_\gamma^{\text{jets}}$ ). The description of the  $(E_{t,1}^{\text{jet}} + E_{t,2}^{\text{jet}})/E_{t,\text{event}}$ -distribution for large  $\eta^{\text{jet}}$  is somewhat worse for the pedestal subtracted sample than for the sample obtained when cutting on  $(E_{t,1}^{\text{jet}} + E_{t,2}^{\text{jet}})/E_{t,\text{event}} > 0.45$ , especially at small  $(E_{t,1}^{\text{jet}} + E_{t,2}^{\text{jet}})/E_{t,\text{event}}$  (not shown). This is probably due to the repeatedly mentioned fact that the pedestal subtraction method does not take into account large fluctuations of the additional energy flow due to *e.g.* multiple interactions, whereas the cut  $(E_{t,1}^{\text{jet}} + E_{t,2}^{\text{jet}})/E_{t,\text{event}} > 0.45$  does. For small  $\eta^{\text{jet}}$ , the description of the  $(E_{t,1}^{\text{jet}} + E_{t,2}^{\text{jet}})/E_{t,\text{event}}$ -distribution is good for both samples.

To sum up, the cut  $(E_{t,1}^{\text{jet}} + E_{t,2}^{\text{jet}})/E_{t,\text{event}} > 0.45$ , which reduces our final data and MC samples of 579 and 1075 (580) events to 399 and 940 (505), respectively, improves the Monte Carlo description of quantities sensitive to an additional transverse energy flow due to *e.g.* multiple interactions (*i.e.*, jet-profiles,  $E_t^{\text{pedestal}}$ -distribution and  $(E_{t,1}^{\text{jet}} + E_{t,2}^{\text{jet}})/E_{t,\text{event}}$ -distribution) considerably. However, the description is not perfect. Despite the above-mentioned uncertainties and limitations, we assume that the

---

<sup>8</sup>Both extreme cases, *i.e.*, the possibility that all rejected events would not have reached the threshold for the jet energy without the large additional energy flow as well as the more unlikely possibility that all events are removed “by mistake” have been compared by checking the description of the shape of different data distributions which should not be affected by the choice of the parton density function parametrization for the photon. However, no significant difference between the two extreme cases can be seen. This notably holds for the jet-profiles in  $\varphi$  and for the  $E_t^{\text{pedestal}}$ -distributions as a function of  $\eta^{\text{jet}}$ .

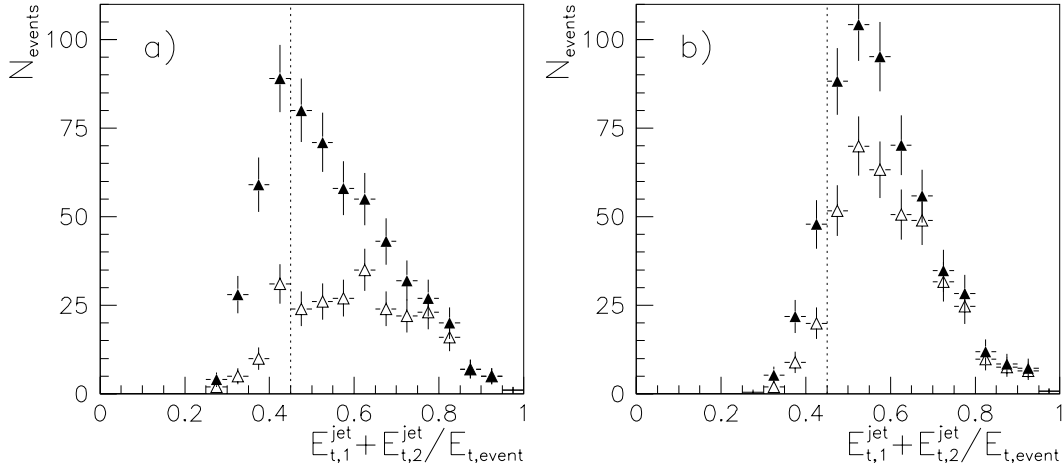


Figure 6.20:  $(E_{t,1}^{\text{jet}} + E_{t,2}^{\text{jet}})/E_{t,\text{event}}$ -distribution before ( $\blacktriangle$ ) and after ( $\triangle$ ) the pedestal subtraction. Shown are the distributions for the data sample (a)) and for the MC sample that includes multiple interactions (b)). The dotted lines indicate the cut at  $(E_{t,1}^{\text{jet}} + E_{t,2}^{\text{jet}})/E_{t,\text{event}} = 0.45$ . Note that the jet energies used for the determination of  $(E_{t,1}^{\text{jet}} + E_{t,2}^{\text{jet}})/E_{t,\text{event}}$  are the uncorrected ones for the pedestal subtracted samples.

cut  $(E_{t,1}^{\text{jet}} + E_{t,2}^{\text{jet}})/E_{t,\text{event}} > 0.45$  is a reasonable alternative to the pedestal subtraction method to “correct” for the poor description of the data by the MC simulation. We will use this alternative energy flow correction method to estimate the systematic error of the results obtained with the final, pedestal subtracted data and MC samples. We expect the same results for large  $x_\gamma$  since both correction methods have their main impact at small  $x_\gamma^{\text{jet}}$ s or, equivalently, large  $\eta^{\text{jet}}$  and hence a possible systematic difference should only show up at small  $x_\gamma$ .

The second alternative to improve the Monte Carlo description of the data is suggested by the following idea [88]. If multiple interactions do exist in our data sample, we assume that the  $k_\perp$ -algorithm often clusters together jets due to the hard parton parton scattering and energy concentrations originating from soft multiple interactions independently, before eventually merging them to a larger “jet”. Hence, we need to resolve the jet-structure to prevent such a “late” clustering of jets and “energy lumps” due to soft interactions. This can be done by setting  $\delta_{\text{cut}}$  to a value smaller than unity (see section 4.3). To explore this idea, we repeat the jet-finding (see section 5.5) with the following parameters for the  $k_\perp$ -algorithm (*cf.* equations (5.4) and (5.5)):

$$d_{\text{cut}} = 6^2 \text{ GeV}^2/c^2 \quad (6.6)$$

$$\delta_{\text{cut}} = 0.05 \quad . \quad (6.7)$$

The value  $\delta_{\text{cut}} = 0.05$  translates to a maximal relative transverse momentum (small

angle limit) of the two sub-jets of  $\sqrt{0.05} \cdot 6 \text{ GeV}/c \approx 1.35 \text{ GeV}/c$ , *i.e.*, objects with a distance  $d_{kl}$  larger than  $(1.35)^2 \text{ GeV}^2/c^2$  will not be merged. We ask for at least two hard final state jets to be found. We then again apply the cuts on  $\eta^{\text{jet}}$  (*cf.* equations (5.6) and (5.7)) and ask for more than  $6 \text{ GeV}/c$  transverse momentum for the two  $p_t$ -leading sub-jets (henceforth called jets) to ensure a hard photoproduction process.

The jet-profiles in  $\varphi$  for the resulting data and MC samples, consisting of 121 and 327 (145) events, respectively (the reduction of events compared to the final samples is strongest at low  $x_\gamma^{\text{jets}}$ ), are depicted in figure 6.21.

Except for  $\eta^{\text{jet}} \lesssim 1$ , the description of the jet-profiles by the MC is very good! Note that the above procedure is not just a complicated way of selecting narrower and therefore harder jets (which would be the case for a cone-type algorithm when lowering the cone-radius) — a selection of harder jets (roughly the same statistics) does not lead to a comparable improvement in the description of the jet-profiles.

Additionally, we show the  $E_t^{\text{pedestal}}$ - and  $(E_{t,1}^{\text{jet}} + E_{t,2}^{\text{jet}})/E_{t,\text{event}}$ -distribution for the resulting samples in figures 6.22 and 6.23, respectively.

Both the  $E_t^{\text{pedestal}}$ - and the  $(E_{t,1}^{\text{jet}} + E_{t,2}^{\text{jet}})/E_{t,\text{event}}$ -distribution are fairly well described by the Monte Carlo simulation.

The major drawback of this energy flow correction method is that the statistics of the resulting data and MC samples are rather poor (only half the events compared to the pedestal subtracted samples). We may nevertheless use these samples for another estimation of the systematic errors of the results obtained with the two other energy flow correction methods described above (emphasis on small  $x_\gamma$  due to the problems for small  $\eta^{\text{jet}}$ ).

### 6.4.5 Choice of energy flow correction method

None of the energy flow correction methods described above is perfect. Common to all three methods is the fact that the results obtained are highly model-dependent.

The major drawbacks of the pedestal subtraction method and the imperfections of the two alternative energy flow correction methods have been discussed in the last subsection.

All three methods result in a better description of distributions sensitive to an additional transverse energy flow due to soft processes and they all give a reasonably good description of the jet properties and jet jet correlations (*cf.* section 6.1; not shown). The latter is not very surprising since this is already true for the final, uncorrected sample (see section 6.1). However, since the event reduction due to the different energy flow correction methods is more severe for the data than for the MC sample, the absolute prediction of the MC simulation (*i.e.*, the 2-jet rate) overshoots the 2-jet rate seen in the data and hence only the shape of the distributions are well described after applying the different corrections.

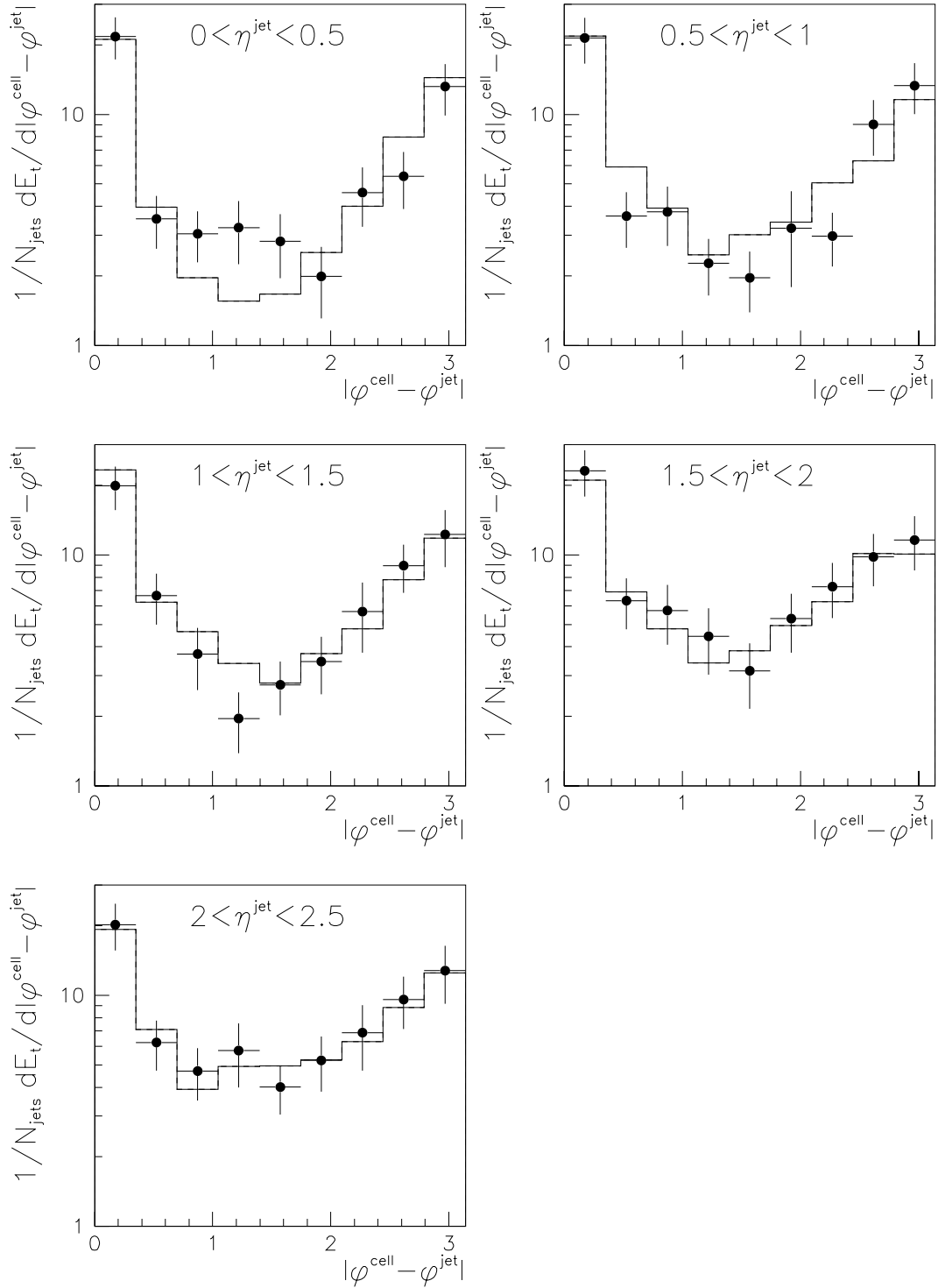


Figure 6.21: Jet-profiles in  $\varphi$  as a function of  $\eta^{\text{jet}}$  for  $\delta_{\text{cut}} = 0.05$ . Jets are selected with  $6 \text{ GeV}/c < p_t^{\text{jet}} < 8 \text{ GeV}/c$ . Data (points) is compared with a Monte Carlo simulation that includes multiple interactions (full histogram).

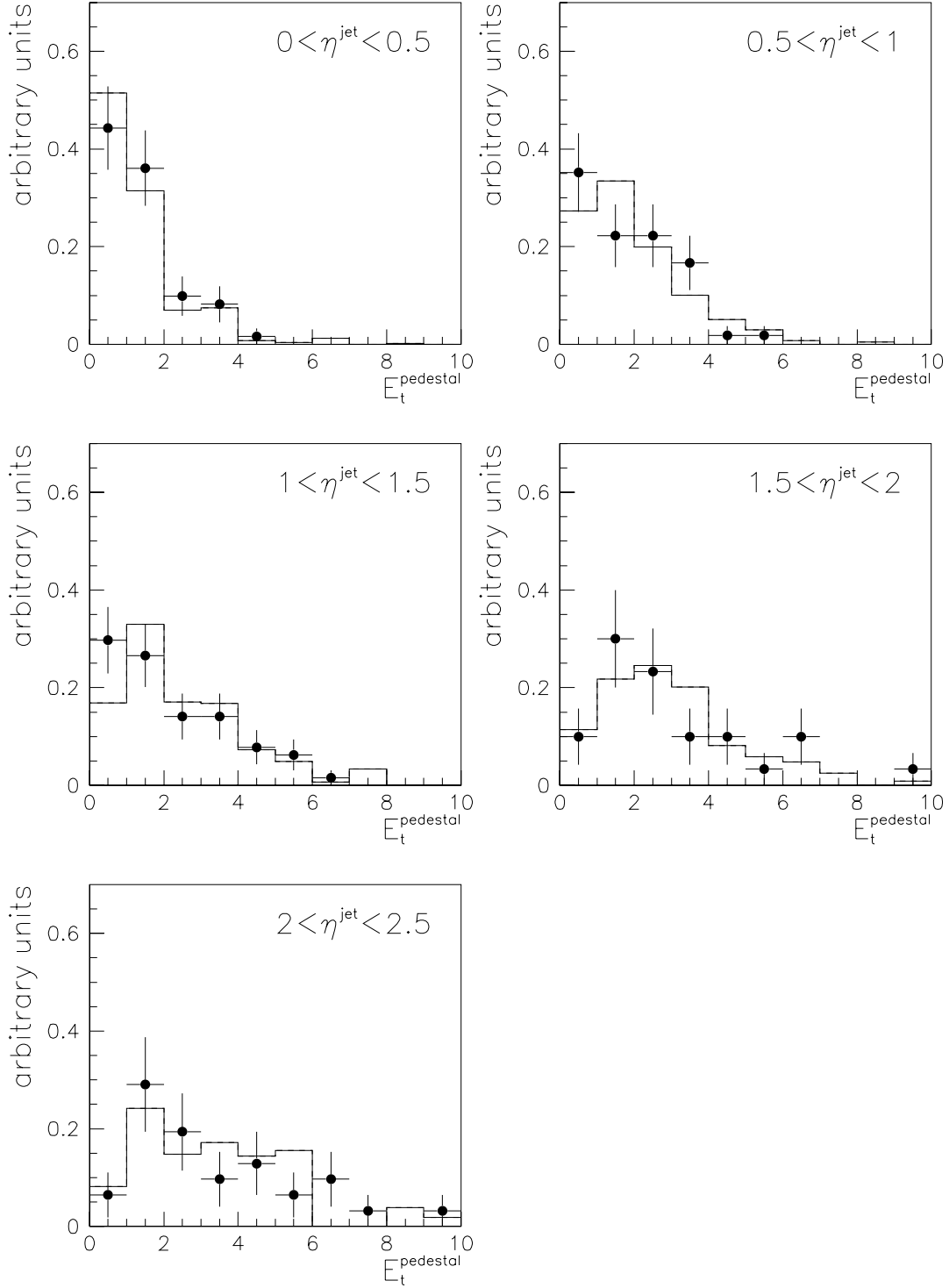


Figure 6.22:  $E_t^{\text{pedestal}}$ -distribution as a function of  $\eta^{\text{jet}}$  for  $\delta_{\text{cut}} = 0.05$ . Comparison of data (points) and MC (histogram). The MC sample used includes multiple interactions. The distributions are normalized to unit area.

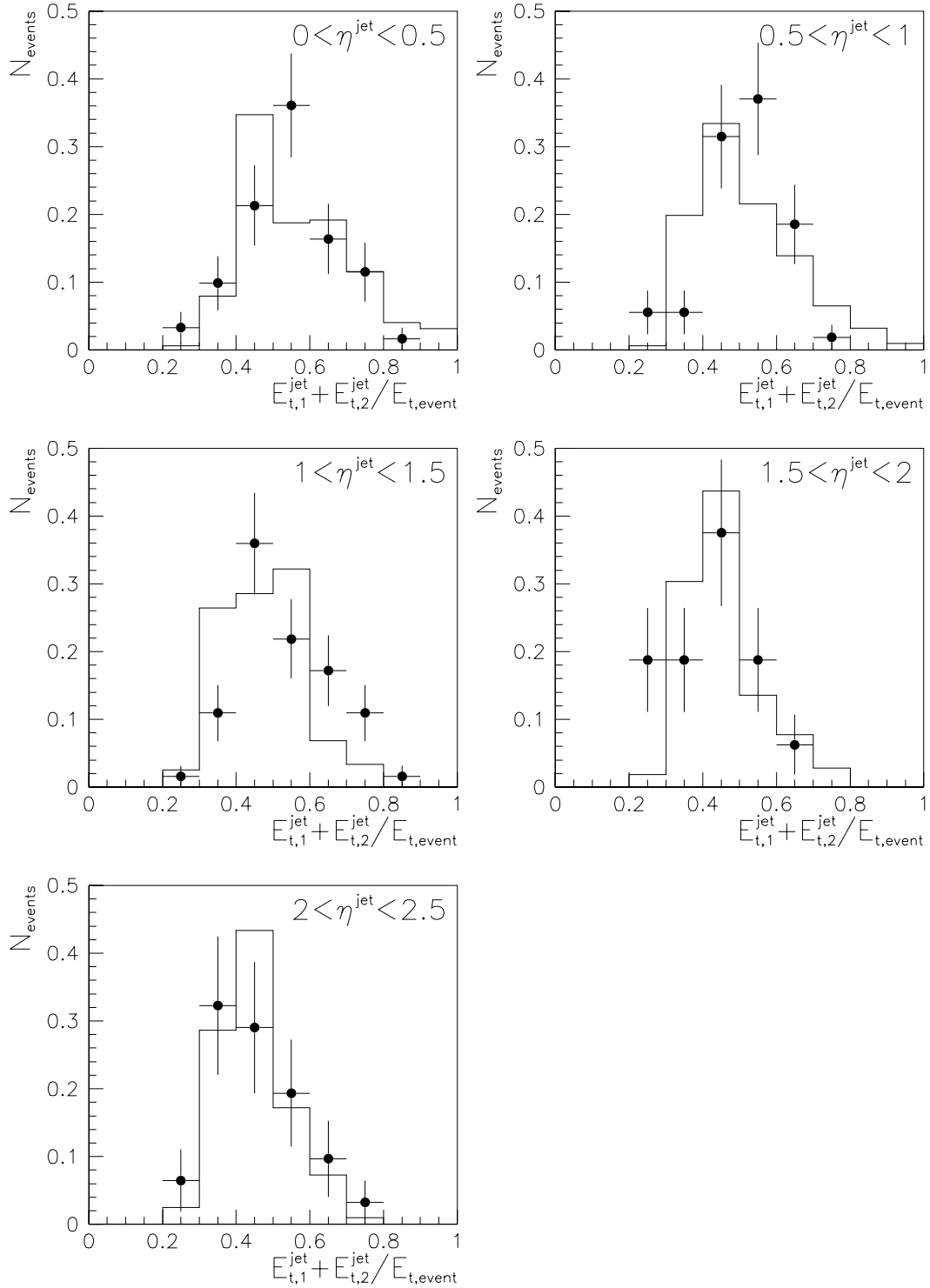


Figure 6.23:  $(E_{t,1}^{\text{jet}} + E_{t,2}^{\text{jet}})/E_{t,\text{event}}$ -distribution as a function of  $\eta^{\text{jet}}$  for  $\delta_{\text{cut}} = 0.05$ . Comparison of data (points) and MC (histogram; the MC is normalized to the integrated luminosity of the data sample). The MC sample used includes multiple interactions. The distributions are normalized to unit area.

---

We will use all three samples (*i.e.*, the pedestal subtracted sample, the “fluctuation reduced” sample — owing its name to the ability of the cut on  $(E_{t,1}^{\text{jet}} + E_{t,2}^{\text{jet}})/E_{t,\text{event}}$  to remove events with a large additional energy flow due to *e.g.* multiple interactions — and the “sub-jet” sample) and regard the difference in the results obtained with the three samples as a measure of the systematic error introduced by the three energy flow correction methods.

# Chapter 7

## Measurement of $d\sigma/dp_t$ , $d\sigma/d\eta$ and $f_{g/\gamma}(x_\gamma)$

The aim of this analysis is to measure quantities which are sensitive to the partonic structure of the (quasi-real) photon, *i.e.*, the parton density functions of the photon. As discussed in sections 1.2.3 (particularly section 1.2.3.3) and 6.1, inclusive parton cross-sections such as  $d\sigma/dp_t$  and  $d\sigma/d\eta$  are such quantities. The different parametrizations for the parton density functions of the photon mainly influence the absolute value of  $d\sigma/dp_t$  and  $d\sigma/d\eta$  as well as the shape of the differential cross-section  $d\sigma/d\eta$ . Another quantity which is sensitive to the partonic structure of the photon is the  $x_\gamma$ -distribution in 2-jet events,  $dN_{\text{events}}/dx_\gamma$ .

To measure differential parton cross-sections such as  $d\sigma/dp_t$  and  $d\sigma/d\eta$  and to determine the  $x_\gamma$ -distribution in 2-jet events we have to rely on a Monte Carlo simulation which connects measured quantities ( $p_t^{\text{jet}}$ ,  $\eta^{\text{jet}}$  and  $x_\gamma^{\text{jets}}$ ) with the “true” quantities  $p_t^{\text{parton}}$ ,  $\eta^{\text{parton}}$  and  $x_\gamma$ . The MC simulation used for this purpose makes use of the event generator PYTHIA (see section 3.1). Since PYTHIA is based on leading order (LO) QCD matrix elements and higher orders are only included approximately by means of a parton shower model, we will determine leading order parton cross-sections. Consistently, the parton density functions of the photon extracted from the measured  $x_\gamma$ -distribution in 2-jet events will be a leading order parton density function (for the MC simulation, the leading order parametrization of Glück, Reya and Vogt (GRV-LO) is used for the parton density function of the photon).

The correlation between the measured quantities  $p_t^{\text{jet}}$ ,  $\eta^{\text{jet}}$  and  $x_\gamma^{\text{jets}}$  and the respective true values  $p_t^{\text{parton}}$ ,  $\eta^{\text{parton}}$  and  $x_\gamma$  has already been discussed in section 4.4. We will however repeat the correlation plots for  $p_t$ ,  $\eta$  and  $x_\gamma$  due to the following reasons:

- For the parton kinematics ( $p_t^{\text{parton}}$  and  $\eta^{\text{parton}}$ ), the leading order quantities as given by the event generator are used. Hence, partons are balanced in transverse momentum.

- As input data for this investigation, the final MC sample after all selection cuts and after pedestal subtraction (see section 6.4.3) is used. Similar results are found for the final, fluctuation reduced sample and for the final sub-jet sample (see section 6.4.4).

The jet parton correlation for  $p_t$  and  $\eta$  and the correlation between  $x_\gamma^{\text{jets}}$  and  $x_\gamma$  is shown in figures 7.1 and 7.2, respectively.

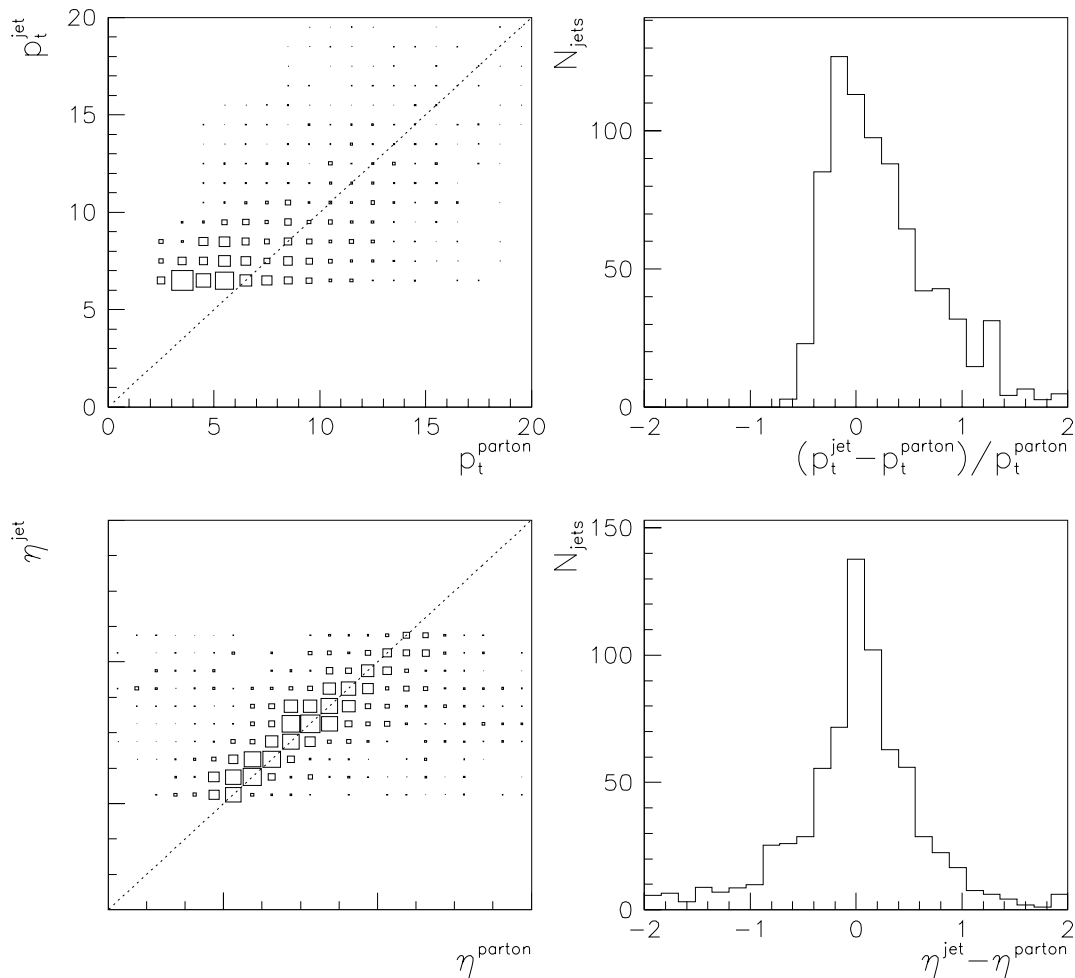


Figure 7.1: Jet parton correlation (LO) for  $p_t$  and  $\eta$ .

The somewhat poor correlation in  $p_t$  and  $x_\gamma$  asks for an unfolding procedure which extracts the true values  $p_t^{\text{parton}}$  and  $x_\gamma$  from the measured quantities  $p_t^{\text{jet}}$  and  $x_\gamma^{\text{jets}}$  rather than simply identify  $p_t^{\text{jet}} \approx p_t^{\text{parton}}$  and  $x_\gamma^{\text{jets}} \approx x_\gamma$ , respectively. Such an unfolding procedure will be described in the next section. The remaining two sections will then be devoted to the measurement of  $d\sigma/dp_t$  and  $d\sigma/d\eta$  and to the measurement of the gluon density function of the photon,  $f_{g/\gamma}(x_\gamma)$ , respectively.

Before we set off to measure the above-mentioned quantities which are pretended to be sensitive to the parton density functions of the photon, we demonstrate that

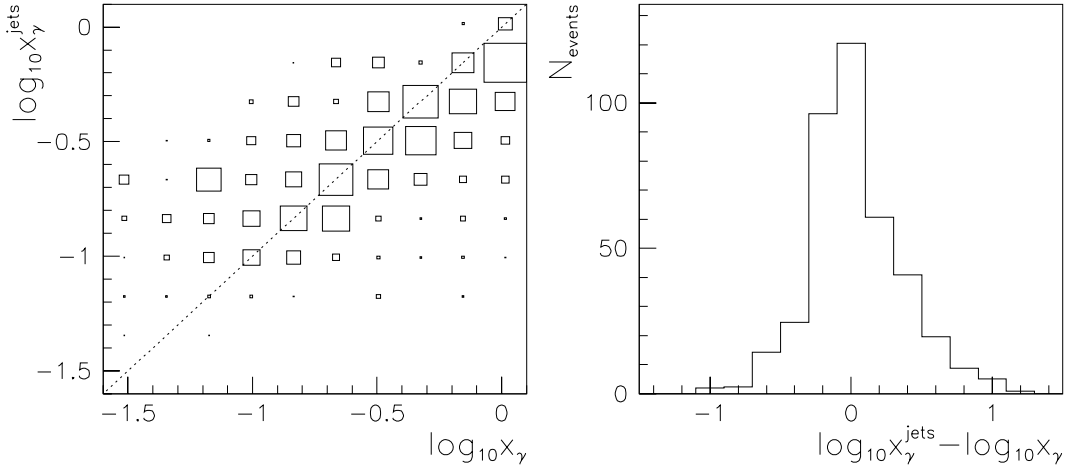


Figure 7.2: Correlation between  $x_\gamma^{\text{jets}}$  and  $x_\gamma$ .

resolved processes do actually contribute dominantly to our event samples. The contribution of resolved processes to the  $p_t^{\text{jet}}$ - and  $\eta^{\text{jet}}$ -distribution has already been discussed in section 6.1. Here, we concentrate on the  $x_\gamma^{\text{jets}}$ -distribution. The fact that the correlation plot for  $x_\gamma$  (cf. figure 7.2) does not only have entries for  $\log_{10}x_\gamma = 0$  already implies that we need resolved processes to describe our data. To emphasize the importance of the resolved contribution to the  $x_\gamma^{\text{jets}}$ -distribution, figure 7.3 shows the  $x_\gamma^{\text{jets}}$ -distribution seen in data in comparison to the  $x_\gamma^{\text{jets}}$ -distribution expected from the MC simulation. For the latter, the contributions due to direct and resolved processes are given separately. If not mentioned otherwise, we will henceforth always use the final, pedestal subtracted data and MC sample as an example for the three different, final samples (*i.e.*, the pedestal subtracted sample, the fluctuation reduced sample and the sub-jet sample) described in the last chapter. All results and conclusions obtained from the pedestal subtracted sample agree with the findings for the other two samples if not quoted differently.

The first observation is that we clearly need resolved processes to describe the observed  $x_\gamma^{\text{jets}}$ -distribution! Under the assumption that the absolute rate predicted by the Monte Carlo simulation is not totally off (next to leading order (NLO) corrections are estimated to be of the order of  $\lesssim 30\%$ , see section 6.1) and considering the fact that the quark content of the photon is already known fairly well from  $\gamma\gamma$  interactions, we can even state that we need direct processes to describe the  $x_\gamma^{\text{jets}}$ -distribution, too, although the data selection described in chapter 5 already rejected a substantial amount of events due to direct processes.

The question whether the gluon induced resolved processes (we will in the forthcoming always talk about gluons or quarks *from the photon*) are needed to explain the observed  $x_\gamma^{\text{jets}}$ -distribution or whether the quark induced resolved processes alone can account for the measured  $x_\gamma^{\text{jets}}$ -distribution will be the main topic of the last section of this chapter.

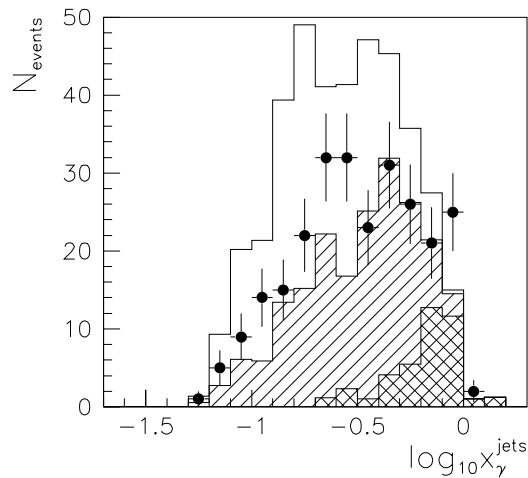


Figure 7.3:  $\log_{10}x_{\gamma}^{\text{jets}}$ -distribution. Comparison of data (points) and MC (histogram; the MC is normalized to the integrated luminosity of the data sample). The contributions to the  $x_{\gamma}^{\text{jets}}$ -distribution due to direct (double hatched) and resolved processes are given separately (MC only). The latter are further subdivided into processes initiated by a quark (single hatched) or a gluon (open histogram) from the photon. The final, pedestal subtracted samples are used.

We will now turn towards the description of the above-mentioned unfolding procedure.

## 7.1 Unfolding procedure

In a typical experiment, one wants to measure the distribution  $f(x)$  of some physical variable  $x$  (in our case *e.g.*  $d\sigma(p_t)/dp_t$  or  $f_{g/\gamma}(x_{\gamma})$ ). However, what one really determines is a (related) distribution  $g(y)$  of the actually measured quantity  $y$  (in our case  $dN_{\text{jets}}(p_t^{\text{jet}})/dp_t^{\text{jet}}$  and  $dN_{\text{events}}(x_{\gamma}^{\text{jets}})/dx_{\gamma}^{\text{jets}}$ ). The relation between  $f(x)$  and  $g(y)$  can be expressed by the following formula:

$$g(y) = \int A(x, y) f(x) dx + \epsilon(y) \quad . \quad (7.1)$$

$A(x, y)$  is called the response function and describes all effects that are common to most measurements:

- Transformation between the quantity  $x$  and the related quantity  $y$  (*e.g.* the transformation between  $x_{\gamma}$  and  $x_{\gamma}^{\text{jets}}$  as determined from the transverse momenta and the pseudo-rapidities of the two  $p_t$ -leading jets, *cf.* equation (4.15)).
- Limited acceptance of the detector and effects due to the selection of the data.

- Limited resolution of the measured quantity, *e.g.* due to the finite resolution of the detector or due to physical processes such as hadronization.

The response function  $A(x, y)$  is often given implicitly by a Monte Carlo simulation.  $\epsilon(y)$  describes the statistical fluctuations in the measured distribution  $g(y)$ . The above-given formula can be generalized even further, *e.g.* by introducing multidimensional variables or by adding a term  $b(y)$  for a possible background contribution to  $g(y)$ . We will however stick to this somewhat simplified formulation of the problem.

The unfolding procedure now has to determine  $f(x)$  from the measured distribution  $g(y)$ . Usually, measured distributions are given in histograms, *i.e.*, the variables  $x$  and  $y$  can be thought of as discrete variables. The integral of equation (7.1) then turns into a sum and we can write

$$g_i = \sum_j A_{ij} f_j + \epsilon_i \quad ; \quad i = 1 \dots n, \quad j = 1 \dots m \quad (7.2)$$

or short

$$\vec{g} = \mathbb{A} \vec{f} + \vec{\epsilon} \quad , \quad (7.3)$$

where  $g_i = g(y_i) \cdot \Delta_y$ ,  $f_j = f(x_j) \cdot \Delta_x$  and  $A_{ij} = A(x_j, y_i)$ . In case of a square matrix  $\mathbb{A}$  ( $n = m$ , *i.e.*, equal number of bins for  $x$  and  $y$ ), the solution for the unfolding problem is straightforward ( $\vec{f}_e$  is the estimator for the solution):

$$\vec{f}_e = \mathbb{A}^{-1} \vec{g} \quad . \quad (7.4)$$

This is called the “matrix inversion method”. Unfortunately, this simple solution to the unfolding problem is often unsatisfactory, since bin contents  $f_{e,j}$  of adjacent bins tend to vary strongly, *i.e.*, the result has a strongly oscillating behaviour (see *e.g.* [89, 90]). There are various more sophisticated procedures than the matrix inversion method (see *e.g.* [90] and references therein) which lead to more satisfactory results.

One such unfolding procedure [89, 91], which will be used for this analysis, is based on a regularization method (see *e.g.* [89, 90] and references therein). The main ingredients for this unfolding procedure are sketched below. For a detailed description of this “regularized unfolding method” see [89].

We start with two input distributions for the unfolding program, the data distribution  $g(y)$  and the corresponding Monte Carlo distribution  $g_{\text{MC}}(y)$ . The response function  $A(x, y)$  is taken from the Monte Carlo simulation, *i.e.*,  $A(x, y) = A_{\text{MC}}(x, y)$ . Hence, an accurate description of the response function by the Monte Carlo simulation is essential for a reliable unfolding.

We thus have (we neglect statistical errors for simplicity)

$$g(y) = \int A(x, y) f(x) dx \quad (7.5)$$

$$g_{\text{MC}}(y) = \int A(x, y) f_{\text{MC}}(x) dx \quad . \quad (7.6)$$

The data distribution  $g(y)$  and the Monte Carlo distribution  $g_{\text{MC}}(y)$  do not necessarily coincide and we therefore have to find a weight function  $f_w(x)$  such that the Monte Carlo distribution  $\tilde{g}_{\text{MC}}(y)$  derived from the reweighted input distribution  $\tilde{f}_{\text{MC}}(x) := f_{\text{MC}}(x)f_w(x)$  describes the data, *i.e.*,

$$g(y) \stackrel{!}{=} \tilde{g}_{\text{MC}}(y) := \int A(x, y) f_{\text{MC}}(x) f_w(x) dx \quad . \quad (7.7)$$

In the following, we will call  $\tilde{g}_{\text{MC}}(y)$  the “reweighted” Monte Carlo distribution. The main “*a priori*” input for the unfolding procedure used in this analysis is the assumption that the distribution  $f_w(x)$  is smooth. Therefore, it is assumed that the function  $f_w(x)$  can be described by a set of cubic B-splines (see *e.g.* [92]) and that its (local) curvature  $f_w''(x)/(1 + (f_w'(x))^2)^{3/2}$  is small in the entire  $x$ -region. Hence, the unfolding problem is solved by fitting a function  $f_w(x)$  (given by a finite superposition of cubic B-splines) to the data  $g(y)$ , where the relation between  $f_w(x)$  and  $g(y)$  is given by equation (7.7). The reweighted input distribution  $\tilde{f}_{\text{MC}}(x)$  is the result of the unfolding, *i.e.*, the estimator for  $f(x)$ .

The actual fit consists in the minimization of a negative log likelihood function  $-\ln L$ , where a regularization term is added to ensure for a smooth solution:

$$-\ln L = -\ln L_{\text{stat}} + \frac{1}{2}\tau R \quad ; \quad R = \int |f_w''(x)|^2 dx \quad . \quad (7.8)$$

The likelihood function  $L_{\text{stat}}$  thereby describes the probability that the observed data histogram  $g_i$  (the problem is again reformulated in a discrete way) is consistent with the fitted histogram  $(\tilde{g}_{\text{MC}}(\vec{\alpha}))_i$  with fit parameters  $\vec{\alpha}$  as follows. The measured bin content  $g_i$  of a histogram bin  $i$  follows a certain probability distribution  $l(g_i, \mu_i)$  of observing  $g_i$  given the “true” value  $\mu_i$  (*i.e.*, the Poisson distribution).  $L_{\text{stat}}$  then is the joint product of these probability distributions,  $L_{\text{stat}} = \prod_i l(g_i, \mu_i)$ , with  $\mu_i = (\tilde{g}_{\text{MC}}(\vec{\alpha}))_i$ . By minimizing  $-\ln L_{\text{stat}}$ , one finds the most likely parameter set  $\vec{\alpha}$ , *i.e.*, the best fit function. In our case, the fit function is  $\tilde{g}_{\text{MC}}(y; \vec{\alpha}) := \int A(x, y) f_{\text{MC}}(x) f_w(x; \vec{\alpha}) dx$  (*cf.* equation (7.7)) and the parameters  $\vec{\alpha}$  describe the superposition of the different cubic B-splines. For the explicit form of  $\ln L_{\text{stat}}$  see *e.g.* [89, 90].

The term  $R$  is the so called total curvature and is equal to the integrated local curvature squared (assuming  $|f_w'(x)| \ll 1$ ) and  $\tau$  is the regularization parameter. The results obtained by this unfolding procedure do not suffer from oscillations as do results obtained with the simple matrix inversion method described above.

Before we actually apply this unfolding procedure to our data, let's make some remarks on technical aspects of the unfolding program. The program for regularized unfolding [91] used for this analysis only allows for one variable to be unfolded, in other words, an unfolding of  $p_t^{\text{jet}}$  and  $\eta^{\text{jet}}$  at the same time is not possible. The binning (*i.e.*, (suggested) number of bins, position and bin size) of the unfolded variable is optimized for minimal bin-to-bin correlations (the resulting value for  $\tilde{f}_{\text{MC}}(x)$  is the average value for the respective bin) and the errors given represent the statistical errors of the data distribution  $g(y)$ .

To control the output of the unfolding program, two cross-checks can be performed:

- An explicit comparison of the data distribution  $g(y)$  with the “reweighted” distribution  $\tilde{g}_{\text{MC}}(y)$  allows to verify that the unfolding fit converged:  $g(y)$  and  $\tilde{g}_{\text{MC}}(y)$  have to coincide (*cf.* equation (7.7))!
- Since the unfolding program returns the results of the unfolding fit as a weight for every MC event ( $f_w(x)$ ), the following additional test can be made. Under the assumption that the unfolding procedure “corrected” for all possible deficiencies of the Monte Carlo description (*e.g.* by “correcting” for a wrong parton density function of the photon), *all* data distributions  $h(z)$  should be correctly described by the “reweighted” Monte Carlo distribution  $\tilde{h}_{\text{MC}}(z) := \int h_{\text{MC}}(z, x) f_w(x) dx$ . This can be checked by comparing other distributions than the one used for the unfolding, in our case *e.g.*  $\eta^{\text{jet}}$ ,  $|p_{t,1}^{\text{jet}} - p_{t,2}^{\text{jet}}|$ ,  $\eta_1^{\text{jet}} - \eta_2^{\text{jet}}$ ,  $|\varphi_1^{\text{jet}} - \varphi_2^{\text{jet}}|$ , *etc.*

The unfolded distribution  $\tilde{f}_{\text{MC}}(x)$  can only be considered physically reasonable if *both* checks give satisfactory results.

Note that we will differentiate between the *unfolded* distribution  $\tilde{f}_{\text{MC}}(x)$  (which represents the result for  $f(x)$ , hence we will mostly omit the  $\tilde{\phantom{x}}$  and the index “MC” for unfolded distributions) and the *reweighted* distribution  $\tilde{g}_{\text{MC}}(y)$ <sup>1</sup>. Other reweighted distributions not used for the unfolding fit, which allow to check the quality of the unfolding procedure (see above), will be called *reweighted* distributions, too.

## 7.2 Measurement of $d\sigma/dp_t$ and $d\sigma/d\eta$

The measurement of the inclusive parton cross-section  $d\sigma/dp_t$  is done in two steps. First, the  $p_t^{\text{jet}}$ -distribution in 2-jet events,  $dN_{\text{jets}}(p_t^{\text{jet}})/dp_t^{\text{jet}}$ , is unfolded to the corresponding leading order (LO) distribution for partons (*i.e.*, we use leading order parton quantities),  $dN_{\text{partons}}(p_t^{\text{parton}})/dp_t^{\text{parton}}$  (we henceforth identify  $p_t$  and  $\eta$  with  $p_t^{\text{parton}}$  and  $\eta^{\text{parton}}$ , respectively), *i.e.*, the unfolding corrects for the transformation and limited resolution (see above). To get the inclusive parton cross-section

<sup>1</sup> $\tilde{\phantom{x}}$  always refers to a “reweighted” *Monte Carlo* distribution. We will in the forthcoming suppress the index “MC”.

$d\sigma(p_t)/dp_t$ , this distribution is then scaled bin by bin with a factor that describes all losses due to the data selection (including acceptance of detector, efficiencies of triggers, jet-finding, *etc.*). This scaling factor  $r(p_t)$  is determined by means of a Monte Carlo simulation, *i.e.*, we use the ratio

$$r(p_t) = \frac{\text{number of partons generated } (p_t, \text{ kinematical range})}{\text{number of partons in final MC sample } (p_t)} \quad (7.9)$$

The kinematical range is thereby given by  $Q^2 < 0.01 \text{ GeV}^2$ ,  $0.25 < y < 0.7$  and  $0 < \eta < 2.5$ . Analogous cuts have been applied to the final data and MC samples by cutting on  $\vartheta_e < 0.3^\circ$ ,  $0.25 < y_{\text{tag}} < 0.7$  and  $0 < \eta^{\text{jet}} < 2.5$  (see chapter 5).

Note that we hereby determine the *inclusive* parton cross-section  $d\sigma/dp_t$ , *i.e.*, every parton fulfilling the above requirements is used for the calculation of the scaling factor  $r(p_t)$ .

The unfolding is performed by using the  $(p_t^{\text{jet}})^{1/2}$ -distribution rather than the  $p_t^{\text{jet}}$ -distribution. The reason for this is that the resulting, unfolded distribution produced by the unfolding program has bins of roughly equal size. To account for the limited statistics at large  $p_t^{\text{jet}}$ , we therefore use  $(p_t^{\text{jet}})^{1/2}$  as unfolding variable which results in somewhat larger bins at larger  $p_t$ . One may be tempted to use other functions of  $p_t^{\text{jet}}$  as unfolding variable which have an even stronger impact on the bin size in  $p_t$  (*e.g.*  $1/(p_t^{\text{jet}})^{1/2}$ ,  $1/p_t^{\text{jet}}$ , *etc.*). However, since the unfolded result is binned in between  $p_{t,\text{min}}$  and  $p_{t,\text{max}}$  as given by the  $p_t$ -distribution of the final MC sample (*i.e.*,  $p_t \gtrsim 2 \text{ GeV}/c$ ), the “uninteresting”  $p_t$ -range (*i.e.*,  $p_t \lesssim 6 \text{ GeV}/c$ ) becomes more and more important and the total number of bins in the interesting  $p_t$ -range smaller and smaller. Another advantage when unfolding the  $(p_t^{\text{jet}})^{1/2}$ -distribution rather than some other function of  $p_t^{\text{jet}}$  is that the error due to the resolution of the calorimeter,  $\sigma(\sqrt{E})$ , is constant as a function of  $\sqrt{E}$  (see section 2.2).

The determination of the inclusive parton cross-section  $d\sigma(\eta)/d\eta$  is similar to the procedure described above. Because the resolution in the transverse momentum  $p_t$  is worse than the resolution in the pseudo-rapidity  $\eta$  (*cf.* figure 7.1) and because the  $p_t$ -distribution  $d\sigma(p_t)/dp_t$  is steeply falling as a function of  $p_t$ , the inclusive differential parton cross-section  $d\sigma(\eta)/d\eta$  is determined by unfolding the  $(p_t^{\text{jet}})^{1/2}$ -distribution for three different bins in  $\eta$ . The  $p_t$ -integrated results ( $p_t > 6 \text{ GeV}/c$ ) then give the inclusive parton cross-section  $d\sigma(\eta)/d\eta$ .

Before we apply the above-sketched procedures to our final data samples, we prove that the unfolding<sup>2</sup> can reproduce the correct distributions. This is done by unfolding the  $(p_t^{\text{jet}})^{1/2}$ -distribution of a Monte Carlo sample and comparing the result  $d\tilde{\sigma}(p_t)/dp_t$  with the input distribution  $d\sigma(p_t)/dp_t$ . We use the final Monte Carlo sample without additional interactions as a toy model for data and the final, pedestal subtracted MC sample that includes multiple interactions as our

---

<sup>2</sup>We will in the forthcoming refer to the unfolding as both the unfolding step and the subsequent scaling.

MC sample. To account for the different  $\hat{p}_t$ -cut applied when generating the MC samples (see section 3.1), we apply the cut  $\hat{p}_t > 4 \text{ GeV}/c$  also to the final, pedestal subtracted MC sample. We show the unfolded  $d\tilde{\sigma}(p_t)/dp_t$ -distribution (*i.e.*,  $d\tilde{\sigma}(p_t)/dp_t = (d\sigma(p_t)/dp_t)_{\text{mi}} \cdot f_w(p_t)$ ) together with the input distribution  $(d\sigma(p_t)/dp_t)_{\text{non-mi}}$  in figure 7.4.

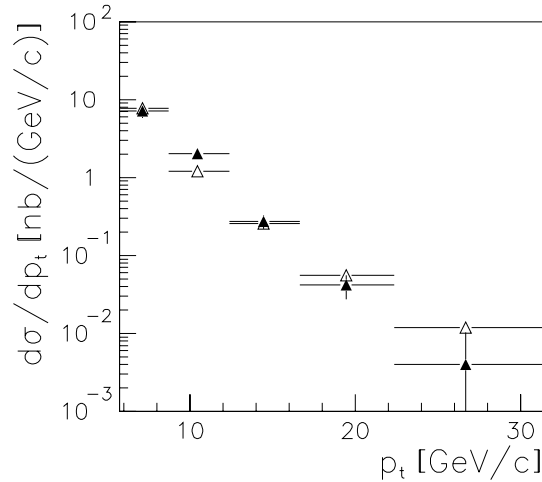


Figure 7.4:  $d\sigma(p_t)/dp_t$ -distribution. Comparison of the unfolded  $d\tilde{\sigma}(p_t)/dp_t$ -distribution ( $\blacktriangle$ ) with the input distribution  $d\sigma(p_t)/dp_t$  ( $\Delta$ ).

The unfolding procedure reproduces the input distribution reasonably well.

### 7.2.1 Determination of $d\sigma/dp_t$

For the determination of the inclusive parton cross-section  $d\sigma/dp_t$  we unfold the  $(p_t^{\text{jet}})^{1/2}$ -distribution for all three final data samples. For the correlation between  $p_t^{\text{jet}}$  and  $p_t$ , the respective final Monte Carlo samples are used.

To check that the result of the unfolding procedure can be trusted, we compare the  $(p_t^{\text{jet}})^{1/2}$ -distribution in the data with the reweighted  $(p_t^{\text{jet}})^{1/2}$ -distribution of the Monte Carlo simulation (see figure 7.5; we show the plots for the final, pedestal subtracted samples as an example).

The reweighted  $(p_t^{\text{jet}})^{1/2}$ -distribution describes the data well.

In addition, we check some other distributions to make sure that the unfolding procedure not only leads to a good description of the  $(p_t^{\text{jet}})^{1/2}$ -distribution (which is used for the unfolding fit), but also results in a good description of all other possible distributions. In figures 7.6 and 7.7, all jet properties and jet jet correlations already discussed in section 6.1 are shown for data and for the reweighted Monte Carlo sample (final, pedestal subtracted samples).

All distributions are reasonably well described by the reweighted distributions.

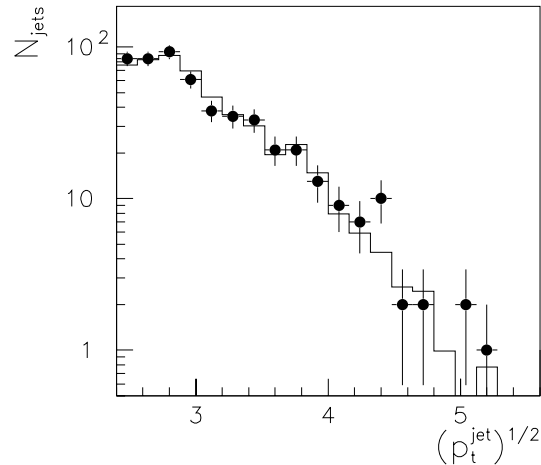


Figure 7.5:  $(p_t^{\text{jet}})^{1/2}$ -distribution. Comparison of the data distribution (points) with the reweighted Monte Carlo distribution (histogram). The MC is normalized to the integrated luminosity of the data sample. The final, pedestal subtracted samples are used.

The resulting inclusive parton cross-sections  $d\sigma/dp_t$  for the three final data samples are shown in figures 7.8–7.10 (see also tables 7.1–7.3). Additionally, the theoretical predictions (taken from the event generator PYTHIA) for different parametrizations of the parton density function for the photon are shown.

### 7.2.2 Determination of $d\sigma/d\eta$

As mentioned above, the inclusive parton cross-section  $d\sigma/d\eta$  is determined by unfolding the  $(p_t^{\text{jet}})^{1/2}$ -distribution for three different bins in  $\eta$ . The  $p_t$ -integrated results ( $p_t > 6 \text{ GeV}/c$ ) then represent the cross-section values for the three bins. This is done for all three final data samples. For the correlation between  $p_t^{\text{jet}}$  and  $p_t$ , the respective final Monte Carlo samples are used.

The unfolding is checked by examining the description of the  $(p_t^{\text{jet}})^{1/2}$ -distributions and other distributions not included for the unfolding fit, as was done above. We do however not show the plots again.

The inclusive parton cross-sections  $d\sigma/d\eta$  determined with the three final data samples are shown in figures 7.11–7.13 (see also tables 7.4–7.6) together with the theoretical predictions (taken from the event generator PYTHIA) for different parametrizations for the parton density function of the photon.

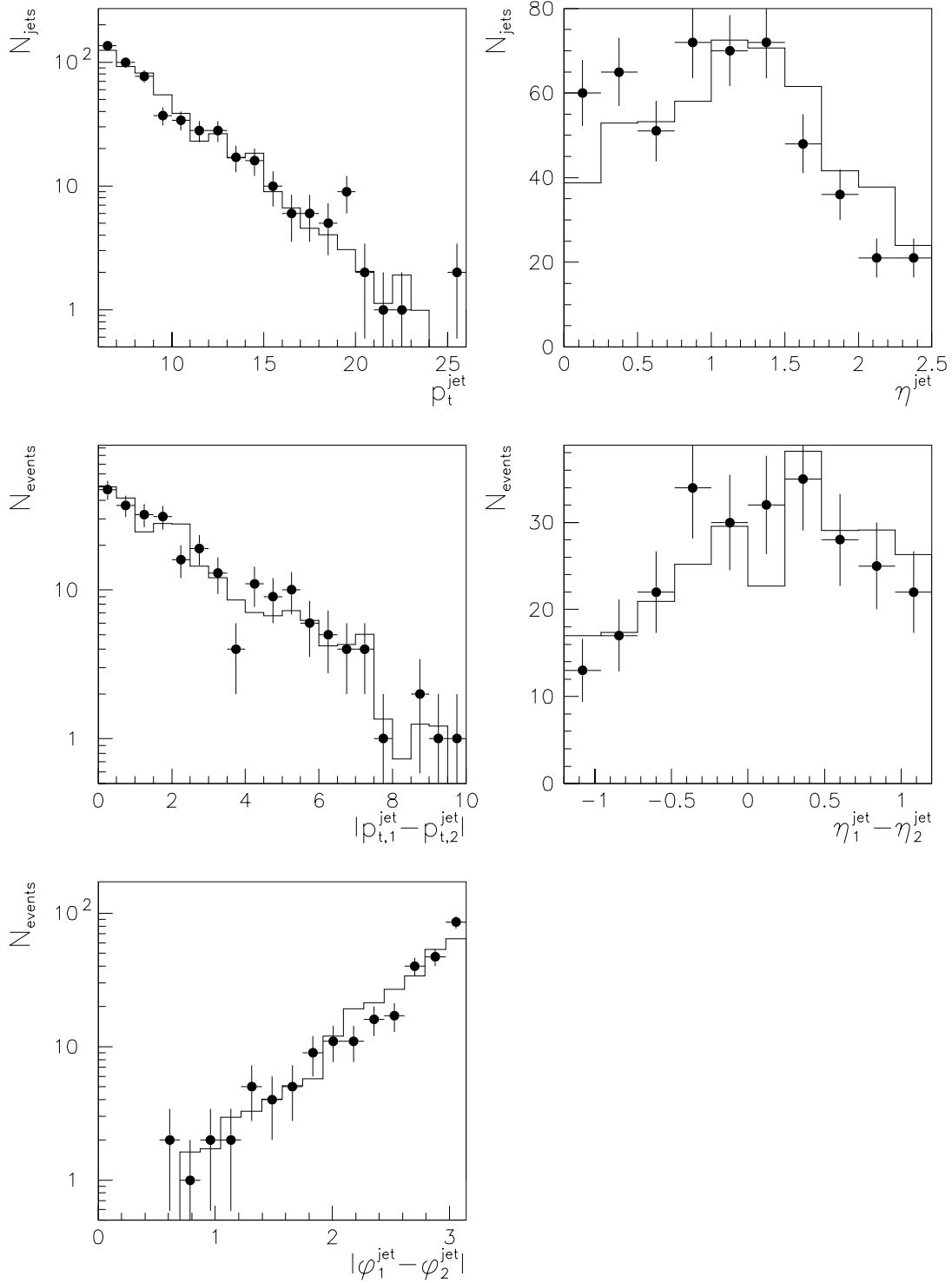


Figure 7.6:  $p_t^{\text{jet}}$ ,  $\eta^{\text{jet}}$ ,  $|p_{t,1}^{\text{jet}} - p_{t,2}^{\text{jet}}|$ ,  $\eta_1^{\text{jet}} - \eta_2^{\text{jet}}$  and  $|\varphi_1^{\text{jet}} - \varphi_2^{\text{jet}}|$  distribution. Comparison of data (points) and reweighted Monte Carlo distribution (histogram). The MC is normalized to the integrated luminosity of the data sample. The final, pedestal subtracted samples are used.

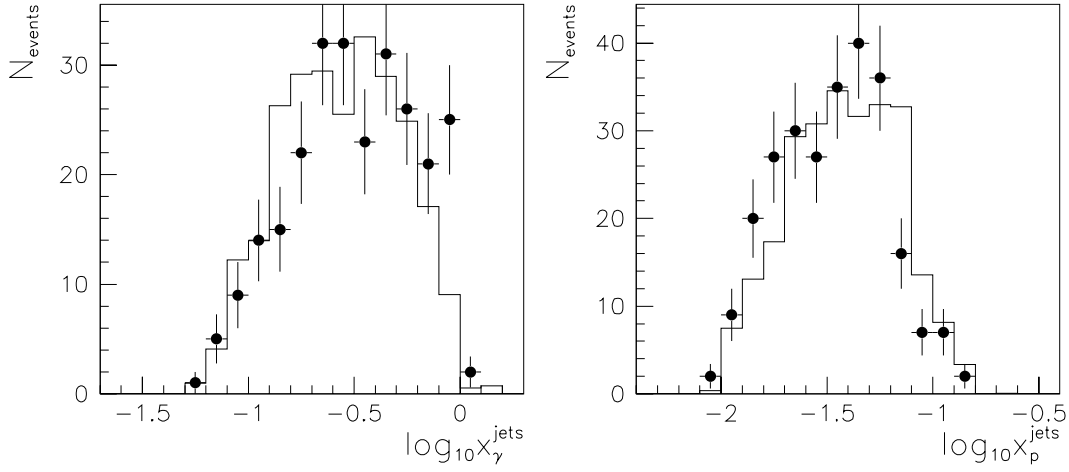


Figure 7.7:  $\log_{10}x_\gamma^{\text{jets}}$ - and  $\log_{10}x_p^{\text{jets}}$ -distribution. Comparison of data (points) and reweighted Monte Carlo distribution (histogram). The MC is normalized to the integrated luminosity of the data sample. The final, pedestal subtracted samples are used.

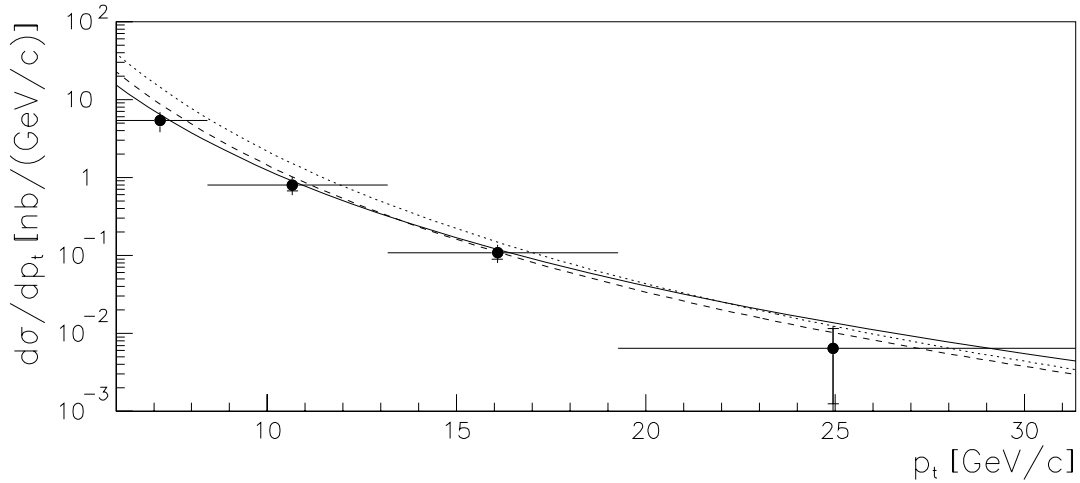


Figure 7.8: Inclusive parton cross-section  $d\sigma/dp_t$  in  $ep$  scattering versus the transverse momentum  $p_t$  for  $\sqrt{s_{ep}} = 296$  GeV,  $Q^2 < 0.01$  GeV<sup>2</sup>,  $0.25 < y < 0.7$  and  $0 < \eta < 2.5$  determined for the pedestal subtracted sample. Inner error-bars show statistical errors, whereas outer error-bars are the (square root of the) quadratic sum of statistical and systematic errors, thereby neglecting the systematic error  $\sigma_{\text{others}}$  of 29.5%. The unfolding is performed by means of a Monte Carlo simulation which is based on leading order (partonic) matrix elements (see text). Comparison with theoretical predictions using the parton density function parametrizations of the photon by Glück, Reya and Vogt (GRV-LO, full line) and Abramowicz, Charchuła and Levy (LAC I, dashed line; LAC III, dotted line).

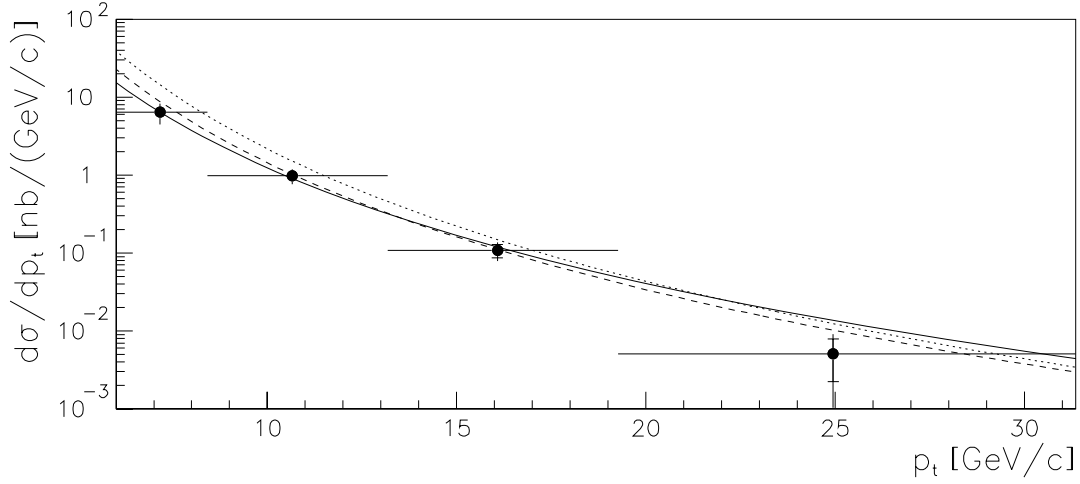


Figure 7.9: Inclusive parton cross-section  $d\sigma/dp_t$  in  $ep$  scattering versus the transverse momentum  $p_t$  for  $\sqrt{s_{ep}} = 296$  GeV,  $Q^2 < 0.01$  GeV<sup>2</sup>,  $0.25 < y < 0.7$  and  $0 < \eta < 2.5$  determined for the fluctuation reduced sample. Inner error-bars show statistical errors, whereas outer error-bars are the (square root of the) quadratic sum of statistical and systematic errors, thereby neglecting the systematic error  $\sigma_{\text{others}}$  of 29.5%. The unfolding is performed by means of a Monte Carlo simulation which is based on leading order (partonic) matrix elements (see text). Comparison with theoretical predictions using the parton density function parametrizations of the photon by Glück, Reya and Vogt (GRV-LO, full line) and Abramowicz, Charchuła and Levy (LAC I, dashed line; LAC III, dotted line).

### 7.2.3 Systematic errors

The results for the inclusive parton cross-sections  $d\sigma/dp_t$  and  $d\sigma/d\eta$  discussed in the last two subsections only include statistical errors. There are however a few sources of systematic uncertainty:

- Uncertainty of energy flow correction method:

We have used three different methods to correct for the deficiency of the Monte Carlo simulation to describe the energy flow measured in data. We will therefore use the difference of the results obtained with the three different methods as a measure of the systematic error introduced by each of the different methods. This systematic error additionally provides a measure of the systematic error due to the model-dependence of the three energy flow correction methods.

The obtained systematic error for  $d\sigma/d\eta$  is largest for large  $\eta$ , as expected from the fact that the deficiency of the MC simulation is most prominent at large  $\eta^{\text{jet}}$ .

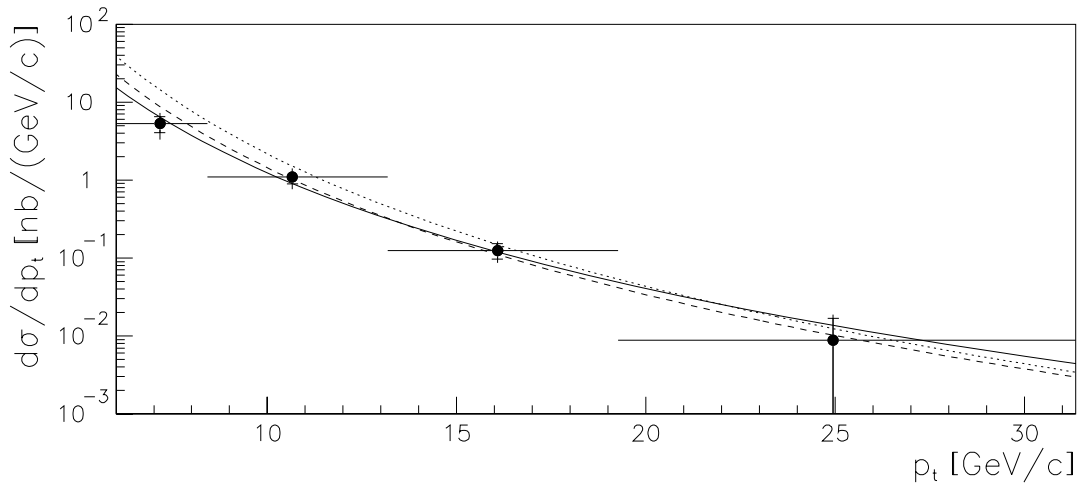


Figure 7.10: Inclusive parton cross-section  $d\sigma/dp_t$  in  $ep$  scattering versus the transverse momentum  $p_t$  for  $\sqrt{s_{ep}} = 296$  GeV,  $Q^2 < 0.01$  GeV<sup>2</sup>,  $0.25 < y < 0.7$  and  $0 < \eta < 2.5$  determined for the sub-jet sample. Inner error-bars show statistical errors, whereas outer error-bars are the (square root of the) quadratic sum of statistical and systematic errors, thereby neglecting the systematic error  $\sigma_{\text{others}}$  of 29.5%. The unfolding is performed by means of a Monte Carlo simulation which is based on leading order (partonic) matrix elements (see text). Comparison with theoretical predictions using the parton density function parametrizations of the photon by Glück, Reya and Vogt (GRV-LO, full line) and Abramowicz, Charchuła and Levy (LAC I, dashed line; LAC III, dotted line).

- Uncertainty in the absolute hadronic energy scale of 5%:  
The absolute hadronic energy scale as determined from studies of the transverse momentum energy balance in deep inelastic scattering events is known to a precision of 5%. To determine the possible systematic error due to this uncertainty, the entire analysis was repeated with rescaled cluster and cell energies ( $\pm 5\%$ , data only). The differences in the measured inclusive parton cross-sections  $d\sigma/dp_t$  and  $d\sigma/d\eta$  compared to the results described above are used as systematic errors,  $\sigma_{E\text{-scale}}$ .
- Uncertainty due to cuts on  $\eta$ ,  $y$  and  $Q^2$ :  
An additional systematic uncertainty is due to the cuts on  $\eta$ ,  $y$  and  $Q^2$ . The cuts applied to the final data and MC samples used for the unfolding of the  $(p_t^{\text{jet}})^{1/2}$ -distribution are  $0 < \eta^{\text{jet}} < 2.5$ ,  $0.25 < y_{\text{tag}} < 0.7$  and  $\vartheta_e < 0.3^\circ$  rather than  $0 < \eta < 2.5$ ,  $0.25 < y < 0.7$  and  $Q^2 < 0.01$  GeV<sup>2</sup> (correspondingly for the determination of  $d\sigma/d\eta$ ). To account for the possibly inaccurate correlation between  $p_t^{\text{jet}}$  and  $p_t$  due to these “smeared” cuts, an additional systematic error of 25%, determined from the observed migrations in  $\eta$ ,  $y$  and  $Q^2$  (Monte Carlo), is included.

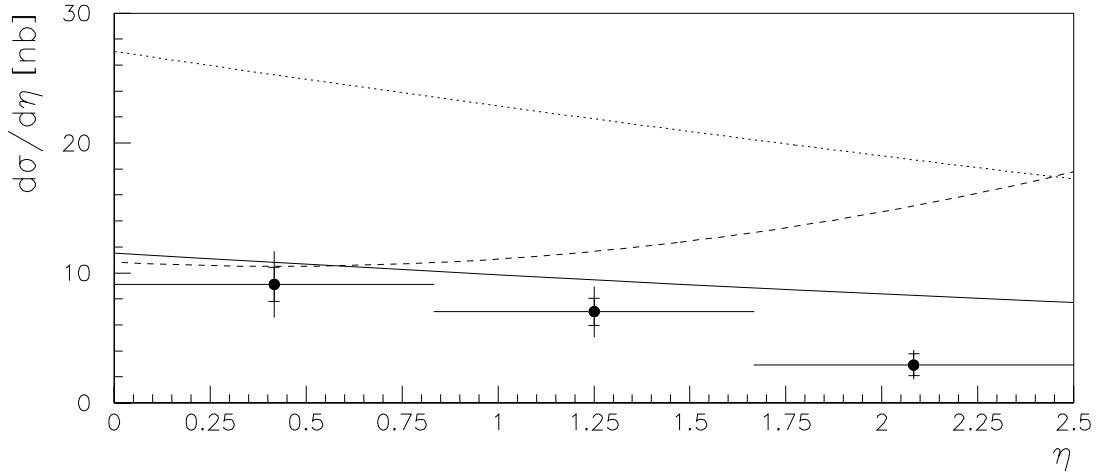


Figure 7.11: Inclusive parton cross-section  $d\sigma/d\eta$  in  $ep$  scattering versus the pseudorapidity  $\eta$  for  $\sqrt{s_{ep}} = 296 \text{ GeV}$ ,  $Q^2 < 0.01 \text{ GeV}^2$ ,  $0.25 < y < 0.7$  and  $p_t > 6 \text{ GeV}/c$  determined for the pedestal subtracted sample. Inner error-bars show statistical errors, whereas outer error-bars are the (square root of the) quadratic sum of statistical and systematic errors, thereby neglecting the systematic error  $\sigma_{\text{others}}$  of 29.5%. The unfolding is performed by means of a Monte Carlo simulation which is based on leading order (partonic) matrix elements (see text). Comparison with theoretical predictions using the parton density function parametrizations of the photon by Glück, Reya and Vogt (GRV-LO, full line) and Abramowicz, Charchuła and Levy (LAC I, dashed line; LAC III, dotted line).

For the inclusive parton cross-section  $d\sigma/dp_t$ , the systematic errors due to the uncertainty in the hadronic energy scale and the uncertainty because of the cuts on  $\eta$ ,  $y$  and  $Q^2$  are the most important ones. For the cross-section  $d\sigma/d\eta$ , the systematic uncertainty introduced by the different energy flow correction methods is of equal importance at small  $\eta$  and apparently is the dominant systematic error at large  $\eta$ .

Another minor systematic error is due to the uncertainty in the integrated luminosity of 4.5%. This systematic error, together with the systematic error related to the uncertainty due to the cuts on  $\eta$ ,  $y$  and  $Q^2$ , is included in the systematic error  $\sigma_{\text{others}}$ . A possible systematic error arising from the uncertainty in the parton density function of the *proton* is neglected, since the  $x_p^{\text{jets}}$ -distribution is reasonably well described by the Monte Carlo simulation after the reweighting (*cf.* figure 7.7).

Furthermore, it has been checked that the results do not depend on the parameters used for the unfolding program (*i.e.*, number of bins used for the input and result distributions, maximal number of B-splines used for the unfolding fit, *etc.*)<sup>3</sup> by varying the unfolding parameters. The different results for one energy flow correction

<sup>3</sup>The limited statistics of the final samples, especially the sub-jet sample, restrict the set of possible unfolding parameters considerably. Only a few unfolding parameters actually lead to reasonable results, that is, to a successful unfolding fit.

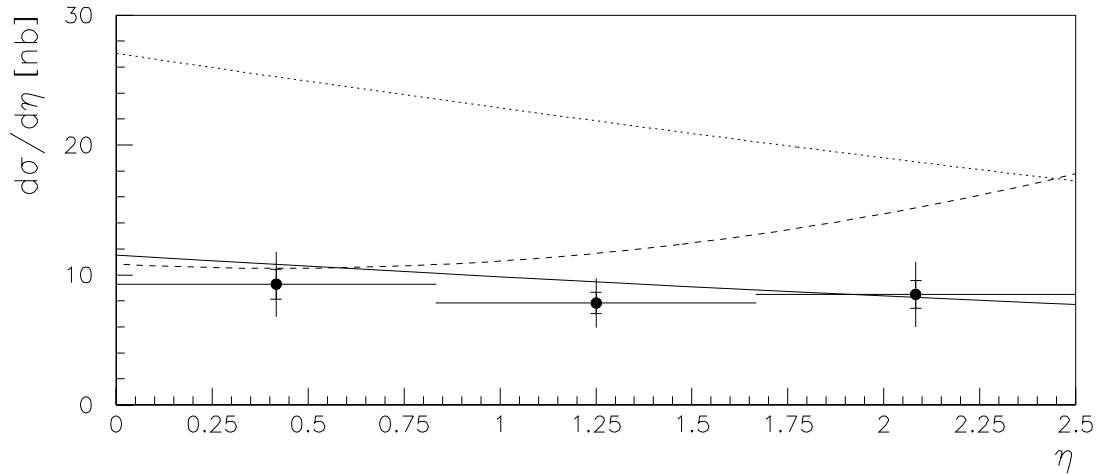


Figure 7.12: Inclusive parton cross-section  $d\sigma/d\eta$  in  $ep$  scattering versus the pseudorapidity  $\eta$  for  $\sqrt{s_{ep}} = 296 \text{ GeV}$ ,  $Q^2 < 0.01 \text{ GeV}^2$ ,  $0.25 < y < 0.7$  and  $p_t > 6 \text{ GeV}/c$  determined for the fluctuation reduced sample. Inner error-bars show statistical errors, whereas outer error-bars are the (square root of the) quadratic sum of statistical and systematic errors, thereby neglecting the systematic error  $\sigma_{\text{others}}$  of 29.5%. The unfolding is performed by means of a Monte Carlo simulation which is based on leading order (partonic) matrix elements (see text). Comparison with theoretical predictions using the parton density function parametrizations of the photon by Glück, Reya and Vogt (GRV-LO, full line) and Abramowicz, Charchuła and Levy (LAC I, dashed line; LAC III, dotted line).

method agree well, *i.e.*, the difference of the results is smaller than the statistical error.

No extra systematic error for the dependence of the result on the Monte Carlo simulation (*e.g.* multiple interaction model, parton shower model or hadronization) is given due to the lack of another MC sample that describes the data (reasonably) well. Part of this systematic error may already be contained in the systematic error obtained from the different energy flow correction methods.

The final results for the inclusive parton cross-sections  $d\sigma/dp_t$  and  $d\sigma/d\eta$  together with the statistical and systematic errors are shown in figures 7.8–7.10 and 7.11–7.13, respectively (see tables 7.1–7.3 and 7.4–7.6, too).

The measured cross-sections, especially the inclusive parton cross-section  $d\sigma/d\eta$ , favour a parton density function of the photon as predicted by the parametrization of Glück, Reya and Vogt (GRV-LO).

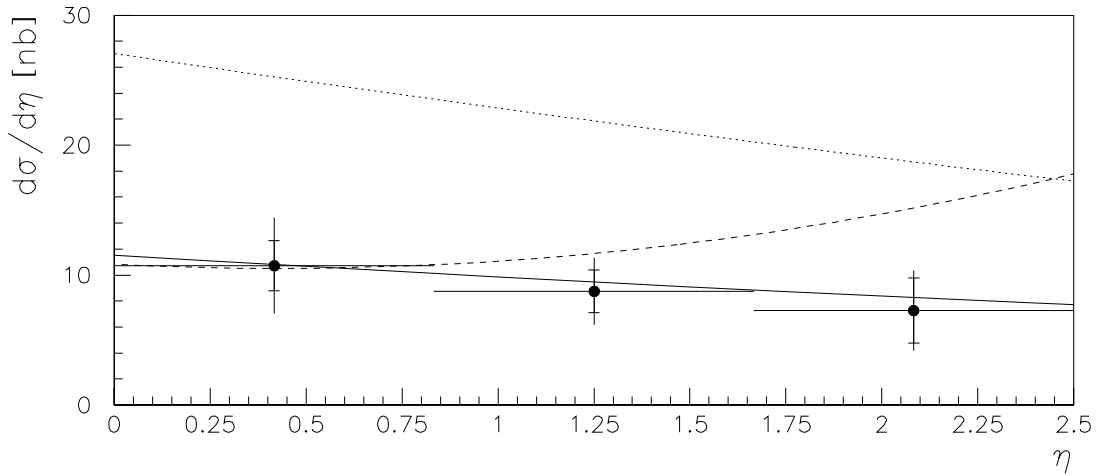


Figure 7.13: Inclusive parton cross-section  $d\sigma/d\eta$  in  $ep$  scattering versus the pseudorapidity  $\eta$  for  $\sqrt{s_{ep}} = 296 \text{ GeV}$ ,  $Q^2 < 0.01 \text{ GeV}^2$ ,  $0.25 < y < 0.7$  and  $p_t > 6 \text{ GeV}/c$  determined for the sub-jet sample. Inner error-bars show statistical errors, whereas outer error-bars are the (square root of the) quadratic sum of statistical and systematic errors, thereby neglecting the systematic error  $\sigma_{\text{others}}$  of 29.5%. The unfolding is performed by means of a Monte Carlo simulation which is based on leading order (partonic) matrix elements (see text). Comparison with theoretical predictions using the parton density function parametrizations of the photon by Glück, Reya and Vogt (GRV-LO, full line) and Abramowicz, Charchuła and Levy (LAC I, dashed line; LAC III, dotted line).

pedestal subtracted sample				
$p_t$ [GeV/ $c$ ]	7.16	10.66	16.08	24.95
$p_{t,\min}, p_{t,\max}$ [GeV/ $c$ ]	6.00 – 8.41	8.41 – 13.18	13.18 – 19.27	19.27 – 31.36
$d\sigma/dp_t$ [nb/(GeV/ $c$ )]	5.36	0.80	0.108	0.006
$\sigma_{\text{stat}}$ [nb/(GeV/ $c$ )]	0.66	0.13	0.019	0.005
$\sigma_{E\text{-scale}}$ [nb/(GeV/ $c$ )]	1.40	0.16	0.021	0.003
$\sigma_{\text{others}}$ [nb/(GeV/ $c$ )]	1.58	0.24	0.032	0.002
$\sigma_{\text{syst}}$ [nb/(GeV/ $c$ )]	2.11	0.29	0.038	0.004
$\sigma_{\text{tot}}$ [nb/(GeV/ $c$ )]	2.21	0.32	0.043	0.006

Table 7.1: Inclusive parton cross-section  $d\sigma/dp_t$  in  $ep$  scattering for  $\sqrt{s_{ep}} = 296$  GeV,  $Q^2 < 0.01$  GeV<sup>2</sup>,  $0.25 < y < 0.7$  and  $0 < \eta < 2.5$  together with its statistical and systematic errors determined for the pedestal subtracted sample.  $\sigma_{\text{syst}}$  is the combined total systematic error and  $\sigma_{\text{tot}}$  is the quadratic sum of the statistical and total systematic errors. The unfolding is performed by means of a Monte Carlo simulation which is based on leading order (partonic) matrix elements (see text).

fluctuation reduced sample				
$p_t$ [GeV/c]	7.16	10.66	16.08	24.95
$p_{t,\min}, p_{t,\max}$ [GeV/c]	6.00 – 8.41	8.41 – 13.18	13.18 – 19.27	19.27 – 31.36
$d\sigma/dp_t$ [nb/(GeV/c)]	6.36	0.98	0.107	0.005
$\sigma_{\text{stat}}$ [nb/(GeV/c)]	0.66	0.13	0.021	0.003
$\sigma_{E\text{-scale}}$ [nb/(GeV/c)]	1.78	0.17	0.020	0.003
$\sigma_{\text{others}}$ [nb/(GeV/c)]	1.88	0.29	0.032	0.001
$\sigma_{\text{syst}}$ [nb/(GeV/c)]	2.59	0.34	0.038	0.003
$\sigma_{\text{tot}}$ [nb/(GeV/c)]	2.67	0.36	0.043	0.004

Table 7.2: Inclusive parton cross-section  $d\sigma/dp_t$  in  $ep$  scattering for  $\sqrt{s_{ep}} = 296$  GeV,  $Q^2 < 0.01$  GeV<sup>2</sup>,  $0.25 < y < 0.7$  and  $0 < \eta < 2.5$  together with its statistical and systematic errors determined for the fluctuation reduced sample.  $\sigma_{\text{syst}}$  is the combined total systematic error and  $\sigma_{\text{tot}}$  is the quadratic sum of the statistical and total systematic errors. The unfolding is performed by means of a Monte Carlo simulation which is based on leading order (partonic) matrix elements (see text).

sub-jet sample				
$p_t$ [GeV/ $c$ ]	7.16	10.66	16.08	24.95
$p_{t,\min}, p_{t,\max}$ [GeV/ $c$ ]	6.00 – 8.41	8.41 – 13.18	13.18 – 19.27	19.27 – 31.36
$d\sigma/dp_t$ [nb/(GeV/ $c$ )]	5.26	1.09	0.124	0.009
$\sigma_{\text{stat}}$ [nb/(GeV/ $c$ )]	1.22	0.19	0.028	0.008
$\sigma_{E\text{-scale}}$ [nb/(GeV/ $c$ )]	1.52	0.27	0.025	0.006
$\sigma_{\text{others}}$ [nb/(GeV/ $c$ )]	1.55	0.32	0.037	0.003
$\sigma_{\text{syst}}$ [nb/(GeV/ $c$ )]	2.17	0.42	0.045	0.007
$\sigma_{\text{tot}}$ [nb/(GeV/ $c$ )]	2.49	0.46	0.053	0.010

Table 7.3: Inclusive parton cross-section  $d\sigma/dp_t$  in  $ep$  scattering for  $\sqrt{s_{ep}} = 296$  GeV,  $Q^2 < 0.01$  GeV<sup>2</sup>,  $0.25 < y < 0.7$  and  $0 < \eta < 2.5$  together with its statistical and systematic errors determined for the sub-jet sample.  $\sigma_{\text{syst}}$  is the combined total systematic error and  $\sigma_{\text{tot}}$  is the quadratic sum of the statistical and total systematic errors. The unfolding is performed by means of a Monte Carlo simulation which is based on leading order (partonic) matrix elements (see text).

pedestal subtracted sample			
$\eta$ $\eta_{\min}, \eta_{\max}$	0.42 0.00 – 0.83	1.25 0.83 – 1.67	2.08 1.67 – 2.50
$d\sigma/d\eta$ [nb]	9.13	7.01	2.93
$\sigma_{\text{stat}}$ [nb]	1.31	1.04	0.85
$\sigma_{E\text{-scale}}$ [nb] $\sigma_{\text{others}}$ [nb]	2.19 2.69	1.64 2.07	0.75 0.86
$\sigma_{\text{syst}}$ [nb]	3.47	2.64	1.14
$\sigma_{\text{tot}}$ [nb]	3.71	2.84	1.42

Table 7.4: Inclusive parton cross-section  $d\sigma/d\eta$  in  $ep$  scattering for  $\sqrt{s_{ep}} = 296$  GeV,  $Q^2 < 0.01$  GeV<sup>2</sup>,  $0.25 < y < 0.7$  and  $p_t > 6$  GeV/ $c$  together with its statistical and systematic errors determined for the pedestal subtracted sample.  $\sigma_{\text{syst}}$  is the combined total systematic error and  $\sigma_{\text{tot}}$  is the quadratic sum of the statistical and total systematic errors. The unfolding is performed by means of a Monte Carlo simulation which is based on leading order (partonic) matrix elements (see text).

fluctuation reduced sample			
$\eta$ $\eta_{\min}, \eta_{\max}$	0.42 0.00 – 0.83	1.25 0.83 – 1.67	2.08 1.67 – 2.50
$d\sigma/d\eta$ [nb]	9.29	7.84	8.51
$\sigma_{\text{stat}}$ [nb]	1.16	0.81	1.06
$\sigma_{E\text{-scale}}$ [nb] $\sigma_{\text{others}}$ [nb]	2.24 2.74	1.71 2.31	2.28 2.51
$\sigma_{\text{syst}}$ [nb]	3.54	2.87	3.39
$\sigma_{\text{tot}}$ [nb]	3.72	2.99	3.55

Table 7.5: Inclusive parton cross-section  $d\sigma/d\eta$  in  $ep$  scattering for  $\sqrt{s_{ep}} = 296$  GeV,  $Q^2 < 0.01$  GeV<sup>2</sup>,  $0.25 < y < 0.7$  and  $p_t > 6$  GeV/ $c$  together with its statistical and systematic errors determined for the fluctuation reduced sample.  $\sigma_{\text{syst}}$  is the combined total systematic error and  $\sigma_{\text{tot}}$  is the quadratic sum of the statistical and total systematic errors. The unfolding is performed by means of a Monte Carlo simulation which is based on leading order (partonic) matrix elements (see text).

sub-jet sample			
$\eta$ $\eta_{\min}, \eta_{\max}$	0.42 0.00 – 0.83	1.25 0.83 – 1.67	2.08 1.67 – 2.50
$d\sigma/d\eta$ [nb]	10.72	8.74	7.28
$\sigma_{\text{stat}}$ [nb]	1.94	1.63	2.51
$\sigma_{E\text{-scale}}$ [nb] $\sigma_{\text{others}}$ [nb]	3.14 3.16	2.01 2.58	1.80 2.15
$\sigma_{\text{syst}}$ [nb]	4.45	3.27	2.80
$\sigma_{\text{tot}}$ [nb]	4.86	3.65	3.76

Table 7.6: Inclusive parton cross-section  $d\sigma/d\eta$  in  $ep$  scattering for  $\sqrt{s_{ep}} = 296$  GeV,  $Q^2 < 0.01$  GeV<sup>2</sup>,  $0.25 < y < 0.7$  and  $p_t > 6$  GeV/ $c$  together with its statistical and systematic errors determined for the sub-jet sample.  $\sigma_{\text{syst}}$  is the combined total systematic error and  $\sigma_{\text{tot}}$  is the quadratic sum of the statistical and total systematic errors. The unfolding is performed by means of a Monte Carlo simulation which is based on leading order (partonic) matrix elements (see text).

### 7.3 Measurement of $f_{g/\gamma}(x_\gamma)$

To measure the gluon density function  $f_{g/\gamma}(x_\gamma)$ , we unfold the  $x_\gamma^{\text{jets}}$ -distribution in 2-jet events. By subtracting the predicted contributions to this distribution from direct and quark induced resolved processes, we get a measured  $x_\gamma$ -distribution which is due to gluons from the photon alone. Comparing this latter distribution with the expected distribution for gluon induced processes then leads to correction factors (as a function of  $x_\gamma$ ) which have to be applied to the gluon density function used in the Monte Carlo simulation. This then results in a measurement of  $f_{g/\gamma}(x_\gamma)$ . We will in the following describe the different steps towards a measurement of  $f_{g/\gamma}(x_\gamma)$  in more detail.

Before we unfold the measured  $x_\gamma^{\text{jets}}$ -distribution, we again prove that the unfolding procedure works. This can be done by unfolding the  $x_\gamma^{\text{jets}}$ -distribution of a MC sample and comparing the unfolded result  $d\tilde{N}_{\text{events}}(x_\gamma)/dx_\gamma$  with the input distribution  $dN_{\text{events}}(x_\gamma)/dx_\gamma$ . The unfolding procedure only works if these distributions coincide! For this purpose, we use the MC sample without multiple interactions as a “data” sample and unfold the  $x_\gamma^{\text{jets}}$ -distribution with the help of the final, pedestal subtracted MC sample which includes multiple interactions as the “MC” sample. In addition to the selection cuts described in chapters 5 and 6, a cut on  $\hat{p}_t > 4 \text{ GeV}/c$  has been applied for the “MC” sample (no effect for the “data” sample since this cut was already applied when generating the events, see section 3.1). For the unfolding procedure,  $\log_{10}x_\gamma^{\text{jets}}$  is used as unfolding variable rather than  $x_\gamma^{\text{jets}}$ . This results in a flatter distribution to be unfolded and gives a better resolution at small  $x_\gamma$ .

Figure 7.14 shows the unfolded  $d\tilde{N}_{\text{events}}(x_\gamma)/dx_\gamma$ -distribution together with the input distribution  $dN_{\text{events}}(x_\gamma)/dx_\gamma$ .

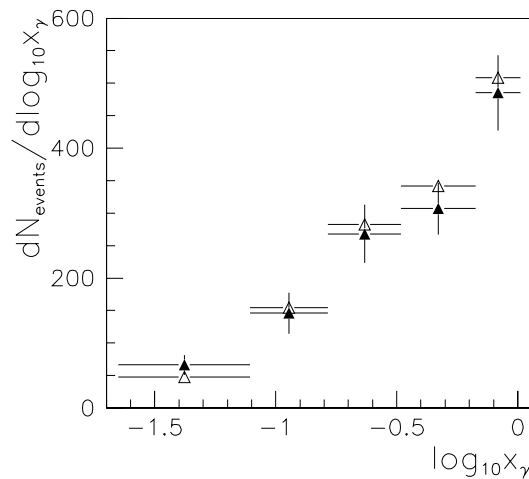


Figure 7.14:  $\log_{10}x_\gamma$ -distribution. Comparison of the unfolded  $d\tilde{N}_{\text{events}}(x_\gamma)/dx_\gamma$ -distribution ( $\blacktriangle$ ) with the input distribution  $dN_{\text{events}}(x_\gamma)/dx_\gamma$  ( $\Delta$ ).

The unfolding procedure reproduces the input distribution well.

### 7.3.1 Unfolding the $x_\gamma^{\text{jets}}$ -distribution

The unfolding of the  $x_\gamma^{\text{jets}}$ -distribution in 2-jet events is done for all three final data samples. For the correlation between  $x_\gamma^{\text{jets}}$  and  $x_\gamma$ , the respective final MC samples are used. Again, we use the final, pedestal subtracted sample to discuss the different steps of the unfolding procedure. As before, the unfolding is done in  $\log_{10}x_\gamma^{\text{jets}}$  rather than  $x_\gamma^{\text{jets}}$ . Figure 7.15 shows the unfolded  $x_\gamma$ -distribution.

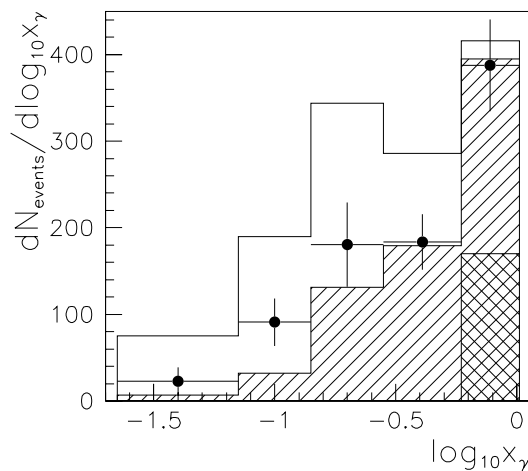


Figure 7.15: Unfolded  $\log_{10}x_\gamma$ -distribution. Comparison of data (points) and MC (histogram; the MC is normalized to the integrated luminosity of the data sample). The contributions to the  $x_\gamma$ -distribution due to direct (double hatched) and resolved processes are given separately (MC only). The latter are further subdivided into processes initiated by a quark (single hatched) or a gluon (open histogram) from the photon. The final, pedestal subtracted samples are used.

Analogous to figure 7.3, we show the  $x_\gamma$ -distribution expected from the Monte Carlo simulation, too. The observation that we need both resolved and direct processes to describe the measured  $x_\gamma^{\text{jets}}$ -distribution is nicely confirmed by the unfolded  $x_\gamma$ -distribution.

To check the unfolding, we first compare the  $x_\gamma^{\text{jets}}$ -distribution in the data with the reweighted  $x_\gamma^{\text{jets}}$ -distribution obtained from the Monte Carlo simulation after the unfolding process (*cf.* figure 7.16).

The reweighted  $x_\gamma^{\text{jets}}$ -distribution describes the data well.

As before, we check some other distributions to make sure that the unfolding procedure not only leads to a good description of the  $x_\gamma^{\text{jets}}$ -distribution, but also results in a good description of all other possible distributions. Only in the latter case can we assume that the extracted parton density function is physically sensible, *i.e.*,

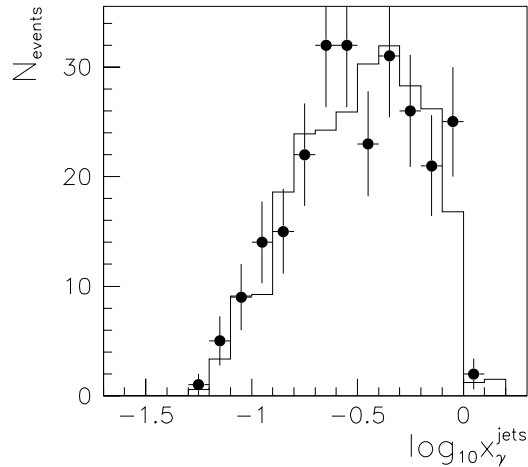


Figure 7.16:  $\log_{10}x_\gamma^{\text{jets}}$ -distribution. Comparison of the data distribution (points) with the reweighted Monte Carlo distribution (histogram). The MC is normalized to the integrated luminosity of the data sample. The final, pedestal subtracted samples are used.

that all other ingredients to the modeling of the data are correct. In figures 7.17 and 7.18, all jet properties and jet jet correlations are shown for data and for the reweighted Monte Carlo sample. In addition, the  $y_{\text{tag}}$ -distribution is given.

All distributions are well described by the MC after the reweighting. Note that the unfolding procedure has a rather strong impact on the shape of the  $\eta^{\text{jet}}$ -distribution and leads to a better description of the data as compared to before the unfolding procedure. This is not surprising but rather expected, since the shape of the  $\eta^{\text{jet}}$ -distribution is sensitive to the parton density function of the photon. For all other distributions (apart from  $x_\gamma^{\text{jets}}$ ), the reweighting of the MC events owing to the unfolding procedure mainly results in a change of the total rate.

### 7.3.2 Determination of $f_{g/\gamma}(x_\gamma)$

After having unfolded the  $x_\gamma^{\text{jets}}$ -distribution in 2-jet events (*i.e.*, we corrected for the transformation between  $x_\gamma^{\text{jets}}$  and  $x_\gamma$  and for the limited resolution in  $x_\gamma$ ), we can now proceed and subtract the predicted contributions to the  $x_\gamma$ -distribution from direct and quark induced resolved processes.

The contributions to the  $x_\gamma$ -distribution from direct and quark induced resolved processes are expected to be described fairly well by the Monte Carlo simulation. For direct processes, one does not need to know the parton density functions of the photon and for the quark induced resolved processes, measurements of  $F_2^\gamma(x, Q^2)$  at  $e^+e^-$  experiments provide a good constraint for the quark density function  $f_{q/\gamma}(x_\gamma)$  in the entire  $x_\gamma$ -range explored by this analysis (see section 1.2.3.4). Therefore,

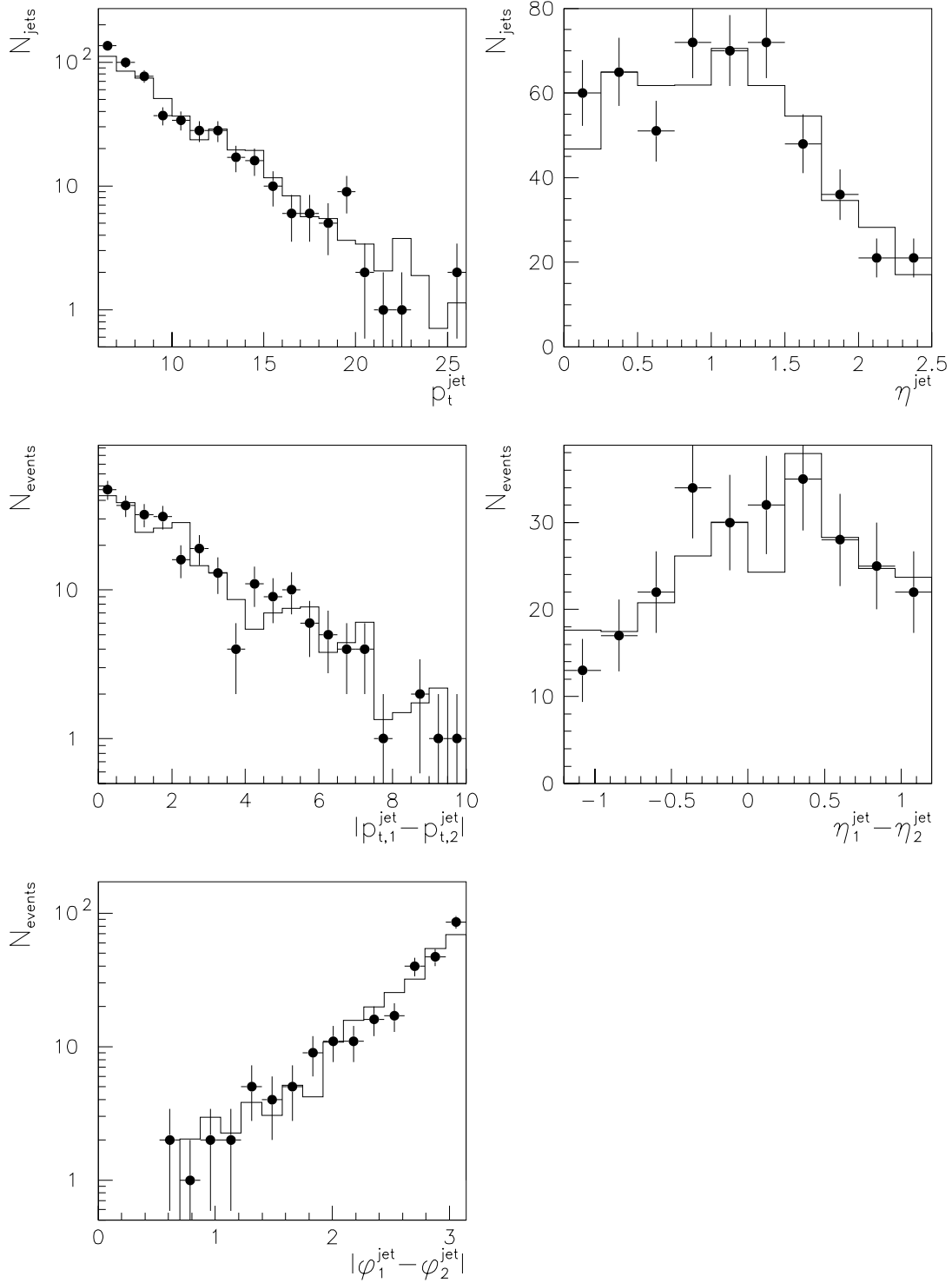


Figure 7.17:  $p_t^{\text{jet}}$ ,  $\eta^{\text{jet}}$ ,  $|p_{t,1}^{\text{jet}} - p_{t,2}^{\text{jet}}|$ ,  $\eta_1^{\text{jet}} - \eta_2^{\text{jet}}$  and  $|\varphi_1^{\text{jet}} - \varphi_2^{\text{jet}}|$  distribution. Comparison of data (points) and reweighted Monte Carlo distribution (histogram). The MC is normalized to the integrated luminosity of the data sample. The final, pedestal subtracted samples are used.

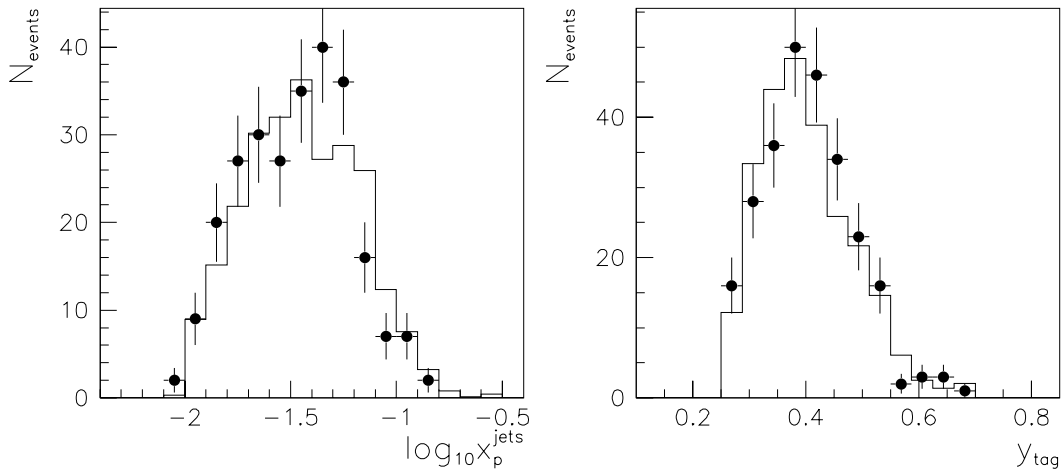


Figure 7.18:  $\log_{10}x_p^{\text{jets}}$ - and  $y_{\text{tag}}$ -distribution. Comparison of data (points) and reweighted Monte Carlo distribution (histogram). The MC is normalized to the integrated luminosity of the data sample. The final, pedestal subtracted samples are used.

the only (major) uncertainty left for the prediction of the direct and quark induced resolved processes is due to higher order corrections, which are estimated to be of the order of  $\lesssim 30\%$  (see section 6.1).

In figure 7.15 above, the unfolded  $x_\gamma$ -distribution is compared with the  $x_\gamma^{\text{jets}}$ -distribution expected from the MC simulation. For the latter, the contributions due to direct, quark induced resolved and gluon induced resolved processes are given separately. At very large  $x_\gamma$ , where the expected contribution due to gluon induced resolved processes is small, the Monte Carlo simulation gives a good description of the data. We may therefore state that the *rate* for direct and quark induced resolved processes at large  $x_\gamma$  is well predicted by the MC simulation, *i.e.*, that the leading order calculation gives a good description of the data. By assuming that the shape of the quark density function  $f_{q/\gamma}(x_\gamma)$  is reasonably well known from  $\gamma\gamma$  interactions at  $e^+e^-$  experiments, we can then expect that the predicted contribution to the  $x_\gamma$ -distribution from quark induced resolved processes is good for the entire accessible  $x_\gamma$ -range.

For low  $x_\gamma$  (see again figure 7.15), the quark induced resolved processes do not seem to fully account for the observed  $x_\gamma$ -distribution. We may assign the additional events in the  $x_\gamma$ -distribution to gluon induced resolved processes. Systematic errors have to be checked before we can claim that gluon induced resolved processes are needed to describe the measured  $x_\gamma$ -distribution.

To get a measurement of  $f_{g/\gamma}(x_\gamma)$  rather than just  $dN_{\text{events}}(x_\gamma)/dx_\gamma$  from gluon induced processes alone, we correct for the effects due to the limited acceptance of the detector and due to the selection of the data by calculating the following scaling factor:

$$\frac{dN_{\text{events}}(x_\gamma)/dx_\gamma - dN_{\text{events,MC}}^{g,\gamma}(x_\gamma)/dx_\gamma}{dN_{\text{events,MC}}^g(x_\gamma)/dx_\gamma} . \quad (7.10)$$

This  $x_\gamma$ -dependent scaling factor can now be multiplied with the gluon density function used for the Monte Carlo simulation, in our case GRV-LO. The resulting distribution is the *measured* gluon density function  $f_{g/\gamma}(x_\gamma, \mu^2)$ . The dependence of the gluon density function on the scale  $\mu^2$  is thereby neglected. The average value used for the determination of the measured gluon density function is taken from the (LO)  $p_t$ -distribution of the final, pedestal subtracted MC sample:  $\mu^2 = \langle \hat{p}_t \rangle^2 = 75 \text{ GeV}^2$ . For the fluctuation reduced sample, the average transverse momentum squared amounts to  $\langle \hat{p}_t \rangle^2 = 65 \text{ GeV}^2$ , whereas for the sub-jet sample it amounts to  $\langle \hat{p}_t \rangle^2 = 130 \text{ GeV}^2$ . We nevertheless neglect these differences (see also discussion on systematic error below) and quote the final results for the scale  $\mu^2 = \langle \hat{p}_t \rangle^2 = 75 \text{ GeV}^2$ .

Figures 7.20–7.22 show the measured momentum weighted gluon density function  $x_\gamma f_{g/\gamma}(x_\gamma, \mu^2)/\alpha$  ( $\alpha = 1/137$ ) of the photon together with some parametrizations of the same quantity for the three final samples (see also tables 7.7–7.9).

The results quoted do not depend on the parameters used for the unfolding program (*i.e.*, number of bins used for the input and result distributions, maximal number of B-splines used for the unfolding fit, *etc.*) nor do they depend on the parton density function parametrization used for the Monte Carlo simulations. This has been checked by varying the unfolding parameters as well as by using different parton density function parametrizations for the photon, *i.e.*, LAC I and LAC III instead of GRV-LO. The different results for one energy flow correction method agree, *i.e.*, the difference of the results is smaller than the statistical error.

Note that the three results obtained from the three different samples are systematically different. The difference is largest at small  $x_\gamma$ .

### 7.3.3 Systematic errors

We have only considered statistical errors so far. However, there are a few sources of systematic uncertainty. Some of them were already discussed in section 7.2.3.

- Uncertainty of energy flow correction method:

We again use the difference of the results obtained with the three different methods as a measure of the systematic error introduced by each of the different methods.

The obtained systematic error is large for small  $x_\gamma$  and less important at large  $x_\gamma$ , as expected from the fact that the deficiency of the MC simulation is most prominent at small  $x_\gamma^{\text{jets}}$  or, equivalently, large  $\eta^{\text{jet}}$ .

- Uncertainty in the absolute hadronic energy scale of 5%:

The possible systematic error due to this uncertainty was determined by repeating the entire analysis with rescaled cluster and cell energies ( $\pm 5\%$ , data only). The difference in the measured gluon density function compared to the results described above is used as systematic error,  $\sigma_{E\text{-scale}}$ .

The systematic error due to the uncertainty in the energy scale is largest at small  $x_\gamma$  (see tables 7.7–7.9).

- Uncertainty in the quark density function of the photon:

Although the quark density function of the photon is fairly well known from  $\gamma\gamma$  interactions, an uncertainty in the exact form of  $f_{q/\gamma}(x_\gamma)$  remains. From the quoted errors of existing measurements of  $F_2^\gamma(x, Q^2)$  (e.g. [35]) and from the variation of parametrizations of the quark density function of the photon, we estimate the uncertainty to be at most 30%. The systematic error for the gluon density function from this uncertainty,  $\sigma_{f_{q/\gamma}}$ , is determined by rescaling the quark density functions used in the Monte Carlo simulation by  $\pm 30\%$ .

The resulting systematic error is almost independent of  $x_\gamma$  (for the exact figures see tables 7.7–7.9).

At small  $x_\gamma$ , the main systematic error stems from the uncertainty in the energy flow correction method used and to a lesser extent from the uncertainty of the absolute hadronic energy scale. At large  $x_\gamma$ , all three contributions to the total systematic error are of similar importance.

In addition to the systematic errors described above, there are some minor contributions to the total systematic error. One is the uncertainty in the integrated luminosity of 4.5%. Its contribution to the systematic error is listed in tables 7.7–7.9. Another systematic error stems from the uncertainty in the dependence of the gluon density function  $f_{g/\gamma}(x_\gamma, \mu^2)$  on the scale  $\mu^2 = \langle \hat{p}_t \rangle^2$ . Figure 7.19 shows the variation in the gluon density function between  $\mu^2 = 50 \text{ GeV}^2$  and  $\mu^2 = 100 \text{ GeV}^2$ .

The variation is very small and will be neglected. Note that using a different scale for  $\mu^2$ , i.e.,  $\mu^2 = 2\langle \hat{p}_t \rangle^2$  or  $\mu^2 = 2\langle \hat{p}_t \rangle^2/2$ , would not change the result significantly, either. Finally, we have to estimate the systematic error due to the uncertainty in the parton density functions of the *proton*. Since the observed  $x_p^{\text{jets}}$ -distribution is well described by the Monte Carlo after the reweighting, we do not expect large effects due to different parton density functions for the proton. A variation of the gluon density function for the proton by  $\pm 15\%$  [93] changes the gluon density function of the photon at small<sup>4</sup>  $x_\gamma$  by  $\approx \mp 15\%$ .

Again, no extra systematic error for the dependence of the results on the Monte Carlo simulation (e.g. multiple interaction model, parton shower model or fragmentation)

---

<sup>4</sup>At large  $x_\gamma$ , the absolute variation is also small but the relative variation big, since the absolute values for  $x_\gamma f_{g/\gamma}(x_\gamma, \mu^2)/\alpha$  get very small towards large  $x_\gamma$ .

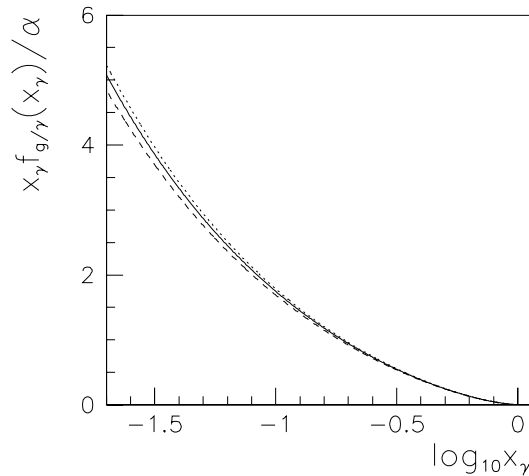


Figure 7.19: Momentum weighted gluon density function  $x_\gamma f_{g/\gamma}(x_\gamma, \mu^2)/\alpha$  of the photon for different scales  $\mu^2 = \langle \hat{p}_t \rangle^2$ . Comparison of the GRV-LO parametrization for  $\mu^2 = 75 \text{ GeV}^2$  (full line),  $\mu^2 = 50 \text{ GeV}^2$  (dashed line) and  $\mu^2 = 100 \text{ GeV}^2$  (dotted line).

is given. As mentioned earlier, part of this systematic error may be contained in the systematic error obtained from the different energy flow correction methods.

The final results for the gluon density function together with the statistical and systematic errors are depicted in figures 7.20–7.22 (see also tables 7.7–7.9).

The errors, most importantly the systematic difference of the results from the three energy flow correction methods, do not allow to claim that we need gluon induced resolved processes to describe the measured  $x_\gamma$ -distribution.

We can however exclude a high gluon density at large  $x_\gamma$  as predicted by the LAC III parametrization as well as a steeply rising gluon density function for small  $x_\gamma$  as suggested by the LAC I parametrization. The former is consistent with earlier measurements at TRISTAN [94] and LEP [95] whereas the latter has been reported recently by the DELPHI Collaboration [96]. The same conclusions have been drawn from a similar analysis of the 1993 HERA data by other members of the H1 Collaboration [97].

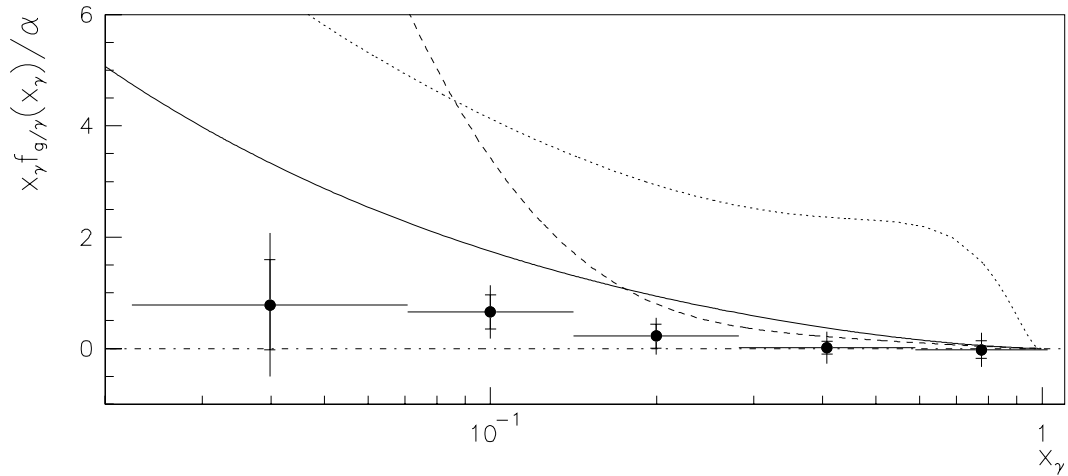


Figure 7.20: Momentum weighted gluon density function  $x_\gamma f_{g/\gamma}(x_\gamma, \mu^2)/\alpha$  of the photon at  $\mu^2 = \langle \hat{p}_t \rangle^2 = 75 \text{ GeV}^2$  determined with the pedestal subtracted sample. Inner error-bars show statistical errors, whereas outer error-bars are the (square root of the) quadratic sum of statistical and systematic errors. Comparison with the parametrizations of Glück, Reya and Vogt (GRV-LO, full line) and Abramowicz, Charchuła and Levy (LAC I, dashed line; LAC III, dotted line).

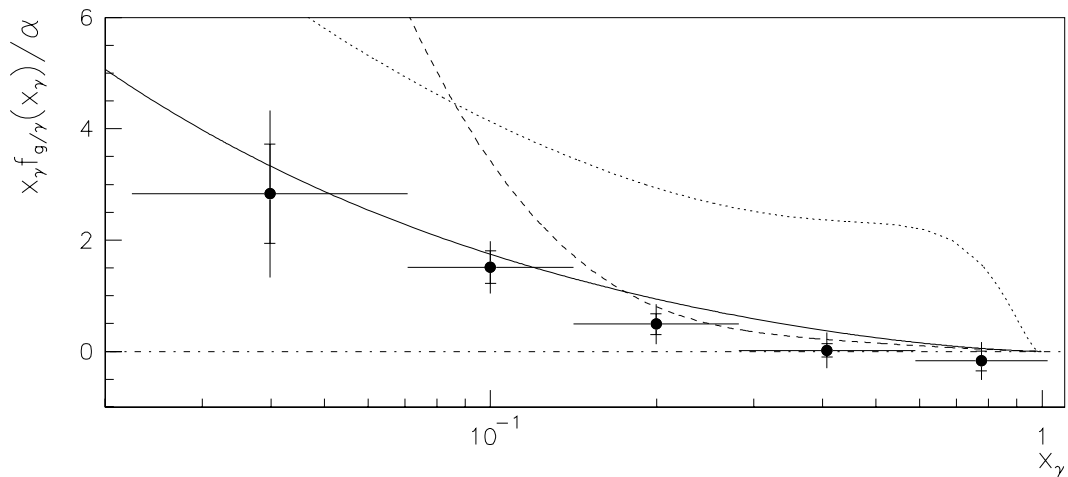


Figure 7.21: Momentum weighted gluon density function  $x_\gamma f_{g/\gamma}(x_\gamma, \mu^2)/\alpha$  of the photon at  $\mu^2 = \langle \hat{p}_t \rangle^2 = 75 \text{ GeV}^2$  determined with the fluctuation reduced sample. Inner error-bars show statistical errors, whereas outer error-bars are the (square root of the) quadratic sum of statistical and systematic errors. Comparison with the parametrizations of Glück, Reya and Vogt (GRV-LO, full line) and Abramowicz, Charchuła and Levy (LAC I, dashed line; LAC III, dotted line).

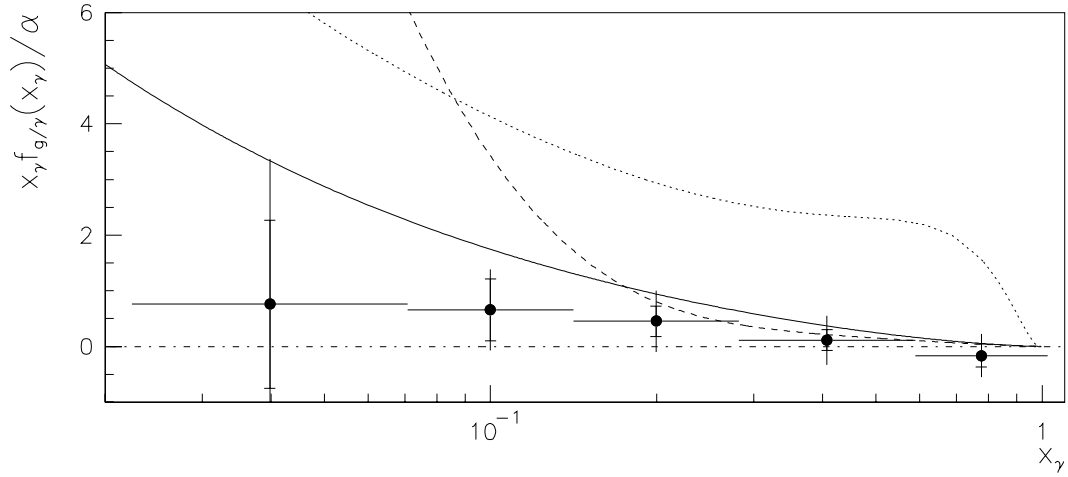


Figure 7.22: Momentum weighted gluon density function  $x_\gamma f_{g/\gamma}(x_\gamma, \mu^2)/\alpha$  of the photon at  $\mu^2 = \langle \hat{p}_t \rangle^2 = 75 \text{ GeV}^2$  determined with the sub-jet sample. Inner error-bars show statistical errors, whereas outer error-bars are the (square root of the) quadratic sum of statistical and systematic errors. Comparison with the parametrizations of Glück, Reya and Vogt (GRV-LO, full line) and Abramowicz, Charchuła and Levy (LAC I, dashed line; LAC III, dotted line).

pedestal subtracted sample					
$x_\gamma$ $x_{\gamma,\min}, x_{\gamma,\max}$	0.040 0.022–0.071	0.10 0.071–0.14	0.20 0.14–0.28	0.41 0.28–0.59	0.78 0.59–1.02
$x_\gamma f_{g/\gamma}(x_\gamma, \mu^2)/\alpha$	0.79	0.66	0.22	0.02	–0.02
$\sigma_{\text{stat}}$	0.81	0.31	0.22	0.11	0.16
$\sigma_{E\text{-scale}}$	0.96	0.33	0.21	0.15	0.15
$\sigma_{f_{q/\gamma}}$	0.31	0.15	0.13	0.22	0.22
$\sigma_{\text{lumi}}$	0.05	0.05	0.04	0.03	0.05
$\sigma_{\text{syst}}$	1.01	0.37	0.25	0.27	0.27
$\sigma_{\text{tot}}$	1.29	0.48	0.33	0.29	0.31

Table 7.7: Momentum weighted gluon density function  $x_\gamma f_{g/\gamma}(x_\gamma, \mu^2)/\alpha$  of the photon at  $\mu^2 = \langle \hat{p}_t \rangle^2 = 75 \text{ GeV}^2$  together with its statistical and systematic errors determined with the pedestal subtracted sample.  $\sigma_{\text{syst}}$  is the combined total systematic error and  $\sigma_{\text{tot}}$  is the quadratic sum of the statistical and total systematic errors.

fluctuation reduced sample					
$x_\gamma$ $x_{\gamma,\min}, x_{\gamma,\max}$	0.040 0.022–0.071	0.10 0.071–0.14	0.20 0.14–0.28	0.41 0.28–0.59	0.78 0.59–1.02
$x_\gamma f_{g/\gamma}(x_\gamma, \mu^2)/\alpha$	2.83	1.52	0.49	0.02	–0.17
$\sigma_{\text{stat}}$	0.89	0.30	0.18	0.12	0.18
$\sigma_{E\text{-scale}}$	1.13	0.33	0.24	0.20	0.15
$\sigma_{f_{q/\gamma}}$	0.39	0.11	0.20	0.21	0.24
$\sigma_{\text{lumi}}$	0.15	0.09	0.05	0.03	0.05
$\sigma_{\text{syst}}$	1.20	0.36	0.32	0.29	0.29
$\sigma_{\text{tot}}$	1.50	0.47	0.36	0.32	0.34

Table 7.8: Momentum weighted gluon density function  $x_\gamma f_{g/\gamma}(x_\gamma, \mu^2)/\alpha$  of the photon at  $\mu^2 = \langle \hat{p}_t \rangle^2 = 75 \text{ GeV}^2$  together with its statistical and systematic errors determined with the fluctuation reduced sample.  $\sigma_{\text{syst}}$  is the combined total systematic error and  $\sigma_{\text{tot}}$  is the quadratic sum of the statistical and total systematic errors.

sub-jet sample					
$x_\gamma$ $x_{\gamma,\min}, x_{\gamma,\max}$	0.040 0.022–0.071	0.10 0.071–0.14	0.20 0.14–0.28	0.41 0.28–0.59	0.78 0.59–1.02
$x_\gamma f_{g/\gamma}(x_\gamma, \mu^2)/\alpha$	0.76	0.66	0.46	0.12	–0.16
$\sigma_{\text{stat}}$	1.51	0.56	0.27	0.19	0.21
$\sigma_{E\text{-scale}}$	2.10	0.45	0.38	0.28	0.22
$\sigma_{f_{q/\gamma}}$	0.32	0.14	0.28	0.27	0.23
$\sigma_{\text{lumi}}$	0.05	0.05	0.06	0.05	0.06
$\sigma_{\text{syst}}$	2.12	0.47	0.48	0.39	0.32
$\sigma_{\text{tot}}$	2.61	0.73	0.55	0.44	0.39

Table 7.9: Momentum weighted gluon density function  $x_\gamma f_{g/\gamma}(x_\gamma, \mu^2)/\alpha$  of the photon at  $\mu^2 = \langle \hat{p}_t \rangle^2 = 75 \text{ GeV}^2$  together with its statistical and systematic errors determined with the sub-jet sample.  $\sigma_{\text{syst}}$  is the combined total systematic error and  $\sigma_{\text{tot}}$  is the quadratic sum of the statistical and total systematic errors.

# Summary

We have presented the measurements of the inclusive parton cross-sections  $d\sigma/dp_t$  and  $d\sigma/d\eta$  in electron proton scattering for the kinematical range  $\sqrt{s_{ep}} = 296$  GeV,  $Q^2 < 0.01$  GeV<sup>2</sup> and  $0.25 < y < 0.7$  for  $0 < \eta < 2.5$  ( $d\sigma/dp_t$ ) and  $p_t > 6$  GeV/ $c$  ( $d\sigma/d\eta$ ) as well as a measurement of the gluon density function of the (quasi-real) photon,  $f_{g/\gamma}(x_\gamma)$ .

It has been shown that both resolved and direct photon proton scattering processes are needed to describe the data. It has further been shown that the direct processes together with the quark induced resolved processes can well describe the measured  $x_\gamma$ -distribution in 2-jet events at large  $x_\gamma$ . At small  $x_\gamma$ , direct and quark induced resolved processes do not seem to fully account for the observed  $x_\gamma$ -distribution. However, we can not claim that gluon induced resolved processes are needed to describe the data.

What prevents us from better understanding the partonic structure of the photon at low  $x_\gamma$  is the presence of a transverse energy flow observed in photoproduction events which is not predicted by theoretical models. We have used three different methods to account for this poor description of the data. The systematic error introduced by these energy flow correction methods dominates the errors for the above-mentioned measurements. It is therefore mandatory that future investigations on the partonic structure of the photon concentrate on a better understanding of this transverse energy flow.

Despite the large systematic errors of our measurements, we can exclude a high gluon density at large  $x_\gamma$  as well as a steeply rising gluon density function for small  $x_\gamma$ .

# Bibliography

- [1] J.I. Friedman, Nobel lecture, reprinted in *Rev. Mod. Phys.* 63 (1991) 615;  
H.W. Kendall, Nobel lecture, reprinted in *Rev. Mod. Phys.* 63 (1991) 597;  
R.E. Taylor, Nobel lecture, reprinted in *Rev. Mod. Phys.* 63 (1991) 573
- [2] see *e.g.*  
S. Bentvelsen, J. Engelen and P. Kooijman, Proc. of the workshop “Physics at HERA”, Hamburg (1991), Vol. 1, 23;  
K.C. Hoeger, Proc. of the workshop “Physics at HERA”, Hamburg (1991), Vol. 1, 43
- [3] “Review of Particle Properties”, *Phys. Rev. D* 50 (1994) 1173
- [4] see any textbook on particle physics, *e.g.*  
F. Halzen and A.D. Martin, “Quarks & Leptons”, John Wiley & Sons (1984);  
I.J.R. Aitchison and A.J.G. Hey, “Gauge Theories in Particle Physics”, Adam Hilger (1989)
- [5] J.D. Bjørken and E.A. Paschos, *Phys. Rev.* 185 (1969) 1975;  
R.P. Feynman, *Phys. Rev. Lett.* 23 (1969) 1415
- [6] C.G. Callan and D. Gross, *Phys. Rev. Lett.* 22 (1969) 156
- [7] J.D. Bjørken, *Phys. Rev.* 179 (1969) 1547
- [8] H1 Collaboration, *Nucl. Phys.* B439 (1995) 471;  
H1 Collaboration, *Nucl. Phys.* B407 (1993) 515;  
ZEUS Collaboration, *Z. Phys.* C65 (1995) 379;  
ZEUS Collaboration, *Phys. Lett.* B316 (1993) 412
- [9] J.C. Collins, D.E. Soper and G. Sterman, in “Perturbative Quantum Chromodynamics”, ed. A.H. Mueller, World Scientific (1989), 1, and references therein
- [10] G. Altarelli and G. Parisi, *Nucl. Phys.* B126 (1977) 298;  
V.N. Gribov and L.N. Lipatov, *Sov. J. Nucl. Phys.* 15 (1972) 438;  
Yu.L. Dokshitzer, *Sov. Phys. JETP* 46 (1977) 641
- [11] T.H. Bauer *et al.*, *Rev. of Mod. Phys.* 50 (1978) 261

- 
- [12] J.J. Sakurai, *Ann. Phys.* 11 (1960) 1;  
M. Gell-Mann and F. Zachariasen, *Phys. Rev.* 124 (1961) 953
- [13] J.J. Sakurai and D. Schildknecht, *Phys. Lett.* B40 (1972) 121;  
M. Greco, *Nucl. Phys.* B63 (1973) 398
- [14] B.L. Ioffe, V.A. Khoze and L.N. Lipatov, "Hard processes", North Holland (1984), Vol. 1
- [15] D.O. Caldwell *et al.*, *Phys. Rev. Lett.* 40 (1978) 1222
- [16] E. Gotsman, D. Silverman and A. Soni, *Phys. Rev.* D20 (1979) 2220
- [17] C. Berger and W. Wagner, *Phys. Rep.* 146 (1987) 1;  
H. Kolanoski and P. Zerwas, in "High Energy  $e^+e^-$  Physics", eds. A. Ali and P. Söding, World Scientific (1988), 695
- [18] J.H. Da Luz Vieira and J.K. Storrow, *Z. Phys.* C51 (1991) 241
- [19] J.K. Storrow, *J. Phys.* G19 (1993) 1641
- [20] T.F. Walsh and P. Zerwas, *Phys. Lett.* B44 (1973) 195;  
R.L. Kingsley, *Nucl. Phys.* B60 (1973) 45;  
E. Witten, *Nucl. Phys.* B120 (1977) 189
- [21] R.J. DeWitt *et al.*, *Phys. Rev.* D19 (1979) 2046, *Phys. Rev.* D20 (1980) 1751 (Erratum)
- [22] G.A. Schuler, Proc. of the workshop "Physics at HERA", Hamburg (1991), Vol. 1, 461
- [23] C.F. Weizsäcker, *Z. Phys.* 88 (1934) 612;  
E.J. Williams, *Phys. Rev.* 45 (1934) 729
- [24] A. Levy, *J. Phys.* G19 (1993) 1489
- [25] G.A. Schuler and T. Sjöstrand, *Nucl. Phys.* B407 (1993) 539
- [26] NA14 Collaboration, *Phys. Lett.* B168 (1986) 163;  
NA14 Collaboration, *Phys. Lett.* B174 (1986) 458
- [27] OMEGA Photon Collaboration, *Z. Phys.* C43 (1989) 63;  
OMEGA Photon Collaboration, *Z. Phys.* C46 (1990) 35
- [28] JADE Collaboration, *Phys. Lett.* B107 (1981) 163;  
TASSO Collaboration, *Phys. Lett.* B107 (1981) 290;  
PLUTO Collaboration, *Z. Phys.* C26 (1984) 191
- [29] AMY Collaboration, *Phys. Lett.* B277 (1992) 215;  
TOPAZ Collaboration, *Phys. Lett.* B314 (1993) 149

- 
- [30] ALEPH Collaboration, Phys. Lett. B313 (1993) 509;  
DELPHI Collaboration, Z. Phys. C62 (1994) 357;  
DELPHI Collaboration, Phys. Lett. B342 (1995) 402
- [31] European Muon Collaboration (EMC), Phys. Lett. B100 (1981) 433;  
European Muon Collaboration (EMC), Z. Phys. C36 (1987) 527
- [32] H1 Collaboration, Phys. Lett. B297 (1992) 205;  
ZEUS Collaboration, Phys. Lett. B297 (1992) 404
- [33] see *e.g.*  
G. D'Agostini and D. Monaldi, Proc. of the workshop "Physics at HERA",  
Hamburg (1991), Vol. 1, 527;  
A. Valkarova, Proc. of the workshop "Physics at HERA", Hamburg (1991),  
Vol. 1, 535
- [34] H1 Collaboration, Nucl. Phys. B449 (1995) 3
- [35] TOPAZ Collaboration, Phys. Lett. B332 (1994) 477;  
OPAL Collaboration, Z. Phys. C61 (1994) 199;  
DELPHI Collaboration, CERN-PPE/95-87, to be submitted to Z. Phys. C
- [36] AMY Collaboration, Phys. Lett. B325 (1994) 248
- [37] M. Glück, E. Reya and A. Vogt, Phys. Rev. D46 (1992) 1973
- [38] H. Abramowicz, K. Charchuła and A. Levy, Phys. Lett. B269 (1991) 458
- [39] M. Drees and K. Grassie, Z. Phys. C28 (1985) 451
- [40] L.E. Gordon and J.K. Storrow, Z. Phys. C56 (1992) 307
- [41] H. Abramowicz *et al.*, Int. J. Mod. Phys. A8 (1993) 1005;  
F.M. Borzumati and G.A. Schuler, Z. Phys. C58 (1993) 139;  
L.E. Gordon, D.M. Holling and J.K. Storrow, J. Phys. G20 (1994) 549
- [42] B.H. Wiik, Proc. of the workshop "Physics at HERA", Hamburg (1991), Vol. 1,  
1, and references therein;  
F. Willeke, Int. J. Mod. Phys. A (Proc. Suppl.) 2A (1993) 28, and references  
therein
- [43] H1 Collaboration, DESY 93-103, to be submitted to Nucl. Instr. and Meth. A
- [44] H1 Calorimeter Group, Nucl. Instr. and Meth. A336 (1993) 460
- [45] H1 Calorimeter Group, Nucl. Instr. and Meth. A336 (1993) 499
- [46] H1 Calorimeter Group, Nucl. Instr. and Meth. A350 (1994) 57
- [47] H1 BEMC Group, DESY 95-177, submitted to Nucl. Instr. and Meth. A

- [48] T. Wolff *et al.*, Nucl. Instr. and Meth. A323 (1992) 537
- [49] S. Eichenberger *et al.*, Nucl. Instr. and Meth. A323 (1992) 532
- [50] H.U. Bengtsson and T. Sjöstrand, Comput. Phys. Commun. 46 (1987) 43
- [51] T. Sjöstrand, Comput. Phys. Commun. 39 (1986) 347;  
T. Sjöstrand and M. Bengtsson, Comput. Phys. Commun. 43 (1987) 367
- [52] B. Andersson *et al.*, Phys. Rep. 97 (1983) 31
- [53] H1 Collaboration, Phys. Lett. B299 (1993) 374;  
ZEUS Collaboration, Z. Phys. C63 (1994) 391;  
ZEUS Collaboration, Phys. Lett. B293 (1992) 465
- [54] M. Glück, E. Reya and A. Vogt, Z. Phys. C53 (1992) 127
- [55] T. Sjöstrand and M. van Zijl, Phys. Rev. D36 (1987) 2019
- [56] Axial Field Spectrometer (AFS) Collaboration, Z. Phys. C34 (1987) 163
- [57] UA2 Collaboration, Phys. Lett. B268 (1991) 145
- [58] CDF Collaboration, Phys. Rev. D47 (1993) 4857
- [59] S.D. Ellis, J. Phys. G17 (1991) 1552
- [60] J.E. Huth *et al.*, Proc. of the workshop “Research Directions for the Decade; Summer Study on High Energy Physics”, Snowmass (1990), 134
- [61] H1 Collaboration, Phys. Lett. B346 (1995) 415
- [62] ZEUS Collaboration, Phys. Lett. B354 (1995) 163
- [63] S. Catani, Yu.L. Dokshitzer and B.R. Webber, Phys. Lett. B285 (1992) 291
- [64] S. Catani *et al.*, Nucl. Phys. B406 (1993) 187
- [65] Yu.L. Dokshitzer, contribution to the workshop “Jets at LEP and HERA”, Durham (1990);  
S. Catani *et al.*, Phys. Lett. B269 (1991) 432
- [66] S.D. Ellis and D.E. Soper, Phys. Rev. D48 (1993) 3160
- [67] S. Wälti, diploma thesis, ETH Zürich (1993), unpublished
- [68] U. Amaldi *et al.*, Proc. of the workshop “Study of an *ep* facility for Europe”, Hamburg (1979), 377
- [69] R. Bernet, Ph. D. thesis, ETH Zürich (1995), unpublished

- 
- [70] S. Levonian, LPI Moscow, private communication (1995);  
H. Beck, University of Zurich, private communication (1995)
- [71] R. Bernet, ETH Zürich, private communication (1995)
- [72] H1 internal note 08/92-234, unpublished
- [73] H1 Collaboration, Z. Phys. C66 (1995) 529
- [74] S. Levonian, LPI Moscow, private communication (1994)
- [75] L.E. Gordon and J.K. Storrow, Phys. Lett. B291 (1992) 320
- [76] D. Bödeker, G. Kramer and S.G. Salesch, Z. Phys. C63 (1994) 471;  
G. Kramer and S.G. Salesch, Z. Phys. C61 (1994) 277;  
D. Bödeker, Z. Phys. C59 (1993) 501;  
D. Bödeker, Phys. Lett. B292 (1992) 164
- [77] M. Greco and A. Vicini, Nucl. Phys. B415 (1994) 386
- [78] P. Aurenche, J.-Ph. Guillet and M. Fontannaz, Phys. Lett. B338 (1994) 98
- [79] J. Gayler, DESY Hamburg, private communication (1995)
- [80] S. Eichenberger, Ph. D. thesis, University of Zurich (1993), unpublished
- [81] H1 internal note 09/94-383, unpublished
- [82] T. Sjöstrand, Comput. Phys. Commun. 82 (1994) 74
- [83] G. Marchesini *et al.*, Comput. Phys. Commun. 67 (1992) 465
- [84] R. Engel, Z. Phys. C66 (1995) 203
- [85] H1 Collaboration, DESY 95-219, to be published in Z. Phys. C
- [86] H1 Collaboration, Phys. Lett. B314 (1993) 436
- [87] C. Schwanenberger, diploma thesis, University of Heidelberg (1995), unpublished
- [88] W. Erdmann, ETH Zürich, private communication (1995)
- [89] V. Blobel, Proc. of the 1984 CERN School of Computing, Aiguablava, CERN 85-09 (1985), 88
- [90] G. Zech, DESY 95-113
- [91] V. Blobel, “RUN — generalized program for Regularized UNfolding”, program and manual (1984), unpublished

- [92] C. de Boor, "A practical guide to splines", Springer-Verlag (1978)
- [93] New Muon Collaboration (NMC), Phys. Lett. B258 (1991) 493;  
UA2 Collaboration, Phys. Lett. B299 (1993) 174;  
New Muon Collaboration (NMC), Phys. Lett. B309 (1993) 222
- [94] TOPAZ Collaboration, Phys. Lett. B314 (1993) 149;  
AMY Collaboration, Phys. Lett. B325 (1994) 248
- [95] DELPHI Collaboration, Phys. Lett. B342 (1995) 402
- [96] DELPHI Collaboration, CERN-PPE/95-87, to be submitted to Z. Phys. C
- [97] H1 Collaboration, Nucl. Phys. B445 (1995) 195;  
H. Hufnagel, Ph. D. thesis, University of Heidelberg (1994), unpublished;  
R. Kaschowitz, Ph. D. thesis, University of Aachen (1995), unpublished

# List of Figures

1.1	Kinematics of electron proton scattering. . . . .	8
1.2	Deep inelastic scattering off a proton or a photon. . . . .	13
1.3	$\gamma^*\gamma \rightarrow q_1q_2$ . . . . .	15
1.4	Hard scattering in photoproduction. . . . .	16
1.5	Direct processes (LO QCD) in photon proton scattering. . . . .	18
1.6	Resolved processes (LO QCD) in photon proton scattering. . . . .	19
1.7	Hard parton parton scattering. . . . .	22
1.8	Different parametrizations of $x_\gamma f_{g/\gamma}(x_\gamma, \mu^2)/\alpha$ . . . . .	25
2.1	HERA and its pre-accelerators. . . . .	26
2.2	The H1 detector with its main components. . . . .	28
4.1	$\eta^{\text{jet}}$ -distribution for matched and mismatched jets. . . . .	41
4.2	Jet parton correlation for $p_t$ , $\eta$ and $\varphi$ . . . . .	42
4.3	$ \eta_1^{\text{jet}} - \eta_2^{\text{jet}} $ -distribution for matched and mismatched jets. . . . .	44
4.4	Jet parton correlation for $\eta$ after $ \Delta\eta^{\text{jets}} $ -cut. . . . .	45
4.5	$y_{\text{tag}}$ and $y_{\text{JB}}$ versus true $y$ . . . . .	46
4.6	Correlation between $x_\gamma^{\text{jets}}$ and true $x_\gamma$ for different $y$ . . . . .	47
5.1	Efficiency of the DCRPh-Ta trigger-element. . . . .	54
5.2	$z$ -distribution of the event-vertex. . . . .	58
5.3	$E_{\text{tag}}$ -distribution for data, MC and background events. . . . .	59
5.4	2-jet event. Candidate for a resolved photoproduction event. . . . .	61
5.5	2-jet event. Candidate for a direct photoproduction event. . . . .	62
6.1	$p_t^{\text{jet}}$ - and $\eta^{\text{jet}}$ -distribution for 2-jet events. . . . .	65
6.2	$\hat{p}_t$ -distribution for the final MC sample. . . . .	67

6.3	$ p_{t,1}^{\text{jet}} - p_{t,2}^{\text{jet}} , \eta_1^{\text{jet}} - \eta_2^{\text{jet}}$ and $ \varphi_1^{\text{jet}} - \varphi_2^{\text{jet}} $ distribution for 2-jet events. . .	68
6.4	$\log_{10} x_\gamma^{\text{jets}}$ - and $\log_{10} x_p^{\text{jets}}$ -distribution for 2-jet events. . . . .	69
6.5	Jet-profiles in $\varphi$ as a function of $\eta^{\text{jet}}$ . . . . .	70
6.6	Jet-profile in $\eta$ for the final data sample. . . . .	77
6.7	Jet-profile in $\eta$ for the MC simulations. . . . .	77
6.8	Transverse energy flow as a function of $R_{(\eta,\varphi)}$ . . . . .	80
6.9	$E_t^{\text{pedestal}}$ -distribution as a function of $\eta^{\text{jet}}$ . . . . .	81
6.10	Average $E_t^{\text{pedestal}}$ as a function of $\eta^{\text{jet}}$ . . . . .	82
6.11	$R_{(\eta,\varphi),\text{max}}$ -distribution. . . . .	83
6.12	$p_t^{\text{jet}}$ - and $\eta^{\text{jet}}$ -distribution for different MC samples. . . . .	84
6.13	$x_\gamma^{\text{jets}}$ - and $x_\gamma$ -distribution for different MC samples. . . . .	85
6.14	$E_t^{\text{pedestal}} - \Delta E_t^{\text{pedestal}}$ as a function of $\eta^{\text{jet}}$ . . . . .	86
6.15	$\hat{p}_t$ -distribution for the final, pedestal subtracted MC sample. . . . .	87
6.16	$(E_{t,1}^{\text{jet}} + E_{t,2}^{\text{jet}})/E_{t,\text{event}}$ -distribution for data and MC. . . . .	88
6.17	$(E_{t,1}^{\text{jet}} + E_{t,2}^{\text{jet}})/E_{t,\text{event}}$ -distribution as a function of $\eta^{\text{jet}}$ . . . . .	89
6.18	Jet-profiles in $\varphi$ after the cut on $(E_{t,1}^{\text{jet}} + E_{t,2}^{\text{jet}})/E_{t,\text{event}}$ . . . . .	91
6.19	$E_t^{\text{pedestal}}$ -distribution after the cut on $(E_{t,1}^{\text{jet}} + E_{t,2}^{\text{jet}})/E_{t,\text{event}}$ . . . . .	92
6.20	$(E_{t,1}^{\text{jet}} + E_{t,2}^{\text{jet}})/E_{t,\text{event}}$ -distribution before and after pedestal subtraction. . . . .	94
6.21	Jet-profiles in $\varphi$ for $\delta_{\text{cut}} = 0.05$ . . . . .	96
6.22	$E_t^{\text{pedestal}}$ -distribution for $\delta_{\text{cut}} = 0.05$ . . . . .	97
6.23	$(E_{t,1}^{\text{jet}} + E_{t,2}^{\text{jet}})/E_{t,\text{event}}$ -distribution for $\delta_{\text{cut}} = 0.05$ . . . . .	98
7.1	Jet parton correlation (LO) for $p_t$ and $\eta$ . . . . .	101
7.2	Correlation between $x_\gamma^{\text{jets}}$ and $x_\gamma$ . . . . .	102
7.3	$\log_{10} x_\gamma^{\text{jets}}$ -distribution for data and MC. . . . .	103
7.4	Unfolded $d\sigma(p_t)/dp_t$ -distribution for a MC sample. . . . .	108
7.5	$(p_t^{\text{jet}})^{1/2}$ -distribution after unfolding. . . . .	109
7.6	$p_t^{\text{jet}}, \eta^{\text{jet}},  p_{t,1}^{\text{jet}} - p_{t,2}^{\text{jet}} , \eta_1^{\text{jet}} - \eta_2^{\text{jet}}$ and $ \varphi_1^{\text{jet}} - \varphi_2^{\text{jet}} $ distribution after unfolding. . . . .	110
7.7	$\log_{10} x_\gamma^{\text{jets}}$ - and $\log_{10} x_p^{\text{jets}}$ -distribution after unfolding. . . . .	111
7.8	$d\sigma/dp_t$ , pedestal subtracted sample. . . . .	111
7.9	$d\sigma/dp_t$ , fluctuation reduced sample. . . . .	112
7.10	$d\sigma/dp_t$ , sub-jet sample. . . . .	113
7.11	$d\sigma/d\eta$ , pedestal subtracted sample. . . . .	114

7.12	$d\sigma/d\eta$ , fluctuation sample. . . . .	115
7.13	$d\sigma/d\eta$ , sub-jet sample. . . . .	116
7.14	Unfolded $\log_{10}x_\gamma$ -distribution for a MC sample. . . . .	123
7.15	Unfolded $\log_{10}x_\gamma$ -distribution. . . . .	124
7.16	$\log_{10}x_\gamma^{\text{jets}}$ -distribution after unfolding. . . . .	125
7.17	$p_t^{\text{jet}}$ , $\eta^{\text{jet}}$ , $ p_{t,1}^{\text{jet}}-p_{t,2}^{\text{jet}} $ , $\eta_1^{\text{jet}}-\eta_2^{\text{jet}}$ and $ \varphi_1^{\text{jet}}-\varphi_2^{\text{jet}} $ distribution after unfolding.	126
7.18	$\log_{10}x_p^{\text{jets}}$ - and $y_{\text{tag}}$ -distribution after unfolding. . . . .	127
7.19	Momentum weighted gluon density function for different scales. . . . .	130
7.20	Gluon density function of the photon, pedestal subtracted sample. . . . .	131
7.21	Gluon density function of the photon, fluctuation reduced sample. . . . .	131
7.22	Gluon density function of the photon, sub-jet sample. . . . .	132

# List of Tables

3.1	MC samples used for this analysis. . . . .	34
7.1	$d\sigma/dp_t$ , pedestal subtracted sample. . . . .	117
7.2	$d\sigma/dp_t$ , fluctuation reduced sample. . . . .	118
7.3	$d\sigma/dp_t$ , sub-jet sample. . . . .	119
7.4	$d\sigma/d\eta$ , pedestal subtracted sample. . . . .	120
7.5	$d\sigma/d\eta$ , fluctuation reduced sample. . . . .	121
7.6	$d\sigma/d\eta$ , sub-jet sample. . . . .	122
7.7	Gluon density function of the photon, pedestal subtracted sample. . .	133
7.8	Gluon density function of the photon, fluctuation reduced sample. . .	134
7.9	Gluon density function of the photon, sub-jet sample. . . . .	135

# Acknowledgements

When working in such a large collaboration as H1 is, the list of people to thank naturally gets long. Therefore, let's cut it short: thanks to everybody! However, there are a few people who deserve to be mentioned explicitly:

I would like to express my gratitude to Ralph Eichler who gave me the opportunity to work in his fabulous group. Beyond that, he was a constant source of valuable advice and the thesis would not be as complete as it is now if he did not insist on clarifying several points.

Felicitas Paus readily accepted to be co-examiner and was motivating me to get it done. Thank you!

A sincere "thank you" goes to Christoph Grab who was my teacher for whatever one may think of — computing, the art of programming, a healthy scepticism towards rushed physics conclusions, *etc.* It was a pleasure working with him! Who knows, one day, we may even work on the same subject . . .

I would like to thank Thom Wolff and Josef Riedlberger for their patient introduction to the miracles and foot-traps of the DC- $r\varphi$  trigger as well as Roland Bernet for deepening this knowledge considerably. Besides that, I thank Roland for the great times we had during our post- and undergraduate studies.

Wolfram Erdmann deserves thanks for the many helpful discussions we had during the last year of my postgraduate education.

Special thanks also go to Urs Langenegger for his never-ending optimism, to Thomas Schietinger for his final proof-reading of the manuscript, to Stefano Wälti for the patience with his supervisor and to Helmut Hufnagel, Richard Kaschowitz, Martin Erdmann and Hartmut Rick for many helpful discussions.

I wish to sincerely thank my parents for their continuous moral support.

Last and certainly not least, I thank my beloved wife Theres Flury, to whom I dedicate this thesis as well as the following short piece of German poetry:

spruch mit kurzem o  
ssso  
(E. Jandl)

Finally, thanks go to YOU, who not only reads *this* page but all the other pages too!

# Curriculum vitae

Name Marco Arpagaus  
Born 1st November 1965, in Zurich  
Citizenship Uors-Peiden (GR) and Illnau-Effretikon (ZH), Switzerland

## *Education*

1972 – 1978 Primary School, Effretikon  
1978 – 1980 Secondary School, Effretikon  
1980 – 1984 High School, Kantonsschule im Lee, Winterthur  
1984 Eidgenössische Matura Typus C, Winterthur  
1985 – 1990 Study of Physics at the Swiss Federal Institute of  
Technology Zurich (ETH-Zürich), Zurich  
1990 Diploma in Experimental Physics at the ETH-Zürich  
Title of thesis: “Contributions to the optimization of the  
drift chamber trigger for the H1 experiment at HERA”  
1991 – 1995 Graduate Education in Experimental Physics at the Swiss  
Federal Institute of Technology Zurich (ETH-Zürich), Zurich